Springer Series in Chemical Physics 115

Kaoru Yamanouchi *Editor*

Progress in Photon Science

Basics and Applications

Springer

Springer Series in Chemical Physics

Volume 115

The purpose of this series is to provide comprehensive up-to-date monographs in both well established disciplines and emerging research areas within the broad fields of chemical physics and physical chemistry. The books deal with both fundamental science and applications, and may have either a theoretical or an experimental emphasis. They are aimed primarily at researchers and graduate students in chemical physics and related fields.

More information about this series at http://www.springer.com/series/676

Kaoru Yamanouchi
Editor

Progress in Photon Science

Basics and Applications

Springer

Editor
Kaoru Yamanouchi
Department of Chemistry
The University of Tokyo
Tokyo
Japan

ISSN 0172-6218
Springer Series in Chemical Physics
ISBN 978-3-319-52430-6 ISBN 978-3-319-52431-3 (eBook)
DOI 10.1007/978-3-319-52431-3

Library of Congress Control Number: 2017934062

Printed on acid-free paper

This Springer imprint is published by Springer Nature
The registered company is Springer International Publishing AG
The registered company address is: Gewerbestrasse 11, 6330 Cham, Switzerland

Preface

In October, 2014, School of Science, the University of Tokyo (UTokyo), jointly with Department of Civil Engineering, School of Engineering, established the Students and Researchers Exchange Program in Sciences (STEPS) with Lomonosov Moscow State University (MSU) and Saint Petersburg State University (SPBU) with financial support from the Re-Inventing Japan Project of the Ministry of Education, Culture, Sports, Science and Technology. Since then, we have been working to promote the STEPS program not only by exchanging students and researchers but also by holding scientific symposia and gatherings. The 1st STEPS Symposium on Photon Science was held on March 21 and 22, 2015 in the auditorium of the Chemistry Main Building on the Hongo Campus of the University of Tokyo, and was the first scientific gathering sponsored by the STEPS program.

In the symposium, a total of 28 talks were given by invited speakers from the three universities, and a variety of subjects in photon science were covered as represented by the titles of the nine chapters in this book: laser–plasma interaction, electron scattering, exotic properties of light, imaging, molecules and clusters in intense laser fields, new methods in spectroscopy, photochemistry of novel materials, light propagation and its applications, and material synthesis.

Invited talks were given by the following 28 professors: Mikhail Fedorov (International Laser Center), Maria Khrenova (Faculty of Chemistry), Olga Kosareva (International Laser Center and Faculty of Physics), Konstantin Kouzakov (Department of Nuclear Physics and Quantum Theory of Collisions, and Faculty of Physics), Vladimir Makarov (Chair of General Physics and Wave Processes, International Laser Center, and Faculty of Physics), Andrey Savel'ev

(Chair of General Physics and Wave Processes, International Laser Center, and Faculty of Physics), Alexander Shkurinov (Faculty of Physics and International Laser Center), Svyatoslav Shlenov (Faculty of Physics and International Laser Center), and Andrey Stolyarov (Faculty of Chemistry) from MSU; Alexander Andreev (Department of Quantum Electronics, Faculty of Physics), Alexander Konev (Department of Organic Chemistry, Institute of Chemistry), Alina Manshina (Department of Laser Chemistry and Laser Materials Science, Institute of Chemistry), Alexander Pastor (Department of Optics, Faculty of Physics), Alexey Povolotskiy (Institute of Chemistry), Sergey Pulkin (Department of General Physics 1, Faculty of Physics), Nikolay Timofeev (Department of Optics, Faculty of Physics), Sergey Tunik (Department of General and Inorganic Chemistry, Institute of Chemistry), Yury Tver'yanovich (Department of Laser Chemistry and Laser Materials Science, Institute of Chemistry), and Oleg Vyvenko (V. A. Fok Institute of Physics and Interdisciplinary Resource Center) from SPBU; Keisuke Goda (Department of Chemistry, School of Science), Masahiro Hoshino (Department of Earth and Planetary Science, School of Science), Shin Inouye (Department of Applied Physics, School of Engineering and Photon Science Center), Reika Kanya (Department of Chemistry, School of Science), Erik Lötstedt (Department of Chemistry, School of Science), Shinichi Ohkoshi (Department of Chemistry, School of Science), Takeaki Ozawa (Department of Chemistry, School of Science), Tatsuya Tsukuda (Department of Chemistry, School of Science), Junji Yumoto (Department of Physics, School of Science, and Institute for Photon Science and Technology) from UTokyo.

All of the lectures were well-prepared, and were very exciting and informative. The attendees enjoyed taking part in discussion, not only during the short discussion periods that were held right after the presentations, but also during the coffee breaks and lunch breaks. We, therefore, thought it appropriate to record the topics at the forefront of photon science addressed in the lectures in the form of a book for the benefit of researchers and graduate students in a variety of research fields in science, and have asked the lecturers to arrange their chapters based on transcriptions of the actual lectures.

I greatly appreciate the effort and cooperation made by the invited lecturers to modify their transcribed manuscripts into these completed forms. I would also like to thank the two secretaries at Center for Ultrafast Intense Laser Science, School of Science, the University of Tokyo, Ms. Tomoko Natalie Tateyama and Ms. Kaoru Kikuchi, and also Ms. Mihoshi Abe for their help with the preparation of this book. I hope this book will be regarded as a valued record of the STEPS program, facilitating its further promotion.

Finally, I would like to thank Ms. Valeria Shatilova at the STEPS office of School of Science, the University of Tokyo for helping us prepare for the 1st STEPS Symposium on Photon Science, and Dr. Claus Ascheron, Physics Editor at Springer, for kindly accepting this compilation of lectures as a volume in the Springer Series in Chemical Physics.

Tokyo
November 2016

Kaoru Yamanouchi

Contents

Part IX Material Synthesis

Contributors

Alexander Andreev Department of QE, Faculty of Physics, St. Petersburg State University, St. Petersburg, Russia; Max-Born Institute, Berlin, Germany; ELI-ALPS, Szeged, Hungary

V.A. Andreeva International Laser Center and Faculty of Physics, Lomonosov Moscow State University, Moscow, Russia

E. Borisov Center for Optical and Laser Materials Research, St. Petersburg State University, St. Petersburg, Russia

Pavel Chelushkin Institute of Chemistry, St. Petersburg State University, St. Petersburg, Russia

Mikhail Fedorov Lomonosov Moscow State University, Moskow, Russia

S. Fokina Institute of Chemistry, St. Petersburg State University, St. Petersburg, Russia

Keisuke Goda Department of Chemistry, School of Science, The University of Tokyo, Tokyo, Japan

Masahiro Hoshino Department of Earth and Planetary Science, School of Science, The University of Tokyo, Tokyo, Japan

Shin Inouye The University of Tokyo, Bunkyo, Japan; Graduate School of Science, Osaka City University, Osaka, Japan

Konstantin Ivanov International Laser Center and Faculty of Physics, Lomonosov Moscow State University, Moscow, Russia

V.P. Kandidov International Laser Center and Faculty of Physics, Lomonosov Moscow State University, Moscow, Russia

Reika Kanya Department of Chemistry, School of Science, The University of Tokyo, Tokyo, Japan

Tsuyoshi Kato Department of Chemistry, School of Science, The University of Tokyo, Tokyo, Japan

Mikhail Khodorkovskii Center "Nanobiotechnology", St. Petersburg State Technical University, St. Petersburg, Russia

Maria Khrenova Faculty of Chemistry, Moscow State University, Moscow, Russia

Alexander Konev Department of Organic Chemistry, Institute of Chemistry, St. Petersburg State University, St. Petersburg, Russia

O.G. Kosareva International Laser Center and Faculty of Physics, Lomonosov Moscow State University, Moscow, Russia

Igor Koshevoy Department of Chemistry, University of Eastern Finland, Joensuu, Finland

Konstantin Kouzakov Department of Nuclear Physics and Quantum Theory of Collisions, Faculty of Physics, Lomonosov Moscow State University, Moscow, Russia

Alexei Lar'kin International Laser Center and Faculty of Physics, M.V. Lomonosov Moscow State University, Moscow, Russia

Erik Lötstedt Department of Chemistry, School of Science, The University of Tokyo, Bunkyo-ku, Tokyo, Japan

Vladimir Makarov Chair of General Physics and Wave Processes, and International Laser Center, Lomonosov Moscow State University, Moscow, Russia

Alina Manshina Institute of Chemistry, St. Petersburg State University, St. Petersburg, Russia

Katsumi Midorikawa RIKEN Center for Advanced Photonics, Saitama, Japan

Yuya Morimoto Max-Planck-Institut für Quantenoptik, Garching, Germany

Shin-ichi Ohkoshi Department of Chemistry, School of Science, The University of Tokyo, Tokyo, Japan

Takeaki Ozawa Department of Chemistry School of Science, The University of Tokyo, Tokyo, Japan

N.A. Panov International Laser Center and Faculty of Physics, Lomonosov Moscow State University, Moscow, Russia

Alexander Pastor Department of Physics, St. Petersburg State University, St. Petersburg, Russia

Alexey Povolotskiy Institute of Chemistry, St. Petersburg State University, St. Petersburg, Russia

Sergey Pulkin Department of General Physics 1, Faculty of Physics, St. Petersburg State University, St. Petersburg, Russia

Andrey Savel'ev International Laser Center and Faculty of Physics, Lomonosov Moscow State University, Moscow, Russia

Pavel Serdobintsev Center "Nanobiotechnology", St. Petersburg State Technical University, St. Petersburg, Russia

D.E. Shipilo International Laser Center and Faculty of Physics, Lomonosov Moscow State University, Moscow, Russia

A.P. Shkurinov Faculty of Physics and International Laser Center, Lomonosov Moscow State University, Moscow, Russia

Svyatoslav Shlenov Faculty of Physics and International Laser Center, Lomonosov Moscow State University, Moscow, Russia

Sergei Shulyapov International Laser Center and Faculty of Physics, Lomonosov Moscow State University, Moscow, Russia

Andrey Stolyarov Faculty of Chemistry, Lomonosov Moscow State University, Moscow, Russia

Tatsuya Tsukuda Department of Chemistry, School of Science, The University of Tokyo, Tokyo, Japan

Ivan Tsymbalov International Laser Center and Faculty of Physics, Lomonosov Moscow State University, Moscow, Russia

Sergey Tunik Institute of Chemistry, St. Petersburg State University, St. Petersburg, Russia

Yury Tver'yanovich Institute of Chemistry, St. Petersburg State University, St. Petersburg, Russia

Roman Volkov International Laser Center and Faculty of Physics, Lomonosov Moscow State University, Moscow, Russia

Oleg Vyvenko V.A. Fok Institute of Physics and Interdisciplicary Resource Center, St. Petersburg State University, St. Petersburg, Russia

Kaoru Yamanouchi Department of Chemistry, School of Science, The University of Tokyo, Tokyo, Japan

Junji Yumoto School of Science, Institute of Photon Science and Technology, The University of Tokyo, Tokyo, Japan

Part I
Laser-plasma Interaction

Chapter 1
Relativistic Nano-Plasma Photonics

Alexander Andreev

Nano-plasma photonics is a field that deals with optical processes in a plasma at the nanoscale, much shorter than the wavelength of laser radiation. The laser-matter interactions, which include nano-scale confinement of radiation or matter and its transformation, present numerous opportunities for both fundamental research and technological applications.

I am going to talk about fast particle generation in a nano-foil target. Also I will talk about X-ray generation and its short-pulse production.

I want to remind you that this is a well-known diagram that shows how laser intensity has increased over that time period and where we are now. Currently, the intensity is slightly above 10^{21} Wcm^{-2}. But before the development of the CPA method, laser intensity was about 10^{15} Wcm^{-2}. So, as shown in Fig. 1.1, there was a big jump as laser intensity was enhanced about seven orders of magnitude. This was due to recent events in physics because such big enhancements are difficult to find in other fields of physics. This advance is connected with compression of laser pulses to achieve the power that can be produced from the known laser NIF, which is located in US, and which has an area about the size of a football field. Today, one optical table is needed to produce about the same laser power and of high intensity. In this case, with on one or two laboratory tables, we can investigate many interesting fields besides the well-known atomic "era". By increasing laser intensity, we can progress to the plasma "era" which is connected with plasma production, and,

A. Andreev (✉)
Department of QE, Faculty of Physics, St. Petersburg State University,
GOI, house 5, bld. 2, Kadetskaya liniya, V.O., St. Petersburg 199053, Russia
e-mail: alexanderandreev72@yahoo.com

A. Andreev
Max-Born Institute, Berlin, Germany

A. Andreev
ELI-ALPS, Szeged, Hungary

K. Yamanouchi (ed.), *Progress in Photon Science*, Springer Series
in Chemical Physics 115, DOI 10.1007/978-3-319-52431-3_1

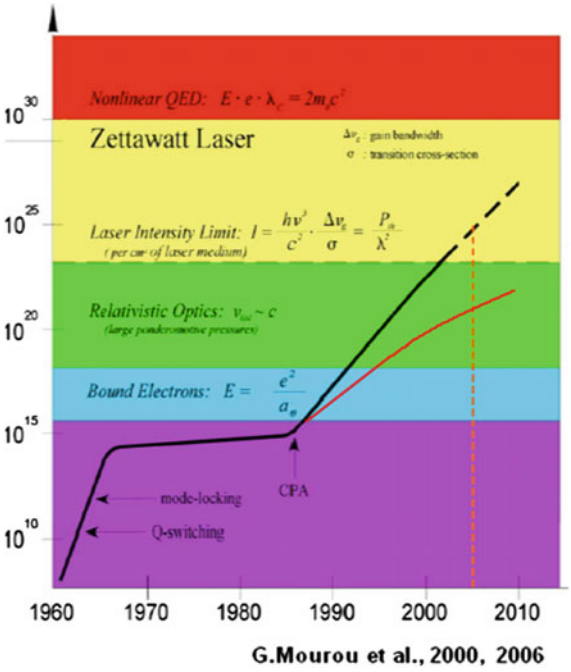

Fig. 1.1 The history of laser-intensity development

when we increase electron velocity up to the speed of light, we reach the field of 'relativistic objects' [1]. This is why 'relativistic' is an important word in my article's title. Even at higher laser intensities, we expect to investigate quantum electro-dynamic effects.

But, as you remember from my title, I am going to use nanostructure targets. In this case, we have a kind of contradiction because, from one side, we have a very high intensity, and, from the other side, we have the structure of the target. Intuitively, it seems that such high intensity will destroy any structure very quickly, and in this case there is no reason to use a nanostructure target. I will show that this is incorrect, and that, under some conditions, a relativistic-intensity laser interacting with nanostructure target gives us some positive enhancement and good results.

First of all, we should have a high-contrast laser pulse, because usually this laser pulse, which could be considered as Gaussian, has a long pre-pulse, and this pre-pulse can destroy any structure before the main pulse comes.

For this case, various techniques have been developed. One is shown in Fig. 1.2a and titled the "plasma mirror" technique, which enables us to increase the contrast ratio between the maximum and minimum of laser intensity up to 10^6; another technique, which is named XPD for "cross-polarization wave", enables us to enhance this value by eight orders of magnitude. Moreover, one, e.g., at Max-Born-Institute (MBI), has a contrast about 10^{14} (Fig. 1.2b), so it is the first technology developed recently to do this research.

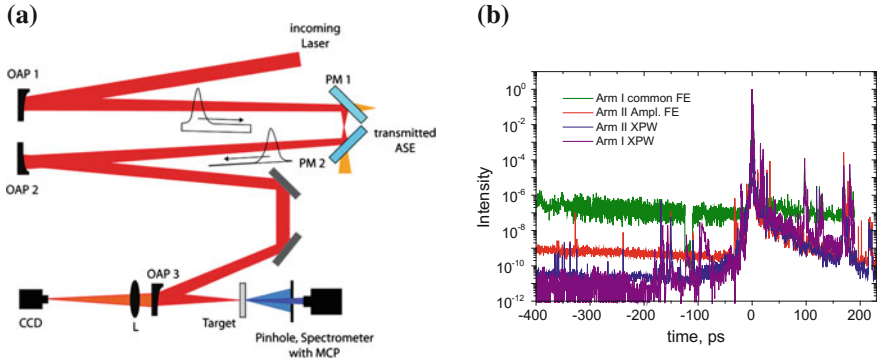

Fig. 1.2 **a** Double–plasma mirror (DPM) schema. **b** Laser-pulse temporal shape

Since we are going to do photonics in this case, we want to transform our laser light into another spectrum of radiation, and it could be X-rays or gamma quanta. There are a few processes that help us to generate hard X-ray or gamma photons. In this case, besides the standard scheme, when laser pulses generate fast electrons that later it transforms into X-ray, we can produce gamma photons or hard X-rays with the help of fast ions, for example, by nuclear reaction. In this case, we can do "photonics" not only with the help of electrons, but also with the help of ions. That is why I am going to explain ion generation and acceleration in my presentation.

One variant of a nanostructure target is a very simple, well–known, and very popular case in an experiment wherein one takes thin foil, hits this foil with a laser pulse, and produces fast-electrons. Usually, in an experiment, researchers use a foil thickness of few microns because it is easy to obtain. However, recently, there have been developments in technology to enable us to manufacture a foil of a few nanometers in thickness [2]. Of course, you know about grapheme, the thickness of which foil could be even less.

In this case, besides the standard TNSA regime, we can get an interesting acceleration regime which is named RPA "radiation pressure acceleration", when one can directly accelerate part of the matter with the help of a high-intensity laser, as you may remember, a relativistic intense laser pulse. In this case, we can get the best result if we are using in some sense semitransparent regime, wherein part of the laser pulse penetrates through this ultrathin foil and generates fast electrons and ions. Unfortunately in this case, we do not have a high efficiency, only about 10% for recent relativistic laser intensity and even ultra-relativistic. If we get an intensity $>10^{22}$ Wcm^{-2}, we will achieve a pure RPA regime, and, in this case, the efficiency is 100%, but in reality, currently, we are working with much lower efficiency. The question is how we can enhance the current efficiency?

The answer is to use nanostructure targets [3].

The key point here is we can make such nanostructures such as those that are shown in Fig. 1.3a and b.

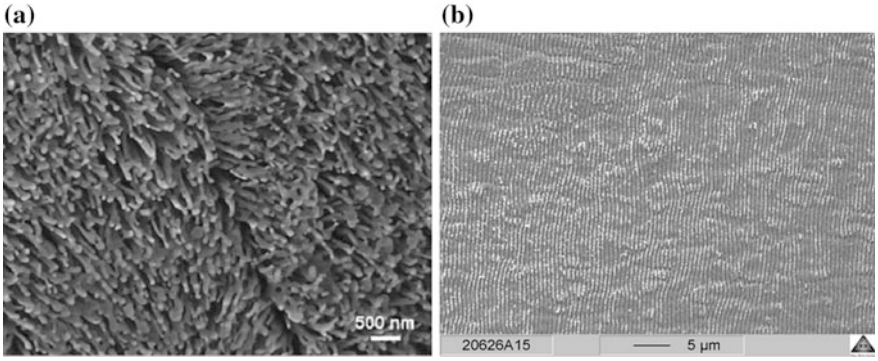

Fig. 1.3 **a** FESEM image of nano-rods and **b** image of super-long aligned brush-like CNT [8]

For example, first variant we named nanoforest while the other variant we named nanograting. These variants of nanostructures: nanorods, nanotubes, and nanogratings we can make now quite quickly and cover a large area. For example, in MBI, such a kind of target can be made with an area few millimeters by few millimeters in one day with the help of a low-intensity femtosecond laser. It provides a big advantage that we can make such a target with the same or similar laser and use it in an interaction with a relativistic pulse.

Having at least such possibilities at MBI, we decided to analyze how it can be used in reality.

We simulated the interaction of short intense laser pulses with such a nanostructure target; the magnification of the structure is shown in Fig. 1.4a [4]. In the 2D PIC simulation (see Fig. 1.4b), we found that if we irradiate the target from the nanostructure side, the electric field which accelerates electrons and ions is quite homogenous on the rear side. We hit the target and produce a quite homogenous electric field with high amplitude, and this field accelerates particles from the rear side. We have achieved a big enhancement, i.e., at least three times the proton energy when we used such a scheme, and a quite narrow diagram of generated ions.

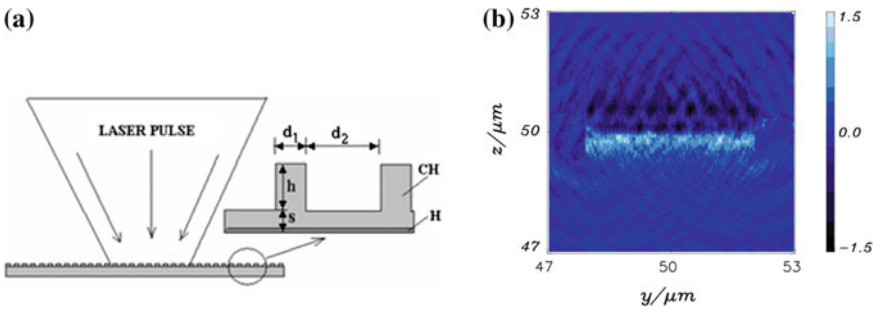

Fig. 1.4 **a** Schematic of the nanostructure target. **b** Spatial distribution of electric field component normal to the target surface. d_1 = 0.15 μm; d_2 = 0.35 μm; h = 0.3 μm

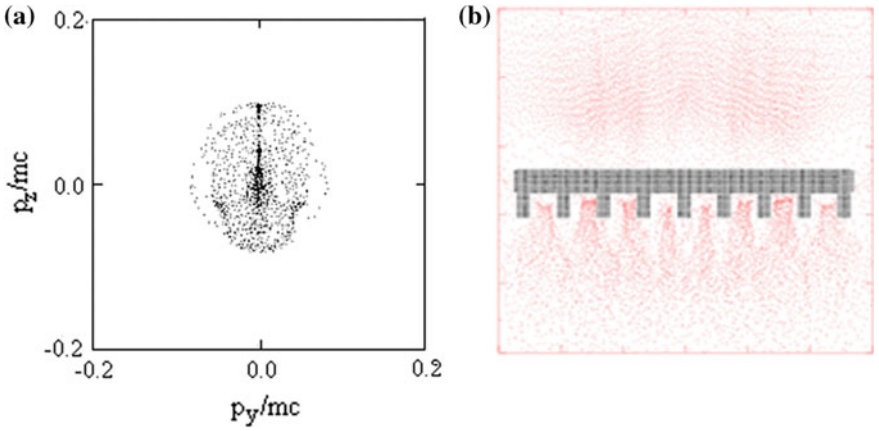

Fig. 1.5 **a** Proton angular distribution (laser-hit target from the *bottom*). **b** *Black* initial density, *red* density at 100 fs

At first we did it for at a very short laser pulse (15 fs) to avoid structure smoothing, but later we found that, at 100 fs and even more, we got another structure, which we named 'dynamic structure', because at first (see Fig. 1.5b), this black structure, we transformed into this red structure, and this red nanostructure help us again to enhance the interaction of the laser pulse with the target.

In Fig. 1.6a, one can see the dependences of absorption in the units of the plain target, so here it is seen that relative absorption (the ratio) shows us that we can enhance absorption six times compared to a plain target, and we can enhance the energy of the particles as well. This means that we can increase the efficiency for the nanostructure target compared to a plain target by up to 60% and, under some conditions, even up to 90%.

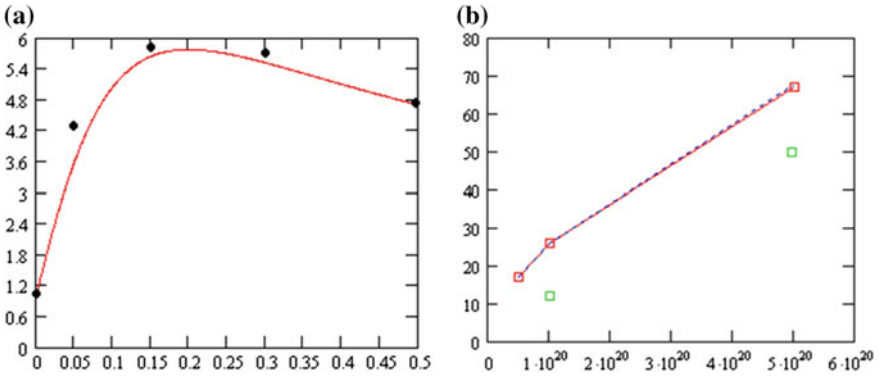

Fig. 1.6 **a** Absorption in the units of the plane of 300 nm foil. **b** Proton-energy dependence on laser intensity where the *green squares* are for the plane target and the *red* ones are for the structured target

There are some limitations for this effective interaction, and this limitation is shown here. First, we can thermally destroy our structure that we named 'thermal smoothing'.

$$\tau_p \sqrt{Z_p T_p / m_i} = \tau_p \sqrt{\eta_p I_p \tau_p / m_i n_i s} < 0.5\ d_2 \tag{1.1}$$

In this case, we should have a pre-pulse of duration τ_p of about one nanosecond on this level, so it means, for example, that for the ultra-relativistic intensity, we should have a contrast of 10^{10}. But, as it was shown at the beginning, we have one even higher, i.e., 10^{14}, so we don't worry about this limitation. Another limitation is connected with ponder motive smoothing when we remove electrons from our ledges, and in this case we have limitations [4].

$$E_L^2/4\pi < (en_e h)^2/8\pi \quad I_L \leq 10^{21}\ \mathrm{W/cm^2} \tag{1.2}$$

This means we can get the value of laser intensity close to the intensity where the RPA regime already gives us almost 100% efficiency, and, so, in between we can use a nanostructure target effectively.

Besides ion acceleration, because we effectively produce fast electrons, we can organize the transformation of this electron into X-ray radiation, and one example was considered sometime ago together with Japanese researchers from NTT BRL.

We developed some theory and simulations that show a good correlation between experimental and theoretical results (Fig. 1.7) [5]. At that time we have got an efficiency of about 10^{-5}, but later we analyzed this process with thin foil and nanostructure, and finally got an efficiency of about 10^{-3}. So it is a good result, because this means that, with the help of nanostructure foil, it could use a made heavy material, like silver, through the laser intensity 10^{19} W/cm^2, to generate an X-ray radiation of intensity 10^{16} W/cm^2 at about a photon energy of 20 keV.

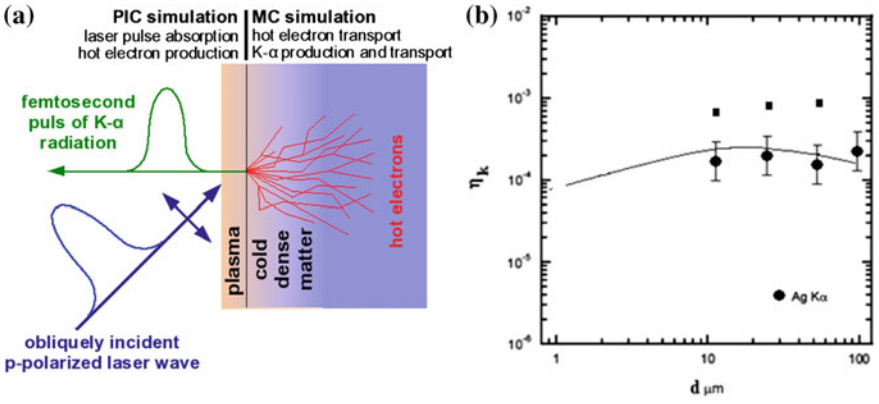

Fig. 1.7 **a** The schema of hybrid calculations. **b** Conversion efficiency of laser energy into the energy of *K*-alpha radiation

Earlier we considered nanostructure which we should implement in advance, and now the question is can we produce nanostructure on a target during the interaction.

The answer is—yes, and one example is the simulation results shown in Fig. 1.8, where we used semi-limited foil, denoted by solid black line, and a laser beam, denoted by blue line, interacting with this foil at oblique incidence [6]. The produced electron density is shown by red, black, and white, i.e., electromagnetic-field density. This electron density is modulated, and the bunch thickness has a nano-scale (see Fig. 1.8). Beside these nano-bunches, additionally, electromagnetic pulses were generated (see inset of Fig. 1.8). Their duration has an attosecond scale, which also is quite interesting for various applications.

The directionality of these electron bunches and atto-pulses is narrow enough, and the distribution function is quite interesting because it raises the question, where is the peak. Well, here's how we can obtain the parameter of electron nano-bunches and ATA pulses. For example, in Fig. 1.9, the dependence of the energy on the angle of incidence is shown. You can see that it is better to operate at very oblique incidence.

The dependence of electron energy on laser intensity is almost linear. There are different directions of electron-bunch propagation at oblique laser-pulse incidence: directly along the laser pulse, in a specular direction, and inside the target. Figure 1.10c shows how the duration of atto-pulse depends on the angle of incidence, so one can get about 100 pulse duration in such interaction.

We analyzed more details of this situation, and one example of the target constructed from two foils we named DREAM, Double Relativistic Electron Amplification Mirror where not only can we get a train of atto-pulses, but a single pulse and one nano-bunch as well (Fig. 1.11) [2].

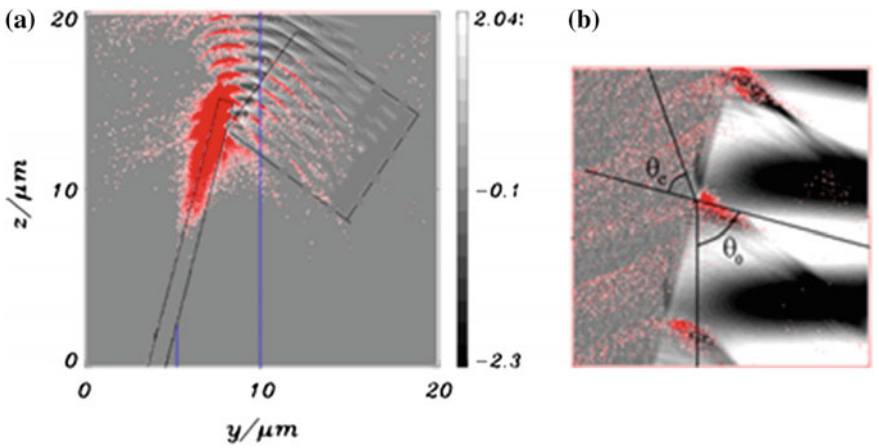

Fig. 1.8 **a** Laser field (*white*, *black*) and hot (>0.5 meV) electron density (*red*) at $t = 85$ fs. **b** Magnification of the surface target area. The laser and target parameters: 10^{20} W/cm^2, 26 fs, linear pol, diameter 4 μm, $C^{+6}H^{+1}$ target, ion density 6×10^{22} cm^{-3}, thickness 1 μm, 75° angle of incidence

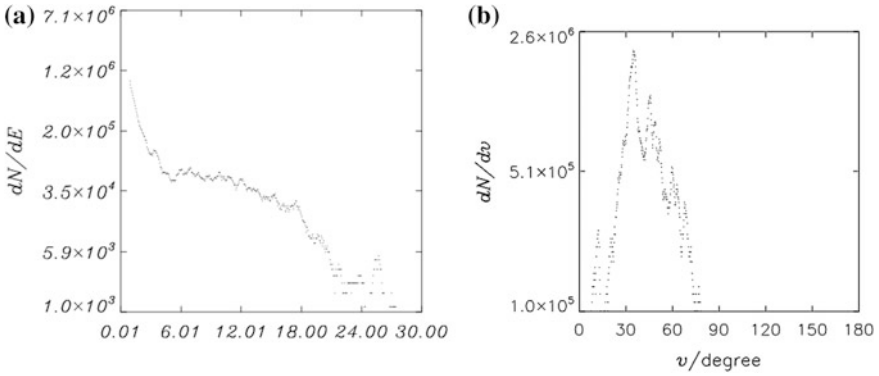

Fig. 1.9 **a** Electrons distribution function (in the *rectangle*) and **b** its angular distribution

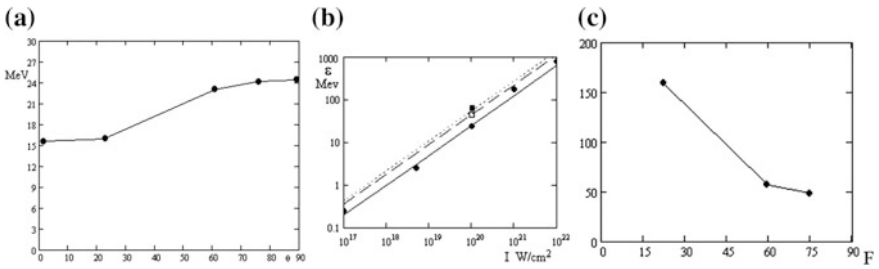

Fig. 1.10 **a** Max electron energy for s-bunch in dependence on laser incidence angle. **b** Max electron energy in s-bunch on laser intensity (angle 75°): *solid line* is limited target (of laser spot size); *dot line* is nonlimited, and *dash line* (1.5 laser spot size) **c** the dependence of atto-pulse duration (in nm) on the angle (in *degrees*) of laser-beam incidence on the target

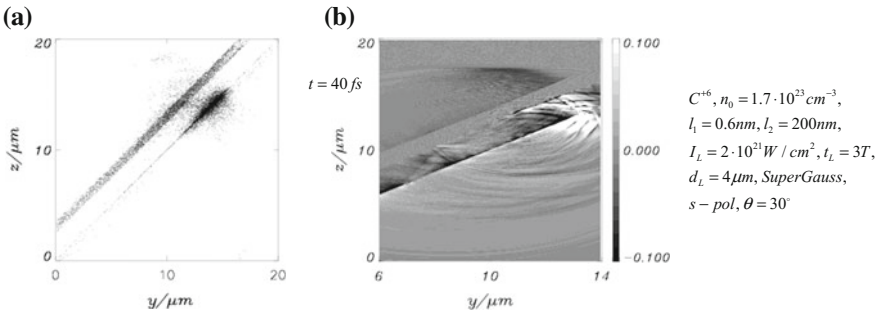

Fig. 1.11 The spatial distributions of electron density (**a**) and the electric field (**b**) for two foil cases interacting, where the laser pulse hits the thin foil from the *bottom* along the *z*-axis

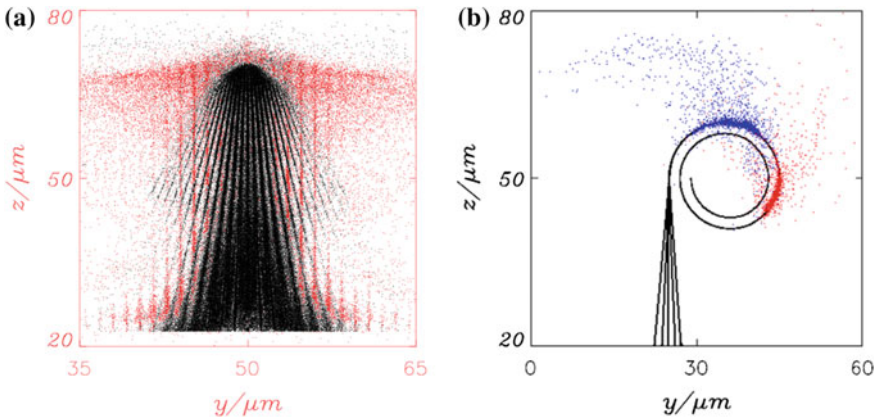

Fig. 1.12 **a** Electron density distribution at t = 210 fs, in cone (*black*) and straight (*red*) targets. **b** Electron density distribution at t = 277 fs in cone and dented wire targets

At the beginning, it was shown that we can make not only a nano-grating target, but also a nano-forest from nano-wires, which is shown in Fig. 1.12 by red straight lines.

In the case of a bulk target, due to the instability, the electron beam was usually destroyed, and we cannot achieve narrow beam propagation. But in the case of a wire target, we can deliver electrons very far away and even accumulate them, if we consider a cone target (black lines) at some point (see Fig. 1.12a). Moreover, we considered the variant where, at the top of nano-wire cone, was additionally attached a nano-wire (see Fig. 1.12b). When we hit this construction by a laser beam, our fast electrons propagate in this nano-wire as a separated bunch. For the dented wire, this bunch of fast electrons is following the wire and rotates, as shown in Fig. 1.12b, which could be interesting for some applications.

Because our electrons propagate and rotate along the wire, along the trajectories like spirals, they generate betatron radiation, and this variant of betatron-radiation production has a much higher efficiency as compared to the standard variant when we have the under-dense plasma that is well known in the literature. In this case, we can attain quite high efficiency of such betatron radiation production with a very high energy of photon [7].

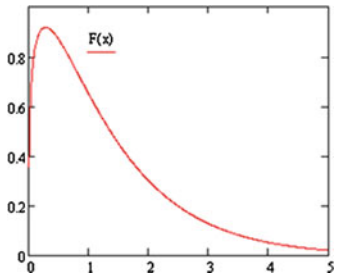

$$\frac{dP}{d\omega} = \frac{\sqrt{3}e^2\gamma_z}{2\pi r_E}\mu^2 F\left(\frac{\omega}{3\omega_c}\right) \qquad \mu = \frac{2e^2 N_{eh}}{m_e c^3 t_L \gamma_z}$$

$$dP/d\omega \approx 400 \cdot dP^{(BG)}/d\omega$$

$$\kappa = \frac{N_{eh}P_{1e}}{I_L \pi r_{\max}^2} \approx 0.02$$

$$\omega_c \approx \omega_L \gamma_z^3 \pi c / \upsilon_E (1.5 + 2\mu^{-1/2}) \approx 3MeV$$

$I_L = 10^{21} Wcm^{-2}, t_L = 30\,fs;$

The following is the conclusion:

- Optimal structure of a foil target enables attaining almost total absorption of the laser pulse. Profile shape has an influence on absorption.
- The absorbed laser energy is mainly transformed into an energy of heavy ions in a homogeneous composite target, and redistribution of this energy into light ions is possible for a heterogeneous target.
- For effective acceleration of ions, the volume of the relief should be less than the volume of the substrate foil.
- In our case, degradation of a structure by a laser pre-pulse is the most important factor. For this scheme to work, one needs a very high-contrast laser pulse and not more than nanosecond laser pre-pulse duration.
- Superposing relief raises the absorption and improves *K*-alpha photon yield. An optimally thick and laterally limited target with the optimal relief exhibits the highest laser to *K*-alpha line radiation conversion efficiency, up to 0.1%.
- The scheme of generation of short, energetic, dense electron bunches is offered for the interaction at large angles of incidence of the laser pulse with a thin semi-limited target. Such a target creates three streams of electron bunches propagating in specular, incident, and refracted directions in relation to the laser one. Conversion efficiency into fast electrons is about 4%.
- It is shown that a relativistic-intensity laser wave can be effectively (a few %) converted into a sequence of atto-pulses at the reflection point from a foil with a large angle of incidence.

The main conclusion is that a combination of relativistic-intensity laser pulse and nanostructure target help us to enhance many important parameters and to get a better results. This combination helps us to do very good photonics.

Acknowledgements I want to thank my contributors from Russia—Dr. K. Platonov, from Germany—the group of Dr. M. Schnurer and Dr. M. Kalashnikov and two groups from Japan of Dr. H. Nakano and Prof. S. Kawata.

References

1. A. Andreev, *Theory of laser-overdense plasma interaction in the book laser-plasma interactions and applications* (Springer, Scottish Graduate Series, 2013)
2. A. Andreev, K. Platonov, S. Sadykova, Appl. Sci. **3**, 94 (2013)
3. A. Andreev, K. Platonov, Contrib. Plasma Phys. **53**, 173 (2013)
4. A. Zigler, S. Eisenman, M. Botton, E. Nahum, E. Schleifer, A. Baspaly, I. Pomerantz, F. Abicht, J. Branzel, G. Priebe, S. Steinke, A. Andreev, M. Schnuerer, W. Sandner, D. Gordon, P. Sprangle, K.W.D. Ledingham, Phys. Rev. Lett. **110**, 215004 (2013)
5. N. Zhavoronkov, A. Andreev, K. Platonov, Laser Part. Beams **31**, 635 (2013)
6. A. Andreev, K. Platonov, Opt. Spectrosc. **114**(5), 788 (2013)
7. A.A. Andreev, P.V. Nickles, K.Yu. Platonov, Plasma Phys. & Control Fusion **56,** 084005 (2014)
8. S.K. Das, A. Andreev, H. Messaoudi, J. Braenzel, M. Schnuerer, R. Grunwald, J Appl Phys. **119**, 113101 (2016)
9. G.A. Mourou et al., Optics Communications **285**, 720 (2012)
10. A. Andreev, K.Yu. Platonov, Optics and Spectroscopy, **110**, 20 (2011)

Chapter 2
Super-Intense Laser-Plasma Interaction in Real-World Applications

Andrey Savel'ev, Konstantin Ivanov, Roman Volkov, Sergei Shulyapov, Ivan Tsymbalov and Alexei Lar'kin

In my talk, I would like to address the issue of super-intense laser-plasma interaction in relation to some applications in fundamental and applied science with potential in biology, medicine, nuclear non-proliferation, etc. This is why we would like not to think of some huge laser machines which are needed to produce intensities above 10^{20} W/cm^2, but would like to deal with really table-top femtosecond lasers that can be installed in any university-scale laboratory quite easily.

The parameters of our tetawatt Ti:sapphire laser are: energy per pulse 1–50 mJ, pulse duration $\sim$45 fs, central wavelength 805 nm, repetition rate 10 Hz with M^2 1.2–1.7. Figure 2.1 presents third-order correlation traces of our pulse in two configurations, and now we have also an XPW option, so the ultimate available contrast is some two orders of magnitude better.

The main activity of our laboratory is relativistic laser-plasma interaction with underdense plasma; with structured targets, we are trying to look at electron and ion

A. Savel'ev (✉) · K. Ivanov · R. Volkov · S. Shulyapov · I. Tsymbalov · A. Lar'kin
International Laser Center & Physics Faculty, M.V. Lomonosov Moscow State University, GSP-1, Leninskie Gory 1, Bld. 62, Moscow 119991, Russia
e-mail: abst@physics.msu.ru

K. Ivanov
e-mail: akvonavi@gmail.com

R. Volkov
e-mail: rv_volkov@phys.msu.ru

S. Shulyapov
e-mail: ser270489@ya.ru

I. Tsymbalov
e-mail: ivankrupenin2@gmail.com

A. Lar'kin
e-mail: alexeylarkin@ya.ru

K. Yamanouchi (ed.), *Progress in Photon Science*, Springer Series in Chemical Physics 115, DOI 10.1007/978-3-319-52431-3_2

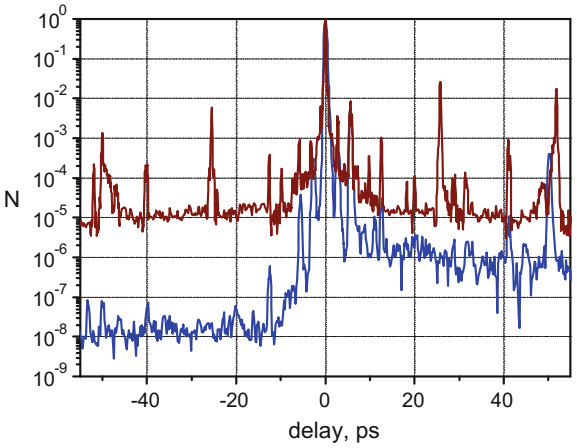

Fig. 2.1 Third-order correlation traces of the terawatt femtosecond laser pulse for two different setups

acceleration, and X-ray and γ production, and also we are working on laser-induced nuclear processes such as nuclear excitation, nuclear reaction, and so on, but I will not touch this topic in my talk. Also, we are working on femtosecond filamentation in gases and solids. Please refer to the talks by Prof. Kosareva and Prof. Shkurinov to get more details on this latter activity.

The following talk is divided by two parts. The first one deals with hard X-ray sources. It is not a good idea to use a simple solid target, because you need to move the target from shot to shot to have a clean, undamaged surface, and this task is quite complicated even at 10 Hz or at higher repetition rates, especially if you would like to use your source for hours.

We introduced a liquid-gallium target setup [1, 2], which has a lot of different advantages such as self-healing of the surface after laser action and extremely easy target setup (it does not contain any moving parts). For such a target, you can use various materials such as Ga, In, Bi, and Pb. They should have low-saturated vapor pressure, so you cannot use mercury. All these materials are metals, so they have high thermal conductivity, and this is also good (you cannot use water). But we are concentrated mostly on Ga because of its extremely low melting temperature, and so it is very nice to use it without some of the implications of the hot temperature inside the chamber.

First, we observed that we could work at 10 Hz or even at 1 kHz [3], i.e., we can produce stable hard X-rays without changing or moving something inside the chamber, and this is very nice for applications. Also, we observed very interesting physics inside, and that means that, if we play with short nanosecond pre-pulse coming 12 ns in advance of the main pulse (we can play with the amplitude of this pulse; we can play with advancing time of this pulse with respect to the main pulse), we significantly enhance the hard X-ray yield and the mean energy of hot electrons. For example, in Fig. 2.2, we plotted experimental data for Ga.

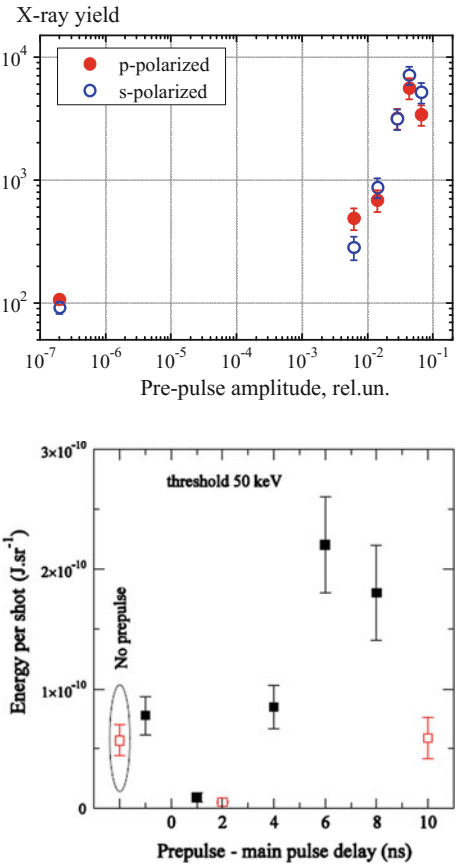

Fig. 2.2 Hard X-ray yield dependencies on the amplitude and advancing time of the pre-pulse. The main pulse intensity is 10^{17} W/cm^2. The latter dependence was measured in a collaborative experiment with CELIA [2, 4]

To get more insight into the physics, we made shadowgraphy measurements of the plasma plume created by the pre-pulse (Fig. 2.3) [2]. One can see here that there are something like jets, something like micro-structuring. So we assume that those micro jets are the main cause, and those micro jets are not produced by the main pulse but by the pre-pulse.

To understand physics inside this liquid jet generation, we have collaborated with Prof. Tikhonchuk's group from CELIA (University of Bordeaux), and one can see 2D hydrodynamic simulations in Fig. 2.4 [4]. From these simulations, it follows, that, if we assume inhomogeneous energy deposition on the target, we immediately come to microjet production.

Also, we checked in an experiment that the jet geometry closely correlates with energy distribution in the focal area [4], and we can play with energy distribution just by changing the focus position. Now we are trying to make some regular jets and to optimize jets to get even better and more stable results.

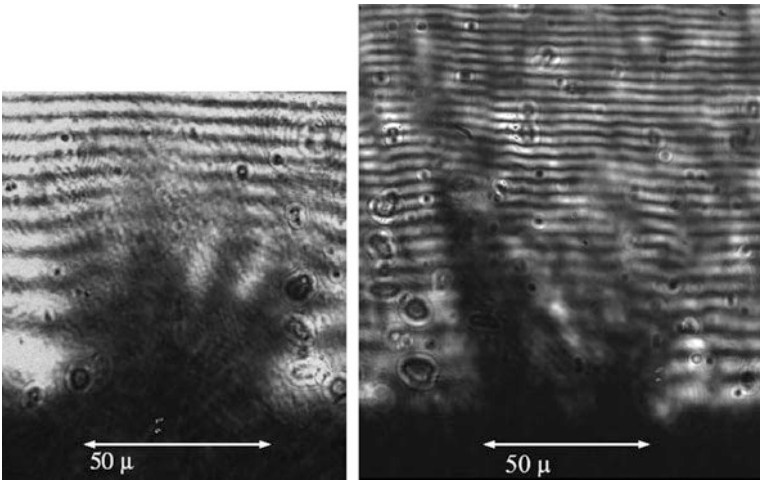

Fig. 2.3 Shadowgraphy images of jets produced by the pre-pulse acting at the melted gallium surface (intensity 10^{16} W/cm^2): along the laser-beam direction (*left pane*) and in the perpendicular direction (*right pane*)

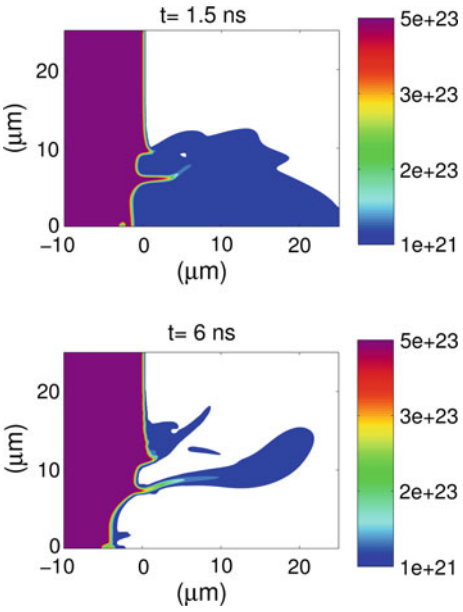

Fig. 2.4 2D hydrodynamic simulations of a liquid aluminum ablation. The energy density in the central spot (4 μm in diameter) was 14 J/cm^2, and in the outer ring (7.5 μm radius, width of 1 μm) it was few times less [4] (calculations by the group of Prof. V. Tikhonchuk)

To understand why interaction of the main laser pulse with jets leads to hard X-ray yield enhancement, we made 3D PIC simulations in tight collaboration with Prof. Bychenkov's group from the Lebedev Institute [2]. We observed that the long

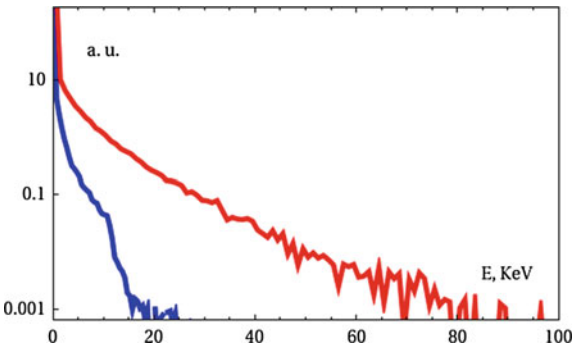

Fig. 2.5 Electron spectra from plasma with (*red line*) and without (*blue line*) jets [5]

tail of hot electrons appears if we have jets and that means that those hot electrons are produced due to the existence of these jets (Fig. 2.5).

The main application of our designed source could be so-called phase-contrast imaging of biological tissues (see, for example [5]). Note that phase-contrast images are excellent if one needs to reveal the boundaries between weakly absorbing tissues. This method is extensively used with synchrotron-radiation sources, but our aim is to bring the process to a small-scale laboratory, thus providing for the feasibility to use this method in medicine.

The next part of the talk concerns γ-ray production, so here we are talking about X-rays with quantum energies well above 100 keV. Recently we tried [6] to understand how the real temporal structure of the pre-pulse impacts hard X-ray and γ-ray yields. The main outcome was that having really high contrast femtosecond pulse is not good and efficient for γ production, and a short pre-pulse, which comes 12 ns in advance (a more-or-less normal feature of femtosecond lasers with CPA), again is not good. It is much better to have long and arbitrarily intense amplified spontaneous emission, and then one has enhanced γ-ray yield.

Note that amplified spontaneous emission is not a good thing because you cannot control it, you cannot play with its intensity and its duration, and it is unstable from shot to shot. That is why we turned to a different scheme where we have a femtosecond laser pulse and we have a pre-pulse, which is artificial. Here we have the high-contrast femtosecond pulse and artificial pre-pulse, so we can control energy deposition by the pre-pulse, plasma-plume velocity, timing between the two pulses, and plume extent. We can use pre-pulse at 1064 or 532 nm, and that helps us with optical plasma diagnostics.

Our experimental scheme is presented in Fig. 2.6. The main pulse comes from the Ti:sapphire system, and the pre-pulse comes from the Q-switched Nd:YAG laser (Surelite III) with pulse duration of 6 ns. The latter produces intensities up to 10^{12} W/cm^2. We have various diagnostics around the chamber: γ-ray detectors, X-ray detectors, some visible diagnostics, and an optical spectrometer. We also have ionic diagnostics which is not shown here.

Figure 2.7a presents the dependence of the hard X-ray yield on the delay between the two pulses. Zero delay corresponds to the coincidence of the maxima

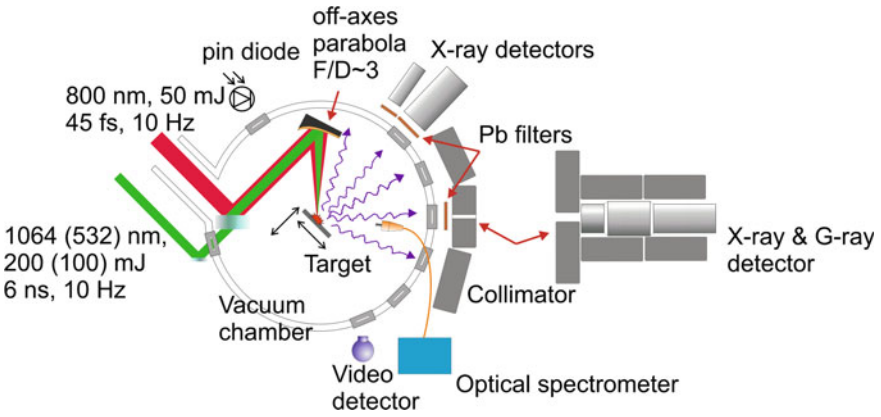

Fig. 2.6 Experimental scheme for γ-ray production

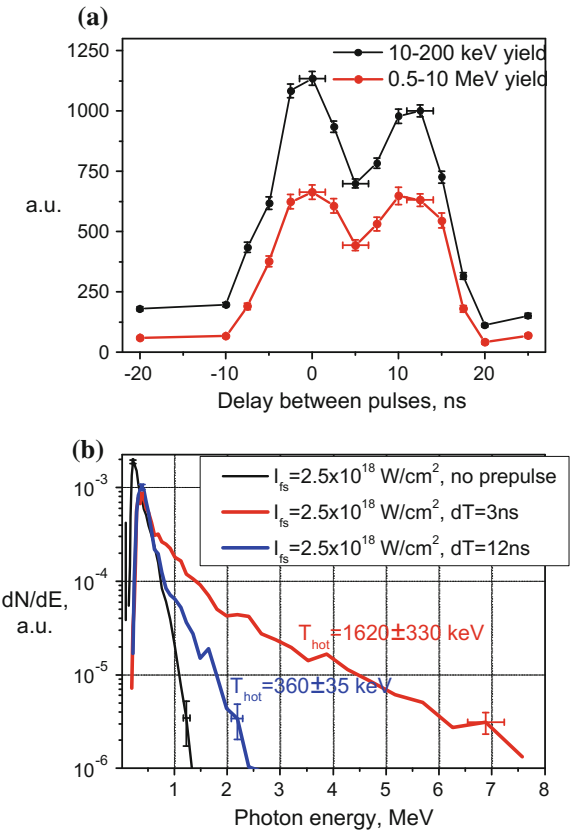

Fig. 2.7 γ-yield dependence on the time delay between the pre-pulse and the main pulse (**a**) and γ spectra at different delays (**b**)

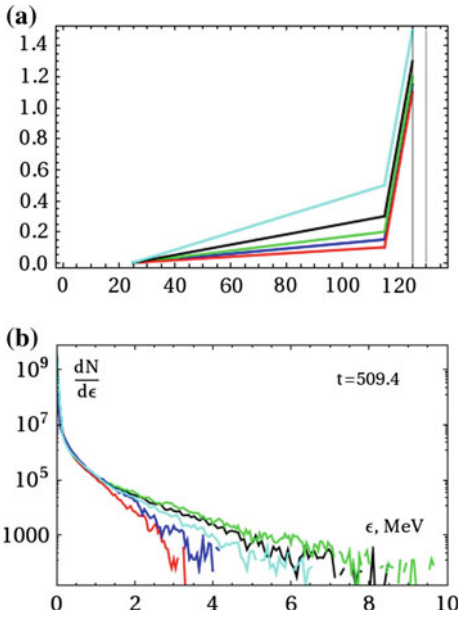

Fig. 2.8 Plasma densities used in 2D PIC modeling (**a**) and corresponding spectra of electrons (**b**)

of two pulses, and negative delays means that the nanosecond pulse comes in advance with respect to the main pulse. One can see two maxima and a deep, so this is again indicating some interesting physics inside. For applications, the most interesting data are presented in Fig. 2.7b. The spectrum obtained with a properly timed pre-pulse generated many more gammas and the mean energy (slope of the curve) of those gammas is much higher. Surprisingly, at an intensity a little bit above 10^{18} W/cm^2, we obtained few MeV photons (up to 7 MeV).

From optical diagnostics, we can assume that the laser-plasma plume looks like something presented in Fig. 2.8a: we have two slopes and a long tail of under-critical plasma. Spectra obtained with those slopes using 2D PIC simulations (Prof. Bychenkov group) are shown in Fig. 2.8b [7]. For some special slopes, we can optimize the hard X-ray yield.

Figure 2.9 shows X-ray images obtained with our source with most quanta having energy less than 1 MeV. Even though we can look inside microchips, or distinguish between different metallic foils and plates. In the future, our optimized source can be efficiently used fornuclear safety and non-proliferation issues, warm dense-matter diagnostics, etc.

This activity is supported by the Russian Fund for Basic Research under grants ##13-02-00373 and 16-02-00263 (γ-production and imaging), 14-29-09244 (electron acceleration in tenuous plasma), 15-32-20417 (X-ray phase imaging).

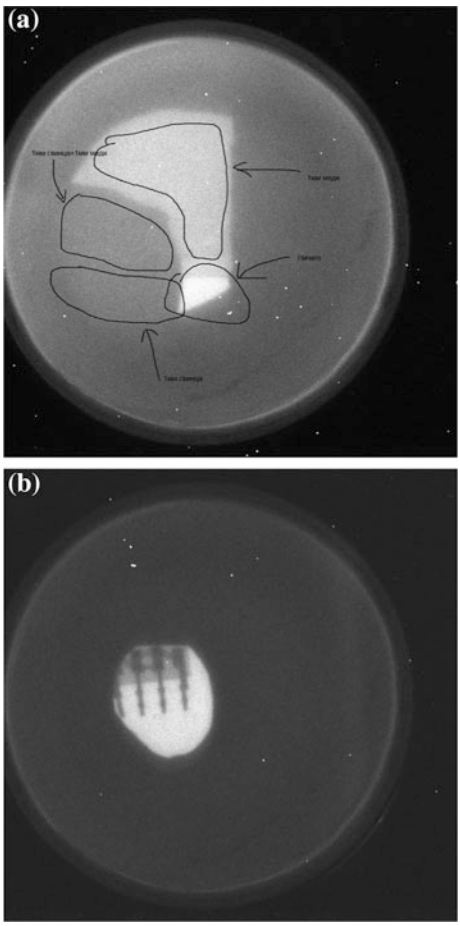

Fig. 2.9 γ-ray images of the filter set (*top*) and a microchip (*bottom*)

References

1. V.M. Gordienko, M.V. Kurilova, E.V. Rakov, A.B. Savel'ev-Trofimov, D.S. Uryupina, Quantum Electron. **37**, 651 (2007)
2. D.S. Uryupina, K.A. Ivanov, A.V.Brantov, A.B. Savel'ev, V. Yu, Bychenkov, M.E. Povarnitsyn, R.V. Volkov, V.T. Tikhonchuk, Phys. Plasmas. **19**, 013104 (2012)
3. K.A. Ivanov, D.S. Uryupina, R.V. Volkov, A.P. Shkurinov, I.A Ozheredov, A.A. Paskhalov, N.V. Eremin, A.B. Savel'ev, Nuclear instruments and methods in physics research section a: accelerators, spectrometers, detectors and associated equipment. Spec. Issue Superstrong 2010. **653**, 58 (2011)
4. D.A. Lar'kin, K. Uryupina, A. Ivanov, T. Savel'ev, F. Bonnet, F. Gobet, M. Hannachi, M. Tarisien, K. Versteegen, K. Spohr, B. Breil, F. Chimier, C. Dorchies, Phys. Plasmas **21**, 093103 (2014)

5. R. Toth, J.C. Kieffer, S. Fourmaux, T. Ozaki, A. Krol, Rev. Sci. Instrum. **76**, 083701 (2005)
6. K.A. Ivanov, S.A. Shulyapov, P.A. Ksenofontov, I.N. Tsymbalov, R.V. Volkov, A.B. Savel'ev, A.V. Brantov, VYu. Bychenkov, A.A. Turinge, A.M. Lapik, A.V. Rusakov, R.M. Djilkibaev, V.G. Nedorezov, Phys. Plasmas **21**, 093110 (2014)
7. K.A. Ivanov, S.A. Shulyapov, A.A. Turinge, A.V. Brantov, D.S. Uryupina, R.V. Volkov, A.V. Rusakov, R.M. Djilkibaev, V.G. Nedorezov, Contr. Plasma Phys. **53**, 116 (2013)

Chapter 3
Frontier in Astrophysical Plasma by Using Laser Experiments

Masahiro Hoshino

Let me show you some images of plasma phenomena in our universe (Fig. 3.1). At the center of the top panel is an aurora of the Earth, and on the left is the Sun taken by the X-ray satellite. The Sun is known to be very active in the X-ray band, and energetic electrons and ions are generated around the surface of the Sun, i.e., the solar corona. The upper right-hand corner represents the energetic phenomenon in the Crab Nebula taken by the Hubble Space Telescope. We know that the interaction between the nebula and the high-speed pulsar wind emanating from the central neutron star produces the energetic particles and the synchrotron radiation. The lower left and center of the panel depict a supernova explosion and the interaction of the supersonic plasma flow generated at the explosion with the interstellar medium, producing a strong shock, which in turn provides the energetic particle acceleration. Let us turn our attention to a much larger scale in the universe. The center-bottom panel shows the active galactic nucleus and its associated pair of jets taken in the radio band. The central object is a massive black hole, and the jets with a relativistic gas flow are emanating from the black hole. Associated with the jets, the energetic particles are created. In these astrophysical phenomena with hot gasses, one of the key elements in understanding the dynamic evolution and structure is the plasma process. We may say that most astrophysical processes involve plasma. It is often said that 99% of the matter in the universe is in the plasma state.

One of the important agents in understanding these phenomena is the multi-scale coupling between the micro-plasma scale and the macro-astronomical scale. I have just shown several astrophysical phenomena in the global scale, and emphasized that one of the important elements to understand the energetic phenomena is the microscale plasma process. In addition to the multi-scale coupling, the multi-energy

M. Hoshino (✉)
Department of Earth and Planetary Science, School of Science, The University of Tokyo, 7-3-1 Hongo, Bunkyo-ku, Tokyo 113-0033, Japan
e-mail: hoshino@eps.s.u-tokyo.ac.jp

K. Yamanouchi (ed.), *Progress in Photon Science*, Springer Series in Chemical Physics 115, DOI 10.1007/978-3-319-52431-3_3

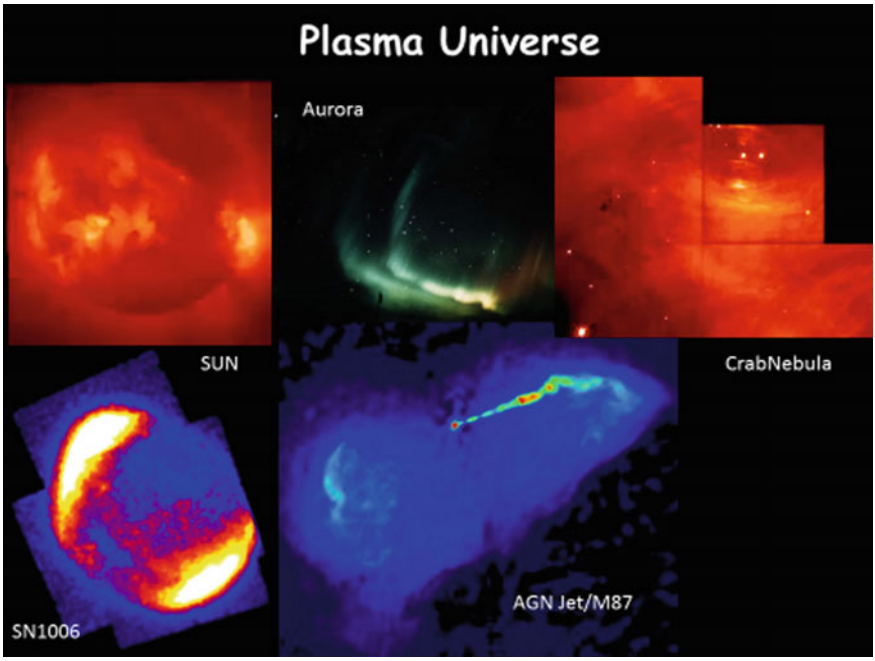

Fig. 3.1 Images of phenomena of the plasma universe

coupling between the thermal and non-thermal plasmas is important as well. This means that, while the temperature of those phenomena is on the order of 10 or 10^3 eV (electron volt), we observe the non-thermal cosmic rays whose energy reaches up to the 10^{20} eV. We can say that the astrophysical plasma state is not in a thermal equilibrium state with a Maxwellian distribution function. We have to understand the origin of the energetic-particle acceleration as well as the hot thermal gas.

To investigate these situations having both multi-scale and multi-energy couplings, laser plasma experiments are very powerful and play a very important role, because laboratory experiments can achieve astrophysically relevant microscopic states. Nowadays, the laser plasma can create a low-collision plasma state, which is a key factor in the high temperature and dilutes astrophysical plasmas. The laser device can also generate high-speed jet/high-speed plasma with large energy densities and electromagnetic fields. Therefore, laser experiments can be regarded as a useful tool to understand the energetics and dynamics of astrophysical plasmas. Laser-plasma experiments should be a key tool to investigate microphysics in the universe.

Let me say, in, detail why the coupling between the macro-scale astrophysical phenomenon and the micro-scale plasma phenomenon are important. Figure 3.2 shows the supernova remnant observed by the Chandra X-ray satellite, the so-called SN1006 that exploded about a thousand years ago. You can see that the shock front

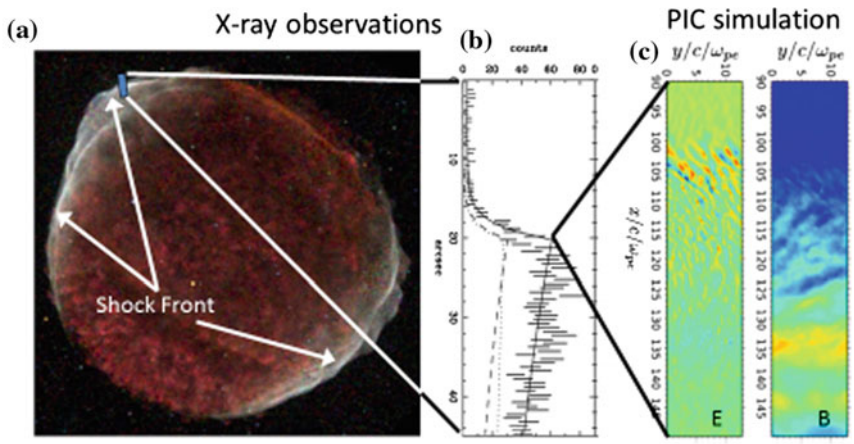

Fig. 3.2 Multi-scale couplings in a supernova shock

can be clearly resolved by modern satellite observation. Let us focus on the front of the shock shown in a bluish box in panel (a). The center panel (b) is the expanded view of the photon count coming from this region. The upstream of the supernova shock shows a very low count, but, across the shock, the X-ray photon count dramatically increases, suggesting that the cosmic rays/energetic particles are being generated at the shock front. To understand the generation of the cosmic rays, the plasma processes that are responsible for the charged-particle acceleration in the shock front should be investigated. The right hand panel (c) is the particle-in-cell (PIC) simulation result, demonstrating that the strong electric and magnetic fields are excited in the shock front. The interaction between the macro-astronomical scale and micro-plasma scale is a key to the cosmic ray acceleration.

In fact, several laboratory-plasma experiments have investigate the micro-scale structure around the shock front. The left-hand image in Fig. 3.3 shows the Omega laser experiment from a group at the University of Rochester in the United States. This group is trying to understand the micro-scale phenomenon in a weakly magnetized shock. By aiming an intense laser beam at two targets, a pair of colliding high-speed plasmas are generated. At the interface of the collision of the supersonic plasma flow, the shock waves are formed. You can see some interesting structures in the center region that correspond to the shock front. Many bubbles in the messy structure perhaps suggest the generation of the magnetic field, because, from the linear theory of the counter streaming plasmas, it is known that two-stream plasma instabilities can happen in association with electric and magnetic field perturbations. From a detailed examination of the plasma condition, Weibel instability is believed to play an important role in the system. The right-hand panel

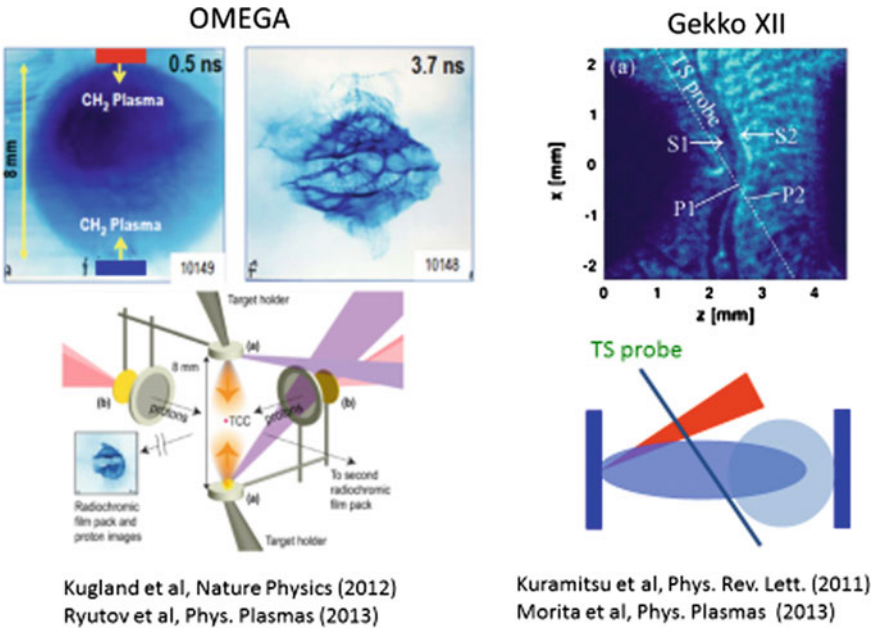

Fig. 3.3 On-going laboratory experiments (I): collisionless shock waves

is another shock experiment, this one using the GEKKO XII at Osaka University. The GEKKO team is investigating the formation of an electrostatic shock. I would like to mention that a collisionless-shock experiment under international collaboration is being conducted by using the NIF facility at LLNL.

One of the reasons why we study the physics of collisionless shocks is to understand the origins of cosmic rays in the universe and the particle acceleration mechanism. Figure 3.4 shows the cosmic ray spectrum in our universe. The horizontal axis is the energy of cosmic rays, ranging from 10^8 eV up to 10^{21} eV, and the vertical axis is the cosmic-ray flux. Both axes are depict logarithmic scales. One can recognize that the cosmic rays coming from the universe can be approximated by a power law of the spectrum, and roughly speaking, the power law index is around two or three. This is an amazing observation, because the cosmic-ray energies extend to more than 12 orders of magnitudes which can be simply described by the power-law function. The common wisdom is that the cosmic rays below the energies of 10^{15} eV are accelerated by supernova remnants in our galaxy, however, the cosmic rays above this energy are believed to be of extragalactic origin. It is still controversial, but the maximum energy, around 10^{20} eV, perhaps comes from the active galactic nuclei containing massive black holes. There are many efforts to understand these phenomena by using laser-plasma experiments,

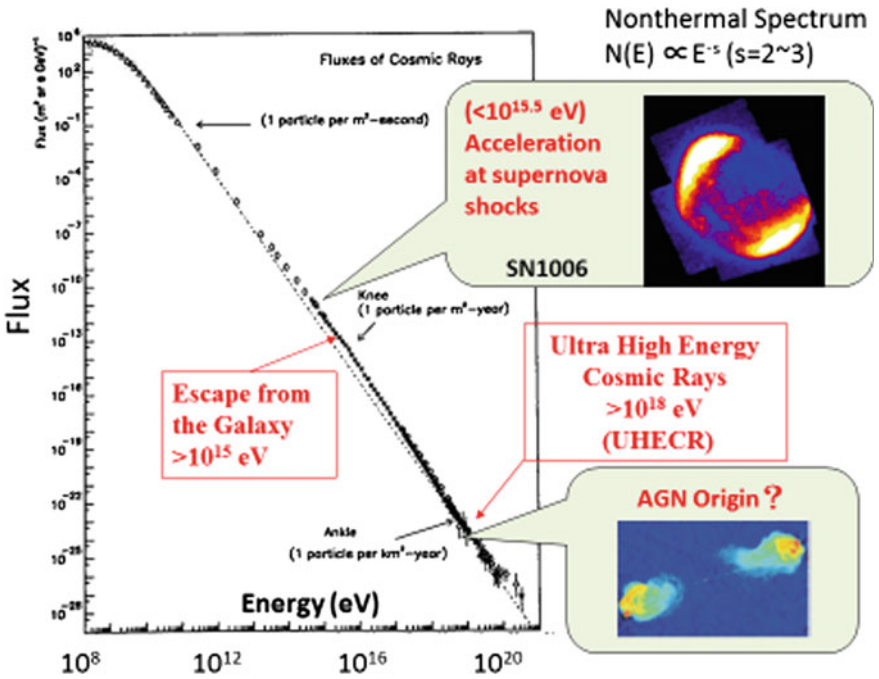

Fig. 3.4 Cosmic rays and the non-thermal universe

combined with theory and numerical simulation. Specifically, the particle-in-cell (PIC) simulation is a very useful tool to reveal the acceleration mechanism involved in such strongly nonlinear systems.

We have started the project of PIC simulation of collisionless-shock study. Shown in the panel is the shock-front region obtained by our PIC simulation using the K supercomputer at RIKEN, Kobe [1]. The right-hand region of Fig. 3.5 corresponds to the shock upstream with a high-speed, supersonic plasma flow, and the left-hand region is the shock downstream with a subsonic plasma. You can see the dynamic evolution of the shock front situated in the center of this panel. The white lines represent the magnetic field lines, and the red square indicates a typical particle trajectory. From this movie, you can see that many magnetic islands are formed around the shock front. These magnetic islands are known to be generated by Weibel instability, so you may think that this simulation shares a common plasma process with the Omega laser-plasma experiment, which I showed on the previous slide.

From the time of evolution of the dynamic shock structure, it is clear that the magnetic field is generated in the shock front, and, in this region, the charged particles interact repeatedly with the many magnetic islands, and, during this interaction, particles can gain their energies (Fig. 3.6). We think this is a very

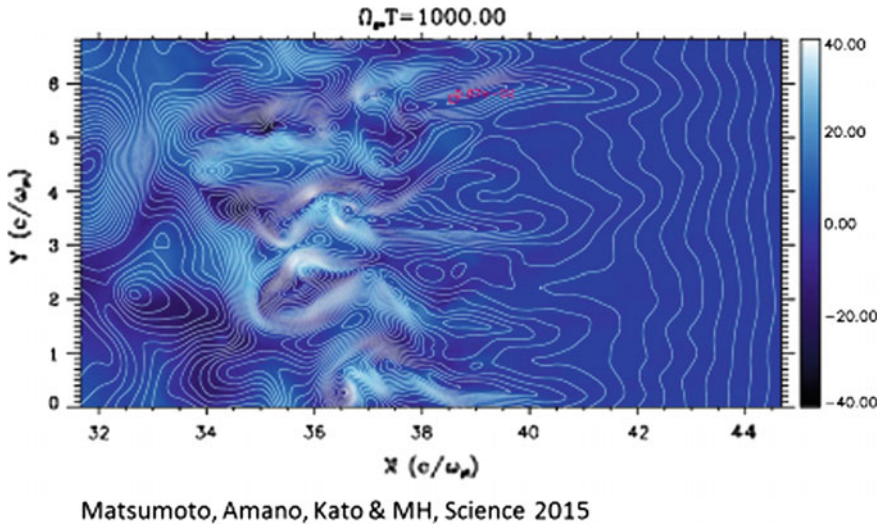

Fig. 3.5 Many magnetic islands in a shock wave

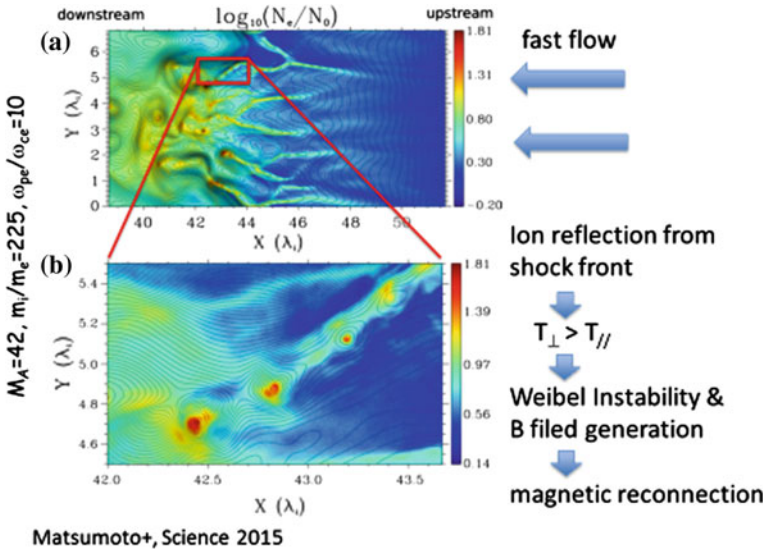

Fig. 3.6 High mach-number shock simulation

important process for explaining the origin of the energetic particles. One of the important points is that the particle acceleration happens under the small, micro-scale island structure embedded in the large, macro-scale shock. Many islands are responsible for generating energetic particles, and, in fact, we found a

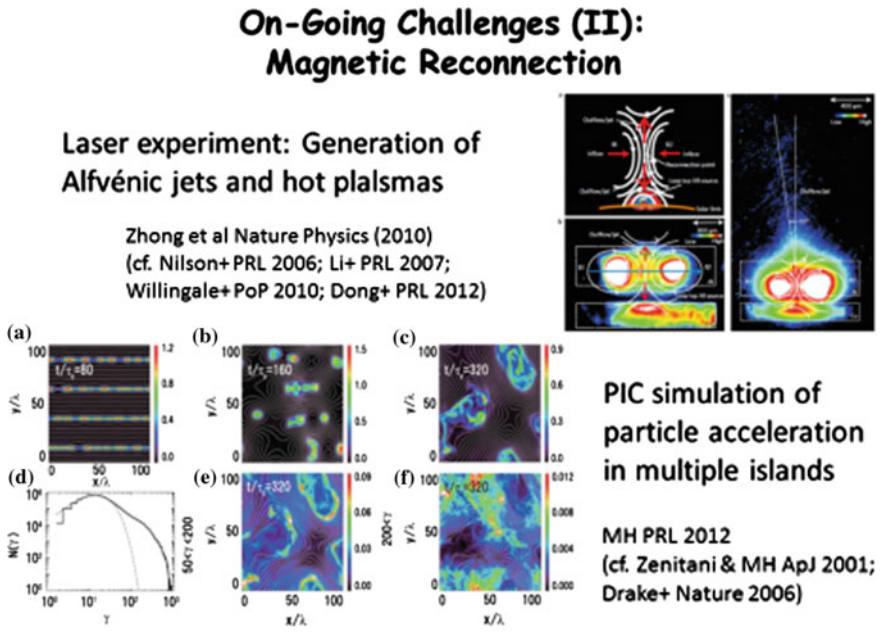

Fig. 3.7 On-going challenges (II): magnetic reconnection

non-thermal particle population in addition to the heated-plasma component from the analysis of the energy distribution function.

In addition to the shock acceleration, another key issue in astroplasma physics is the magnetic reconnection, which happens in the magnetized plasma medium with anti-parallel magnetic-field components (Fig. 3.7). Since the magnetic energy can be quickly converted to thermal and kinetic energy during the magnetic reconnection, reconnection is believed to play an important role in the particle acceleration. The research into magnetic reconnection is also a forefront science, and many people have now started to investigate the magnetic-field reconnections by using the laboratory-laser experiment. In addition, a PIC-simulation study can support the laboratory experiment. As one example, our simulation result is shown here [2]. It can successfully explain some important elements of particle acceleration by magnetic reconnection, which we believe may be happening in the laser experiment.

The third example of laser-related astroplasma physics is the Wakefield acceleration (Fig. 3.8); as mentioned by the previous speaker, strong laser pulses propagating through plasmas generate intense electrostatic wakefields associated with strong charge separation. If a charged particle can be trapped by the wakefield, it is shown that resonant acceleration of the particle with the propagating Wakefield is possible in the seminal paper by Tajima and Dawson [3]. After the discovery of the wakefield acceleration in laser plasmas, several researchers (e.g., Chen et al. [4]) investigated the wakefield acceleration to explain the ultra-high-energy cosmic rays, which possess the greatest energy levels in our universe.

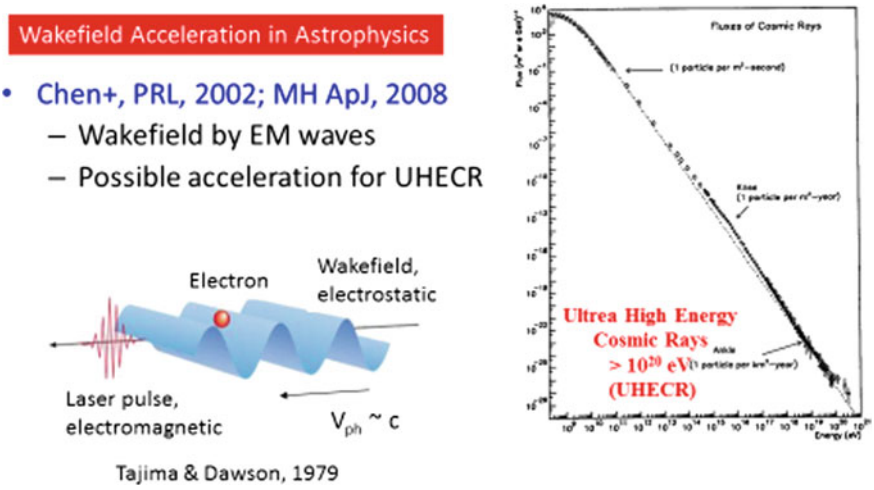

Fig. 3.8 Challenge (III): ultra-high-energy cosmic rays ($\sim 10^{20}$ eV)

We show in Fig. 3.8 the wakefield acceleration initiated by the precursor electromagnetic waves in a relativistic shock, where the upstream plasma flow speed is almost the speed of light. Shown in Fig. 3.9 is a snapshot of the well-developed shock structure obtained by the PIC simulation [5]. From top to bottom, the phase

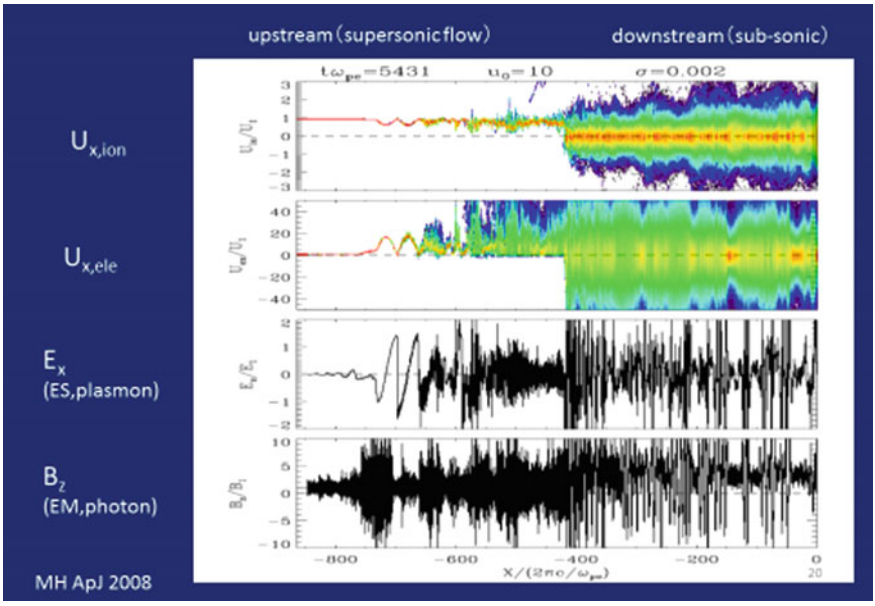

Fig. 3.9 Relativistic shock: wakefield acceleration

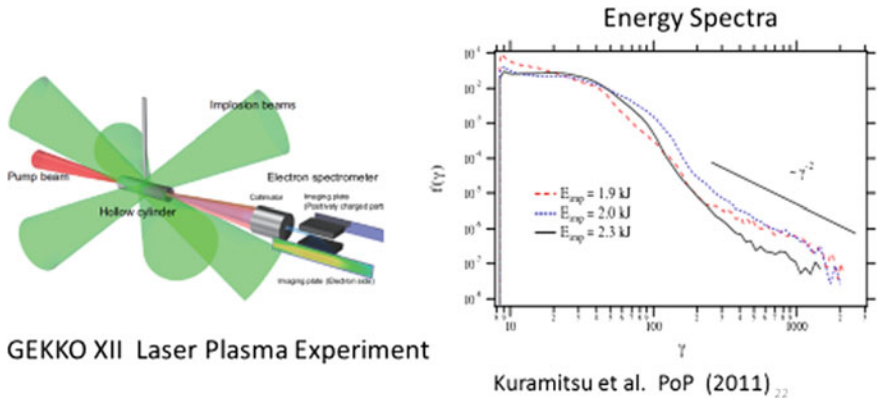

Fig. 3.10 Laboratory experiment (III): incoherent wakefield acceleration

space plot of ions, the phase space of electrons, the electrostatic field (wakefield), and the electromagnetic field (photon) are shown. The horizontal axis is the space X, and we have assumed a one-dimensional shock structure. The left-hand region corresponds to the upstream plasma, while the right-hand region is the downstream. One can clearly see that the strong electromagnetic precursor waves excited in the shock front are propagating toward the upstream, and the electromagnetic waves produce a series of wakefields behind the precursor waves. As time goes on, the coherent wakefield waves cannot maintain their original waveforms and are destroyed. Then the incoherent wakefields lead to a very strong particle acceleration for both ions and electrons.

We have also studied this phenomenon in the GEKKO XII laser experiment. Figure 3.10 shows the energy spectrum, where the horizontal axis is the energy, while the vertical axis is the energy-distribution function [6]. We can successfully demonstrate the power of the nature of the energy spectrum with the power index of two, which is consistent with the cosmic-ray spectrum.

My message is that laboratory-laser experiments have a great potential to answer many long-standing questions in plasma astrophysics.

References

1. Matsumoto et al., Science (2015)
2. Hoshino, PRL (2012)
3. Tajima and Dawson, PRL (1979)
4. Chen et al., PRL (2002)
5. Hoshino, ApJ (2008)
6. Kuramitsu et al., PoP (2011)

Chapter 4
Terahertz and Mid-Infrared Radiation from Femtosecond Filaments in Gases

O.G. Kosareva, N.A. Panov, V.A. Andreeva, D.E. Shipilo, A.B. Savelyev, A.P. Shkurinov, V.P. Kandidov and V.A. Makarov

4.1 Introduction: Filamentation of Femtosecond Laser Pulses in Transparent Media

The phenomenon of ultrashort laser-pulse filamentation is represented by the localization of laser energy in a thin string of light called filament. This string is created under the joint action of radiation self-focusing and defocusing in the plasma, which is produced by the same propagating laser pulse that limits the self-focusing collapse. The filament string is long and thin. The length of the string is much longer than its diffraction length. By filament length, we understand the length of the region where the intensity is high enough to induce the ionization initially of a neutral transparent medium. In air, the filament length may vary from several meters to a kilometer, with a transverse width of about 100 μm. Femtosecond-pulse filamentation is observed in gases, transparent liquids, and solids. It is accompanied by plasma-channel formation and superbroadening of the

O.G. Kosareva (✉) · N.A. Panov · V.A. Andreeva · D.E. Shipilo · A.B. Savelyev · V.P. Kandidov
International Laser Center and Faculty of Physics, Lomonosov Moscow State University, Lenskie Gory 1, bld.62, Moscow 119991, Russia
e-mail: kosareva@physics.msu.ru

A.B. Savelyev
e-mail: abst@physics.msu.ru

A.P. Shkurinov
Department of Physics and International Laser Center, Lomonosov Moscow State University, Leninskie Gory, Moscow 119992, Russia
e-mail: ashkurinov@gmail.com

V.A. Makarov
Wave Processes and International Laser Center, Lomonosov Moscow State University, Leninskie Gory 1, bld.62, Moscow 119991, Russia
e-mail: vamakarov@phys.msu.ru

K. Yamanouchi (ed.), *Progress in Photon Science*, Springer Series in Chemical Physics 115, DOI 10.1007/978-3-319-52431-3_4

frequency-angular spectrum of the pulse. In the course of near-infrared pulse filamentation, the generated supercontinuum extends from the ultraviolet to the terahertz range. Thus, filamentation enables pulse compression and self-compression, as well as other nonlinear effects, such as tunable few-cycle pulse production, harmonic generation, etc.

Self-focusing is the main physical reason for the filamentation. Self-focusing was first predicted by Askarian [1]. The first general explanation of the phenomenon was offered by Talanov and Townes [2, 3] in 1963. The first experimental observation of self-focusing was done by Pilipetskii and Rustamov in 1965 [4] in a condensed medium (Fig. 4.1). Numerical simulations of laser-radiation propagation under the conditions of self-focusing were first performed by Talanov [2] and Kelley [5]. Further on, S.A. Akhmanov, A.P. Sukhorukov, and R.V. Khokhlov developed the theory of stationary self-focusing and found an analytical solution to the parabolic equation for the slowly varying amplitude of the light field in paraxial approximation [6]. Unique observations of nonstationary self-focusing in a condensed medium were performed by Prokhorov and Korobkin [7] and Loy and Shen [8].

Self-focusing is a threshold phenomenon: for the observation of it the radiation power should be larger than the critical power for self-focusing in the medium. This critical power ranges from several megawatts in condensed media to gigawatt power in atmospheric-density gases.

Development of high-peak-power (up to petawatt-level) femtosecond laser systems makes it possible to observe self-focusing in atmospheric air. The first registration of a filament in air formed by a 150 fs 775 nm laser pulse emitted by a Ti:sapphire-laser amplification system was done in Professor G. Mourou's laboratory in the US [9]. The filament length was more than 50 m. Almost at the same time, experiments on femtosecond-pulse filament generation where performed in Professor A. Mysyrowicz's laboratory [10] and in Professor Chin's laboratory, jointly with Professor V.P. Kandidov and Dr. O.G. Kosareva from Lomonosov MSU [11, 12]. In [10] it was registered that, with propagation distance, the central part of the filament becomes white, and the colored conical emission surrounds the central white spot. Thus, the supercontinuum is emitted by the filament (Fig. 4.2). Measurements and simulations presented in [11, 12] have shown the presence of a highly-intense central part of the filament with a diameter less than 500 μm, surrounded by the background with the diameter on the order of the initial beam size at the beginning of the propagation. In the same series of experiments

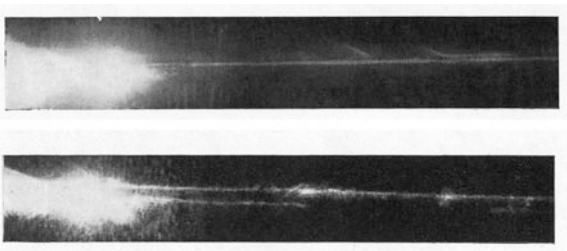

Fig. 4.1 The first photo of self-focusing [4]

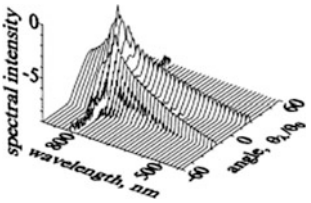

Fig. 4.2 Angular-frequency spectrum of light filament. One can see conical emission in the short-wavelength range [12]

and simulations, the effect of refocusing in the filamentation was discovered [11, 12]. Thus, by the year 1997, there were four pioneering works on femtosecond-pulse filamentation, and two of them were co-authored by O.G. Kosareva, V.P. Kandidov, and S.L. Chin. Further research made by French-German, Canadian, US, Russian, Japanese, and other groups has explained in detail the dynamic localization of energy in the narrow extended filament in gases, the generation of white light in the central part of the transverse filament section, the appearance of color rings surrounding the filament, conductivity along the filament string, multiple filament formation at higher laser energy, and many other phenomena.

O.G. Kosareva, V.P. Kandidov, and S.L. Chin formulated and justified the basic principles of femtosecond-laser pulse filamentation, such as the moving focus model in the conditions of optical-field-ionization of the medium, refocusing, the energy reservoir contained in the wide beam background surrounding the filament, the dynamics and instability of multiple filamentation of high-power laser pulse, superbroadening of the pulse-frequency spectrum, and color conical ring formation. We also considered the joint effect of geometrical focusing and self-focusing on the laser-pulse filamentation, interference of conical emission rings in the process of multiple filamentation, and we suggested temporal and spatial methods for multiple filament control. The consequence of wide spectral broadening is the possibility of pulse compression in the filament. To prove that, we jointly with the team of Professor Savel'ev designed the pulse-compression experimental setup based on the facilities of the Center of Collective Usage of Ti:sapphire laser amplification system at Lomonosov MSU International Laser Center. Both theoretically and experimentally, we obtained a near-infrared (800 nm) pulse with less than a four-cycle duration. Jointly with Professor Makarov's group, we predicted and experimentally demonstrated in Professor Chin's lab birefringence of femtosecond-probe pulse in the high-intensity field of the filament.

More exactly in the field of filamentation, we achieved the following results in the period 1995–2013:

1. Development of the generalized moving-focus model of femtosecond-laser radiation propagating under the condition of the nonlinear refraction in the self-produced laser plasma reproduces the formation of the extended filament with high energy density, the phenomenon of intensity clamping in the filament, formation of multiple rings in the transverse section of the filament (Fig. 4.3),

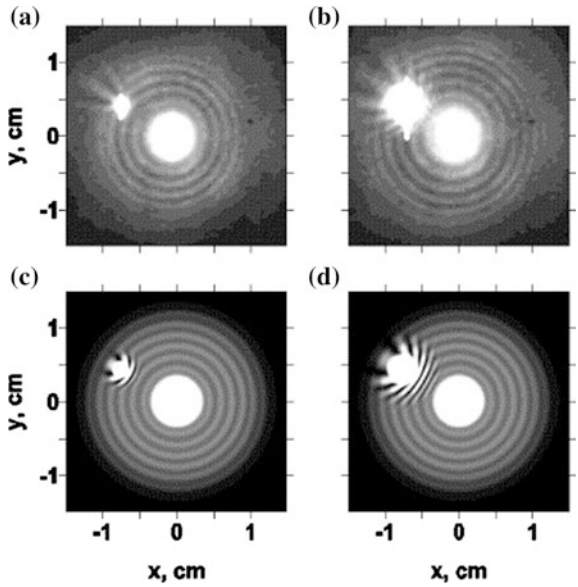

Fig. 4.3 Interference of filaments ring structures (**a**, **b** experiment, **c**, **d** simulations) [13]

and explains the phenomenon of refocusing, which is represented by non-monotonic energy-density variation along the filament [11–16].

2. Theoretical and experimental demonstration that superbroadening of the frequency-angular spectrum and conical emission of the supercontinuum are the results of the spatio-temporal self-phase modulation of femtosecond-laser radiation [12, 17], see Fig. 4.2.
3. Development of the dynamic scenario of multiple filamentation in femtosecond high-peak-power laser pulses. This scenario consists of the formation of parent filaments produced by the perturbations in the laser beam at the laser output, birth of the child filaments, energy interchange between the filaments, and the survival of one or several filaments in the end [18, 19] (Fig. 4.4).
4. By controlling the initial phase modulation and intensity distribution in the laser-beam section, we may govern the positioning of the bunch of filaments, as well as their plasma channels, and perform the pulse compression [20–24], see Fig. 4.5.
5. Femtosecond filaments induce optical anisotropy in the transparent isotropic dielectric [25–28], see Fig. 4.6.

These results are published in more than 65 publications, presented at more than 50 international conferences, and implemented in computer programs, as well as experimental setups in the International Laser Center of Lomonosov MSU. Thus, we have created the solid "filamentation portfolio" that is the basis for teaching Russian and international undergraduate and graduate students the basic and advanced simulation methods and experimental techniques of femtosecond-pulse propagation and filamentation in transparent media.

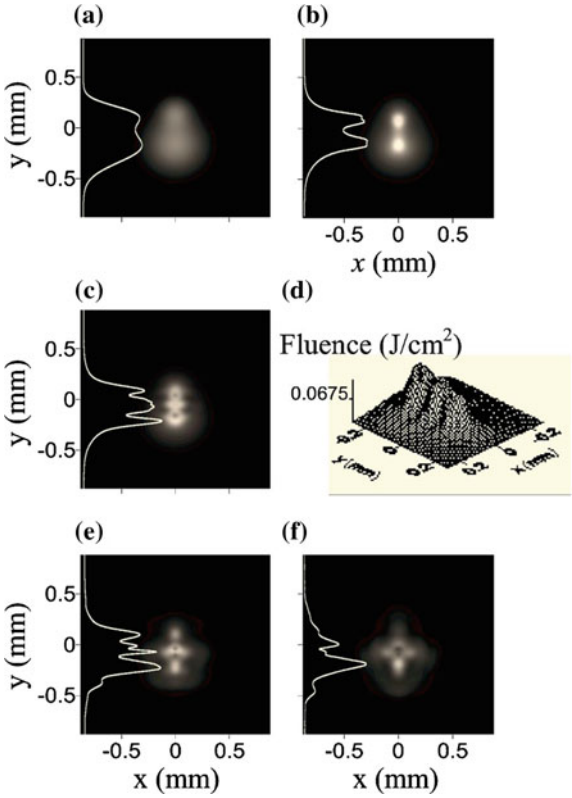

Fig. 4.4 Dynamic scenario of multiple filamentation: **a** initial profile, **b** formation of parent filaments, **c**, **d** birth of the child filament between the parent ones, **e** energy interchange between the filaments, **f** survival of one of them in the end [18]

4.2 Terahertz and Mid-Infrared Radiation from Femtosecond Filaments in Gases

Our current interests include efficient conversion of initial 800 nm-femtosecond laser pulse energy into the mid-infrared (MIR) and terahertz ranges. Generation of mid-infrared ultrashort pulses can be enhanced by seeding the filament with the pulse at the central frequency close to its second harmonic [29, 30]. With an 800 nm filament, the coherent THz radiation can be delivered to the desired position far through the atmosphere, avoiding thereby strong water-vapor absorption [31–33].

We have fully studied the long-wavelength part of the 800 nm filament spectral continuum ($0.8 < \lambda < 3000$ μm) and identified new physical mechanisms supporting experimentally observed phenomena such as the 3D-Raman light bullet in the near-infrared range [29], single-cycle MIR pulse generation and enhancement [30], and the ring-type shape of the spatial distribution of terahertz radiation from the air-based plasma [34–36]. The search for the physical mechanisms was performed numerically, based on the comprehensive unidirectional pulse-propagation

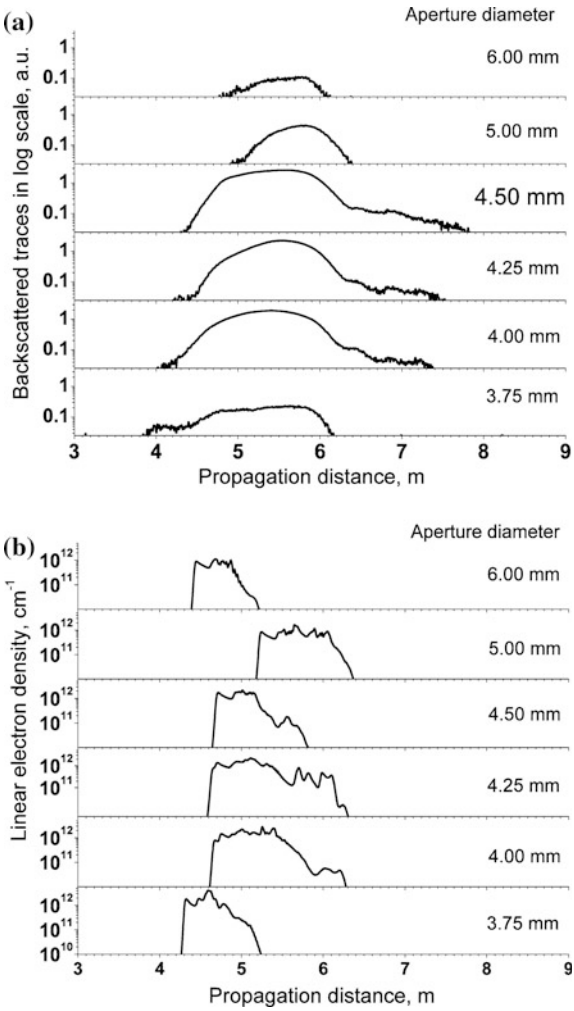

Fig. 4.5 Optimization of the plasma density and the length of filament using the aperture with variable diameter at the laser system output: **a** experiment, **b** simulations [24]

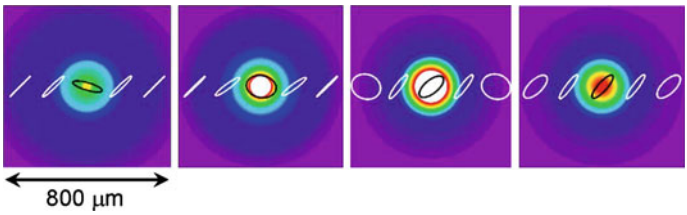

Fig. 4.6 Birefringence in the filament: evolution of polarization of radiation with distance from the beginning to the end of filament [25]

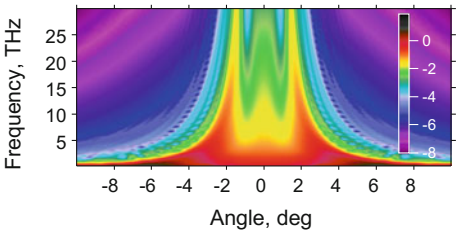

Fig. 4.7 The THz part of the full frequency-angular self-consistently generated spectrum of the (ω − 2ω) pulse in the air filament. The 800 nm pump has 3.2 mJ energy and 50 fs duration; the initial second harmonic energy is 10 μJ. Note the larger ring radii for the lower frequency

equation [37]. The lack of limitations on the range of frequencies and angles relative to the laser beam propagation axis allowed us to consider frequencies down to 0.1 THz and angular divergences of terahertz radiation up to 15°. We find that a 3D-Raman bullet is created on the axis of the extended filament in a gas due to Kerr nonlinearity. Its shift in central wavelength varies from ∼840 to ∼1000 nm with the propagation distance. The retarded Kerr effect leads to an increase in the energy converted into the bullet. In a single-color filament, the radiation in the MIR range spreads out in a ring due to the medium dispersion. Here, we report an order of magnitude increase in the on-axis, few-cycle, MIR pulse energy if a visible seed pulse is added to a 800 nm filament. We show that the emission in the range ∼0.1–15 THz in the (ω − 2ω) filament originates mainly from the nonlinear nonstationary change of the photocurrent. The emission at higher frequencies, which are above 15 THz but below 375THz (corresponding to 800nm pump), is mainly due to the Kerr nonlinearity of neutrals through the 0 = 2ω – ω − ω process. THz radiation originates from the filament axis and diffracts on the plasma obstacle forming a ring in the far zone (Fig. 4.7). By varying the relative contribution of the Kerr and the plasma nonlinearities, we have explicitly proven that this plasma-based THz-generation scenario is of a universal nature. The role of the Kerr nonlinearity in THz generation is limited to the intensity, hence favoring the action of the plasma. Our numerical-simulation results explain and generalize recent experiments in this field [29, 30, 34–36].

4.3 Conclusions

In conclusion, we have developed advanced numerical methods to simulate femtosecond-pulse filamentation in transparent media and satisfied the needs of the experiments. We are well-equipped to teach Russian and international students based on this “filamentation portfolio”.

On the cutting edge of current scientific research, we have performed a completely self-consistent numerical description of near-infrared, mid-infrared, and

terahertz radiation from filaments. We used a unified theoretical and numerical approach to explain the formation of a 3D-Raman bullet sustained in the air for a long distance, mid-infrared radiation enhancement due to four wave mixing, and spatial distribution of THz radiation from the air-based plasma.

Acknowledgements We thank Professor Kaoru Yamanouchi for sponsoring our trip to Japan and his excellent organization of the first STEP symposium. We thank RFBR (15-02-99630, 14-02-31379, 15-32-20966, 14-22-02021), the Council of RF President for Support of Young Scientists (MK-8562.2016.2), RF President grant for Leading Scientific Schools (NSh-9695.2016.2), and Basis Foundation.

References

1. G.A. Askar'yan, Sov. Phys. JETP **15**, 943 (1962)
2. V.I. Talanov, Izv. VuZov. Radiofizika **7**, 564 (1964)
3. R.Y. Chiao, E. Garmire, C.H. Townes, Phys. Rev. Lett. **13**, 479 (1964)
4. N.F. Piliptetskii, A.R. Rustamov, JETP Lett. **2**, 55 (1965)
5. P.L. Kelly, Phys. Rev. Lett. **15**, 1005 (1965)
6. S.A. Akhmanov, A.P. Sukhorukov, R.V. Khokhlov, Sov. Phys. Usp. **10**, 609 (1968)
7. V.V. Korobkin, A.M. Prokhorov, R.V. Serov, M. Ya Shchelev, JETP Lett. **11**, 94 (1970)
8. M.T. Loy, Y.R. Shen, Phys. Rev. Lett. **22**, 994 (1969)
9. A. Braun, G. Korn, X. Liu, D. Du, J. Squier, G. Mourou, Opt. Lett. **20**, 73 (1995)
10. E.T.J. Nibbering, P.F. Curley, G. Grillon, B.S. Prade, M.A. Franco, F. Salin, A. Mysyrowicz, Opt. Lett. **21**, 62 (1996)
11. A. Brodeur, C.Y. Chien, F.A. Ilkov, S.L. Chin, O.G. Kosareva, V.P. Kandidov, Opt. Lett. **22**, 304 (1997)
12. O.G. Kosareva, V.P. Kandidov, A. Brodeur, C.Y. Chien, S.L. Chin, Opt. Lett. **22**, 1332 (1997)
13. S.L. Chin, S. Petit, W. Liu, A. Iwasaki, M.-C. Nadeau, V.P. Kandidov, O.G. Kosareva, KYu. Andrianov, Opt. Commun. **210**, 329 (2002)
14. W. Liu, S.L. Chin, O.G. Kosareva, I.S. Golubtsov, V.P. Kandidov, Opt. Commun. **225**, 193 (2003)
15. Y. Chen, F. Théberge, O. Kosareva, N. Panov, V.P. Kandidov, S.L. Chin, Opt. Lett. **32**, 3477 (2007)
16. O.G. Kosareva, W. Liu, N.A. Panov, J. Bernhardt, Z. Ji, M. Sharifi, R. Li, Z. Xu, J. Liu, Z. Wang, J. Ju, X. Lu, Y. Jiang, Y. Leng, X. Liang, V.P. Kandidov, S.L. Chin, Laser Phys. **19**, 1776 (2009)
17. W. Liu, S.A. Hosseini, Q. Luo, B. Ferland, S.L. Chin, O.G. Kosareva, N.A. Panov, V. P. Kandidov, New J. Phys. **6**, 6.1 (2004)
18. S.A. Hosseini, Q. Luo, B. Ferland, W. Liu, S.L. Chin, O.G. Kosareva, N.A. Panov, N. Aközbek, V.P. Kandidov, Phys. Rev. A **70**, 033802 (2004)
19. V.P. Kandidov, O.G. Kosareva, S.A. Shlenov, N.A. Panov, VYu. Fedorov, A.E. Dormidonov, Quant. Electron. **35**, 59–64 (2005)
20. I.S. Golubtsov, V.P. Kandidov, O.G. Kosareva, Quant. Electron. **33**, 525 (2003)
21. Q. Luo, S.A. Hosseini, W. Liu, J.-F. Gravel, O.G. Kosareva, N.A. Panov, N. Aközbek, V. P. Kandidov, G. Roy, S.L. Chin, Appl. Phys. B **80**, 35 (2005)
22. O.G. Kosareva, N.A. Panov, N. Akozbek, V.P. Kandidov, Q. Luo, S.A. Hosseini, W. Liu, J.-F. Gravel, G. Roy, S.L. Chin, Appl. Phys. B **82**, 111 (2006)
23. N.A. Panov, O.G. Kosareva, V.P. Kandidov, N. Akozbek, M. Scalora, S.L. Chin, Quant. Electron. **37**, 1153 (2007)

24. J.-F. Daigle, O.G. Kosareva, N.A. Panov, M. Begin, F. Lessard, C. Marceau, Y. Kamali, G. Roy, V.P. Kandidov, S.L. Chin, Appl. Phys. B **94**, 249 (2009)
25. O. Kosareva, N. Panov, V. Makarov, I. Perezhogin, C. Marceau, Y. Chen, S. Yuan, T. Wang, H. Zeng, A. Savel'ev, S.L. Chin, Opt. Lett. **35**, 2904 (2010)
26. N.A. Panov, O.G. Kosareva, A.B. Savel'ev-Trofimov, D.S. Uryupina, I.A. Perezhogin, V.A. Makarov, Quant. Electron. **41**, 160 (2011)
27. S. Yuan, T.-J. Wang, O. Kosareva, N. Panov, V. Makarov, H. Zeng, S.L. Chin, Phys. Rev. A **84**, 013838 (2011)
28. N.A. Panov, V.A. Makarov, VYu. Fedorov, O.G. Kosareva, Opt. Lett. **38**, 537 (2013)
29. Y. Chen, F. Théberge, C. Marceau, H. Xu, N. Akozbek, O. Kosareva, S.L. Chin, Appl. Phys. B **91**, 219 (2008)
30. T. Fuji, T. Suzuki, Opt. Lett. **32**, 3330 (2007)
31. X. Xie, J. Dai, X.-C. Zhang, Phys. Rev. Lett. **96**, 075005 (2006)
32. C. D'Amico, A. Houard, M. Franco, B. Prade, A. Mysyrowicz, Phys. Rev. Lett. **98**, 235002 (2007)
33. L. Bergé, S. Skupin, C. Kohler, I. Babushkin, J. Herrmann, Phys. Rev. Lett. **110**, 073901 (2013)
34. Y.S. You, T.I. Oh, K.Y. Kim, Phys. Rev. Lett. **109**, 183902 (2012)
35. P. Klarskov, A.C. Strikwerda, K. Iwaszczuk, Jepsen P. Uhd, New J. Phys. **15**, 075012 (2013)
36. A. Gorodetsky, A.D. Koulouklidis, M. Massaouti, S. Tzortzakis, Phys. Rev. A **89**, 033838 (2014)
37. M. Kolesik, J.V. Moloney, Phys. Rev. E **70**, 036604 (2004)

Part II
Electron Scattering

Chapter 5
Laser-Assisted Electron Scattering and Diffraction for Ultrafast Imaging of Atoms and Molecules

Yuya Morimoto, Reika Kanya and Kaoru Yamanouchi

5.1 Introduction

When an electron is elastically scattered by atoms and molecules in a laser field, the kinetic energy of the scattered electron can be shifted by the unit of photon energy, for example, $E_f = E_i + n\hbar\omega$, where E_i and E_f are the kinetic energies of the incident and the scattered electrons, respectively, n is the integer, and $\hbar\omega$ is the photon energy of the laser field. This process is called laser-assisted elastic electron scattering (LAES) [1, 2]. The LAES process is a fundamental scattering process that occurs in a laser field, and can be regarded as a three-body collision process among an atom, an electron, and photons. The theoretical framework of the LAES process was established by Bunkin and Fedorov [3] in 1966.

They derived a formula of the differential cross section of LAES processes under the non-perturbative laser-electron interaction by treating a potential scattering with the first approximation. In 1973, Kroll and Watson [4] extended the theory to the non-perturbative potential scattering by using a semi-classical treatment.

Experimental study of the LAES process started in 1976. Andrick and Langhans [5] performed electron-argon scattering in a cw-CO_2 laser field, and observed that the electron signals slightly increase at the energy shifts of $\pm\hbar\omega$ in the energy spectrum of the scattered electrons. In the next year, Weingartshofer et al. [6]

Y. Morimoto
Max-Planck-Institut für Quantenoptik, Hans-Kopfermann-Strasse 1, 85748 Garching, Germany
e-mail: Yuya.Morimoto@lmu.de

R. Kanya · K. Yamanouchi (✉)
Department of Chemistry, School of Science, The University of Tokyo, 7-3-1 Hongo, Bunkyo-ku, Tokyo 113-0033, Japan
e-mail: kaoru@chem.s.u-tokyo.ac.jp

R. Kanya
e-mail: kanya@chem.s.u-tokyo.ac.jp

K. Yamanouchi (ed.), *Progress in Photon Science*, Springer Series in Chemical Physics 115, DOI 10.1007/978-3-319-52431-3_5

reported multiphoton energy shifts in kinetic energy of scattered electrons through electron-argon scattering in a pulsed-CO_2 laser field. After these pioneering studies, a number of experimental studies on the LAES process have been performed with cw- or pulsed-CO_2 lasers. The laser-field conditions in those experiments were $\lambda = 10.6$ μm, $I < 10^9$ W/cm^2, and $\tau > 2$ μs, where λ, I, and τ are the wavelength, the peak intensity, and the pulse duration of laser fields. In this study, we report the first observation of the LAES process induced by a femtosecond Ti:Sa laser field ($\lambda = 800$ nm, $I = 1.8 \times 10^{12}$ W/cm^2, and $\tau = 200$ fs) [7], and its application to the ultrafast gas electron diffraction [8].

5.2 Experiments

Figure 5.1 shows an experimental setup for the measurement of femtosecond-LAES processes. Details of the apparatus are described in [9]. An electron pulse was generated through the photoelectric effect from a photocathode-type electron gun by irradiating the photocathode surface with the third harmonics ($\lambda = 267$ nm) of a chirped femtosecond-laser pulse. The generated electron packet was accelerated to 1 keV and was collided with sample gas. Simultaneously, an intense near-infrared laser pulse was introduced to the scattering point. Then, the scattered electrons were introduced into a toroidal-type electron energy analyzer through a slit. The kinetic energy and the scattering angle of the scattered electrons were resolved by the analyzer and imaged onto a two dimensional detector.

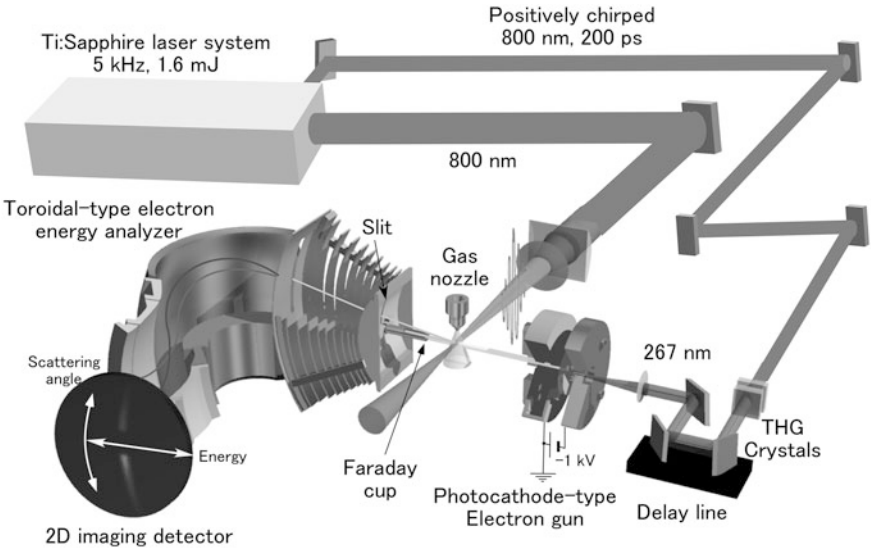

Fig. 5.1 The schematic of the femtosecond-LAES apparatus

5.3 Laser-Assisted Elastic Electron Scattering

The first observation of femtosecond-LAES [7] was achieved through colliding a 1 keV electron pulse with Xe atoms under the laser-field conditions of λ = 800 nm, $I = 1.8 \times 10^{12}$ W/cm^2, and τ = 200 fs. Figure 5.2a shows a two-dimensional image of the electron signals when the vertically polarized laser pulse and the electron pulse were simultaneously introduced into the scattering point, and Fig. 5.2b is an image of the corresponding background signals. This background was obtained by delaying the arrival time of the electron pulse by 100 ps with respect to the laser pulse, so that the electron scattering occurs at the period without the laser field. The accumulation time is 83 h for each image.

The strong arcuate signals at the central part of both images correspond to the elastic scattering process without any kinetic energy shifts. In Fig. 5.2a, weak arcuate signals can be seen at the positive energy side and the negative energy side of the elastic scattering signals. Figure 5.3a shows energy spectra of the scattered electrons that were obtained by integrating the signal intensities shown in Fig. 5.2a, b over the angular distribution. The filled circles show an energy spectrum when the laser pulse and the electron pulse were introduced simultaneously, and the open squares are that of the background signals. In the spectra of the filled circles in Fig. 5.3a, signal increases can be recognized at the kinetic energy shifts of $\pm\hbar\omega$. By subtracting the spectrum of the open squares from that of the filled circles, clear peak structures originating from the femtosecond-LAES process were obtained as shown in Fig. 5.3b. The observed signal intensities are well reproduced by a numerical simulation based on the Kroll-Watson theory (solid line).

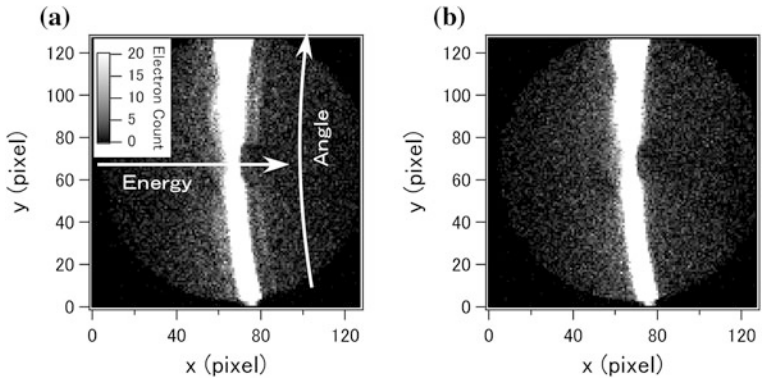

Fig. 5.2 The raw images of scattered electrons: **a** the image of the electron signals when the laser and electron pulses were simultaneously introduced. **b** The image of the background electron signals

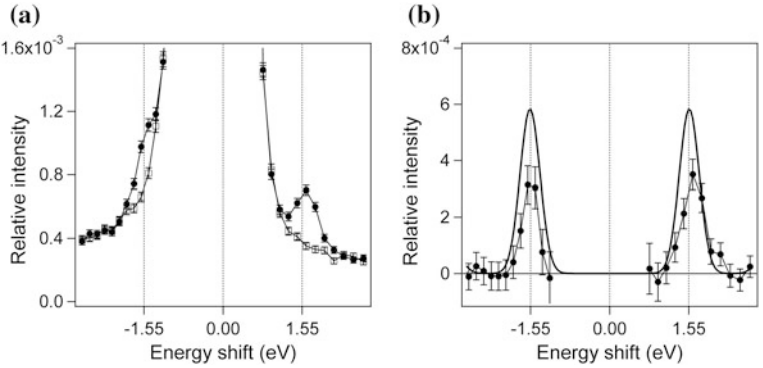

Fig. 5.3 **a** The energy spectra of scattered electrons by Xe when the laser and electron pulses were simultaneously introduced (*filled circles*) and of the background signals (*open squares*). **b** The background-subtracted energy spectra obtained by the experiment (*filled circles*) and the simulation (*solid line*)

5.4 Laser-Assisted Electron Diffraction

The gas electron diffraction method is a standard technique for determining geometrical structures of isolated molecules with high precision and high sensitivity, and time-resolved measurements of the gas electron diffraction have been performed for various molecules [10] through pulsed electron diffraction in which laser pulses excite sample molecules and electron pulses probe molecular structures after a time delay.

However, because of the velocity mismatch between the laser beam and the electron beam [11], the temporal resolution of the pulsed electron diffraction is limited to $\sim$1 ps [12], which is not short enough to probe the instantaneous molecular structure changing within the time scale of 10–100 fs.

Laser-assisted electron diffraction (LAED) was developed in order to overcome the picosecond barrier of the temporal resolution [7]. In the LAED method, angular distributions of the energy-shifted LAES signals are recorded with molecular samples, and electron diffraction patterns appearing in the angular distributions of the LAES signals are analyzed in order to determine geometrical structures of the molecules. Because the LAES process occurs only in the existence of the laser field, the structure determined from the energy-shifted LAES signals should be the instantaneous structure only in the laser-pulse duration. Therefore, the temporal resolution of the LAED method is determined only by the duration of laser pulses, which can reach to <10 fs without significant difficulties.

The LAED method was demonstrated through the scattering of 1 keV electrons by CCl_4 molecules under the laser field conditions of $\lambda = 800$ nm, $I = 6.0 \times 10^{11}$ W/cm^2, and $\tau = 500$ fs [8]. The solid line in Fig. 5.4a is an energy spectrum of the scattered electrons when the laser and electron pulses were simultaneously introduced, and the broken line in Fig. 5.4a is the corresponding

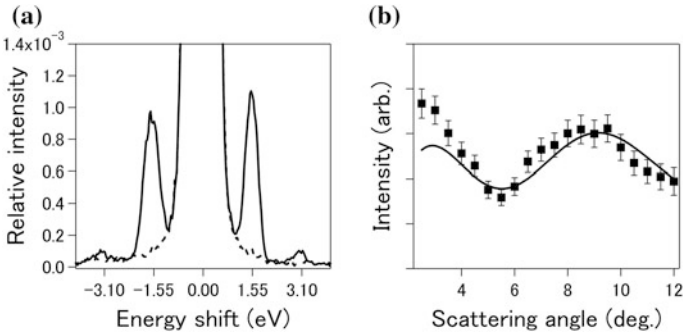

Fig. 5.4 **a** The kinetic energy spectra of scattered electrons by CCl_4 when the laser and electron pulses were simultaneously introduced (*solid line*) and of the background signals (*broken line*). **b** The experimental (*filled squares*) and simulated (*solid line*) angular distributions of the LAES signals at the energy shift of +1.55 eV

background spectrum. LAES signals are clearly recognized at the energies corresponding to $n = \pm 1$ and ± 2. The filled squares in Fig. 5.4b show an angular distribution of the LAES signals of $n = +1$. A clear diffraction pattern with an intensity minimum at around 5.5° and a maximum at around 9.0° can be recognized in the angular distribution. A solid line in Fig. 5.4b is the result of a simulation based on the Kroll-Watson theory [4] and on the independent atomic model [13], where the structural parameters of CCl_4 determined previously by the gas electron diffraction method with a cw-electron beam [14] were adopted. The good agreement between the experimental result and the simulation shows that the instantaneous geometrical structure of the molecules during the laser-pulse irradiation can be determined from the analysis of the LAED patterns with high precision.

Acknowledgements This work was supported by JSPS KAKENHI Grant Numbers 24245003, 24750011, 26288004, 24-4164 and 15H05696.

References

1. N.J. Mason, Rep. Prog. Phys. **56**, 1275 (1993)
2. F. Ehlotzky, A. Jaroń, J.Z. Kamiński, Phys. Rep. **297**, 63 (1998)
3. F.V. Bunkin, M.V. Fedorov, Sov. Phys. JETP **22**, 844 (1966)
4. N.M. Kroll, K.M. Watson, Phys. Rev. A **8**, 804 (1973)
5. D. Andrick, L. Langhans, J. Phys. B **9**, L459 (1976)
6. A. Weingartshofer, J.K. Holmes, G. Caudle, E.M. Clarke, H. Krüger, Phys. Rev. Lett. **39**, 269 (1977)
7. R. Kanya, Y. Morimoto, K. Yamanouchi, Phys. Rev. Lett. **105**, 123202 (2010)
8. Y. Morimoto, R. Kanya, K. Yamanouchi, J. Chem. Phys. **140**, 064201 (2014)
9. R. Kanya, Y. Morimoto, K. Yamanouchi, Rev. Sci. Instrum. **82**, 123105 (2011)

10. R. Srinivasan, V.A. Lobastov, C.Y. Ruan, A.H. Zewail, Helv. Chim. Acta **86**, 1761 (2003)
11. J.C. Williamson, A.H. Zewail, Chem. Phys. Lett. **209**, 10 (1993)
12. H. Ihee, V.A. Lobastov, U.M. Gomez, B.M. Goodson, R. Srinivasan, C.-Y. Ruan, A.H. Zewail, Science **291**, 458 (2001)
13. K. Yamanouchi, *Quantum Mechanics of Molecular Structures* (Springer, Heidelberg, 2012)
14. Y. Morino, Y. Nakamura, T. Iijima, J. Chem. Phys. **32**, 643 (1960)

Chapter 6
Laser-Assisted Electron Momentum Spectroscopy: Theory, Potential, and Perspectives

Konstantin Kouzakov

6.1 Introduction

My talk is devoted to laser-assisted electron momentum spectroscopy: its theory, potential, and perspectives. Here is an outline of my talk. In the first part, I will introduce you to the method of electron momentum spectroscopy and its theory. In the second part, I will speak about the electron momentum spectroscopy in the presence of the laser field, and particularly about the general theory of this method in the presence of the laser field. In the third part, I will present some recent numerical results for laser-assisted electron momentum spectroscopy of the helium atom, in particular, for ionization-excitation and double ionization. This case, i.e., the helium target, is important from the viewpoint of the experimental realization, which is expected in the near future. In the last part, I will briefly outline the potential and perspectives of the laser-assisted electron momentum spectroscopy.

6.2 Laser-Assisted Electron Momentum Spectroscopy

Let me introduce to you the method of electron momentum spectroscopy. This method is based on the (e, 2e) process. The (e, 2e) process means we have an incident electron that collides with the target A (see Fig. 6.1). The target can be an atom, molecule, cluster, or thin film. We have two electrons out, one is scattered and the other one is ejected. The key feature of electron momentum spectroscopy, if compared to the (e, 2e) method in general, is that electron momentum spectroscopy investigates the kinematics of the so-called 'quasielastic knockout', that is, the

K. Kouzakov (✉)
Department of Nuclear Physics & Quantum Theory of Collisions, Faculty of Physics, Lomonosov Moscow State University, Leninskie Gory 1, Moscow 119991, Russia
e-mail: kouzakov@gmail.com

K. Yamanouchi (ed.), *Progress in Photon Science*, Springer Series in Chemical Physics 115, DOI 10.1007/978-3-319-52431-3_6

kinematics that is the closest to the free electron-electron collision. What does it give us? The point is that, under such kinematical conditions, the amplitude of the process is very well approximated within the plane-wave Born approximation, and the differential cross section is directly proportional to the momentum distribution of the electron in the so-called Kohn-Sham orbital. For this reason, it is often called the momentum profile. So, we measure the coincidence energies and momenta of the two final electrons and then, from the energy and momentum conservation laws, obtain the binding energy and momentum of the target electron. That is why it is called the electron momentum spectroscopy. The momentum **of the target electron** is opposite to the recoil-ion momentum **q** and can be scanned by varying the out-of-plane azimuthal angle $\Delta\phi$.

Let me show how this method works. Figure 6.2 (borrowed from [1]) shows measured momentum profiles of atomic hydrogen versus theory. The theory is nothing else but an absolute square of the hydrogen wave function in momentum space.

The results of the more recent measurements from [2] are shown in Fig. 6.3. This case is not for hydrogen; this case is for helium. In the case of helium, in contrast to hydrogen, we do not know the exact wave function. Therefore, in the calculations, we use the different wave functions of helium. Thus we can select good wave functions and poor wave functions of helium (see Fig. 6.3). For example, here, 1 and 3 are poor wave functions.

Now, after introducing the basic principles of EMS, I pass to laser-assisted EMS. This part of my talk is based on the work of [3], where the idea of laser-assisted EMS was formulated and analyzed for the first time. Why laser-assisted EMS? The main reason is that it can be experimentally realized in the near future. The first laser-assisted (e, 2e) measurements have been already realized. However, they were conducted in the kinematical regime of small momentum transfer, which is very far from the kinematical regime of electron momentum spectroscopy. Currently, the first laser-assisted EMS measurements are in preparation, in Tohoku University (Sendai, Japan). The other important motivation is to examine the potential of the EMS method for studying the laser effects on momentum

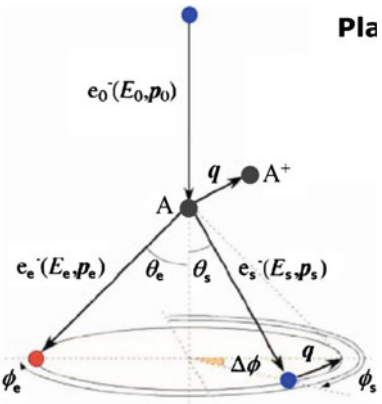

Fig. 6.1 A schematic drawing of the (e, 2e) process for large momentum transfer

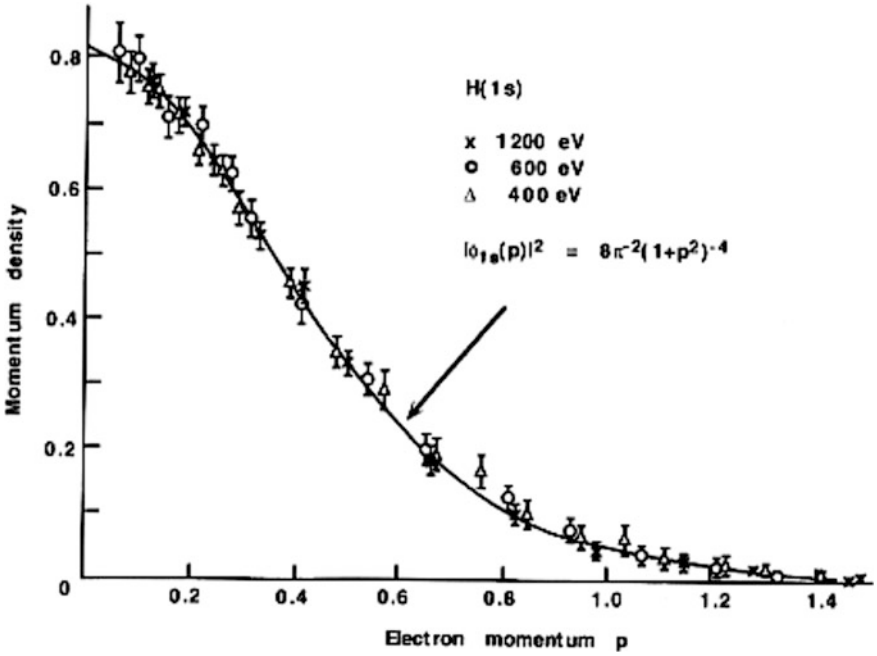

Fig. 6.2 The momentum profile for atomic hydrogen measured at the indicated energies compared with the square of the exact Schrödinger momentum-space wave function (*solid line*)

distributions of electrons in various systems, ranging from atoms and molecules to clusters and solids.

To analyze and interpret the data of such experiments, we need the proper theory. I will briefly present you the general theory of the laser-assisted electron momentum spectroscopy. I start with defining the laser field, so we assume that the laser field switches on and off adiabatically at $t \to \mp\infty$, respectively. The laser wavelengths are much greater than the spatial extent of both the target and the region where the electron-electron collision takes place, so this validates the use of the dipole approximation for the electric-field component of the laser field:

$$\boldsymbol{F}(t) = \boldsymbol{F}_0 \cos \omega t. \tag{6.1}$$

Another important condition is that the electric-field amplitude of the laser F_0 is much weaker than the typical electric field in the target F_T. This condition ensures that the laser field does not ionize the target before the (e, 2e) collision takes place.

The differential cross section, which is measured in the experiment, is derived from the S matrix. In the absence of the laser field, it is given by this formula:

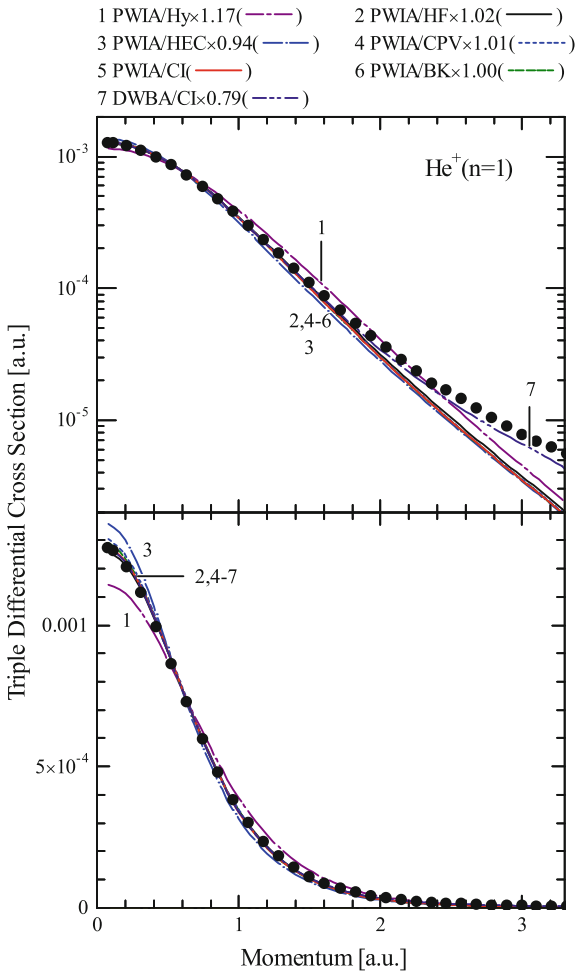

Fig. 6.3 Comparison of experimental momentum profile of He for the transition to the $n = 1$ ground ion state with associated theoretical calculations using various variational wave functions

$$S = -2\pi i \langle \mathbf{p}_s \mathbf{p}_e | \upsilon_{ee} | \mathbf{p}_0 \psi_g \rangle \delta\left(E_0 + E_g - E_s - E_e\right), \tag{6.2}$$

where we have the electron-electron potential υ_{ee} between two two-electron states. In the initial state, we have a plane wave for the incident electron and the ground-state wave function for the bound electron, ψ_g. In the final state, we have plane waves for the scattered and ejected electrons. The laser field modifies the plane waves into the Volkov functions, and so we end up with the Volkov-function Born approximation instead of the plane-wave Born approximation in the field-free case,

$$S = -i \int_{-\infty}^{\infty} \mathrm{d}t \left\langle \chi_{\mathbf{p}_s}(t)\chi_{\mathbf{p}_e}(t)|v_{ee}|\chi_{\mathbf{p}_0}(t)\psi_T(t)\right\rangle. \tag{6.3}$$

Here the bound-electron state ψ_T is also modified by the laser field, so that it is a field-dressed target state.

The Volkov function is a solution to the Schrödinger equation, where we have the vector potential of the laser field. Without the vector potential the solution is a well-known plane wave. The Volkov function differs from the plane wave in phase. Namely, for the laser field that we are considering, it is given by the product of a usual plane wave, where the energy is shifted by a ponderomotive potential U_p, and the sum over the harmonics:

$$\chi_{\mathbf{p}}(\mathbf{r},t) = \exp\left\{i\left[\mathbf{p}\cdot\mathbf{r} - Et - U_p t\right]\right\} \sum_{l,n=-\infty}^{\infty} \mathrm{e}^{-i(l-2n)\omega t} i^l J_l\left(\frac{\mathbf{p}\cdot\mathbf{F}_0}{\omega^2}\right) J_n\left(\frac{U_p}{2\omega}\right). \tag{6.4}$$

Here, J_l and J_n are Bessel functions of integer order.

The field-dressed target state solves the time-dependent Schrödinger equation, with the vector potential of the laser field and the target potential for the bound electron. The boundary condition

$$\psi_T(t \to -\infty) \to \exp\left(-iE_g t\right)\psi_g(\mathbf{r}) \tag{6.5}$$

means that, before the laser field switches on, we have the target electron in the ground state. According to the Floquet theorem, the solution can be presented in the form of the sum over the harmonics:

$$|\psi_T(t)\rangle = \exp\left(-i\tilde{E}_g t\right) \sum_{n=-\infty}^{\infty} \mathrm{e}^{-in\omega t} \left|\psi_T^{(n)}\left(\tilde{E}_g\right)\right\rangle, \quad \tilde{E}_g = E_g + \Delta. \tag{6.6}$$

Here we have the quasi-energy $\tilde{E}_g$, which is shifted from the unperturbed energy E_g by the ac Stark shift. The ket-vectors $\left|\psi_T^{(n)}\left(\tilde{E}_g\right)\right\rangle$ are time-independent.

Thus, the fully differential cross section of the laser-assisted EMS process can be presented as a sum over the N-photon processes:

$$\frac{\mathrm{d}^4\sigma}{\mathrm{d}E_s \mathrm{d}E_e \mathrm{d}\Omega_s \mathrm{d}\Omega_e} = \sum_{N=-\infty}^{\infty} \mathrm{d}^3\sigma_N \delta\left(E_s + E_e - E_0 - \tilde{E}_g + U_p + N\omega\right). \tag{6.7}$$

If N is negative, it corresponds to the net absorption of N photons by the colliding system, and, if N is positive, to the net emission of N photons. The laser-assisted triple-differential cross section or the laser-assisted momentum profile is given by the following formula:

$$\mathrm{d}^3\sigma_N = \frac{p_s p_e}{(2\pi)^3}\left(\frac{\mathrm{d}\sigma}{\mathrm{d}\Omega}\right)_{ee}\left|\psi_{T,N}(\mathbf{q})\right|^2, \quad \mathbf{q} = \mathbf{p}_s + \mathbf{p}_e - \mathbf{p}_0, \tag{6.8}$$

where we have the Mott electron-electron scattering cross section $\left(\frac{\mathrm{d}\sigma}{\mathrm{d}\Omega}\right)_{ee}$. The difference with respect to the field-free case is in the momentum profile:

$$\psi_{T,N}(\mathbf{q}) = \frac{\omega}{2\pi}\int\limits_{-\pi/\omega}^{\pi/\omega} \mathrm{d}t \exp\left\{i\left(\tilde{E}_g - \frac{q^2}{2} - U_p - N\omega\right)t\right\}\left\langle \chi_{\mathbf{q}}(t)\middle|\psi_T(t)\right\rangle. \tag{6.9}$$

Here we have a Volkov function instead of the plane wave. Let me recall that the momentum $\mathbf{q}$ is opposite to the recoil-ion momentum and, in the EMS method, it is interpreted as a momentum of the bound electron before it is knocked-out by the incident electron. Having this general formula, we can obtain numerical results, and further I will present our recent numerical results for the case of the laser-assisted electron momentum spectroscopy of helium.

Why helium? As I already have mentioned, the first laser-assisted EMS measurements are in preparation. They are expected to be conducted on a helium atomic target. The expected laser parameters are as follows: the frequency is 1.55 eV, which is much lower than the excitation energy in helium; the intensity is such that the electric-field amplitude of the laser is much weaker than the typical electric field in helium.

The S matrix of the process is calculated from this formula:

$$S = -i\int\limits_{-\infty}^{\infty} \mathrm{d}t\left\langle \chi_{\mathbf{p}_s}(t)\chi_{\mathbf{p}_e}(t)\psi_f(t)|v_{ee}|\chi_{\mathbf{p}_0}(t)\psi_i(t)\right\rangle. \tag{6.10}$$

Here we have the Volkov functions for the incoming, $\chi_{\mathbf{p}_0}$, and outgoing electrons, $\chi_{\mathbf{p}_s}$ and $\chi_{\mathbf{p}_e}$, and the field-dressed states of the He atom, ψ_i, and the final He^+ ion, ψ_f. v_{ee} is the electron-electron Coulomb potential. Since the laser electric field is weak, we can employ a perturbation theory for the field-dressed atomic and ionic states. This means that the main contribution to the field-dressed state comes from the field-free ground state, while the other field-free target states yield only small corrections.

To estimate first-order corrections to the field-dressed state of He and He^+, we use the so-called closure approximation, where one replaces excitation energies in the systems with some respective average energies, called the closure parameters:

$$\psi_i(\boldsymbol{r}_1, \boldsymbol{r}_2, t) = \mathrm{e}^{-i\mathcal{E}_{\mathrm{He}}t}\left[1 - \frac{\boldsymbol{F}_0\cdot(\boldsymbol{r}_1+\boldsymbol{r}_2)}{\omega_{cl}}\cos\omega t\right]\Phi_i(\boldsymbol{r}_1, \boldsymbol{r}_2), \tag{6.11}$$

$$\psi_f(\boldsymbol{r},t) = \mathrm{e}^{-i\mathcal{E}_{1s}t}\left(1 - \frac{\boldsymbol{F}_0\cdot\boldsymbol{r}}{\omega_{cl}}\cos\omega t\right)\varphi_{1s}(\boldsymbol{r}) \tag{6.12}$$

From these estimates of $\omega_{cl} \sim \left|\mathcal{E}_{\mathrm{He}(1s)}\right|$, $\frac{F_0}{\omega_{cl}} \sim 10^{-3}$ a.u., it follows that the first-order corrections are negligible. Well, here we suppose that the He^+ ion after the ionizing collision remains in the state that corresponds to its unperturbed ground state, $n = 1$.

If the ion remains in the excited state, for example, in the first excited state, $n = 2$, then things become a little bit more complicated. Namely, now we must take into account the degeneracy of this state. We have $2s$ and $2p$ orbitals. Using this ansatz

$$\left|\psi_f(t)\right\rangle = \sum_{l=0,1}\sum_{m=-l}^{l} a_{lm}(t)\mathrm{e}^{-i\mathcal{E}_{n=2}t}|2lm\rangle \tag{6.13}$$

when solving the time-dependent Schrödinger equation, we obtain the following results for the field-dressed states:

$$\begin{aligned}\psi_{2s}(\boldsymbol{r},t) = \mathrm{e}^{-i\mathcal{E}_{n=2}t}\Bigg[&\cos\left(\frac{3F_0}{Z\omega}\sin\omega t\right)\varphi_{2s}(\boldsymbol{r})\\ &- i\sin\left(\frac{3F_0}{Z\omega}\sin\omega t\right)\varphi_{2p_0}(\boldsymbol{r})\Bigg],\end{aligned} \tag{6.14}$$

$$\begin{aligned}\psi_{2p_0}(\boldsymbol{r},t) = \mathrm{e}^{-i\mathcal{E}_{n=2}t}\Bigg[&\cos\left(\frac{3F_0}{Z\omega}\sin\omega t\right)\varphi_{2p_0}(\boldsymbol{r})\\ &-i\sin\left(\frac{3F_0}{Z\omega}\sin\omega t\right)\varphi_{2s}(\boldsymbol{r})\Bigg],\end{aligned} \tag{6.15}$$

$$\psi_{2p\pm1}(\boldsymbol{r},t) = \mathrm{e}^{-i\mathcal{E}_{n=2}t}\varphi_{2p\pm1}(\boldsymbol{r}). \tag{6.16}$$

Further, I will present some numerical results when the He^+ remains in the ground state and when it remains in the first excited state (see Fig. 6.4).

The top panel shows the field-free momentum profiles, that is, the usual EMS, in the absence of a laser field. Four different models of the helium ground-state wave functions are shown in Fig. 6.5. It is important that the two functions, BK and CI, which give accurate values for the helium binding energy and which are strongly correlated, are indistinguishable. The $\mathrm{LP}_{\|}$ and $\mathrm{LP}_{\perp}$ panels correspond to the presence of a laser field: the $\mathrm{LP}_{\|}$ to the geometry, where the laser field is almost perpendicular to the momentum $\mathbf{q}$; and the $\mathrm{LP}_{\perp}$ to the geometry, where the laser field is nearly parallel to the momentum $\mathbf{q}$. So, it is difficult to find any difference between the cases of the absence and the presence of the field. What is most important here is that we do not see any difference between the results using the two accurate correlated functions, BK and CI.

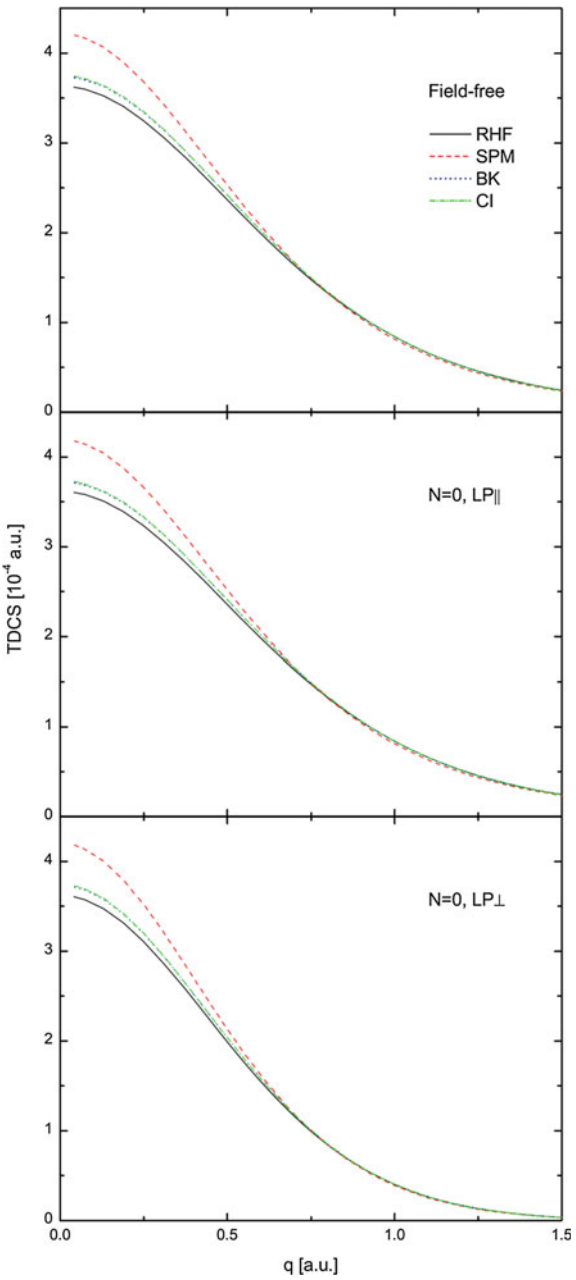

Fig. 6.4 Field-free and $N = 0$ laser-assisted momentum profiles, when the He^+ ion is left in the $n = 1$ state

In Fig. 6.6, the He^+ ion remains in the ground state, but the total number of photons is different from zero. We find that the laser-assisted momentum profiles ares markedly different in the inspected two geometries.

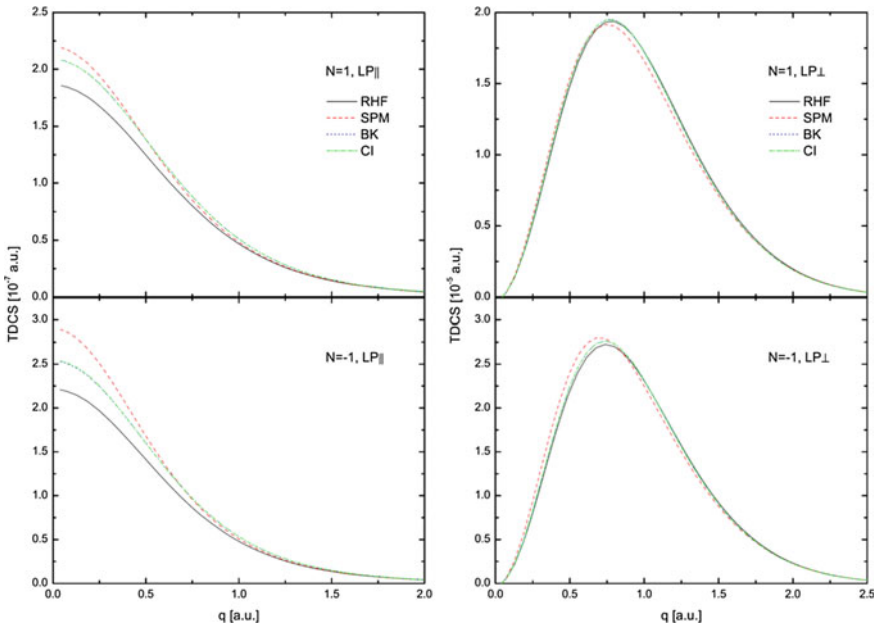

Fig. 6.5 The $N = \pm 1$ laser-assisted momentum profiles corresponding to the (e, 2e) transition to the $n = 1$ state of He^+

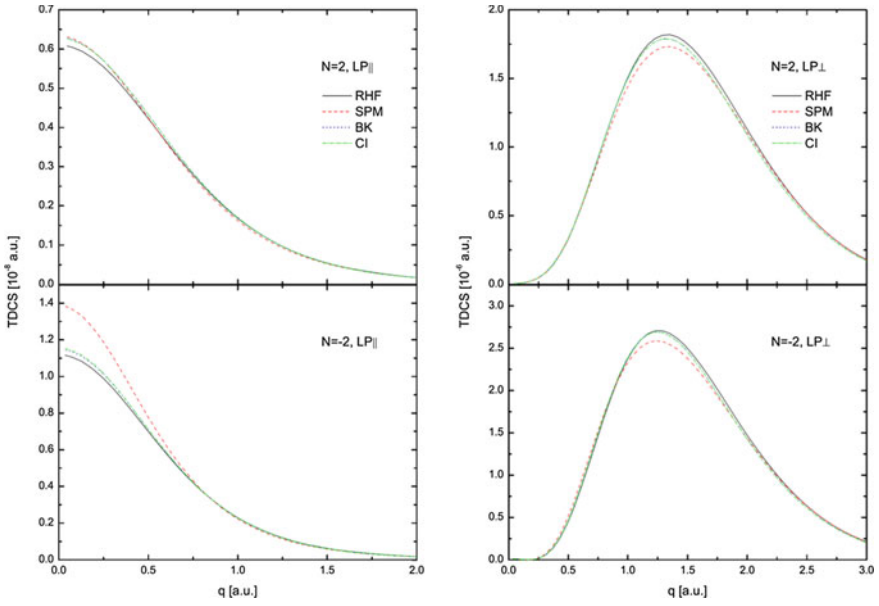

Fig. 6.6 The same as in Fig. 6.2, but for the $N = \pm 2$ case

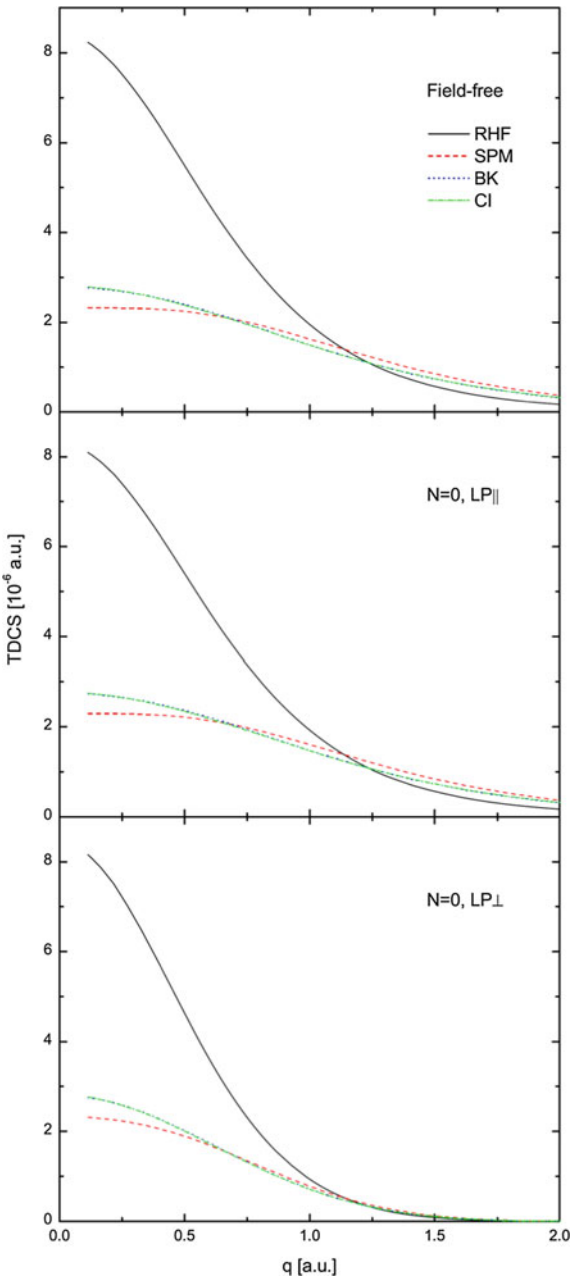

Fig. 6.7 The same as in Fig. 6.4, but for the case when the He^+ ion is left in the $n = 2$ state

In this work [4], we showed that this difference is due to the effect of Volkov states on the fast incoming and outgoing electrons in EMS.

In Fig. 6.7, He^+ remains not in the ground but in the first excited state. The total number of photons is zero. The field-free and laser-assisted results. The same geometries exist, $LP_{\parallel}$ and $LP_{\perp}$. Once again, no difference is found between the accurate functions, BK and CI.

However, if we consider the case of a nonzero number of photons, we can finally see the difference between the accurate functions (see Figs. 6.8 and 6.9).

This is a very important result, because, in EMS of helium in the absence of a laser field, you will never see any measurable difference between the accurate correlated functions (see Fig. 6.7).

Having obtained this finding, we decided to go further and to consider the situation when the He^+ is excited even higher, and as high as into the continuum. This is not the (e, 2e) case anymore, this is the so-called (e, 3e) case (see Fig. 6.10). We still have the fast incoming and two fast outgoing electrons, but, in addition, we measure a slow ejected electron simultaneously with the two fast final electrons.

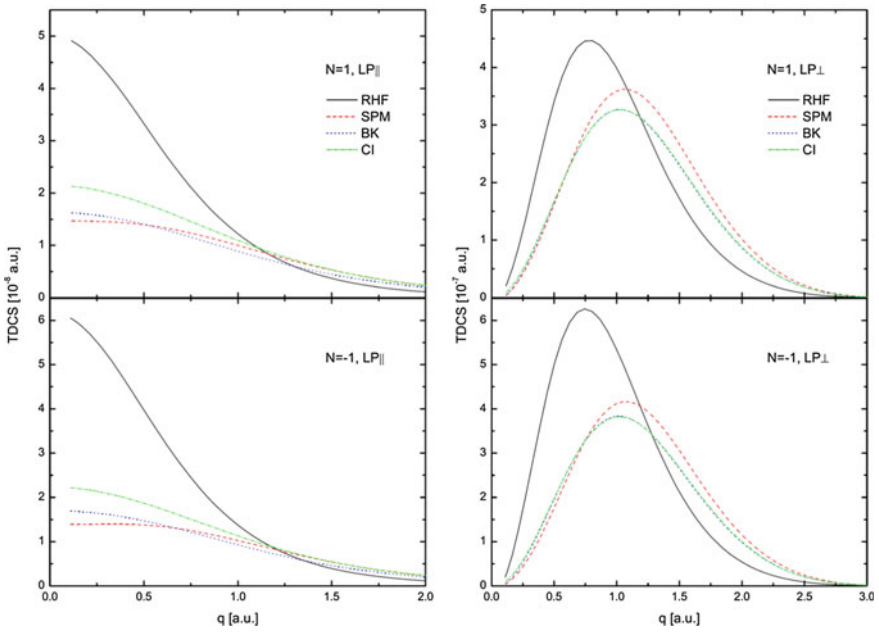

Fig. 6.8 The same as in Fig. 6.5, but for $n = 2$

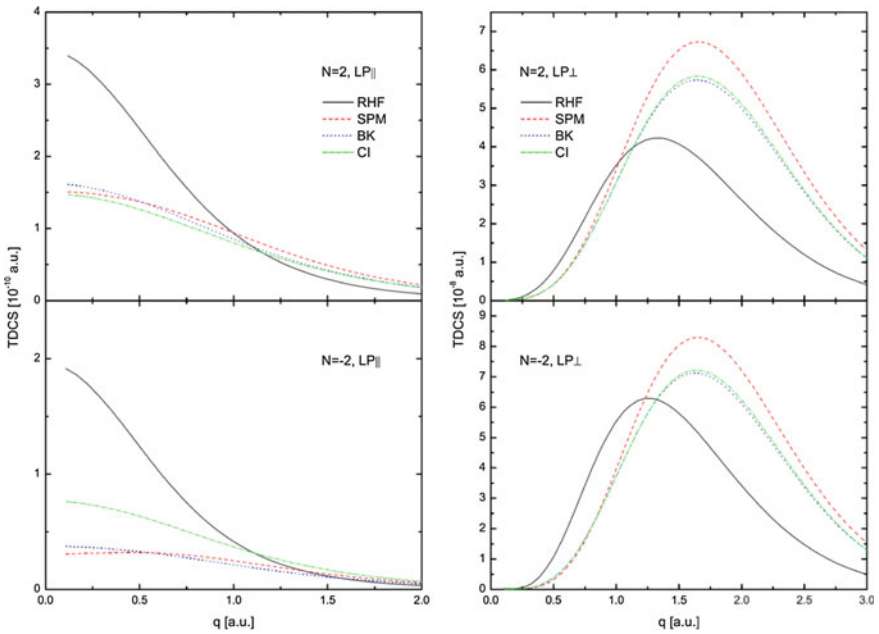

Fig. 6.9 The same as in Fig. 6.6, but for $n = 2$

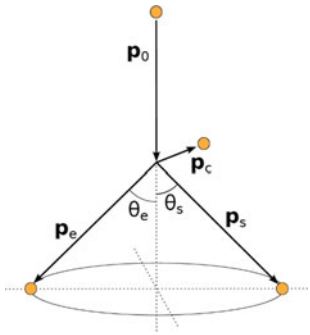

Fig. 6.10 A schematic drawing of the (e, 3e) process

The slow ejected electron goes into the continuum due to the shake-off mechanism. The main problem here is how to describe this electron. We employed the so-called Coulomb-Volkov approximation:

$$\xi_{\vec{p}}(\vec{r},t) = \varphi^{C}_{\vec{p}}(\vec{r})\chi_{\vec{p}}(\vec{r},t)\exp(-i\vec{p}\cdot\vec{r}). \tag{6.17}$$

Here the Coulomb wave takes into account the effect of the Coulomb field of the He nucleus on the slow electron, and the Volkov function takes into account the

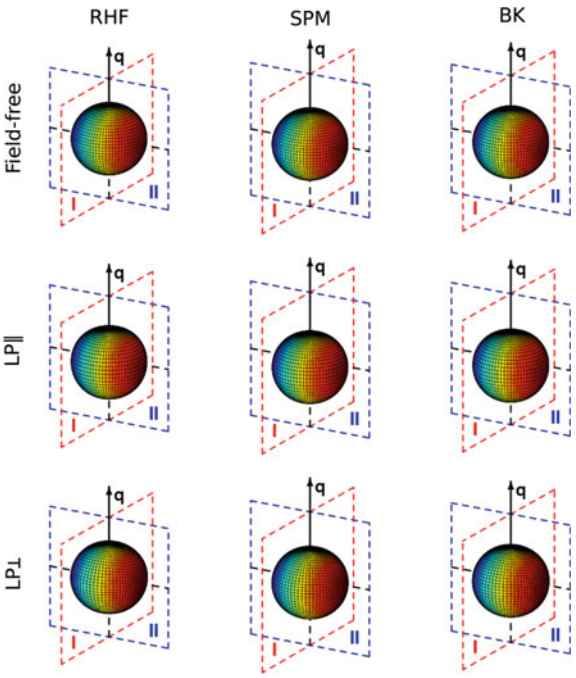

Fig. 6.11 Numerical results for angular distributions of the slow ejected electron in the (e, 3e) process. The scattering (*I*) and perpendicular (*II*) planes are indicated by the *red* and *blue lines*, respectively. The *dashed line* in *plane II* is perpendicular to the q axis and crosses the latter at the origin. The field-free angular distributions are shown in the *top row*, and the $N = 0$ results are shown in the *middle* (LP geometry) and *bottom* ($LP_{\perp}$ geometry) *rows*

effect of the laser field. Fig. 6.11 shows the results for the angular distributions of the slow electron when the momentum of the fast electrons are fixed.

The field-free and laser-assisted results with different functions of He are shown in Fig. 6.12. When the number of photons is zero, we find no difference. But when we consider a non-zero number of photons, we obtain marked differences between various different wave functions of He.

This means that the presence of the laser field strongly enhances the sensitivity of the EMS method to the electron-electron correlations.

What is interesting is that registering the slower electron is crucial to observe the difference between the different models of the He wave function. What is shown in Fig. 6.13 is the situation when the slow electron is not detected, the so-called (e, 3-1e) case.

We find no difference between the field-free and laser-assisted results. Basically, when we do not register the slow ejected electron, we thus sum over different multiphoton processes. Since we consider a weak low-frequency field, we can use the Kroll-Watson sum rule that gives us the field-free result.

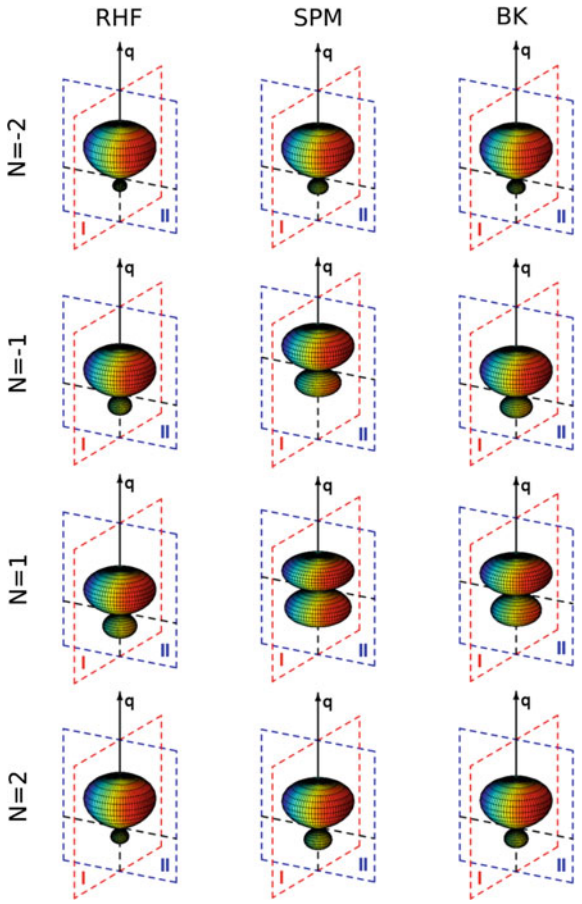

Fig. 6.12 The same as in Fig. 6.11, but for $N = -2, -1, 1, 2$ (from the *top* to the *bottom row*, respectively) in the $LP_{\parallel}$ geometry

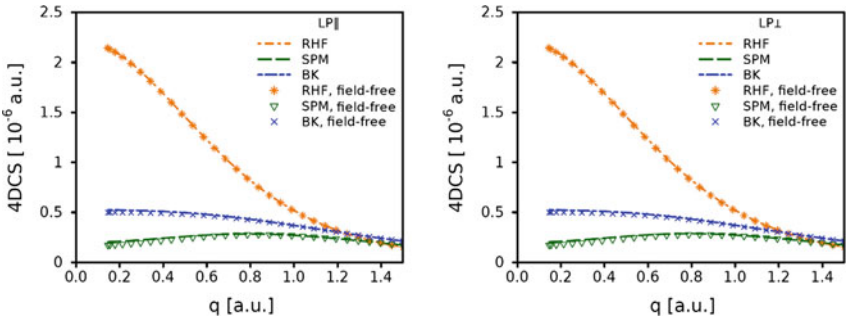

Fig. 6.13 The field-free and laser-assisted (e, 3-1e) momentum profiles in the (*left*) $LP_{\parallel}$ and (*right*) $LP_{\perp}$ geometries

6.3 Conclusion

Let me briefly outline potential and perspectives of the laser-assisted EMS method. Concerning the potential, our theoretical analysis for helium shows that even in the presence of the weak laser field, whose effect on the target state is almost insignificant, the sensitivity of the EMS method to electron-electron correlations in the target can be dramatically enhanced. Another interesting situation, which I did not discuss in my talk, is when the laser field is resonant with the transition in the target. In this case, even a very weak laser field can efficiently couple the ground and excited target states. One thus obtains a unique opportunity to study momentum distributions of electrons in excited states, because, in the absence of the laser field, you study only the ground state.

Finally, about perspectives: From the experimental side, we are waiting for the first laser-assisted measurements. These measurements are expected to be conducted on a helium atomic target with these laser parameters: $\omega = 1.55$ eV, $I = 5 \times 10^{11}$ W/cm^2. From the theoretical side, it will be interesting to consider the case of molecular targets. The other interesting development is the so-called time-resolved electron momentum spectroscopy. The idea is a pump-and-probe experiment, where the pump is a laser pulse and the probe is the electron pulse. Changing the time interval between the laser and electron pulses, one can create a kind of a movie in momentum space. This idea awaits a proper theoretical formulation.

References

1. E. Weigold, I.E. McCarthy, *Electron Momentum Spectroscopy* (Kluwer Academic/Plenum Publishers, New York, 1999)
2. N. Watanabe et al., Phys. Rev. A **72**, 032705 (2005)
3. K.A. Kouzakov, Yu.V. Popov, M. Takahashi, Laser-assisted electron momentum spectroscopy, Phys. Rev. A **82**, 023410 (2010)
4. A.A. Bulychev, K.A. Kouzakov, Yu.V. Popov, The role of Volkov waves in laser-assisted electron momentum spectroscopy. Phys. Lett. A. **376**, 484–487 (2012)

Part III
Exotic Properties of Light

Chapter 7
Evolution of Polarization Singularities of Two Monochromatic Beams in Their Collinear Interaction in an Isotropic Medium with Spatial Dispersion of Cubic Nonlinearity

Vladimir Makarov

7.1 Introduction

I am going talk about the results [1] obtained by our team in the investigation of the appearance of polarization singularities and its interaction in nonlinear optics problems, more specifically, about the interaction of two monochromatic beams with defined structure containing the polarization singularities in the case of their collinear propagation in an isotropic gyrotropic medium with cubic nonlinearity. The simplest example of an isotropic chiral medium is an isotropic solution of large bioorganic molecules, which differ from their mirror images (Fig. 7.1), in a word, chiral molecules.

Inhomogeneously polarized monochromatic electromagnetic fields may contain lines of circular polarization also known as lines of polarization singularity (*C*-lines) [2]. In paraxial beams, the intersections of the *C*-lines with the plane transversal to the propagation direction are treated as *C*-points. The behavior of the *C*-points in various linear media is frequently studied in scientific works (see, for example, [3–6]). Methods for the description of the *C*-point dynamics [7] and their experimental detection [8] have been developed; the statistics of the *C*-points in random light fields have also been studied [9–11]. In addition, there are certain applications of polarization singularities in problems of biology [12].

V. Makarov (✉)
Faculty of Physics and International Laser Center,
Lomonosov Moscow State University, Leninskie Gory 1,
Moscow 119991, Russia
e-mail: vamakarov@phys.msu.ru

K. Yamanouchi (ed.), *Progress in Photon Science*, Springer Series in Chemical Physics 115, DOI 10.1007/978-3-319-52431-3_7

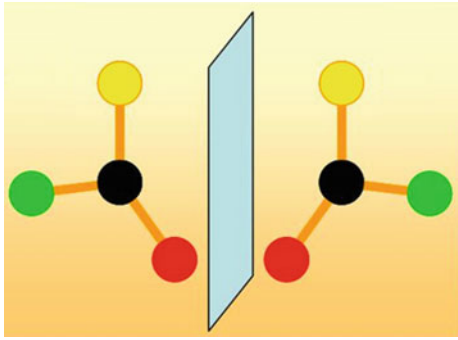

Fig. 7.1 Chiral molecule

The classification scheme for the *C*-points was first proposed in [2], based on the analogous scheme for the degenerate points of the two-dimensional symmetric tensor field. In connection with this, they are assumed to vary among three basic types of *C*-points: the *lemon*, the *monstar,* and the *star*. The most important characteristic of the *C*-point is its topological index, which is the number of full rotations of the polarization ellipse on a counterclockwise loop around the *C*-point. The lemon and the monstar points have a topological index 1/2. This is because the polarization ellipse rotates at 180° on a counterclockwise loop around the *C*-point. The difference between these two types is in the orientation of the polarization ellipses in the vicinity of the *C*-point [13]. The star *C*-point has a topological index −1/2 (see Fig. 7.2).

C-points can also be treated as phase singularities of the circularly polarized components of the electromagnetic radiation [13]. The complex amplitude of one of the circularly polarized components of the field becomes zero at the *C*-point, and

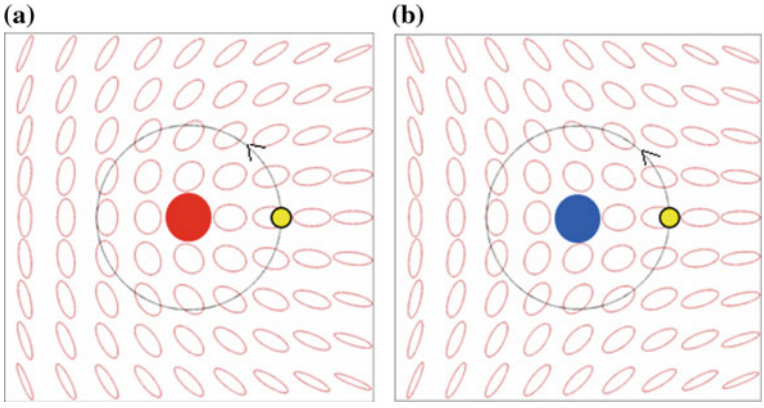

Fig. 7.2 **a** The lemon and the monstar *C*-points (*red circle*) with topological index ½. The polarization ellipse rotates 180° on a counterclockwise loop around the *C*-point and. **b** The star *C*-point (*blue circle*) with topological index −½. The polarization ellipse rotates 180° on a clockwise loop around the *C*-point

the phase of this component becomes indefinite. The points of the phase singularities are also known as "optical vortices". There are a number of fundamental theoretical works [14–16] devoted to the linear interaction of the beams containing phase singularities with various structures, and the results of these works can be generalized for the case of the interacting beams with *C*-points.

Due to the features accompanying the formation of polarization singularities in nonlinear optical processes and their subsequent evolution in a nonlinear medium, there are countless resource-consuming methods for accounting for the polarization evolution in the process of wave propagation. However, such studies could be especially interesting. Formation of polarization singularities is possible due to the three-wave mixing in a nonlocal nonlinear medium, even in the case of uniformly polarized incident beams [17–20]. Moreover, numerical investigations have shown that the nonlocality of nonlinear medium plays the key role in the stabilization of the propagation of singular beams of a specific type [21–23]. Interest in the processes accompanying the filamentation of singular beams also increases [24, 25].

The aim of this work is the investigation of the interaction of two monochromatic beams with defined structure containing the polarization singularities in the case of their collinear propagation in an isotropic gyrotropic medium with cubic nonlinearity.

7.2 Theory

The propagation of the light beam in an isotropic gyrotropic medium with spatial dispersion of cubic nonlinearity can be described in terms of the following system of nonlinear equations [26, 27]:

$$\frac{\partial A_{\pm}}{\partial z} + \frac{i}{2k}\Delta_{\perp}A_{\pm} + i\left[\mp\rho_0 + (\sigma_1/2 \mp \rho_1)|A_{\pm}|^2 + (\sigma_1/2 + \sigma_2)|A_{\mp}|^2\right]A_{\pm} = 0 \tag{7.1}$$

for the slowly varying envelopes $A_{\pm}(z, x, y) = A_x \pm iA_y$ of the circularly polarized components of the light field. Here $\Delta_{\perp}$ is a Laplace operator in transversal coordinates, ω is the frequency of the wave propagating in the z-direction, and k is its wave number. The parameters $\sigma_1 = 4\pi\omega^2\chi_{xyxy}/(kc^2)$ and $\sigma_2 = 2\pi\omega^2\chi_{xxyy}/(kc^2)$ are proportional to the components of the fourth-rank tensor of local cubic optical response $\hat{\chi}^{(3)}(\omega; -\omega, \omega, \omega)$, which possesses a permutation symmetry for the last two indices. Parameter $\rho_{0,1} = 2\pi\omega^2\gamma_{0,1}/c^2$ is proportional to the pseudoscalar constants of linear and nonlinear gyration γ_0 and γ_1, which are the nonzero components of nonlocal linear $\hat{\gamma}^{(1)}$ and nonlinear (cubic) $\hat{\gamma}^{(3)}$ optical susceptibilities, contributing $\hat{\gamma}^{(1)}\vec{\nabla}\vec{E}$ and $\hat{\gamma}^{(3)}\vec{E}\vec{E}\vec{\nabla}\vec{E}$ to the polarization of the medium [28–30]. Further we assume that all of these medium parameters have real values.

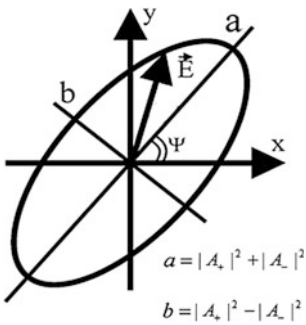

Fig. 7.3 Polarization ellipse parameters

The propagating radiation can be fully characterized by the intensity $I(x,y,z) = \left(|A_+|^2 + |A_-|^2\right)/2$, the ellipticity degree of the polarization ellipse $M(x,y,z) = \left(|A_+|^2 - |A_-|^2\right)/2I$, and the angle of orientation of the polarization ellipse $\Psi(x,y,z) = \mathrm{Arg}\left(A_+ A_-^*\right)/2$ (see Fig. 7.3). Let us consider two coherent monochromatic beams falling along the z-axis onto the medium surface $z = 0$ normally. We assume the beams each have the following structure: the right-handed circularly polarized component has a Gaussian profile, while the left-handed circularly polarized one has a Laguerre–Gaussian profile. Their centers are located on the x-axis at a distance, each at $d/2$ from the zero point. Right-handed circularly polarized components of these beams at $z = 0$ are given by the following expressions:

$$A_{+1}(x,y) = E_0 \exp\left(-\frac{(x+d/2)^2 + y^2}{w^2}\right), \tag{7.2}$$

$$A_{+2}(x,y) = E_0 \exp(i\theta) \exp\left(-\frac{(x-d/2)^2 + y^2}{w^2}\right), \tag{7.3}$$

and the left-handed circularly polarized ones are given as:

$$A_{-1}(x,y) = hE_0\left(\frac{x+d/2 \mp iy}{w}\right) \exp\left(-\frac{(x+d/2)^2 + y^2}{w^2}\right), \tag{7.4}$$

$$A_{-2}(x,y) = hE_0 \exp(i\theta)\left(\frac{x-d/2 \mp iy}{w}\right) \exp\left(-\frac{(x-d/2)^2 + y^2}{w^2}\right). \tag{7.5}$$

Here, $\exp(i\theta)$ determines the phase shift between the beams, E_0 is the amplitude, and h is a real-value coefficient. When $d >> w$, both beams have radial symmetric intensity distributions and C-points in their centers $(-d/2, 0, 0)$ and $(d/2, 0, 0)$.

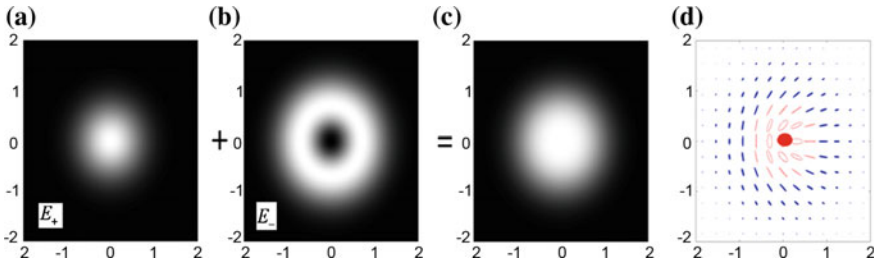

Fig. 7.4 The intensity distribution in *right-handed circularly* polarized component with Gaussian profile (**a**) and in the *left-handed circularly* polarized one with Laguerre–Gaussian profile (**b**), the intensity (**c**), and polarization (**d**) distributions in the resulting beam. The *right-handed circularly* polarized *C*-point (*red circle*) with topological index ½ is located at the center of the beam ($x = 0$; $y = 0$)

The radiation is right-handed circularly polarized in these *C*-points. If there is a "−" in the expression (7.4) and (7.5) before the imaginary unit, then the topological index of the *C*-point is 1/2, and, if there is a "+" in these equations, then the topological index is −1/2. In the case of positive topological index, the *C*-point given by the expressions above will have a "lemon" morphologic type (see Fig. 7.4), and, in the case of negative topological index, it will be a "star". Within the framework of our study, we do not pay attention to the transformation of lemon to monstar and vice versa, neither do we make any difference between these two morphological types with positive topological charge. We limit ourselves to the investigation of topological charge evolution, nucleation, and annihilation of the *C*-points with opposite topological charges. Figure 7.4d shows typical transversal polarization distribution in one of the incident beams in the case of the topological index 1/2. Each ellipse in the figure shows the polarization ellipse in the corresponding point of the beam cross section with the same parameter (ellipticity degree, angle of orientation). The sum of squares of axes of the ellipse is proportional to the intensity of light at the given point. Filled ellipses correspond to the left-handed circularly polarized components, and the open ellipses correspond to the right-handed circularly polarized radiation.

The system of equations (7.1) is symmetrical to the simultaneous change of $E_\pm$ to $E_\mp$ and $\rho_{0,1}$ to $-\rho_{0,1}$. In this case, the indices of the *C*-points of the incident beams, the ellipticity degrees, and the orientation angles of the polarization ellipses in them change their sign to the opposite in each point of space. Moreover, the simultaneous change of the topological indices of the *C*-points in the incident beams, which can be achieved by the change of "∓" to "±" in (7.4) and (7.5), is equivalent to the reversion of the *y*-axis, i.e., the spatial distribution of the electromagnetic field is mirror-reflected from the plane $y = 0$. Owing to the medium symmetry, the trajectories of the singularities (the *C*-lines) will be reflected relative to the plane $y = 0$. The effect of linear gyration ($\rho_0 \neq 0$) causes the rotation of the polarization ellipses in each point in the transversal plane of the propagating field for any value of *z*. The angle of rotation is proportional to the propagation

coordinate z and does not depend on the transversal coordinates. Thus, in this article, we do not take into account the linear gyration, focusing primarily on non-linear effects.

It is important to remark that the *C*-points with the opposite handedness of the polarization rotation do not interact in a linear medium. Thus, we can limit ourselves to the consideration of incident beams with right-handed circular polarization in both *C*-points with equal or opposite topological indices. In these two cases, the equation system (7.1) with boundary conditions (7.2)–(7.5) was solved numerically for various values of the incident radiation and nonlinear medium. Then the polarization distributions, shown in Fig. 7.4 in xy plane for various z values, were analyzed. The positions of *C*-points in these polarization distributions were found as points where the value of the polarization ellipse orientation angle Ψ was undefined. Afterwards, the topological indices of the *C*-points were found by the polarization distribution in their vicinity, and the *C*-lines were built.

It follows from (7.1) that, in a linear medium ($\sigma_{1,2} = 0$, $\rho_1 = 0$), the circularly polarized components of the light field $A_{\pm}$ with opposite handedness do not interact with each other. For any z, the right-handed circularly polarized component is a superposition of two non-coaxial Gaussian beams that spread during the propagation. As the result of merging two Gaussian beams, an intensity maximum is formed between their centers, which we call the "central maximum" hereafter. The left-handed circularly polarized component is a superposition of two non-coaxial Laguerre–Gaussian beams, and its shape experiences more sophisticated changes during the propagation. Each beam loses its cylindrical symmetry. There appear spots at their "rings", where the formation of the intensity maxima take place, which further we call them the "lateral maxima". With the increase of z, these maxima move away from the center. As a result, three intensity maxima appear in the transversal section of superimposed propagating beams.

In the case of the equal sign of the topological charges of the *C*-points in the incident beams, the interference of the beams at $z = 0$ yields one or three *C*-points, depending on d, h, and θ, instead of two. The sum of the topological charges of all of the *C*-points in both cases is equal to +1/2 or −1/2, depending on the sign of the topological charge of the separate *C*-points. The appearance and the propagation of a sole *C*-point is not of a major factor, so, therefore, we consider the situation in which three *C*-points arise at the border of the medium. The third *C*-point, which appears between two initially existing *C*-points, has the topological charge with the sign opposite to that of the initial *C*-points. If $h = 1$, its coordinates are $x_c = 0$, $y_c = -0.5d \cdot \mathrm{tg}\,(\theta/2)$, and they do not change with the propagation when z increases. After traversing a distance of $\tilde{z} = (d^2(1 + \cos\theta)^{-1} - 1)^{1/2}$, a dynamic inversion of its topological charge occurs, first described in [14]: the central *C*-point "exchanges" its topological charge with one of the other two *C*-points (Fig. 7.5a). In other words, two *C*-points with opposite topological charges annihilate, and afterwards another pair of the "oppositely charged" *C*-points appears immediately. Figure 7.5b shows the polarization distribution in the transversal plane for $z = 2L_d$,

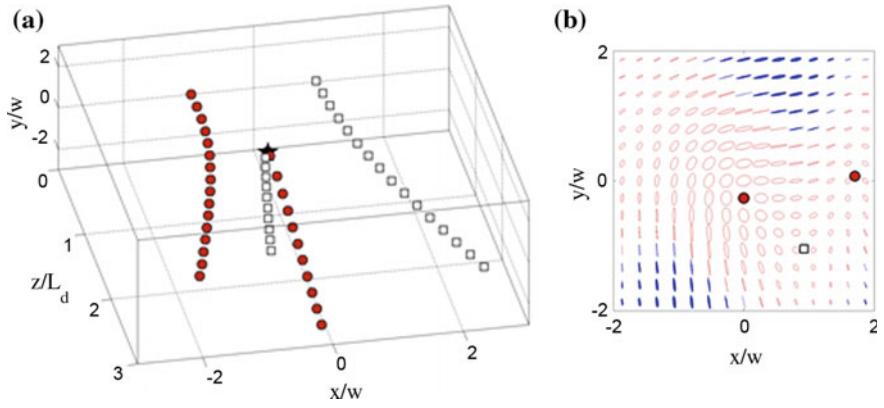

Fig. 7.5 The trajectories of the *C*-points in a linear medium in the case of equal signs of the topological indices of the incident beams (**a**) and the transversal polarization distribution in the propagating light at $z/L_d = 2$ (**b**) The parameters of the incident beams are the following: $d = 2$, $h = 1$, $\theta = 30°$. *Circles* indicate the *C*-line in (**a**) (*C*-points in (**b**)) with +1/2-topological index, and *squares* indicate the *C*-line in (**a**) (C-points in (**b**)) with −1/2-topological index. The point of pairwise creation/annihilation of the *C*-points is designated by a star ($\tilde{z}/L_d \approx 1.07$)

where $L_d = kw^2/2$.The circles indicate the *C*-points with the topological charge +1/2, and a square indicates the *C*-point with a topological charge of −1/2.

In the case of opposite topological charges of the *C*-points in the incident beams, there can be two or four *C*-points at the border of the medium as a result of their interference, depending on d, h, and θ. If four *C*-points appear there, two "additional" *C*-points have opposite topological charges, so that the sum of topological charges of all of the *C*-points is equal to zero. We will consider only the case when there are two *C*-points, located in the centers of incident beams. If $\theta = 0$, then for any value of $z = z_1$ the light in each point of the straight line $\{x = 0; z = z_1\}$ is right-handed circularly polarized, because the left-handed circularly polarized Laguerre–Gaussian components suppress each other at this line. In this case, the abovementioned straight line is a symmetry axis for the intensity distribution in the transversal plane.

Let us consider the case when there is only one pair of *C*-points with the opposite topological charges at the border of the medium. If $\theta \neq 0$ and $d > \sqrt{2}$, then, after traversing some distance, an additional pair of *C*-points with opposite topological charges is nucleated as shown in Fig. 7.6a. The corresponding transversal polarization distribution for $z = 2L_d$ is shown in Fig. 7.6b. If the phase shift θ between the initial beams exceeds a certain critical value $\theta_{cr}(d)$, then one of the "new" *C*-points will subsequently be annihilated with one of the "old" *C*-points having the opposite topological charge (Fig. 7.6c). The transversal polarization distribution at $z = 2L_d$ for this case is shown in Fig. 7.6d. The dependence $\theta_{\mathrm{cr}}(d)$ is monotone (Fig. 7.7).

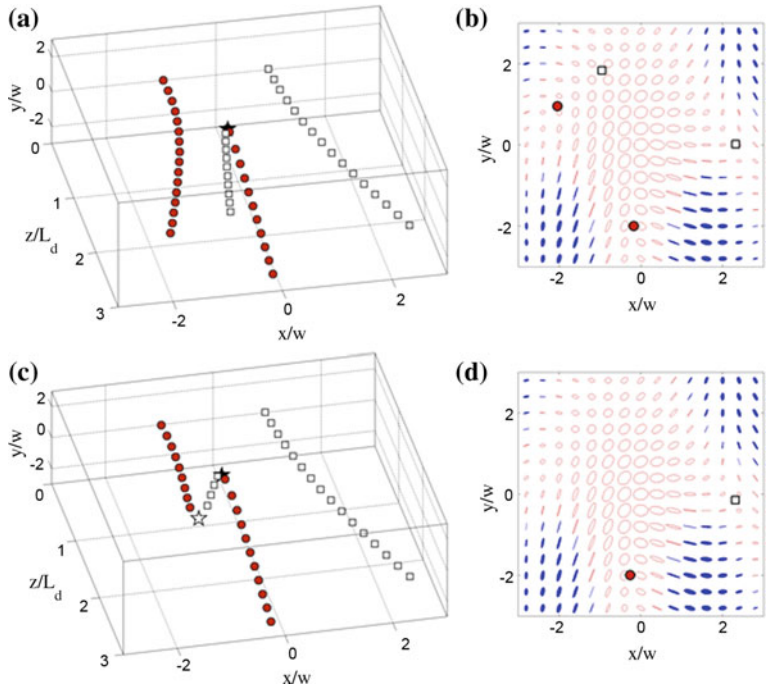

Fig. 7.6 The processes of the nucleation and the annihilation of the *C*-points (**a**, **c**) and the transversal polarization distributions at $z = 3L_d$ (**b**, **d**). Here $\theta = 20°$ in (**a**, **b**), and $\theta = 30°$ in (**c**, **d**). The topological charges of the C-points in the initial (separate) beams are opposite, $d = 2$, $h = 1$. The critical phase shift for this case is $\theta_{cr} \approx 24°$. *Circles* indicate the *C*-points with positive topological charge, and *squares* indicate those with the negative topological charge. Pairwise creation of the *C*-points is indicated by empty stars in (**a**) and (**c**), and pairwise annihilation is indicated by a filled star in (**c**)

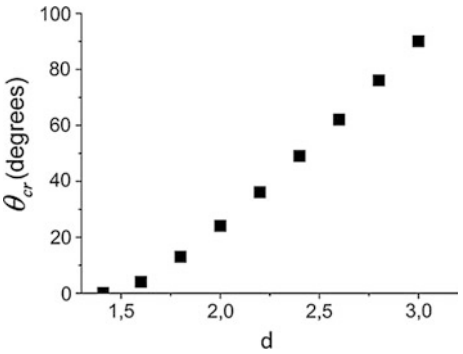

Fig. 7.7 Dependence of θ_{cr} on the distance between the centers of the incident beams d

In a nonlinear medium, the features of the interaction of the polarization singularities is determined by the parameters d/w, h, θ, σ_2/σ_1, ρ_1/σ_1 and the so-called dimensionless power $P = \sigma_1 L_d E_0^2$, which can easily be adjusted in the experiment. Our numerical investigations have shown its predominant influence on the features accompanying the propagation of the *C*-points. With the growth of *P*, these features take place at a smaller value of the nonlinear susceptibility of the medium, or at smaller distances traversed in a medium.

The coefficients $\sigma_1/2 \pm \rho_1$ in (7.1) are responsible for the self-action of the each circularly polarized component. In the case of the equal topological charges of the *C*-points in the initial beams, this self-action promotes the amplification of the central and lateral intensity maxima and their stability during the propagation. If $\sigma_1/2 + \sigma_2 > 0$, the circularly polarized components $A_\pm$ are focused on each other due to the nonlinear cross-interaction. In this case, each of the lateral maxima will be attracted to the corresponding central maxima with the opposite handedness of the polarization. In the case of significant focusing nonlinearity, the central spots of the Gaussian components do not merge, but propagate separately instead. As a result, there appear not three, but only two intense peaks in the transversal section of the propagating light, and their polarization is determined by the value of h. If $h \approx 1$, the polarization is almost linear. The intensity of light in the vicinity of each of the *C*-points, where the radiation is right-handed circularly polarized, tends to zero, since the power of this circularly polarized component is attracted by the component with the opposite rotation, that is the right-handed circularly polarized Gaussian is attracted by the left-handed circularly polarized Laguerre–Gaussian component. If $\sigma_1/2 + \sigma_2 < 0$, then the intensity maxima with opposite handedness of the polarization rotation defocuses on each other and tend to occupy areas in the beam cross section, which do not overlap. The polarization and the intensity distributions in this case become similar to those shown in Figs. 7.5 and 7.6 for approximately the same parameters of the incident beams. The maxima of the intensity maintain their shapes during the propagation owing to the nonlinear self-action and its contrasts. The larger one is the absolute value of the negative quantity σ_2/σ_1; the stronger one is the difference between the polarization state of this maximum and the linear polarization state.

Let us consider now the incidence of two beams with equal topological charges of the singularities onto the nonlinear medium. For any value of $\sigma_1/2 + \sigma_2$, the central *C*-point, originating in this case from the interference, does not move straight along the z-axis, as it does in a linear medium (Fig. 7.5a), and the dynamic inversion of its topological charge does not occur. Instead, two separate events of pairwise creation and annihilation of the *C*-points in a nonlinear medium take place (Fig. 7.8). Depending on the sign of the $\sigma_1/2 + \sigma_2$, the sequence of these two events can be different. Figure 7.9a, b show the dependence of the nucleation/annihilation distance on the dimensionless power parameter. As can be seen, the growth of *P* results in the increase of the z-coordinates of the *C*-points' nucleation/annihilation processes for $\sigma_1/2 + \sigma_2 > 0$ and in the decrease of these characteristic coordinates in the case of $\sigma_1/2 + \sigma_2 < 0$.

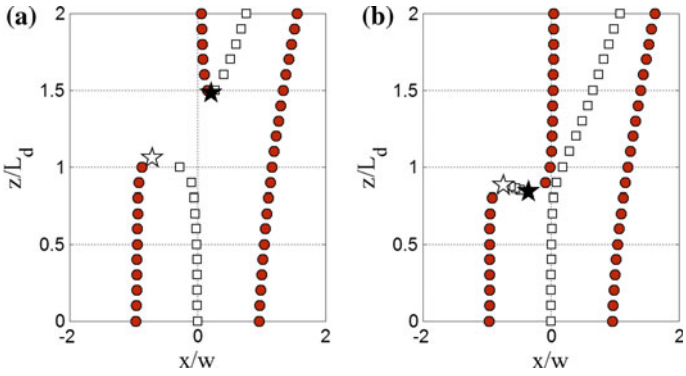

Fig. 7.8 *C*-lines in a nonlinear medium for $P = 1$, $\sigma_2/\sigma_1 = 0.5$, $\sigma_2/\sigma_1 = 0.5$, $\rho_1/\sigma_1 = 0$ (**a**) and $P = 2$, $\sigma_2/\sigma_1 = -0.8$, $\rho_1/\sigma_1 = 0$ (**b**). The parameters of the incident beams are $d = 2$, $\theta = 30^\circ$ and $h = 1$. *Circles* designate the *C*-lines with the topological charge 1/2, while *squares* designate ones with the topological charge −1/2. Pairwise creation of the *C*-points is indicated by *filled stars* and pairwise annihilation is indicated by empty ones

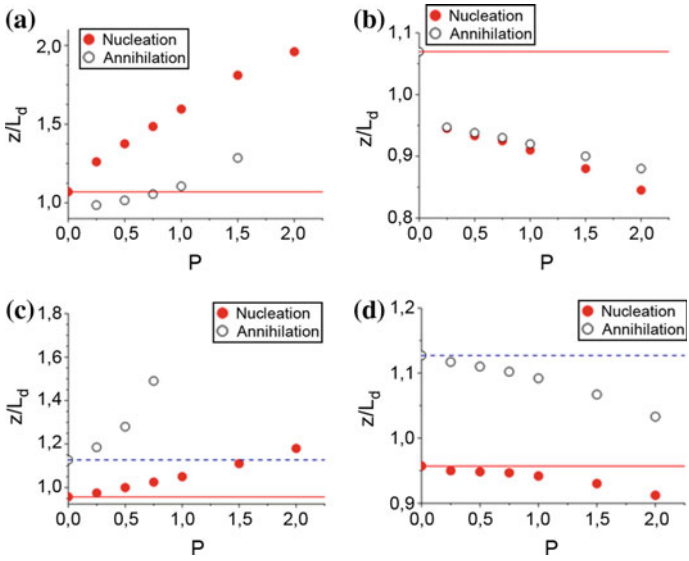

Fig. 7.9 The dependence of the distance from the border of the medium, where the nucleation/annihilation of two *C*-points takes place, on the dimensionless power parameter. *Filled circles* correspond to the nucleation and empty ones to annihilation. **a–b** equal topological charges of the initial singularities, $\theta = 30^\circ$. **c–d** opposite topological charges of the initial singularities, $\theta = 40^\circ$. (**a**, **c**) $\sigma_2/\sigma_1 = 0.5$, (**b**, **d**) $\sigma_2/\sigma_1 = -0.8$. Other parameters: $d = 2$, $h = 1$ and $\rho_1/\sigma_1 = 0$

In the case of the incident beams with the opposite topological charges of the polarization singularities, the trajectories of the *C*-points are similar to those as shown in Fig. 7.6. If we assume that the phase shift θ is greater than θ_{cr}, the pairwise annihilation of *C*-points is observed at certain $z = z^*$ in a linear medium (see Fig. 7.6c). If $\sigma_1/2 + \sigma_2 > 0$, the increase in the dimensionless power results in the increase in the annihilation coordinate z^* until it exceeds the limits of the calculation area. If $\sigma_1/2 + \sigma_2 < 0$, the annihilation occurs at smaller values in z^* with the increase of *P*. In other words, in the first case ($\sigma_1/2 + \sigma_2 > 0$), the evolution of the *C*-points proceeds more slowly, while, in the second case, it proceeds faster, compared to propagation in a linear medium. Such a behavior is common for small values of the dimensionless power ($P_1 \leq P \leq P_2$, where $P_1 \cong 1$, $P_2 \cong 3$). For larger values of *P*, the self-action of the circularly polarized components $A_\pm$ prevents the interaction of the incident beams and, therefore, the interaction of the *C*-points in them. The *z*-coordinate of the pairwise creation of *C*-points is affected by the change of the dimensionless power in a similar way as in Fig. 7.9c, d.

It can be seen from (7.1), that the spatial dispersion of the cubic nonlinearity enhances the self-action of one of the circularly polarized components of propagating light. In the case of equal topological charges of the incident beams, the presence of the spatial dispersion causes faster pairwise creation of the *C*-points with opposite topological charges at smaller distances as compared to the case when the spatial dispersion is absent ($\rho_1 = 0$). Corresponding transversal polarization distribution is shown in Fig. 7.10a. The growth of $|\rho_1|$ leads to the formation of strongly inhomogeneous polarization distribution (Fig. 7.10b). If $\sigma_1/2 + \sigma_2 < 0$, then the spatial dispersion of cubic nonlinearity affects the relative values of the intense peaks in the transversal intensity distribution of the propagating wave.

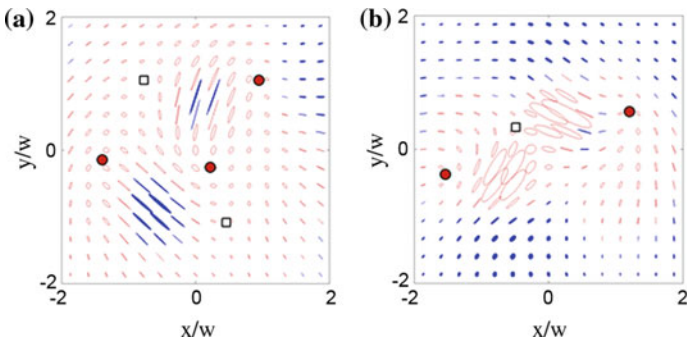

Fig. 7.10 The transversal polarization distribution at $z = 2L_d$ in the propagating wave in the case of equal topological charges of the singularities in the incident beams for the $d = 2$, $h = 1$, $\theta = 30°$, $P = 2$, $\sigma_2/\sigma_1 = 0.5$ and **a** $\rho_1/\sigma_1 = 0.4$, **b** $\rho_1/\sigma_1 = -0.4$

7.3 Conclusion

For the first time the interaction of two collinear specific-kind monochromatic beams with polarization singularities in the nonlinear isotropic gyrotropic medium was theoretically studied. The relations between the components of local and nonlocal cubic optical susceptibility tensors determine possible scenarios of the interaction of circularly polarized components of the light field. In the case of their mutual focusing, the spatial dispersion of cubic nonlinearity determines the polarization states of the intensity maxima in the propagating light. Otherwise, in the case of the defocusing cross-interaction of the circularly polarized components, the spatial dispersion of cubic nonlinearity directly affects the relative intensities of the peaks in the transversal intensity distribution.

The processes of pairwise creation and annihilation of the *C*-points with opposite topological charges in the bulk of the nonlinear medium were observed. The sum of the topological charges of all of the *C*-points in the transversal section of the propagating light remains constant as the z coordinate changes. The nonlinearity of the medium plays a key role in the scenario of the evolution of the *C*-points. In the case of the mutual focusing of the circularly polarized components of the light field, the increase in the intensity of the incident beams leads to the retardation of the interaction of the *C*-points. In the case of the mutual defocusing of the circularly polarized components of the propagating light, the greater the intensity of the incident beams becomes, the faster the processes of pairwise creation/annihilation proceed.

Acknowledgements We acknowledge financial support from the Russian Foundation for Basic Research (Grant No. 13-02-00324) and the support from a grant of the President of the Russian Federation for state support of leading scientific schools (Grant No. NSh-3796.2014.2). I am indeed grateful to Dr. I.A. Perezhogin and Dr. K.S Grigoriev for stimulating discussions with and invaluable help, some results of common work were observe in this report.

References

1. K.S. Grigoriev, V.A. Makarov, I.A. Perezhogin, J. Optics. **16**(105201), 8 (2014)
2. J.F. Nye, Proc. R. Soc. **389**, 279 (1983)
3. KYu. Bliokh, A. Niv, V. Kleiner, E. Hazman, Opt. Express **16**, 709 (2008)
4. F. Flossmann, U.T. Schwarz, M. Maier, M.R. Dennis, Phys. Rev. Lett. **95**, 253901 (2005)
5. M.V. Berry, M.R. Dennis, Proc. Royal. Soc. **459A**, 1261 (2003)
6. YuA Egorov, T.A. Fadeyeva, A.V.J. Volyar, Opt. A **6**, 217 (2004)
7. K. O'Holleran, F. Flossmann, M.R. Dennis, M.J.J. Padgett, Opt. A. Opt. **11**(094020) (2009)
8. O.V. Angelsky, I.I. Mokhun, A.I. Mokhun, M.S. Soskin, Phys. Rev. E **65**, 036602 (2002)
9. M.V. Berry, M.R. Dennis, Proc. Royal. Soc. **457A**, 141 (2001)
10. G.V. Bogatyryova, K.V. Felde, P.V. Polyanskii, M.S. Soskin, Opt. Spectrosc. **97**, 833 (2004)
11. Y.F. Chen, T.H. Lu, K.F. Huang, Phys. Rev. Lett. **96**, 033901 (2006)
12. O.V. Angelsky, A.G. Ushenko, YuA Ushenko, E.G. Ushenko, J. Phys. D **39**, 3547 (2006)
13. M.R. Dennis, Opt. Lett. **33**, 2572 (2008)

14. D. Rozas, C.T. Law, G.A. Jr. Swartzlander, J. Opt. Soc. Amer. B. **14**, 3054–3065 (1997)
15. V. Pyragaite, A. Stabinis, Opt. Comm. **220**, 247 (2003)
16. S. Orlov, A. Stabinis, Opt. Comm. **226**, 97 (2003)
17. V.A. Makarov, I.A. Perezhogin, N.N. Potravkin, Quantum Electron. **41**, 149 (2011)
18. K.S. Grigoriev, V.A. Makarov, I.A. Perezhogin, N.N. Potravkin, Quantum Electron. **41**, 993 (2011)
19. I.A. Perezhogin, V.A. Makarov, J. Opt. A **11**, 074008 (2009)
20. V.A. Makarov, I.A. Perezhogin, N. N. Portavkin. J. Opt. **14**, 055202 (2012)
21. A.S. Desyatnikov, YuS Kivshar, Prog. Opt. **47**, 291 (2005)
22. S. Lopez-Aguayo, J.C. Gutiérrez-Vega, Opt. Express **15**, 18326 (2007)
23. S. Lopez-Aguayo, A.S. Desyatnikov, Yu. S. Kivshar Opt. Express **14**, 7903 (2006)
24. Georgi Maleshkov et al., J. Opt. **13**, 064015 (2011)
25. O. Khasanov, T. Smirnova, O. Fedotova, G. Rusetsky, O. Romanov, App. Opt. **51**, 198 (2012)
26. A.A. Golubkov, V.A. Makarov, Radiophysics and Quantum. Electronics **31**, 1042 (1988)
27. A.A. Golubkov, V.A. Makarov, I.A. Perezhogin, Mosc. Univ. Phys. Bull. **64**, 54 (2009)
28. S.A. Akhmanov, V.I. Zharikov, JETP Lett. **6**, 137 (1967)
29. S.A. Akhmanov, G.A. Lyakhov, V.A. Makarov, V.I. Zharikov, Optica Acta **29**, 1359 (1982)
30. A.A. Golubkov, V.A. Makarov, J. Modern Optics **37**, 1531 (1990)

Chapter 8
Biphoton and Triphoton States, Entanglement, and Schmidt Decompositions

Mikhail Fedorov

8.1 Introduction

In my talk, I will start with the description of the process which produces biphoton states—spontaneous parametric-down conversion (SPDC). In SPDC, the pump-laser wave propagates in a nonlinear birefringent crystal, and some photons of the pump split into two photons and form biphoton pairs. Depending on features of the pump and orientation of a crystal, there are various regimes of SPDC. Usually one differentiates regimes with non-collinear and collinear propagation and the non-degenerate and degenerate frequencies of emitted photons. Also, specific kinds of SPDC processes depend on variables characterizing photon pairs, which can be either continuous or discrete. Examples of continuous variables are angular variables characterizing the directions of the wave vectors of emitted photons or frequencies of photons. The most often met example of discrete variables is that of polarization variables, which can take two values for each photon, corresponding to its horizontal or vertical polarization. At last, all SPDC processes are divided into two classes with different types of phase matching. The first one (type-I) occurs when the pump propagates in a crystal as an extraordinary wave, whereas both emitted photons propagate as ordinary waves. In this case polarizations of the pump and of the emitted photons are different: e.g., horizontal polarization of the pump and vertical polarization of both emitted photons. In the second class of SPDC (type-II phase matching), the pump and one of the emitted photons propagate in a crystal as extraordinary waves, whereas the second emitted photon propagates as the ordinary wave. In this case, polarizations of two photons in each SPDC pair are different: vertical and horizontal.

An important point concerns symmetry of biphoton wave functions. As photons are bosons and they are indistinguishable particles, their wave functions are

M. Fedorov (✉)
Lomonosov Moscow State University, Moskva, Russia
e-mail: fedorovmv@gmail.com

K. Yamanouchi (ed.), *Progress in Photon Science*, Springer Series in Chemical Physics 115, DOI 10.1007/978-3-319-52431-3_8

symmetric with respect to transposition of photon variables. A description of biphoton (bipartite) states in terms of wave functions gives the simplest definition of entanglement: the state is entangled if the biphoton (bipartite) wave function cannot be factorized, i.e., if it cannot be presented in the form of a single product of two one-photon (single-particle) functions each depending on only one variable of one of two photons (particles). Sometimes it is not easy to say immediately whether the biphoton wave function can be factorized or not. The straightforward way of answering this question is related to the use of the so-called Schmidt decomposition of biphoton or bipartite wave functions.

8.2 Theory

The ideas of the Schmidt decompositions originate from the work by Erhard Schmidt [1], published in 1907—long, long ago. This was a purely mathematical work where a purely mathematical theorem was proved. According to this theorem, every sufficiently good function of two variables can be decomposed into a series of products of two functions, each of which depends only on one of two variables (Schmidt modes). In the simplest case of a symmetric function of two variables, the decomposition has the form:

$$\Psi(x_1, x_2) = \sum_n \sqrt{\lambda_n}\, \psi_n(x_1)\psi_n(x_2). \tag{8.1}$$

In applications to quantum bipartite systems, –x $\Psi(x_1, x_2)$ is a bipartite wave function and $\psi_n(x_i)$ are single-particle wave functions in the basis of Schmidt modes. The Schmidt modes are orthogonal and normalized, $\int \mathrm{d}x\, \psi_n^*(x)\psi_{n'}(x) = \delta_{n,n'}$, and they form a complete set of single-particle functions. The decomposition parameters λ_n (as well as $\sqrt{\lambda_n}$) are real and positive. Owing to the unit normalization of $\Psi(x_1, x_2)$, the parameters λ_n also obey the normalization condition $\sum_n \lambda_n = 1$.

Note that the basis of Schmidt modes is unique for any given bipartite state. This is the only basis in which the decomposition contains only one sum. Decomposition of $\Psi(x_1, x_2)$ in products of single-particle functions of any other complete bases ($\varphi_n(x_i)$) contains inevitably double sums like $\sum_{n,m} C_{n,m}\, \varphi_n(x_1)\varphi_m(x_2)$, and only in the Schmidt-mode basis these double sums are reduced to the single sum of (8.1). In other words, the Schmidt-mode basis simplifies maximally the decomposition of bipartite wave functions in sums of products of single-particle wave functions.

As follows directly from the Schmidt decomposition (8.1), the Schmidt modes ψ_n and the decomposition parameters $\sqrt{\lambda_n}$ are eigenfunctions and eigenvalues of the integral equation, the kernel of which is the bipartite wave function itself [1, 2]:

$$\int \mathrm{d}x_2 \Psi(x_1, x_2)\psi_n^*(x_2) = \sqrt{\lambda_n}\,\psi_n(x_1). \tag{8.2}$$

For the biphoton states, the Schmidt decomposition of wave functions can be transformed into the Schmidt decomposition of biphoton state vectors [2, 3]:

$$|\Psi\rangle = \sum_n \sqrt{\lambda_n}\,|2_n\rangle \equiv \sum_n \sqrt{\frac{\lambda_n}{2}}\,a_n^{\dagger 2}\,|0\rangle, \tag{8.3}$$

where $a_n^\dagger$ is the photon-creation operator for the nth Schmidt mode, $|0\rangle$ denotes vacuum, and $|2_n\rangle$ is the state vector of two photons, each in the same nth Schmidt mode ψ_n.

In addition to wave functions, pure bipartite states can be characterized by their density matrix $\rho(x_1, x_2; x_1', x_2') = \Psi(x_1, x_2)\Psi^*(x_1', x_2')$ and reduced density matrix $\rho_r(x_1, x_1') = \int \mathrm{d}x_2\, \rho(x_1, x_2; x_1', x_2)$. As follows, also from the Schmidt decomposition for the wave function (8.1), similar decomposition occurs for the reduced density matrix:

$$\rho_r(x_1, x_1') = \sum_n \lambda_n\, \psi_n(x_1)\psi_n^*(x_1'), \tag{8.4}$$

with the equation for the Schmidt modes in terms of the reduced density matrix given by:

$$\int \mathrm{d}x_1'\, \rho_r(x_1, x_1')\psi_n(x_1') = \lambda_n\, \psi_n(x_1). \tag{8.5}$$

Symbolically, the last equation (8.5) can be written as $\rho_r\psi_n = \lambda_n\,\psi_n$, which shows that Schmidt modes can be considered as eigenfunctions of the reduced density matrix.

The Schmidt decomposition (8.1) determines clearly the conditions when the bipartite wave function factorizes, and the state is disentangled. This situation occurs only if the sum over n contains only one term, i.e., $\lambda_n = \delta_{n,0}$. In all other cases, the bipartite wave function is not factorable, and the state is entangled. The Schmidt decomposition provides an excellent possibility for defining entanglement quantifiers characterizing the degree of entanglement. Two of them are the Schmidt parameter and entropy of the reduced density matrix:

$$K = 1/\sum_n \lambda_n^2 \geq 1, \quad S_r = -\sum_n \lambda_n \log_2 \lambda_n \geq 0. \tag{8.6}$$

In the case of disentangled states, $K = 1$ and $S_r = 0$.

If variables x_1 and x_2 are discrete and each of them can take one of d values, the quantity d is called the dimensionality of the single-particle Hilbert space, and it

determines also the number of terms in the Schmidt decompositions (8.1) and (8.4). In this case, entanglement of a bipartite state is maximal if all λ_n are equal to each other and equal to $1/d$, which gives:

$$K_{\max} = d, \quad S_{\max} = \log_2 d = \log_2 K_{\max}. \tag{8.7}$$

If variables x_1 and x_2 are continuous, $d = \infty$, i.e., the dimensionality of the Hilbert space is infinitely high, and formally the number of terms in the Schmidt decompositions is infinitely large. But, in reality, not all λ_n are equally large, and usually there is some maximal number $n_{\max}$ above which (at $n > n_{\max}$) all constants λ_n are negligibly small. In this case, $n_{\max}$ determines the effective dimensionality of the Hilbert space and the maximal realizable values of the entanglement quantifiers $K_{\max} = n_{\max}, \quad S_{\max} = \log_2 n_{\max}$.

As mentioned above, one of the most often discussed examples of states with discrete variables is that of purely polarization biphoton states. A general form of such states is a superposition of three basic states because of which such states are called biphoton polarization qutrits. Their state vectors are given by

$$|\Psi\rangle = C_1|2_H\rangle + C_2|1_H, 1_V\rangle + C_3|2_V\rangle, \tag{8.8}$$

where H and V stand for horizontal and vertical polarizations of photons (in the plane perpendicular to the direction of their collinear propagation), and $C_{1,2,3}$ are arbitrary complex constants such that $\sum_i |C_i|^2 = 1$. As there are only two possible polarizations for each photon, the dimensionality of the single-photon polarization Hilbert space equals two, $d = 2$. As follows from (8.7, this means that the maximal values of the entanglement quantifiers of biphoton polarization qutrits are $K_{\max} = 2$ and $S_{\max} = 1$. As $d = 2$, the Schmidt decomposition of biphoton qutrits contains only two terms and can be presented in the form:

$$|\Psi\rangle = \cos\vartheta|2_+\rangle + e^{2i\phi}\sin\vartheta|2_-\rangle, \tag{8.9}$$

where ϑ and ϕ are parameters determined by constants $C_{1,2,3}$. There are simple methods for finding these parameters, as well as the Schmidt modes $|1_+\rangle$ and $|1_-\rangle$ both theoretically and experimentally [2, 3]. Not dwelling here on any further details of these general derivations, let me mention only one of the simplest representatives of biphoton polarization qutrits for which $C_1 = C_3 = 0$, $C_2 = 1$ and $|\Psi\rangle = |1_H, 1_V\rangle$. In this case, the Schmidt decomposition is achieved by a simple rewriting of the state vector in the basis turned for 45° with respect to the horizontal-vertical one:

$$|\Psi\rangle = |1_H, 1_V\rangle \equiv \frac{1}{\sqrt{2}}(|2_{45^\circ}\rangle - |2_{-45^\circ}\rangle), \tag{8.10}$$

where $|2_{\pm 45^\circ}\rangle$ are states with two photons linearly polarized in the directions at ±45° with respect to the horizontal axis. By comparing this result with that of (8.8),

we find the Schmidt mode of the state $|1_H, 1_V\rangle$: $|1_+\rangle = |1_{45^\circ}\rangle$ and $|1_-\rangle = i|1_{-45^\circ}\rangle$ with $\lambda_+ = \lambda_- = 1/2$. Experimentally, the transformation (8.10) can be provided with the help of a polarization beam splitter turned 45° around the propagation axis.

Let me discuss now the states with angular variables. Such states arise, e.g., in the non-collinear SPDC process with the type-I phase matching. SPDC photons are emitted in the form of two symmetric beams propagating in the directions at angles θ_0 and $-\theta_0$ with respect to the pump propagation axis. In principle, beams can have structures to be discussed later but let us start with the case when this structure can be ignored. Then, the arising biphoton state can be characterized by the state vector $|\Psi\rangle = |1_{\theta_0}, 1_{-\theta_0}\rangle$, which is very similar to the discussed polarization state $|1_H, 1_V\rangle$. But as the angular variables differ from the polarization ones, the procedure of Schmidt-mode separation also differs from that discussed above. The simplest procedure for angular variables can be based on the well-known interference Hong-Ou-Mandel effect [4], a scheme of which is shown in Fig. 8.1.

Two beams forming the state $|1_{\theta_0}, 1_{-\theta_0}\rangle$ are sent to 50/50% beamsplitter, after which both photons of SPDC pairs are regrouped to propagate together either upward or downward, but they are not split anymore between the two channels. Mathematically the arising state takes the form:

$$|\Psi\rangle = |1_{\theta_0}, 1_{-\theta_0}\rangle \rightarrow \frac{i}{\sqrt{2}}(|2_{45^\circ}\rangle - |2_{-45^\circ}\rangle), \tag{8.11}$$

which is similar to the Schmidt mode decomposition (8.10) for the polarization biphoton state $|1_H, 1_V\rangle$ and to the general form of the Schmidt decomposition (8). The Schmidt modes $|1_\pm\rangle$ are given by $|1_{45^\circ}\rangle$ and $|1_{-45^\circ}\rangle$.

An alternative scheme was suggested in [5], and it is based on manipulations with the polarizations of photons. The scheme is shown in Fig. 8.2. In the first step, polarization of photons in one shoulder ($-\theta_0$) is changed from the horizontal to the vertical one with the help of half- and quarter-wavelength plates. Then both beams are sent to the polarization beamsplitter to merge into a single beam of photons with different polarizations. After this, the polarization beamsplitter turned for 45° splits the beam for two beams again with separated Schmidt modes with two photons propagating together either horizontally or vertically.

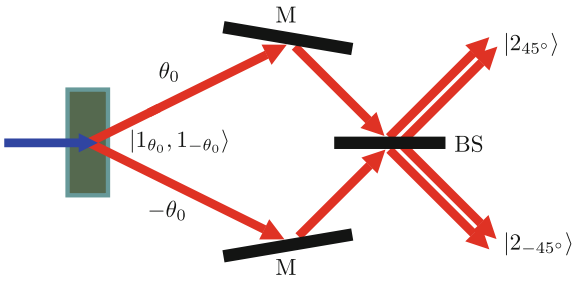

Fig. 8.1 A scheme for separation the angular Schmidt modes based on the Hong-Ou-Mandel effect [4]

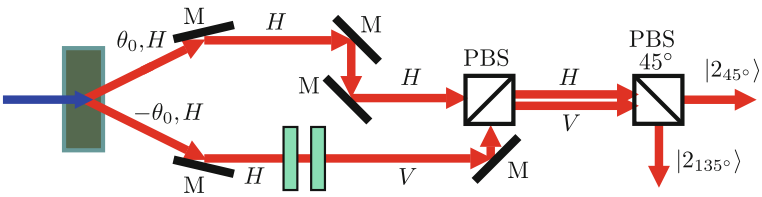

Fig. 8.2 A scheme of for separation of the angular Schmidt modes alternative to that of Fig. 8.1 [5]

Let us take into account now that, in fact, each of two beams in Figs. 8.1 and 8.2 is characterized by some distributions (around $\pm\theta_0$) over angles θ_1 and θ_2 between the photon wave vectors and the pump propagation axis. The biphoton wave function of two continuous variables θ_1 and θ_2 is known to have the form of the product of the pump angular distribution and of the sinc-function ($\mathrm{sinc}(x) = \sin x/x$) describing SPDC process in a crystal. This function can be approximated (modeled) by the sum of two products of two Gaussian functions [5]:

$$\Psi(\theta_1, \theta_2) = N \exp\left[-\frac{(\theta_1+\theta_2)^2}{2(\Delta\theta_p)^2}\right] \sum_{\pm} \exp\left[-\frac{0.78\theta_0^2}{(\Delta\theta_L)^2}(\theta_1 - \theta_2 \mp 2\theta_0)^2\right], \quad (8.12)$$

where $\Delta\theta_p$ is the angular width of the pump envelope and $\Delta\theta_L$ is the width of the distribution related to the propagation in the crystal, $\Delta\theta_L \sim \lambda_p/L$ with L and λ_p being the crystal length and pump wavelength. The structure of the function (8.12) is shown in the two parts of Fig. 8.3.

This picture indicates clearly that there are two reasons for the angular entanglement: (*a*) uncertainty of a given-photon localization in one or another quadrant, $\theta_1 > 0,\ \theta_2 < 0$ or $\theta_1 > 0,\ \theta_2 < 0$ and (*b*) asymmetry of the distribution over θ_1 or θ_2 in each of two quadrants. The Schmidt decomposition, related to the first reason is given by (8.11), can be analyzed experimentally within the schemes of Figs. 8.1 and 8.2, and the degree of entanglement is the same as the maximal degree of

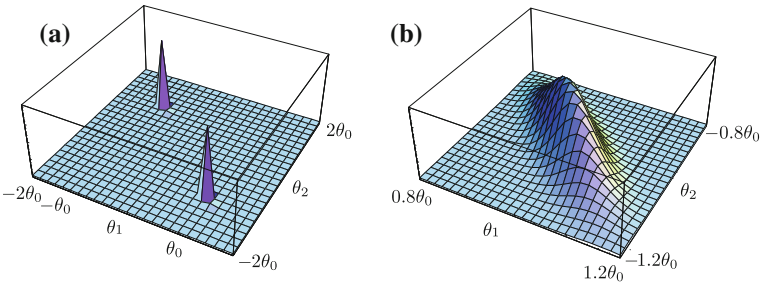

Fig. 8.3 Structure of the squared wave functions (8.12) (**a**) as a whole and (**b**) in the quadrant $\theta_1 > 0,\ \theta_2 < 0$

entanglement for biphoton polarization qutrits, $K = 2$ and $S_r = 1$. As for the asymmetry of distributions, there are several possible approaches to its analysis.

First, as suggested in [6] and used later by many authors, the degree of entanglement can be characterized by an experimentally measurable parameter R defined as the ratio of the widths of the single-particle $\Delta\theta^{(s)}$ and coincidence $\Delta\theta^{(c)}$ distributions, $R = \Delta\theta^{(s)} \Big/ \Delta\theta^{(c)}$. Moreover, as proved, for double-Gaussian wave functions, $R \equiv K$. Thus, by measuring $\Delta\theta^{(s)}$ and $\Delta\theta^{(c)}$, one can find directly the degree of entanglement related to the asymmetry of photon distributions in θ_1 and θ_2.

Second, as shown in [7], the products of two Gaussian functions (to be called double-Gaussian) can be expanded into the sums of products of Hermit–Gaussian functions (to be denoted as ψ_n). This fact can be used to present the angular biphoton wave function of (8.12) in the form:

$$\psi(\theta_1, \theta_2) = \sum_n \sqrt{\frac{\lambda_n}{2}} \sum_{\pm} \psi_n(\theta_1 \mp \theta_0)\psi_n(\theta_2 \pm \theta_0), \tag{8.13}$$

where

$$\psi_n(\theta) = \left(2^n n!\sqrt{\pi ab/2}\right)^{-1/2} \exp\left(-\frac{\theta^2}{ab}\right) H_n\left(\frac{\sqrt{2}\,\theta}{\sqrt{ab}}\right), \quad \lambda_n = \frac{4ab(a-b)^{2n}}{(a+b)^{2(n+1)}}, \tag{8.14}$$

and $a = \Delta\theta_p$, $\quad b = \Delta\theta_L \big/ \left(\theta_0\sqrt{1.56}\right)$. Now we can apply to the wave function (8.13) the procedure of Fig. 8.2. With the changed polarization ($H \to V$) in the lowest channel (around $-\theta_0$), the sum over $\pm$ in (8.13) turns into:

$$\psi_n(\theta_1 - \theta_0)\psi_n(\theta_2 + \theta_0)\delta_{\sigma_1, H}\delta_{\sigma_2, V} + \psi_n(\theta_1 + \theta_0)\psi_n(\theta_2 - \theta_0)\delta_{\sigma_1, V}\delta_{\sigma_2, H}\ , \tag{8.15}$$

where σ_1 and σ_2 are the polarization variables of photons, numbers of which are associated with the numbers of angular variables θ_1 and θ_2. After merging two channels into a single one, the terms $\pm\theta_0$ in arguments of the functions ψ_n disappear because all photons move now in the same direction, which gives, instead of (8.15):

$$\psi_n(\theta_1)\psi_n(\theta_2)\left(\delta_{\sigma_1, H}\delta_{\sigma_2, V} + \delta_{\sigma_1, V}\delta_{\sigma_2, H}\right). \tag{8.16}$$

At last, when the beam splits at the second beamsplitter of Fig. 8.2, the wave function (8.13) takes the form:

$$\Psi(\theta_1,\theta_2)=\sum_n\sqrt{\frac{\lambda_n}{2}}\left(\psi_n(\theta_1)\psi_n(\theta_2)|2_H\rangle+\psi_n(\theta_1+90^\circ)\psi_n(\theta_2+90^\circ)|2_V\rangle\right). \tag{8.17}$$

This result shows that all terms of the Schmidt decompositions are twice degenerate, i.e., there are two pairs of Schmidt modes corresponding to each λ_n. Eigenvalues of the reduced density matrices are equal $\lambda_n/2$, and the normalization condition has the form $2\times\sum_n\lambda_n/2=1$. Parameters characterizing the degree of entanglement of the state (16) are given by:

$$K=\frac{1}{2\times\sum_n(\lambda_n/2)^2}=\frac{a^2+b^2}{ab}\geq 2, \tag{8.18}$$

$$S_r=-2\times\sum_n(\lambda_n/2)\log_2(\lambda_n/2)=1-\sum_n\lambda_n\log_2\lambda_n\geq 1. \tag{8.19}$$

As mentioned above, angular entanglement of non-collinear angular states of biphotons arises owing to two reasons: because of asymmetry of formations in each of two occupied quadrants in the plane (θ_1,θ_2) and because of the quadrant-quadrant symmetry of the photon distributions. The first of these two reasons occurs if $a\neq b$, and it disappears in the case $a=b$ (photon distributions in each occupied quadrant become symmetric). In this case, $\lambda_n=\delta_{n,1}$ but, because of degeneracy, the state (21) remains entangled with the entanglement quantifiers (8.18) and (8.19) equal to $K=2$ and $S_r=1$. This remaining entanglement is related to the symmetry of two-boson wave functions, and the case $\lambda_n=\delta_{n,1}$ corresponds exactly to the case considered above when the angular structure of distributions was ignored.

Experimental measurement of the entanglement parameters of the angular non-collinear states is doable and interesting. In particular, it concerns the width-ratio parameter R and its comparison with the calculated and independently measured Schmidt parameter K. Note finally that for the collinear SPDC-regime separation of the Hermit–Gaussian Schmidt modes was realized experimentally. Similar experimental measurements can be made with non-collinear biphoton states also.

8.3 Conclusion

In conclusion, below is the list of references on the discussed topics. The last two papers have been published rather recently. In the paper [8], a scheme of Fig. 8.2 is described and discussed in more detail. The paper [9] is a review of many aspects in the field of Schmidt modes and Schmidt decompositions.

References

1. E. Schmidt, Math. Ann. **63**, 433 (1907); English translation: G.W. Stewart, *FREDHOLM, ILBERT, SCHMIDT: Three Fundamental Papers on Integral Equations Translated with commentary by* G.W. Stewart, http://www.umiacs.umd.edu/∼stewart/
2. M.V. Fedorov, N. I. Miklin, Contemporary Phys. **55**, 94 (2014)
3. M.V. Chekhova, M.V. Fedorov, J. Phys. B: At. Mol. Opt. Phys. **46**, 095502 (2013)
4. C.K. Hong, Z.Y. Ou, L. Mandel, Phys. Rev. Lett. **59**, 2044 (1987)
5. M.V. Fedorov, Phys. Scripta, July, (2015)
6. M.V. Fedorov, M.A. Efremov, A.E. Kazakov, K.W. Chan, C.K. Law, J.H. Eberly, Phys. Rev. A **69**, 052117 (2004)
7. M.V. Fedorov, M. Yu, P.A. Mikhailova, J. Volkov, Phys. B: At. Mol. Opt. Phys. **42** (2009)
8. M.V. Fedorov, Int J Quantum Info **12**, 1560009 (2014)
9. M.V. Fedorov, N.I. Miklin, Laser Phys. **25**, 035204 (2015)

Part IV
Imaging

Chapter 9
Luminescent Sensors for Single-Cell Analysis

Takeaki Ozawa

My title is Luminescent Sensors for Single-Cell Analysis. The topic is a little bit different from the previous speakers, but I feel happy if you would kindly follow my presentation.

Bioanalysis has strongly contributed to the deep understanding of biological phenomena and applications to medical diagnosis (Fig. 9.1). One of the representative examples is a comprehensive genome analysis of the higher plants and animals. The analysis has been strongly supported by DNA sequencing with high-performance capillary electrophoresis and the development of the fluorophore. Also, mass-spectroscopic analysis has revolutionized proteome analysis, such as the expression of the proteins and the modification of the proteins, etc. However, many of these technologies are destructive analyses.

In contrast, bio-imaging with fluorescence and bioluminescence technology has a strong advantage in terms being noninvasive or less-invasive methods. This imaging with fluorescence started in the 1980s with the development of the calcium-ion indicator, Fura-2. Also, discovery and development of green fluorescent proteins (GFPs) revolutionized the imaging fields of biology. Particularly, application of the green fluorescent protein derivatives, such as FRET imaging, the fluorescence correlation spectroscopy, etc., achieved a great breakthrough to realize visualization of intra-cellular signaling in living cells. With such a background, my laboratory has focused strongly on the development of novel imaging technologies with fluorescent and bioluminescent proteins. By using such fluorescence or bioluminescence probes, we are also interested in the identification of smaller chemical compounds that regulate the intercellular signaling like pharmaceutical drugs. Many of these technologies are based on the complementation or reconstitution analysis which was started in 2000 in my laboratory.

T. Ozawa (✉)
Department of Chemistry School of Science, The University of Tokyo,
7-3-1 Hongo, Bunkyo-ku, Tokyo 113-0033, Japan
e-mail: ozawa@chem.s.u-tokyo.ac.jp

K. Yamanouchi (ed.), *Progress in Photon Science*, Springer Series
in Chemical Physics 115, DOI 10.1007/978-3-319-52431-3_9

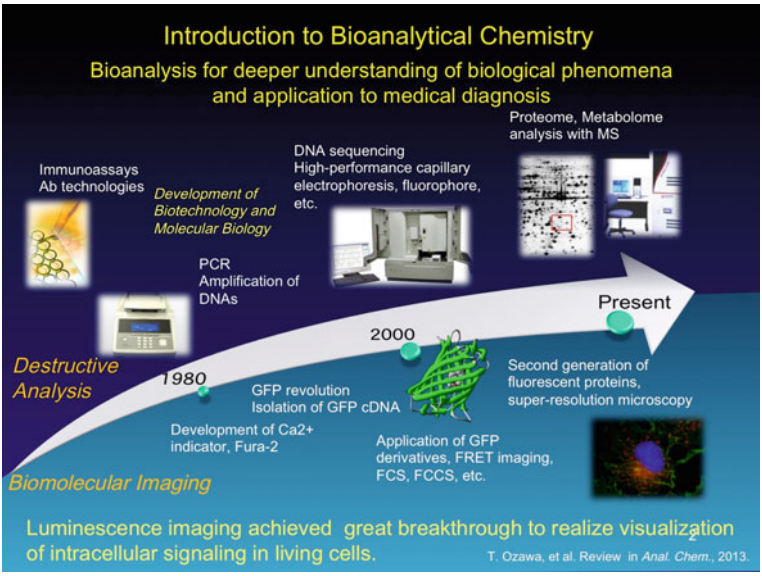

Fig. 9.1 General introduction of bioanalyses

Here, I want to focus on a few topics. First, I want to introduce what is complementation or reconstitution analysis, and then I want to show the application of the complementation analysis. The first one is imaging of the endogenous RNA, and the second one is imaging of the molecular events in the apoptosis.

The green fluorescent protein or the bioluminescent protein is now widely used for the analysis of the protein localization or the morphology of the intracellular organelles or the cell itself. The use of this luminescent protein has a lot of advantages, for example, the protein is encoded in the DNA. This DNA is very easy to be introduced into a living cell. Also, we sometimesgenerate transgenic animals and plants which provide much valuable information. In addition, multi-color fluorescent proteins from blue to red are now available, which is very useful for taking an image of many biological events at the same time. Also, the protein-based probes can be targeted to specific organelles and intracellular organelles. This is a strong advantage for the use of protein-based probe molecules. However, even if we use these luminescent proteins, it's not so easy to detect more complicated cellular processes, such as protein interaction, phosphorylation, enzymatic activities, etc. Because of such reasons, we generated the reconstitution approach to overcome these limitations.

The green fluorescent protein is composed of 238 amino acids. These amino acids form a can-like structure with eleven beta-sheets. A chromophore of this fluorescent protein is generated inside the can-like structure. If the protein is dissected into two fragments, the fluorescence is completely lost. When two fragments are brought closely enough together, we found the fluorescence can be recovered

in vitro and in vivo. This reaction is named complementation or reconstitution. We recently simulated the folding process of the two fragments of the GFP. The blue lines indicates amino-terminal fragments, and the red ones indicates the carboxy-terminal fragments of the GFP. As you see here, i.e., the blue line, the amino-terminal fragment is folded correctly, and then this folded amino-terminal fragment is used as a template. The carboxy-terminal fragment is folded to finalize the folding process of the GFP. This is only a simple simulation, but we also investigate the structure of the two fragments of the GFP with NMR and CD spectra. An amino-terminal fragment has been already folded in a buffer solution, but a carboxy-terminal fragment has variable random motions in the solution.

One of the applications of the complementation analysis is the analysis of protein-protein interactions. If we would like to visualize a pair of interacting proteins, the proteins are directly connected with the fragments of GFP. This fusion protein does not emit fluorescence. But when the protein interaction occurs in living cells, the GFP fragments are brought closely to come together and the GFP is reconstituted which emits fluorescence. This means that we can identify the localization of the interacting protein in living cells.

In the first topic, I want to show the technology of the imaging of endogenous RNA in single living cells. The RNA is transcribed from the DNA with an RNA polymerase. I want to visualize this RNA in living cells. RNA imaging is one of the very important targets in the imaging field of the science [1], but very difficult to visualize with fluorescence technology.

In order to visualize a specific RNA, we are focusing on one of the very interesting proteins whose name is Pumilio (Fig. 9.2). The structure of the Pumilio is composed of eight repeated domains shown in blue and yellow, and each repeated domain recognizes the RNA base with hydrogen bonding and pi-pi stacking interaction like a Watson-Crick base pairing [2]. The specificity of the Pumilio protein to a target mRNA can be changed by replacing the amino acid in each domain. It means that we can design this Pumilio protein to match the sequence of the target mRNA. One Pumilio protein recognizes eight RNA bases. Then we use two Pumilio proteins, meaning that, in total, 16 bases of the RNA can be recognized by two Pumilio proteins [3]. Each Pumilio protein is connected with a fragment of the GFP. This is the probe molecule of the target mRNA. This probe does not emit fluorescence. But if the target mRNA is present, this Pumilio protein binds to this mRNA in tandem and then fluorescence can be recovered. This indicates that we can reconstitute the fluorescence protein on the target mRNA with the probe. Also, we can obtain the fluorescence with very low background fluorescence.

The initial target that I want to show you here is the beta-actin messenger RNA. We would like to visualize the mRNA of the beta-actin. For this purpose, we designed the Pumilio protein to match the sequence of the beta-actin mRNA [4]. This Pumilio protein is connected with fragments of the GFP, and also the tubulin, one of the cytoskeletal protein, is labeled with red-colored fluorescent protein.

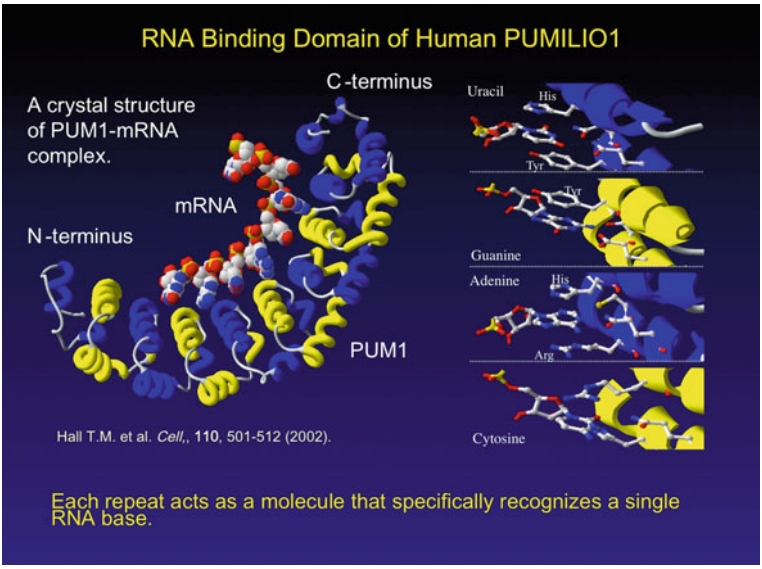

Fig. 9.2 Structure of the RNA-binding protein Pumilio

These three proteins were expressed in single cells and then visualized with beta-actin mRNA and tubulin.

Figure 9.3 shows images obtained using confocal fluorescence microscopy; the green one indicates localization of the beta-actin mRNA, and the tubulin is in the mesh-like structures. The beta-actin mRNA is mainly localized in the nucleus but several mesh-like structures were observed at the edge of the cell. Localization of the beta-actin mRNA is completely overlaid with tubulin. This is an enlarged image. This image suggests that beta-actin mRNA is co-localized on the tubulin. When we use total internal-reflection fluorescence microscopy, TIRF microscopy, we can visualize a single GFP molecule (Fig. 9.3). Each fluorescent spot indicates a single GFP, that is single beta-actin mRNA. The red one indicates the localization of the tubulin. We found that 90% of the beta-actin messenger RNA has very random motions, but the remaining 10% has directional movement along the tubulin. The average velocity was estimated about 1.8 μm per second. This value is almost the same as a motor protein. This indicates that beta-actin mRNA is transported on the motor protein along the tubulins. Also, we visualized beta-actin mRNA with a primary culture of rat hippocampal neurons (Fig. 9.4). We have succeeded in visualizing the endogenous single beta-actin mRNA that was moved along the axon.

The next one we tried to visualize is noncoding RNAs, which is not messenger RNAs. One of the representatives of the noncoding RNAs is the telomeric repeat-containing RNA, TERRA [5]. The telomere is the physical end of the

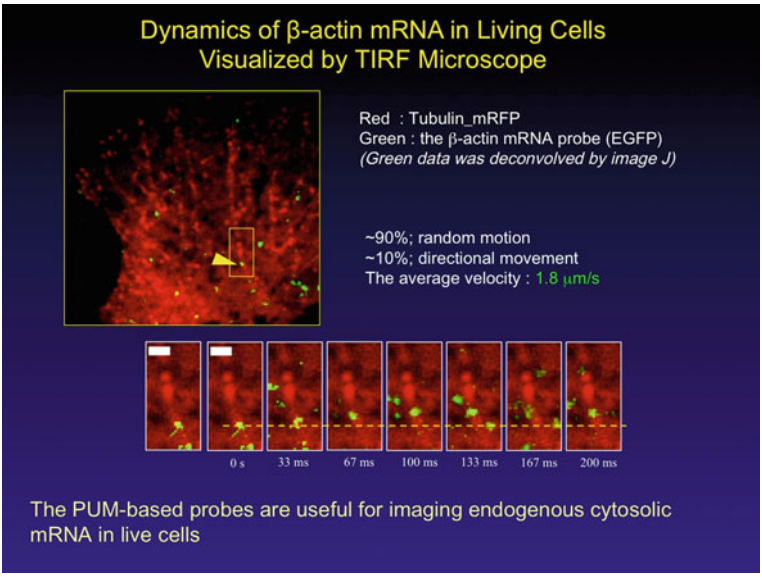

Fig. 9.3 Single molecule imaging of beta-actin mRNA

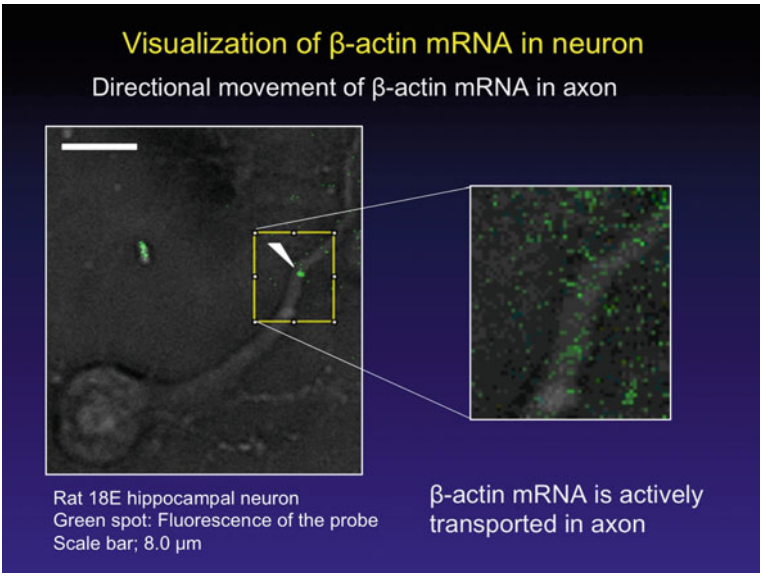

Fig. 9.4 Dynamics of beta-actin mRNA in a hippocampal neuron

chromosome. The length of the telomeric DNA is known to be very close to the length of our life. Thus, it is a very important target for the analysis of this telomeric

DNA. Telomeric RNA has also been discovered, which is transcribed from the telomeric DNAs. Telomeric RNA is composed of a repeated sequence of uracil, adenine, guanine, and cytosine, and the sequence repeats over 100 times. The telomeric DNA has been extensively investigated in the fields of biochemistry, molecular and cellular biology, but the function of telomeric RNA and its localization dynamics are still unclear. Then, we would like to visualize this telomeric RNA directly in living cells. For this purpose, we first designed the Pumilio protein to match the sequence of the UUAGGGUU sequence and then both ends of the Pumilio protein are connected with the fragments of GFP [6]. This fusion protein does not emit fluorescence, but when we express this protein in the nucleus of the cell, this protein binds to the repeated sequence of telomeric RNA. Then the fluorescence can be recovered by complementation of the fragment of the GFP, and we can thus label the telomeric RNA with the fluorescence protein.

We first characterized this probe molecule. The green one indicates the localization of the probe molecule which emits green fluorescence, and localization of the telomeric RNA is labeled with complementary DNA which was connected with a fluorescent molecule of TAMRA. Each red spot indicates localization of the TERRA regions, and each blue one indicates a nucleus of the cell.

We observed a strong background fluorescence, but several green spots were observed. Every green spot was completely overlaid with the telomeric RNA regions, which indicates that each green spot shows the localization of TERRA. This is a result of the fixed cell, but we would like to visualize the dynamics of the TERRA. Then, we next investigated the dynamic motion of this telomeric RNA in a living cell. In this case, we cannot visualize directly telomeric DNA, thus the telomeric-DNA region was labeled with its binding protein of the TRF1, connected with red-colored fluorescent protein.

Each red spot indicates the localization of the telomeric DNA regions, and so here is the nucleus. A green spot indicates the localization of the TERRA, which was labeled with our designed probe molecule. Many TERRA are co-localized on the telomeric DNA regions, but we found, very interestingly, the TERRA exhibits very dynamic motions. This is the trajectory of the movements of TERRA. Telomeric DNA does not move around, but telomeric RNA actually has dynamic motion.

TERRA has a different dynamic motion in the nucleus. We investigated more systematically, and we found that two modes of dynamics are present. The one is a simple diffusive motion around the telomeric DNA region. A single spot indicates TERRA. This TERRA moves just in the telomeric DNA regions. and this is an expected result. Surprisingly, TERRA has more dynamic motions. The RNA moves into this telomeric DNA region and stays a few seconds. And then, this one moves away from the telomere region. This implies that the interaction of the TERRA with telomere is not sustained, but occurs in a transient manner. At this stage, biologist believes that TERRA is completely overlaid with telomeric DNA regions because they have only static information. However, our investigation indicates that the

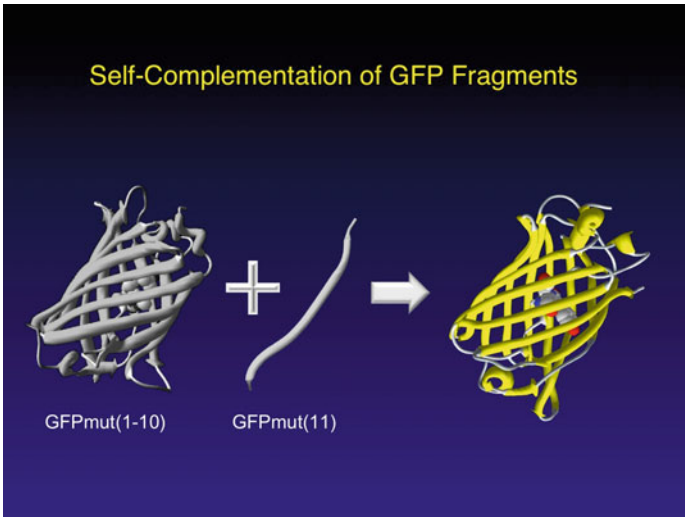

Fig. 9.5 Spontaneous complementation of GFP fragments

TERRA has indeed a dynamic motion. We are now investigating the significance of this dynamic motion in collaboration with biochemists.

I am just talking about the complementation of the two fragments of the GFP. When we remove the interacting protein, no complementation occurs, no fluorescence [7]. But when we change the dissection size of the fluorescent protein, that means only the 11th beta sheet is removed from the structure of the GFP, and, when we insert several amino acid mutations, the complementation spontaneously occurs without interacting proteins (Fig. 9.5) [8]. This is called self-complementation. Next, I introduce the application of the self-complementation technology; the imaging of the apoptosis, and the cell death. When we stimulate a culture cell with the UV light, we see the cell undergoes apoptosis. This is a movie, 12-h long in total, of the apoptotic cells. We would like to visualize dynamic events in living cells during 12 h.

The initial event of the apoptosis is the release of the protein whose name is Smac, or cytochrome C, from mitochondria to the cytosol. This event initiates apoptosis. We would like to visualize the release of the Smac protein from the mitochondria to the cytosol. For this purpose, we connected the fragment of the 11th beta sheet of GFP with Smac protein (Fig. 9.6) [9]. This fusion protein is localized in the mitochondria. The rest of the fluorescent protein is located in the cytosol. The two fragments are separated with mitochondrial membrane. When we stimulate the cell with UV light, the Smac protein is released from the mitochondria to the cytosol. Two fragments meet each other, and then GFP is reconstituted. Actually, after stimulation the cell with UV light, green fluorescence was recovered, which was overlaid with transmission images.

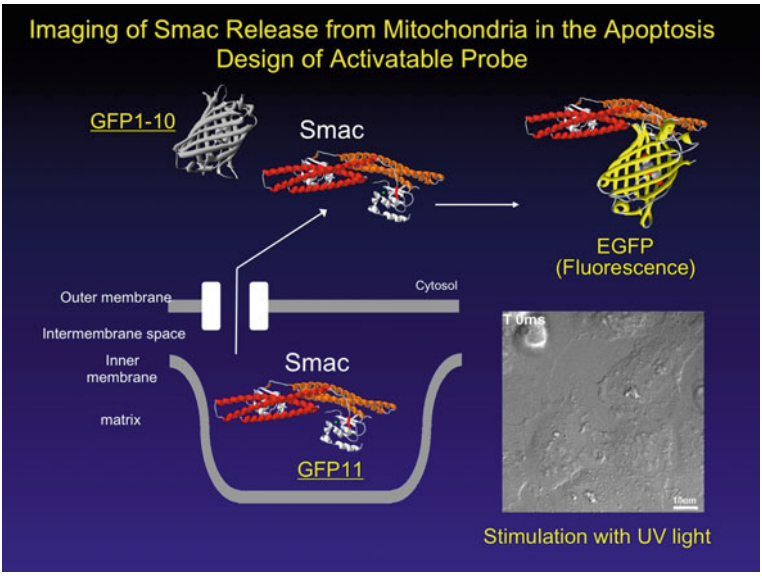

Fig. 9.6 Basic principle of imaging of Smac release from mitochondria

As explained in the introduction section, the advantage of the use of this fluorescence technology is that we can obtain many biological events at the same time in the single cell. The green one indicates the release of the Smac protein, the red one indicates the membrane potential of mitochondria, and blue one indicates the DNA labeled with Hoechst, which is a small organic compound. All the fluorescence images were overlaid with transmission images. After stimulation of UV light, the Smac is immediately released from mitochondria, but membrane potential is still maintained. When the membrane potential disappears, the cell immediately shrinks, and then DNA is fragmented. Such a sequential event of intracellular signaling can be visualized with such fluorescence technology. This is one of the advantages of the use of the luminescence technologies. Also, this probe is an activatable probe—"activatable" means emission from non-fluorescence to fluorescence. Then we can apply this probe to imaging in the living system.

We generated the transgenic zebrafish which expressed the probe molecule, and we stimulated this box region with the blue light. As a result, we obtained a lot of green spots—these are apoptotic cells. The results demonstrate that this probe is applicable to the living zebrafish.

After the release of the Smac protein, one of the important checkpoints is the activation of a protease, caspase 3. Caspase 3 is the protease, and its activity is an important checkpoint of the apoptosis. The final topic I show here is visualization of the caspase 3 with a bioluminescence technology. The caspase 3 recognizes four amino acids, aspartic acid-glutamic acid-valine, and aspartic acid, which is cleaved by the enzyme. The purpose of this study is to visualize activation of the caspase 3

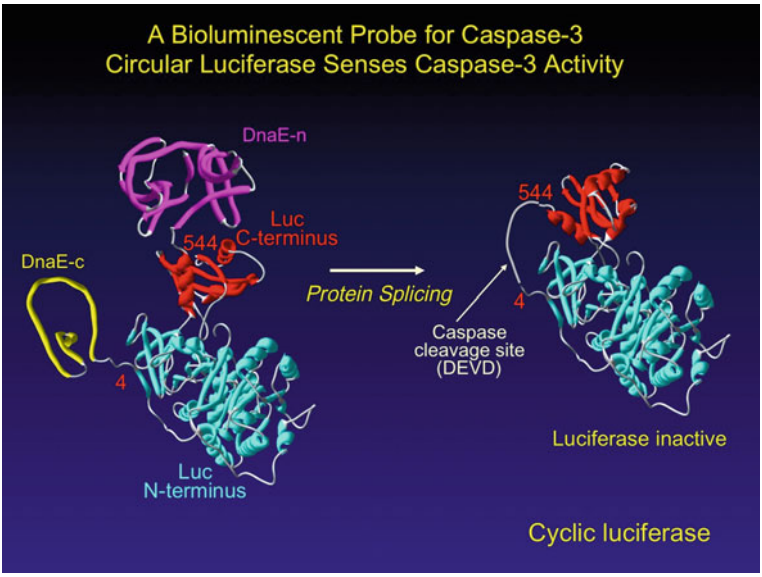

Fig. 9.7 A bioluminescent probe for visualizing caspase-3 activities

enzyme activity with bioluminescence. Many types of the luciferases, the bioluminescent proteins, have been identified, of which we use the luciferase originating from the firefly.

This is an enzyme that uses D-luciferin as its substrate. D-luciferin is converted into oxy-luciferin which emits 560 nm of orange colored light. The structure is of this luciferase is cyclized by a protein-splicing reaction (Fig. 9.7) [10]. Unfortunately, I have no time to explain the mechanism of the protein splicing but the protein splicing connects both ends of the protein by a peptide bond. This means that protein is cyclized by these two proteins, named inteins. By cyclization, it induces distortion of the structure of the luciferase, and then the enzymatic activity is completely lost. We inserted four amino acids of the recognition sequence of the caspase 3, DEVD, in this region.

When the caspase 3 is in the cells, the caspase 3 cleaves this site of DEVD shown here, and the structure is changed into the native form. We first expressed this cyclic luciferase in a living cell as an inactive form. When the caspase 3 is activated and cleaved this side, the cyclic luciferase emits bioluminescence (Fig. 9.8). This is demonstrated in the movie. The cell was stimulated with the staurosporine, an inducer of apoptosis. We can see a clear flashlight of the bioluminescence. This indicates caspase 3 activation.

The bioluminescence technology is also applied for imaging in living mice. This cyclic luciferase was expressed in the right side of the back of mice and the left side included normal luciferase. The staurosporine, an inducer of apoptosis, induced apoptosis. We clearly obtained bioluminescence only in the right side of the mice.

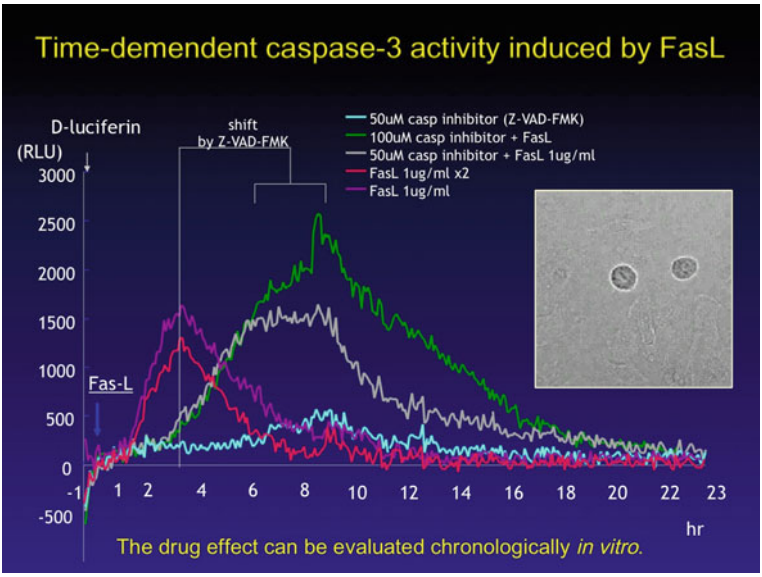

Fig. 9.8 Temporal changes of caspase-3 activities in living cells

Finally, I show you a further application; the post-hepatectomy of liver damage in comparison with fatty liver and non-fatty livers (Fig. 9.9) [11]. When we removed 70% of the liver, the rest of the liver was not damaged as the cells that are

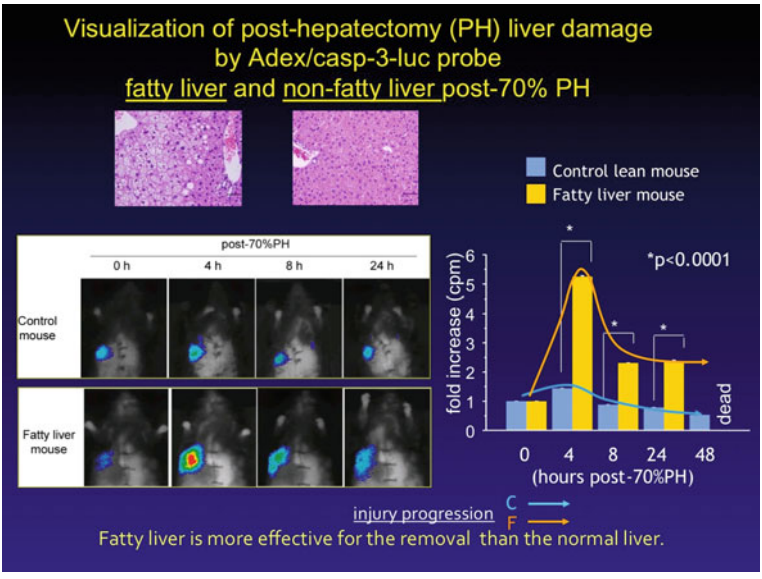

Fig. 9.9 Visualization of apoptotic cells in mice liver using the caspase-3 probe

shown here, but, in the case of fatty livers, the rest of the 30% underwent strong apoptosis after four hours of post hepatectomy. This indicates that the fatty liver is more effective after the removal of the 70% of the liver than is the normal one.

My laboratory is now focusing on the development of such types of probe molecules with protein engineering and protein-fragment complementation or reconstitution techniques, which are very useful for imaging of various intracellular signals in living cells and animals.

I want to say thanks to all my group members and collaborators and supporting funding of the Japanese government.

References

1. D. St, Johnston. Nat. Rev. Mol. Cell Biol. **6**, 363–375 (2005)
2. X. Wang, J. McLachlan, P. D. Zamore, T. M. Hall, Cell **110**, 501–512 (2002)
3. T. Ozawa, et al., Nat. Methods **4**, 413–419 (2007)
4. T. Yamada, et al., Anal. Chem. **83**, 5708–5714 (2011)
5. R. K. Moyzis, et al., Proc. Natl. Acad. Sci. U S A **85**, 6622–6626 (1988)
6. T. Yamada, et al., Sci. Rep. **6**, 38910 (2016)
7. T. Ozawa, Y. Sako, M. Sato, T. Kitamura, Y. Umezawa, Nat. Biotechnol. **21**, 287–293 (2003)
8. S. Cabantous, T. C. Terwilliger, G. S. Waldo, Nat. Biotechnol. **23**, 102−107 (2005)
9. Y. Nasu, et al., Anal. Chem. **88**, 838–844 (2016)
10. A. Kanno, et al., Angew. Chem. Int. Ed. **46**, 7595–7599 (2007)
11. S. Haga, et al., Lab Invest. **90**, 1718–1726 (2010)

Chapter 10
Photophysical Properties of Triplet Emitters Based on Au-Cu, Au-Ag Supramolecular Complexes and Prospective of Application in Sensing, Bioimaging, and OLEDs

Sergey Tunik, Pavel Chelushkin and Igor Koshevoy

The topic of this communication is the chemistry of coinage metals, and this is, in fact, a very old story (Fig. 10.1). The chemistry of coinage metals started thousands years ago with the production of pure metals when copper, silver and gold were used to cast coins. It stimulated the development of relatively simple chemistry, for example, that of halide compounds, but, by the beginning of the twentieth century, organometallic chemistry of these metals came into being. This chemistry is now very well developed and represented by the very interesting area of polynuclear-metal complexes.

In this chemistry, a specific metallophilic (metal–metal) interaction plays a very important role. This type of bonding makes possible the design of complicated supramolecular structures that have revived interest to the chemistry of coinage metals because these compounds possess a very interesting photophysics. Six years ago, my group started to work in this area. Our efforts have resulted in the synthesis of more than 300 heterometallic-polynuclear complexes of coinage metals with unusual and intriguing photophysics. This is what I am going to talk about today.

Our synthetic strategy is based on the application of rigid polyphosphines as a backbone for construction of polymetallic complexes with essentially predefined structures and stoichiometry (Fig. 10.2).

For example, in the case of linear polyphosphines, this strategy makes possible preparation of the heterometallic complexes of two types (Fig. 10.3), one of which is the so-called “rods-in-belt” compounds and the other forms “envelope” structures where the diphosphines play the role of rigid belts, inside which we can find a

S. Tunik (✉) · P. Chelushkin
Institute of Chemistry, St. Petersburg State University, Universitetskii pr., 26, St. Petersburg 198504, Russia
e-mail: s.tunik@spbu.ru

I. Koshevoy
Department of Chemistry, University of Eastern Finland, Joensuu, Finland
e-mail: igor.koshevoy@uef.fi

K. Yamanouchi (ed.), *Progress in Photon Science*, Springer Series in Chemical Physics 115, DOI 10.1007/978-3-319-52431-3_10

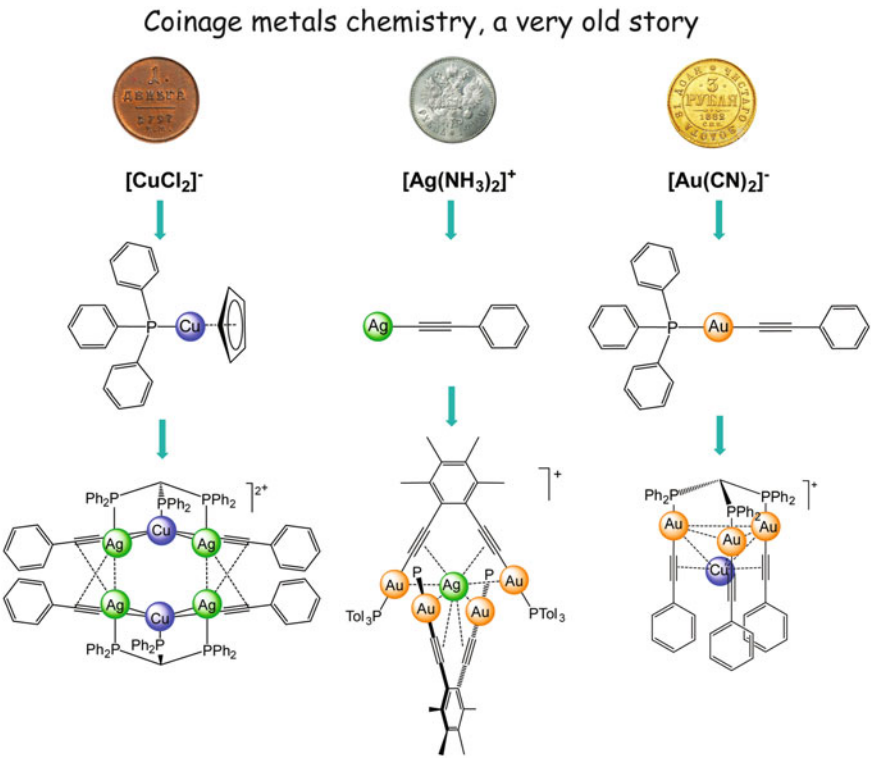

Fig. 10.1 Coinage metals chemistry, a very old story

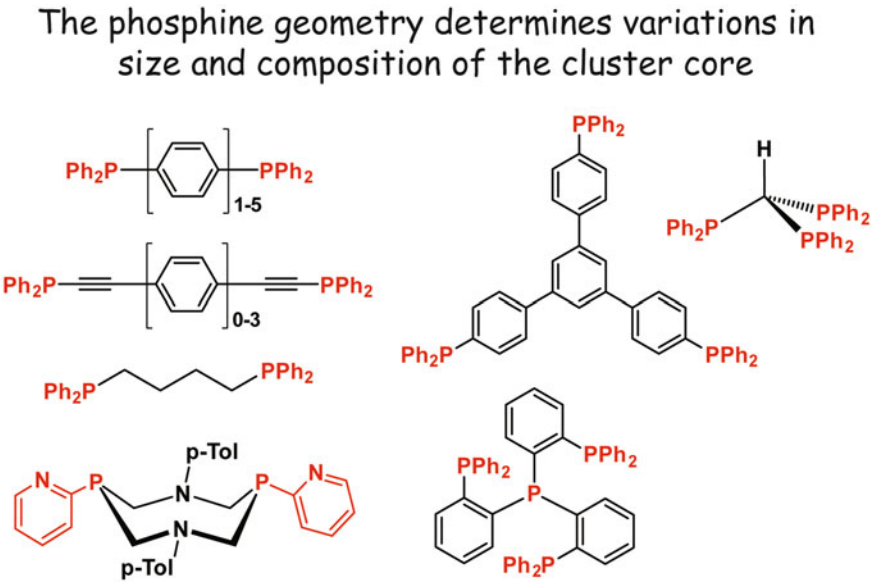

Fig. 10.2 Structure of the phosphine template ligands

polymetallic core. This core consists of a few metal atoms bound together by metal–metal interaction. These compounds may contain from 6 to 40 metal atoms inside the polymetallic core, and the presence of these polymetallic skeleton determines the practically important photophysics because the electronic structure of these metal clusters plays a key role in generating the extremely intense and tunable photoemission in this type of complexes [1–6].

As mentioned above, the metal core (the nature of its components and stoichiometry) plays a key role in the photophysics of these complexes. Using non-linear rigid phosphines, we can synthesize essentially different architectures, which are based on and determined by the geometry of the diphosphine backbone (Fig. 10.4) [7, 8].

As a result, depending on the nature of the polyphosphines used in the synthesis, we can obtain metal clusters with predetermined composition and structure and tunable variations in the emission properties.

What are the properties we have found in the compounds studied? (Fig. 10.5).

These heterometallic clusters display an extremely high phosphorescence-quantum yield, up to 100% [1, 9, 10], that is very unusual for transition metal complexes. You surely know the very popular tris-bipyridine-ruthenium complex, which is a traditional widely-used luminophore, but it has quantum yield of about 5–7%. Some of the complexes studied also display two-photon absorption and double-quantum luminescence that is very important for bio-imaging, which is particularly effective under excitation in the window of tissue transparency [2, 11]. An important feature of the structure of these compounds is the isolation of

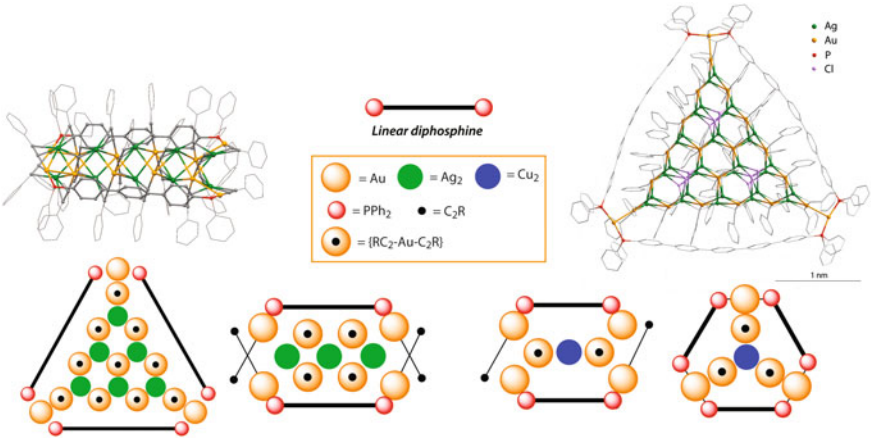

Fig. 10.3 Typical examples of "envelop" and "rods-in-belt" structures based on linear diphosphines

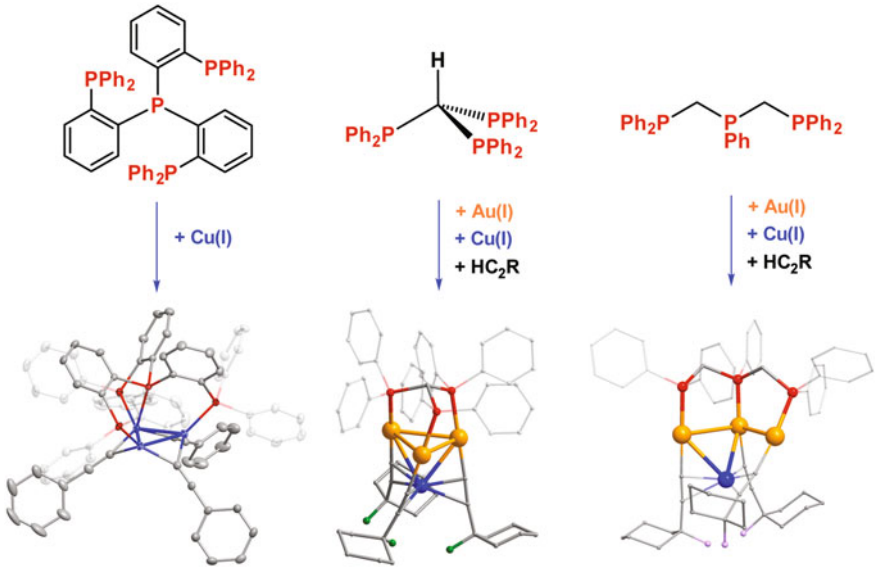

Fig. 10.4 Typical examples of the structural patterns based on nonlinear diphosphines

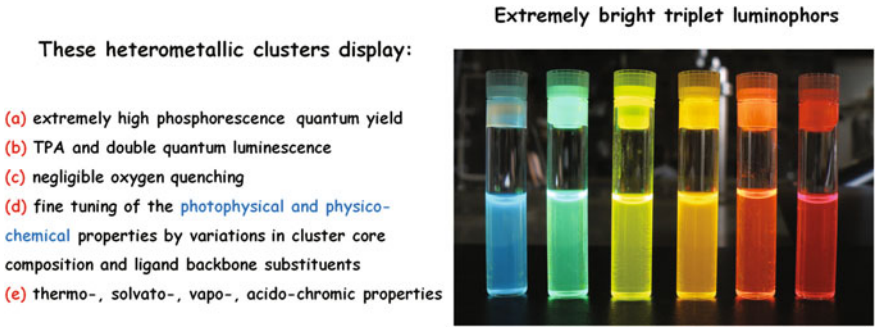

Fig. 10.5 Photoluminescence of coinage metals heterometallic supramolecular complexes

emission of chromophoric centers from the environment that results in negligible oxygen quenching of emission and makes their application for in vivo imaging particularly promising compared with the other triplet luminophores, which suffer from oxygen quenching. Easy modification of the ligand environment provides an effective instrument for fine tuning of the photophysical and physico-chemical properties by the variations in the cluster-core composition and ligand backbone substituents that is clearly demonstrated by the synthesis of emitters (see above), with the emission colors encompassing the entire range of the visible spectrum,

from bright blue to deep red (Fig. 10.5). In fact, these compounds are bright emitters not only in the solid state that is typical for transition metal complexes but also in solution that makes possible to use them as molecular emitters in bioimaging. Additionally, these compounds also display thermochromic [12], solvatochromic [13] and vapochromic [7–13] properties, which can be used for some analytical applications.

The simplest one is reversible changes of emission upon association of sortthe octanuclear $\{Au_6Cu_2\}$ luminescent cluster [14] with acid. This effect is clearly demonstrated by clear changes of color, which is accompanied also by an increase in the emission intensity upon addition of strong acid (Fig. 10.6).

The other example is the ion sensing published by a Chinese research team (Fig. 10.7) [15].

The team used our approach to cluster synthesis, which keeps intact the main structural motif, but modification of the ligand substituents makes possible capture of potassium and fluoride ions accompanied by changing emission characteristics that open a way for analytical application of these compounds.

The thermochromic behavior in solution (temperature-driven changes in emission, intensity, and color) in the case of the compound shown in Fig. 10.8 is a result of thermodynamic interconversion of isomers [9], and this type of behavior was found in the solid state [16], where one can observe not only changes in emission intensity but also drastic changes in the color of the emission.

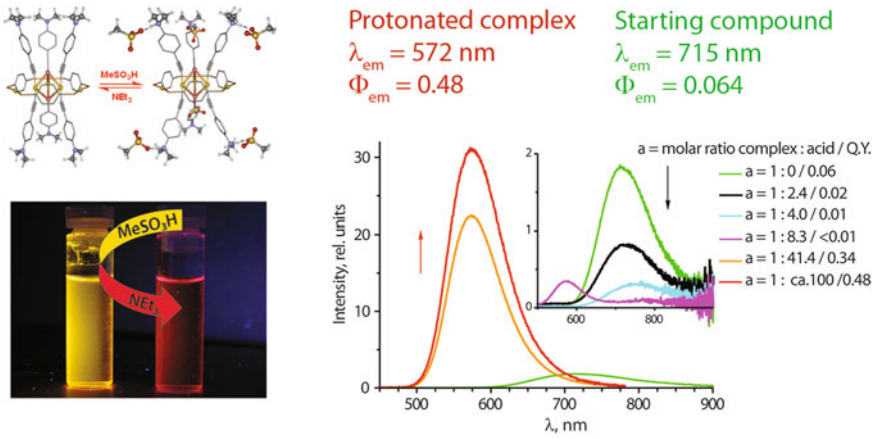

Fig. 10.6 Reversible variations in emission parameters upon association of the {Au6Cu2} luminescent cluster with strong organic acid in dichloromethane solution

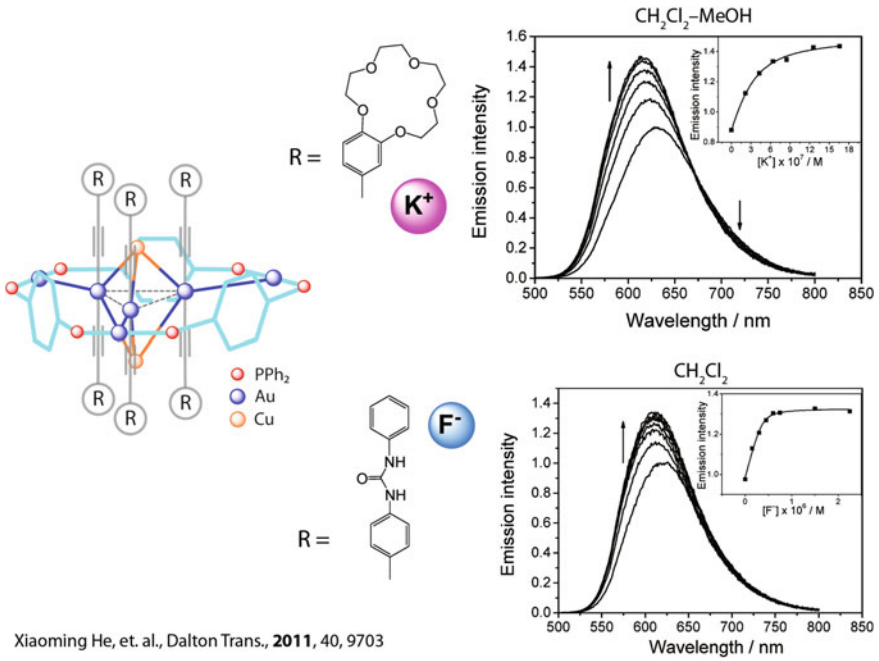

Fig. 10.7 An example of luminescent sensor for K+ and F- ionsThis figure

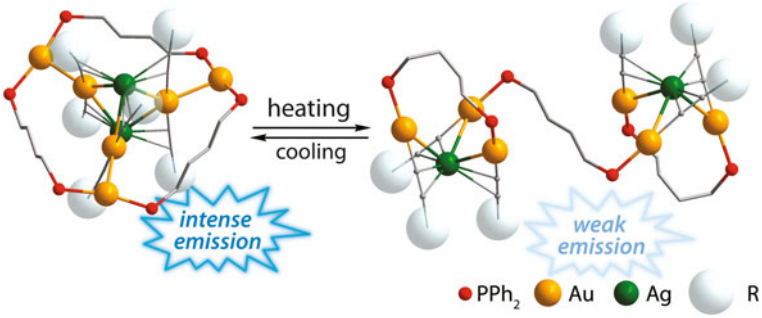

Fig. 10.8 Thermochromic behavior of structurally nonrigid $\{Au_6Ag_2\}$ cluster

Vapochromism is a phenomenon that can be exemplified by variations in the emission characteristics upon absorption of the vapors of organic compounds by the solid samples, and this *stimuli-responsive* behavior can be used as an important instrument for detection of the vapors in an environment (Fig. 10.9).

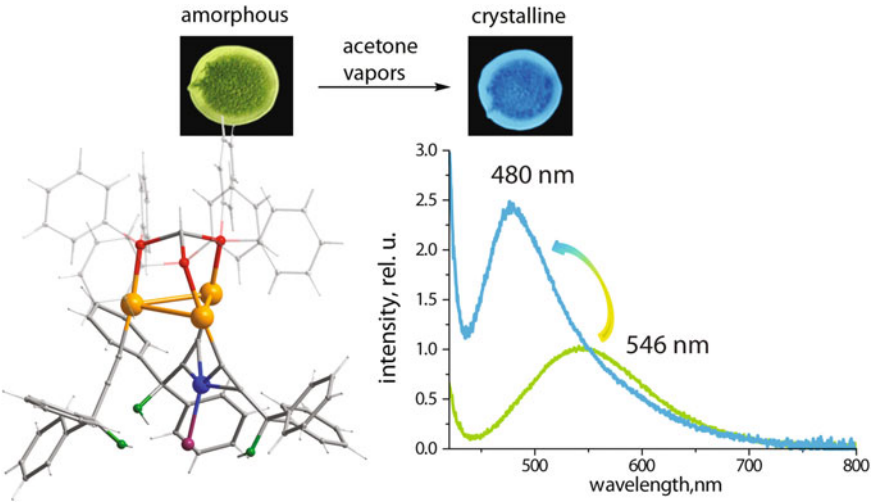

Fig. 10.9 Vapochromism of the tetranuclear alkynyl-triphosphine cluster

For example, the solid sample of the compound shown above exhibits green emission but after interaction with acetone vapor we immediately observe a sharp intensity increase and substantial shift (of ca. 60 nm) from green to blue emission, and this is highly sensitive way of detecting the corresponding vapors [7]. A similar effect was observed not only for acetone but also for methanol and tetrahydrofuran.

What was surprising in this particular case? We know for sure that a chromophoric center is located in the cluster core, but, in the compound studied, absorption of acetone molecule does not affect the chromophor, the solvent molecule does not interact with it, and the observed molecule is evidently unable to change emission parameters through direct interaction with the emitter! However, we found that the green emitter is an amorphous solid, but that, after absorption of acetone, it is converted into crystalline phase. Thus we observe solid-state recrystallization upon interaction with acetone and, in spite of the absence of direct interaction of the solvent molecule with the chromophoric center, a general reconstruction of the solid-state structure results in a considerable change of emission parameters.

Another example of *stimuli-responsive behavior* (vapo- and solvatochromism) is demonstrated by the compound, which displays reorganization of the cluster core (chromophor) upon coordination of the solvent molecule (Fig. 10.10) [13].

The starting complex, after interaction with solvent molecules, shows some slight changes in the metal–metal distances inside the cluster core, which however results in a considerable variation in the color of emissions. The orange emission changes into green, and the wavelength difference between emission bands of these two

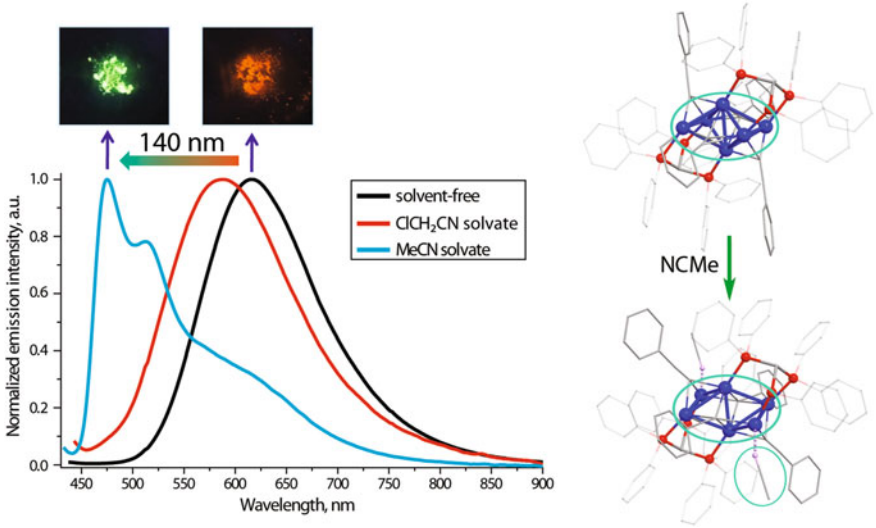

Fig. 10.10 Vapo- and solvatochromism of the hexanuclear copper alkynyl-triphosphine cluster

phases is more than 100 nm. Thus absorption of extremely small amounts of solvent can be detected using these types of complexes with a very high sensitivity, provided that a sensitive photon detector (e.g., a photomultiplier) is used.

Among the variety of compounds we have prepared, there is a certain class of complexes which is based on linear triphosphines. In this class of compounds, we found very strong emitters, which can be used for OLED devices preparation with the spin-coating technique in the PEDOT:PSS system. The OLEDs demonstrate rather good quantum efficiency (slightly higher than 3%) and acceptable voltage characteristics (Fig. 10.11) [17, 18].

Variations in alkynyl substituents, make possible to change the color of these OLEDs in a rather wide optical region.

What we are now trying to do is to break through into a very important area of bioimaging (Fig. 10.12). We would like to develop a new generation of biolabels based on triplet emitters, by which I mean transition-metal complexes with bright phosphorescence. Traditionally, biologists use fluorescent compounds for bioimaging. What is the difference between fluorescence emitters and phosphorescence emitters?

First of all, from the viewpoint of photophysics, triplet emitters demonstrate a large Stokes shift that allows for cuting off the background bio-sample fluorescence that makes imaging resolution and sensitivity much higher. Additionally, in the case of metal complexes, we have an opportunity for easy modification of ligand environment that can be used to fine tune the label properties, including targeted

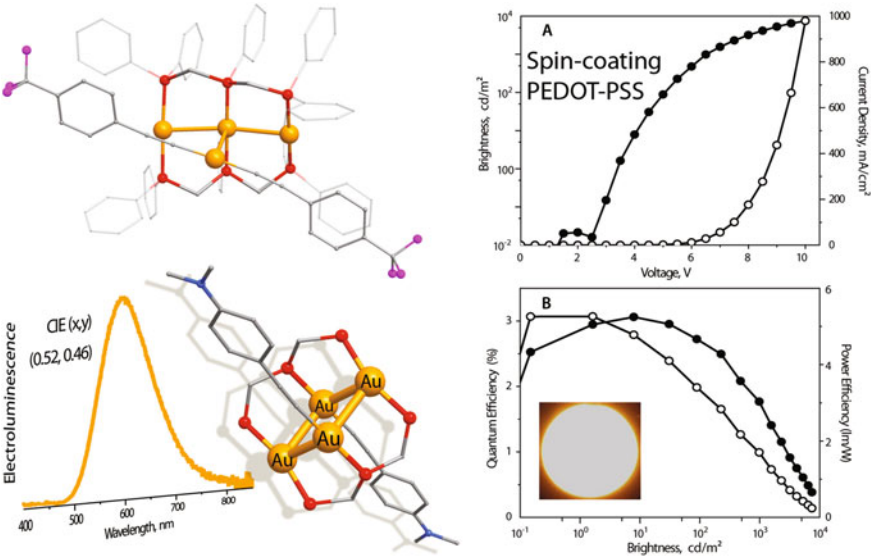

Fig. 10.11 Extremely bright tetranuclear gold(I) alkynyl-triphosphine cluster used for fabrication of OLED device

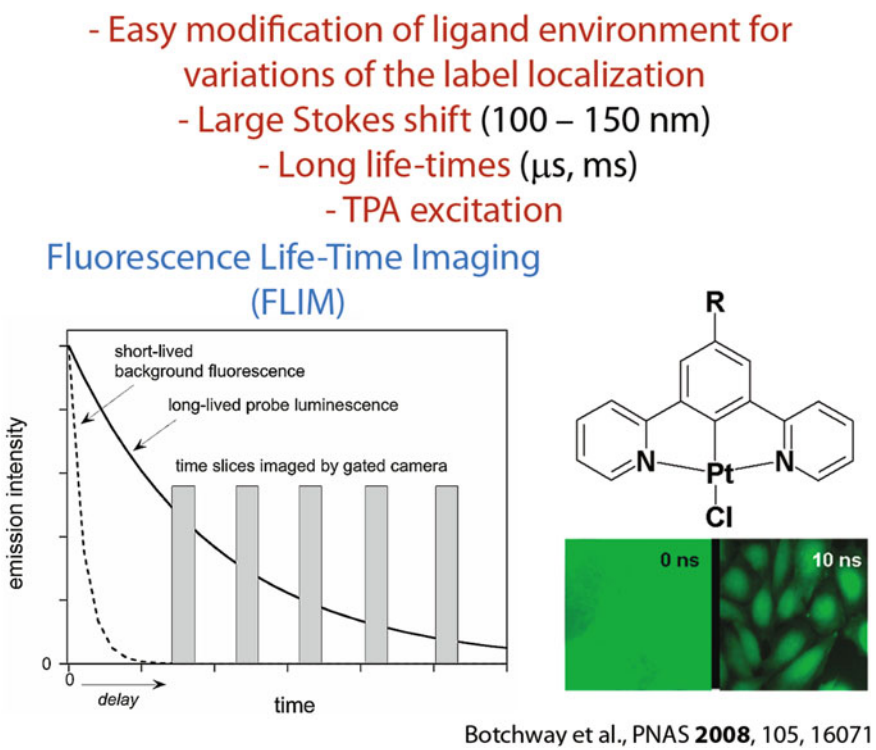

Fig. 10.12 Characteristics of triplet vs singlet emitters and time gated approach in bioimaging

localization of the labels in tissues. Moreover, long lifetimes in microsecond or even millisecond domains make it possible to apply time gating for cutting off background emission, and some of the complexes we are using also demonstrate two-photon absorption [2, 11], which is extremely useful for imaging in the window of transparency of biological tissues.

Time-gated measurements using a platinum complex as a label (Fig. 10.11) [19] have clearly demonstrated the background-cut-off effect and enhanced resolution of imaging under these experimental conditions.

Figure 10.13 shows the imaging of mesenchymal stem cells stained with a silica-encapsulated octonuclear gold–silver complex $\left[Au_4Ag_4(C_2Ph)_{12}(PP)_6\right]^{4+}$ and commonly used rhodamine phalloidin and DAPI dyes [11]. Emission was excited in one-photon (458 nm) and two-photon (760 nm) regimes. In both regimes, images showed different localization of the labels that increase the information concerning the structure of the bio-objects studied, including a 3D image of the cell and its components.

As have been mentioned above, an easy way to vary a ligand environment enables us to change the localization of the label in biosamples. For example, these types of complexes with a very lipophilic alkynyl ligand displays a very high quantum yield both in one- and two-photon excitation regime. One of these complexes was used to obtain high resolution images of pigeon tissues containing liposome and lipid droplets because these organelles absorb strongly the lipophilic luminescent label [20]. Measurements in life-time-imaging mode gave additional information concerning the structure lipoid organelles.

The next step in this direction has been done quite recently. We tried and we managed to prepare "albumin-label" noncovalent conjugates through absorption of the gold–copper complexes in the hydrophobic sites of albumin (Fig. 10.14) [21]. It

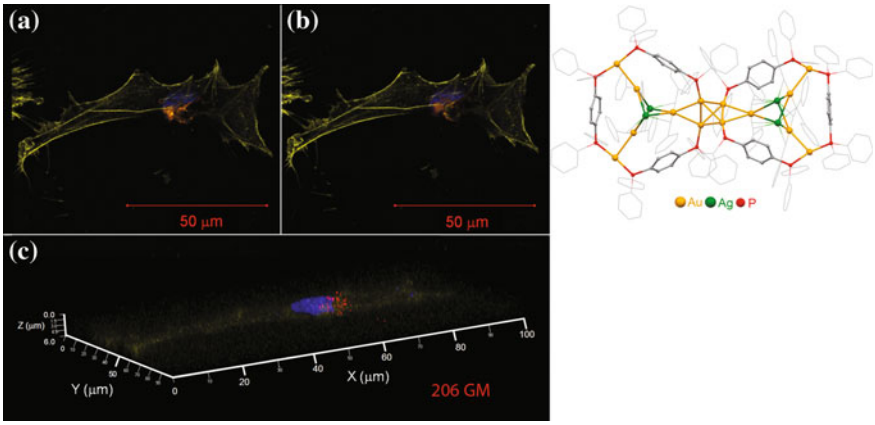

Fig. 10.13 Confocal images of human mesenchymal stem cells stained with DAPI (*blue*), rhodamine phalloidin (*yellow*) and an Au–Ag label in silica (*red*) under two–photon (760 nm) excitation

is well known that albumin is concentrated in inflamed tissue and also in cancer tissues. Formation of the conjugates makes the emitter soluble in physiological media, and, what is of interest, photophysical properties of conjugates are nearly identical to those observed in the case of starting complexes.

Figure 10.15 shows the spectrum of human-serum albumin and its conjugates, it can be easily seen that intensity of emission of the label in the conjugate is quite strong compared to the intrinsic albumin emission, which doesn't contribute considerably into the total emission intensity.

Moreover, emission of the conjugates under one-photon excitation looks very similar to what we obtained in the case of starting complexes, and, for two-photon excitation, the emission parameters of the complexes and conjugates fit each other very well, the two-photon absorption cross-section being even greater in the case of the aggregate.

Confocal microscopy of HeLa cells stained with DAPI and noncovalent conjugates (Fig. 10.16) show that the localization of DAPI and conjugate is different, allowing for detailed characterization of the cell structure.

Applications of the albumin-complex conjugates in the two-photon regime for imaging of the rat spleen, brain, liver and miocardia.

These images show that two-photon excitation images have higher resolution and much greater depths of 3D reconstruction as compared to the one-photon technique (up to 140 μm in the case of brain tissue) (Fig. 10.17).

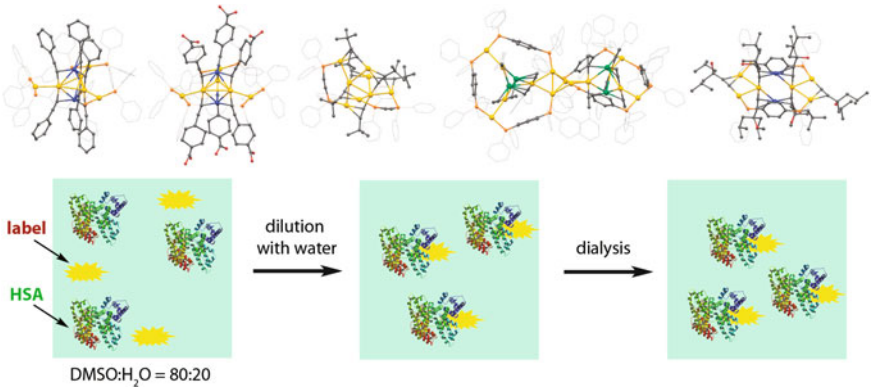

Fig. 10.14 Albumin labelled with heterometallic Au-Ag and Au-Cu luminescent complexes

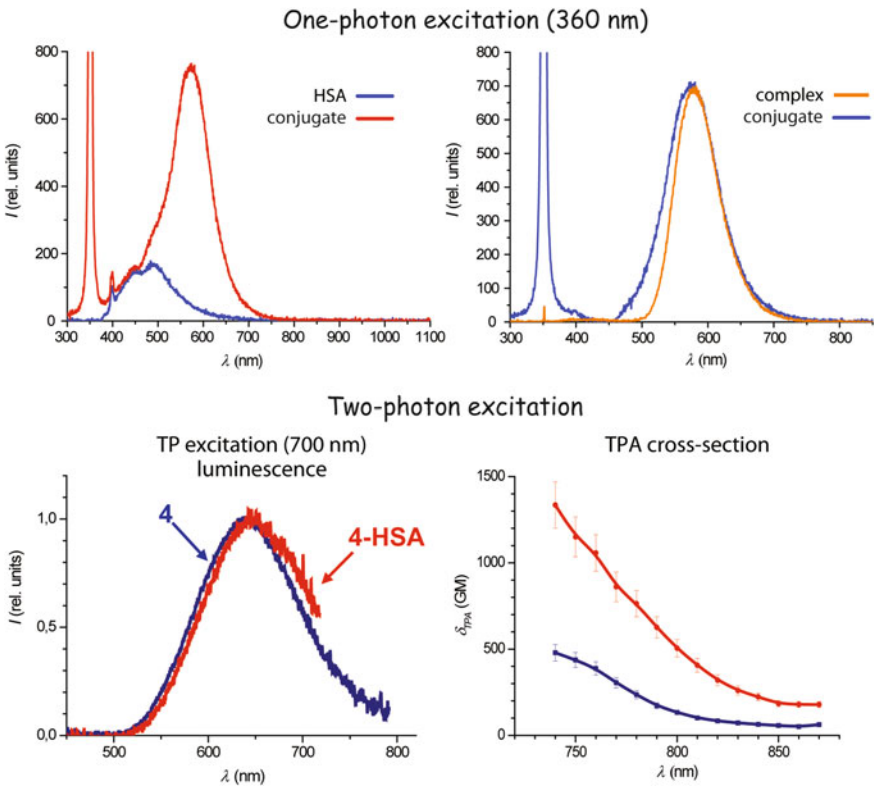

Fig. 10.15 Photophysical characteristics of noncovalent albumin conjugates with {Au6Cu2} label [21]

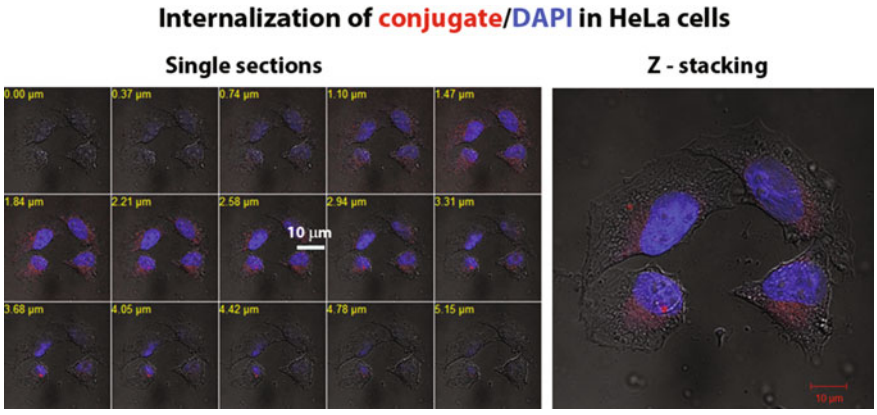

Fig. 10.16 Confocal microscopy of HeLa cells using DAPI and HSA-label conjugate

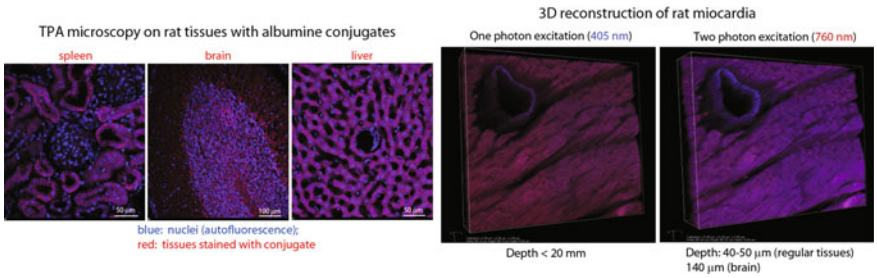

Fig. 10.17 Applications of the albumin-complex aggregates in the two-photon regime for imaging of the spleen, brain, liver and rat miocardia

From the view of prospects for collaboration with our colleagues from the University of Tokyo, I would like to display one of the complexes synthesized in my group (see Fig. 10.18).

The chemical part of the project from the very beginning was targeted to the synthesis of the compounds with specific photophysical properties, namely, the complexes that are able to display dual emission. For the complex shown in

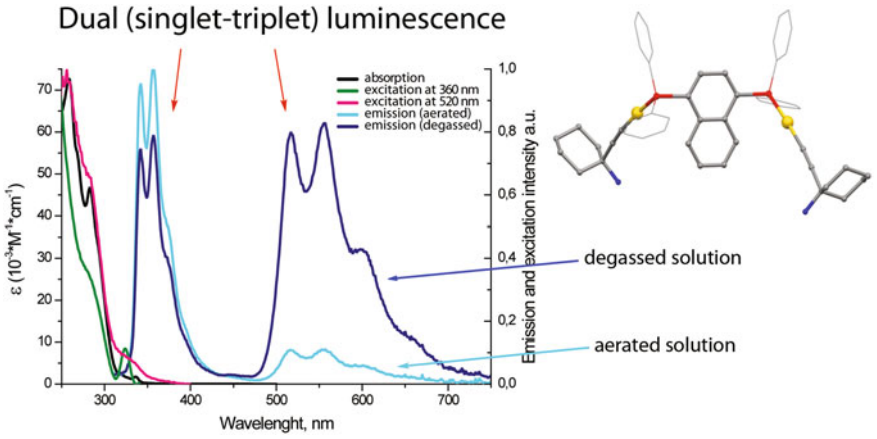

Fig. 10.18 Prospective collaboration

Fig. 10.18, fluorescence comes from naphthalene moiety, and its introduction into the molecular gold center results in generation of triplet emission. At the moment, we do not know what is the actual origin of triplet emission, but this is what we would like to investigate with the physicists and theoreticians from the University of Tokyo, using various spectroscopic techniques available at UofT.

I appreciate greatly the contribution to this project made by my colleagues from the University of Eastern Finland, the High Molecular Compounds Institute of Russian Academy of Science, and the National Taiwan University as well as financial support from Saint Petersburg State University internal funding, RFBR grants, and the Finland Academy of Science.

References

I.O. Koshevoy, L. Koskinen, M. Haukka, S.P. Tunik, P. Yu. Serdobintsev, A.S. Melnikov, and T. A. Pakkanen, Self-Assembly of Supramolecular Luminescent AuI–CuI Complexes: "Wrapping" an Au6Cu6 Cluster in a [Au3(diphosphine)3]3+ "Belt". Angew. Chem. Int. Ed. **47**, 3942–3945 (2008)

I.O. Koshevoy, Y.-C. Lin, A.J. Karttunen, M. Haukka, P.-T. Chou, S.P. Tunik, T.A. Pakkanen, An intensely and oxygen independent phosphorescent gold(I)–silver(I) complex: trapping an Au8Ag10 oligomer by two gold-alkynyl-diphosphine molecules. Chem. Commun. **28**, 60–62 (2009)

I.O. Koshevoy, A.J. Karttunen, J.R. Shakirova, A.S. Melnikov, M. Haukka, S.P. Tunik, T.A. Pakkanen, Halide-directed assembly of the multicomponent systems: highly ordered AuI-AgI molecular aggregates. Angew. Chem. Int. Ed. **49**, 8864–8866 (2010)

I.O. Koshevoy, C.-L. Lin, A.J. Karttunen, J. Jänis, M. Haukka, S.P. Tunik, P.-T. Chou, T.A. Pakkanen, Highly luminescent octanuclear AuI-CuI clusters adopting two structural motifs: the effect of aliphatic alkynyl ligands. Chem. Eur. J. **17**, 11456–11466 (2011)

I.O. Koshevoy, P.V. Ostrova, A.J. Karttunen, A.S. Melnikov, M.l.A. Khodorkovskiy, M. Haukka, J. Jänis, S.P. Tunik and T.A. Pakkanen, Assembly of heterometallic Au(I)-M(I) (M = Cu, Ag) clusters containing dialkyne-derived diphosphines: synthesis, luminescence and theoretical studies. Dalton Trans. **39**, 9022–9031 (2010)

I.O. Koshevoy, C.-L. Lin, A.J. Karttunen, J. Jänis, M. Haukka, S.P. Tunik, P.-T. Chou and T.A. Pakkanen, Stepwise 1D growth of luminescent Au(I)-Ag(I) phosphine-alkynyl clusters: synthesis, photophysical and theoretical studies. Inorg. Chem. **50**, 2395–2403 (2011)

J.R. Shakirova, E.V. Grachova, A.S. Melnikov, V.V. Gurzhiy, S.P. Tunik, M. Haukka, T.A. Pakkanen, I.O. Koshevoy, Towards luminescence vapochromism of the tetranuclear AuI-CuI clusters. Organometallics **32**, 4061–4069 (2013)

I.S. Krytchankou, D.V. Krupenya, A.J. Karttunen, S.P. Tunik, T.A. Pakkanen, P.-T. Chou, I.O. Koshevoy, Triphosphine-supported bimetallic AuI-MI (M = Ag, Cu) alkynyl clusters. Dalton Trans. **43**, 3383–3394 (2014)

I.O. Koshevoy, A.J. Karttunen, I.S. Kritchenkou, D.V. Krupenya, S.I. Selivanov, A.S. Melnikov, S.P. Tunik, M. Haukka, T.A. Pakkanen, Sky-blue luminescent AuI-AgI alkynyl-phosphine clusters, Inorg. Chem. **52**(2013), 3663–3673 (2013)

I.O. Koshevoy, Y.-C. Chang, A.J. Karttunen, S.I. Selivanov, J. Janis, M. Haukka, T. Pakkanen, S. P. Tunik, P.-T. Chou, Intensely luminescent homoleptic alkynyl decanuclear gold(i) clusters and their cationic octanuclear phosphine derivatives. Inorg. Chem. **51**, 7392–7403 (2012)

I.O. Koshevoy, Y.-C. Lin, A.J. Karttunen, M. Haukka, P.-T. Chou, S.P. Tunik, T.A. Pakkanen, Rational reductive fusion of two heterometallic clusters: formation of a highly stable, intensely

phosphorescent Au–Ag aggregate and application in two-photon imaging in human mesenchymal stem cells. Chem. Comm. **46**, 1440–1442 (2010)
I.O. Koshevoy, C.-L. Lin, A.J. Karttunen, M. Haukka, C.-W. Shih, P.-T. Chou, S.P. Tunik and T. A. Pakkanen, Octanuclear gold(I) alkynyl-diphosphine clusters showing thermochromic luminescence. Chem. Commun. **47**, 5533–5535 (2011)
I.S. Krytchankou, I.O. Koshevoy, V.V. Gurzhiy, V.A. Pomogaev, S.P. Tunik. Luminescence solvato- and vapochromism of alkynyl-phosphine copper clusters. Inorg. Chem. **54**(17), 8288–8297 (2015)
I.O. Koshevoy, A.J. Karttunen, S.P. Tunik, J. Jänis, M. Haukka, A.S. Melnikov, P. Yu. Serdobintsev, T.A. Pakkanen, Reversible protonation of the amine-functionalized luminescent Au-Cu clusters: characterization, photophysical and theoretical studies. Dalton Trans. **39**, 2676–2683 (2010)
X. He, N. Zhu, V.W.-W. Yam, Design and synthesis of luminescence chemosensors based on alkynyl phosphine gold(I)–copper(I) aggregates. Dalton Trans. **40**, 9703–9710 (2011)
I.O. Koshevoy, Y.-C. Chang, A.J. Karttunen, J.R. Shakirova, J. Janis, M. Haukka, T. Pakkanen, P.-T. Chou, Solid-State luminescence of Au_Cu_Alkynyl complexes induced by metallophilicity-driven aggregation. Chem. Eur. J. **19**, 5104–5112 (2013)
M.T. Dau, J.R. Shakirova, A.J. Karttunen, E.V. Grachova, S.P. Tunik, A.S. Melnikov, T.A. Pakkanen, I.O. Koshevoy, Coinage metal complexes supported by the Tri- and Tetraphosphine, ligands. Inorg. Chem. **53**, 4705–4715 (2014)
T.M. Dau , Y.-A. Chen , A.J. Karttunen, E.V. Grachova, S.P. Tunik, K.-T. Lin, W.-Y. Hung, P.-T. Chou, T.A. Pakkanen, I.O. Koshevoy, Tetragold (I) Complexes: solution isomerization and tunable solid-state luminescence. Inorg. Chem. **53**, 12720–12731 (2014)
S.W. Botchway, M. Charnley, J.W. Haycock, A.W. Parker, D.L. Rochester, J.A. Weinstein, J.A. Gareth Williams, Time-resolved and two-photon emission imaging microscopy of live cells with inert platinum complexes. Proc. Natl. Acad. Sci. USA. **105**(42): 16071–16076 (2008)
E.I. Koshel, P.S. Chelushkinb, A.S. Melnikov, P.Y. Serdobintsev, A.Y. Stolbovaia, A.F. Saifitdinova, V.I. Shcheslavskiy, O. Chernyavskiyh, E.R. Gaginskaya, I.O. Koshevoy, S. P. Tunik, Lipophilic phosphorescent gold(I) clusters as selective probes for visualization of lipid droplets by two-photon microscopy. J. Photochem. Photobiol. A Chem. **332**(2017), 122–130 (2017)
P.S. Chelushkin, N.V. Nukolova, A.S. Melnikov, P.Y. Serdobintsev, A.S. Melnikov, D.V. Krupenya, I.O. Koshevoy, S.V. Burov, S.P. Tunik, HSA-based phosphorescent probe for two-photon in vitro visualization. J. Inorg. Biochem. **149**(2015) 108–111 (2015)

Chapter 11
Extreme Imaging and Beyond

Keisuke Goda

There is an analogy between microscopy and high-speed imaging. The microscope makes small things bigger so that we can see things with human eyes. On the other hand, the high-speed camera makes fast things slower so that we can see dynamics with human eyes. So if we compare the physical limits of optical resolution, our human eyes can see things down to roughly 100 μm, but, with the help of the microscope, we can see things down to 100 nm, which is basically the physical limit of the conventional microscope based on the diffraction limit. On the other hand, in the time domain, we can see things probably down to 10 ms, but, with the help of a high-speed camera, we can see things down to nanoseconds.

We have not reached a limit yet. We are currently limited by inertia, and fundamentally, we are going to be limited by the Fourier-transform limit. Of course, as you know, last year three people received the Nobel Prize in chemistry for breaking the diffraction limit. I want to talk about the limitations of the conventional-camera interval speed. So here is the basic architecture of the conventional camera, and it actually consists of two major components: the image-acquisition component which is optical and image-processing component which is digital.

At the heart of this conventional digital camera is the CCD or CMOS image sensor. Basically, we have an array of many photo diodes. Here, we are limited by charge-download rate because we have to read out the charge from every pixel. So, that gives us about a 100-kHz frame rate, but this is not the fundamental limit. The fundamental limit actually comes from the tradeoff between sensitivity and speed, which is nothing but the number of photons you detect during each frame. In other words, there is a tradeoff between sensitivity and speed so that, if you want to take a picture at a high frame rate, you need to sacrifice photons or sensitivity, or vice versa. If you need a high sensitivity, you sacrifice speed. There is also another the

K. Goda (✉)
Department of Chemistry, School of Science, The University of Tokyo,
7-3-1 Hongo, Bunkyo-Ku, Tokyo 113-0033, Japan
e-mail: goda@chem.s.u-tokyo.ac.jp

K. Yamanouchi (ed.), *Progress in Photon Science*, Springer Series
in Chemical Physics 115, DOI 10.1007/978-3-319-52431-3_11

predicament in high-speed microscopy. In the case of macroscopy or macroscopic imaging, you can compensate for the loss of sensitivity by using high-intensity illuminators such as this, but this doesn't work for microscopy because you focus all the light onto the sample using the objective lens. So you end up cooking the sample. So here I want to propose two new techniques to circumvent these fundamental limitations in imaging. Here I introduce STEAM and STAMP. STEAM stands for Serial Time-encoded Amplified Microscopy, which is the world's fastest continuous-mode imaging, and STAMP that stands for Sequentially Timed All-optical Mapping Photography which is the world's fastest burst-mode imaging.

So I want to talk about the principles and applications of these two techniques. Figure 11.1 is a little picture that shows the evolution of shutter technology.

Basically, the imaging speed is limited by how we create shutters, how we shutter the event. So we used to have this kind of bulky camera with a mechanical shutter under 1 μs; so then this evolved into a CCD or CMOS image sensor that uses an electrical shutter that can operate under 1 μs. Now, we are entering the era of optical shuttering, which can operate under 1 ns or less.

So let me start with the STEAM technology. So STEAM is roughly 1000 times faster than CCD or CMOS image sensors in terms of shutter speed and frame rate. It is also 1000 times more sensitive than CCD or CMOS cameras. This is possible by the first demonstration of optical image amplification. Figure 11.2 contains the specifications.

The frame rate can go as high as 10 mega-frames per second; the shutter speed is 10 because the number of pixels is a couple of hundred by a couple of hundred. The optical image gain, which is the most important parameter of all, is about 30 dB. It means it amplifies an image-encoded-photon before photon-to-electron conversion with the detector.

So STEAM is basically an all-optical camera that can perform image processing in the optical domain so that we do not have to suffer from the fundamental limits in digital signal processing. So let me sort of talk about how this camera functions. It actually consists of spectral structured illumination and amplified dispersive Fourier transformation. This thing shows a sort of unstructured random illumination which

Fig. 11.1 Evolution of motion-picture photography

Parameter	Value
Frame Rate	~10 Mfps
Shutter Speed	~10 ps
Number of Pixels	~200 x 200
Optical Image Gain	~1,000x (30 dB)

Fig. 11.2 Specifications of STEAM

is something that we use on a daily basis, or this kind of illumination is unstructured illumination. On the other hand, STEAM uses structured illumination. So here, spectral structured illumination maps the spectrum and optical pulses in space for illumination.

Figure 11.3 shows that, in the case of 1D imaging, the white pulses are passing through the 1D special disperser—this laser pointer is dying—. This 1D special disperser maps the spectrum of each pulse into one-dimensional space for illumination, so that each frequency component of the light illuminates different spatial coordinates on the imaging target. In the case of 2D imaging, the same thing happens but in 2D. The spectrum of each pulse is mapped into two-dimensional space, so there is a one-to-one mapping relationship between the frequency of the

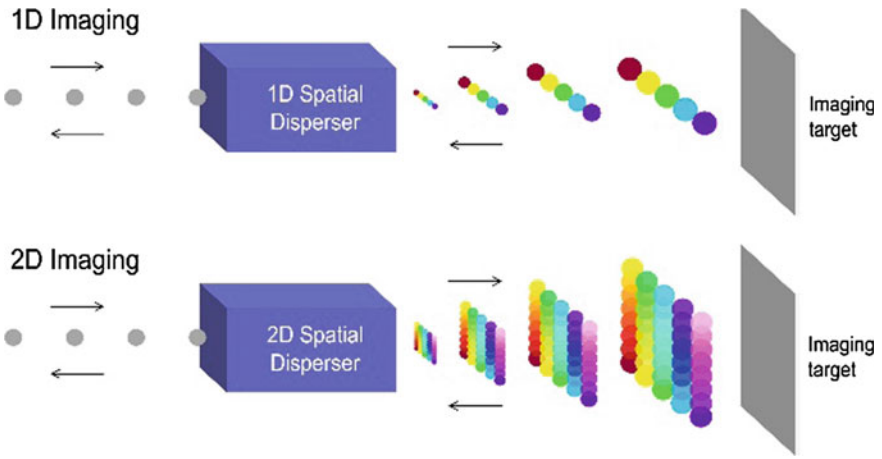

Fig. 11.3 Spectrally structured illumination for image encoding

light and the spatial coordinates of the target, and then the lights get refracted for imaging acquisition.

How do we decode these spectrally encoded images? So we use the technique of spectroscopy in the time domain. So here the spectrum of optical pulses is mapped into a temporal waveform so that it can be measured by a single photodiode. So we start with a very short pulse, i.e., the image encoded pulse, and it travels to some kind of sample or image target so that the spectrum of the pulse—sorry, the imaging information of the spectrum of the sample imprinted onto the spectrum of the pulse—then it enters the dispersive fiber to map the pulse or the spectrum of the pulse into the time domain.

We can also optically pump this dispersive fiber for optical image amplification, and this is a sort of actual implementation. So basically, a single-pulse image encoded or spectral-encoded pulse evolves into the spectrum of its own using this dispersive component in the fiber. So this is a better demonstration, so here, after this output, we have a pulse train separated by 11 ns, so if we zoom into one of the pulses, we see that the temporal waveform pattern of the pulse matches its spectrum measured by the conventional spectrum analyzer. So it is a one-to-one mapping between time and wavelengths. Because of this, we can decode the temporal waveform so that we can perform real-time pulse-resolved spectrum measurement, which can be performed at a 100-MHz scan rate which is roughly 100,000 times faster than conventional spectrometers.

By combining these two techniques, we demonstrate STEAM. Basically, we start with a broadband pulse laser. Each pulse enters the two-dimensional spatial disperser that matches the spectrum of each pulse into two-dimensional space and image is encoded into the spectrum; the spectrum is now mapped into the temporal domain; and we detect each image frame with a single-pixel photodiode to reconstruct 2D images. So that is the principle. Let me talk about applications.

Japan used to have a good industry for organic LED, so we now use a lot of organic LED thin films. The important part of this organic LED manufacturing is high-speed inspection of the surface of the organic LEDs, so this is what happens in the factory. So this is organic LED thin-film propagation, and there are a lot of defects and particles on top of the thin film. We need to inspect the surface roughly 20 times per display. So here we have the sample with the CMOS images; this is the transferring speed, the flow speed. As flow speed increases, the CMOS camera cannot see those things clearly because of the motion blur, but a STEAM image can clearly show the features. Another application is the measurements of surface vibration. The measuring surface vibration is critical for nondestructive inspection of aerospace components, MEMS oscillators, acoustic instruments, and biological cells. For example, we can see the vibrations of a drum in real-time with the world's fastest 3D surface vibrometer; here the frame rate is 1 MHz, the shutter speed is 100 ps, and the axial resolution is 0.5 nm. So we can see sound with imaging.

Another application is medical. So, here in Japan, about 50% of people get cancer and about 60% of cancer patients die from it; but 90% of cancer deaths are actually caused by cancer metastasis or cancer spread [1]. It is not caused by the primary tumor. So this is how this cancer metastasis occurs. Cancer cells detach

from the original tumor, enter either a blood vessel or the lymphatic vessel, circulate inside the body, move to a new location, and create a secondary tumor. These cells are called circulating tumor cells. So it would be very effective to detect these circulating tumor cells for medical diagnosis. However, these cells are actually very difficult to detect, and here is the reason. What I mean by "the reason" is the statement that follows, i.e., the next paragraph which describes the table.

So this table shows the blood components and their concentration in cells per milliliter of blood. These are red blood cells which number about 5 billion cells per milliliter, and these are platelets which number about 350 million. When you look all the way down, you find circulating tumor cells which number only 10 cells per milliliter of blood, so it's very, very difficult to detect with conventional blood analyzers because of this extreme rareness. So in order to detect these cells, I combined STEAM with microfluidics and high-speed signal processing to perform nonstop real-time image recording and image-based cell classification at 100,000 sets per seconds. So basically we do imaging with a high-throughput capability. In order to detect the circulating tumor cells, we compare cancer cells with the red and white blood cells. Red blood cells are roughly sized about 7 μm, and white blood cells are sized about 10–20 μm, so cancer cells are a little larger and also their shape is quite distorted. So by imaging, we can tell the difference.

Also, in order to increase the detection specificity, we coated the cancer cell with surface expression, with metal beads on the surface using the molecule, the so-called epicam. So by imaging, we can see size, we can see shape, we can see the beads, and also we can see the presence of clusters, and cancer cells tend to cluster more than blood cells, simultaneously. With the sort of microfluidic technology that we use, randomly distributed cells start to form into a single stream with this zigzag pattern because of the interaction between the cells and the walls of the microfluidic device, and the STEAM can thus take pictures of every single cell nicely. Here is a movie that shows how this integrated system works. So we start with very short pulses in a train, and then these pulses disperse into one-dimensional space. Then these pulses are focused onto the microfluidic chip through an objective lens, and blood is subject to lysis. That means we destroyed all the red blood cells, so what remains are white blood cells and cancer cells which are yellowish. Then, after the zigzag pattern, all the white blood cells and cancer cells are lying in a single stream, and then these STEAM pulses are focused onto the cells, one by one, like one-dimensional scanning. Then, image-encoded pulses return retro-reflected from these cancer cells, morphologically distorted, and you can see the metal beads on the surface.

Then, image-encoded pulses return to the same optics and are directed toward the dispersive fiber that maps the spectrum of each pulse into the time domain due to dispersion, and simultaneously this fiber spool is optically amplified for optical amplification of each image. Subsequently, each optically processed image frame is detected by the photodiode, and then the signal is sent to our custom-built image processor. Now, we go to the digital world, and, in this world, we reconstruct the two-dimensional images based on the many 1D slices. We then perform match detection digitally against a cancer-cell database. So basically, we pare down to

select suspicious-looking cell images, and then we send these cell images to the CPU for fine screening. Finally, these images are displayed on the monitor so that the medical doctor sees them and tries to identify the cancer cells.

Here is a sort of comparison between CCD, CMOS, and STEAM images. The CCD camera, has a shutter speed of 70 ms. This is how we can see the cells, the unbudded yeast cells, budding yeast cells, white blood cells, and cancer cells coated with metal beads. Now, we flow them at high speed, but we cannot see them clearly with a CMOS camera because of the motion blur. So we cannot see the difference between unbudded and budding yeast cells, and, of course, we cannot tell the difference between white blood cells and cancer cells, but, with STEAM, we can see these things rather clearly because of the ultrafast shutter speed of 27 ps. With this, we can see the difference between the budding and unbudded yeast cells and the white blood cells and cancer cells. So here the flow speed is 4 m/s, which corresponds to 100,000 sets per second. We designed a programmable integrated circuit to detect suspicious looking cancer cells. The real-time image processor we built detects extremely rare cancer cells in 3 ml of blood, which contains about 24 million white blood cells, in 3 min, which would otherwise take a few days to a week with conventional technology.

Let me move onto the next topic, which is the second technology, namely, sequentially timed all-optical mapping photography which is the world's fastest burst-mode imaging. So it is the world's fastest burst camera as opposed to a continuously-running camera. This demonstration is a fast optical 2D-image separation. The frame rate can go as high as 5 trillion frames per second with a shutter speed of 300 fs, and number of pixels is 500×500. The number of frames is limited, about 10, which can be increased to 100, but this is burst mode. So the concept of this is the following: we use the different wavelength of light to encode, to take pictures at different times, and then different image frames that correspond to different times are detected in different regions of space. Then, we combine all these images to create the movie. Let me sort of talk about this and let me show the movie of how this thing, sequentially timed all-optical mapping photography, works. That is the overall picture of the optical set-up, and then we zoom in. We start with a very short pulse from a laser source, and this is dispersed in the time domain by the pulse stretcher, basically by dispersion. Then the stretched pulse enters the pulse shaper that tailors the intensity of each sub-pulse or daughter pulse, and here we have a train of six daughter pulses. These daughter pulses with different spectra are focused onto the dynamic event at different times for picture taking. Then, these image-encoded pulses are directed towards a special mapping device that maps these image-encoded spectra in the special domain without distorting the image formation. These image encoded pulses, which are now separated spatially, are then directed onto different sections of the CCD image sensor.

After this, in the digital domain, we reconstruct a movie based on stacking these image frames, and then eventually we play back and see the dynamic event. This camera is useful for macroscopy and microscopy. So one of the applications is to see laser-ablation dynamics with STAMP because laser ablation dynamics are a quite fast event that occurs under a nanosecond or less. We have an excitation pulse

which is illuminated and monitored with STAMP flashes. Air and glass layers, and, after this illumination pulse excites the glass plate, basically this thing explodes, but we can see it slowly. So here we can see the generation of free electrons indicated by the white arrow, and the black ones are caused by the laser pulse, followed by the formation of a plume. Another application is to see the so-called phonons. A phonon is basically a collective oscillation of atoms and molecules in a crystal such as this, and imaging of phonons is important for studying the properties of materials, especially for semiconductor physics in which heat is a major problem. Moreover, currently phononics is a hot topic of research. So we wanted to see how a phonon is created and how it propagates. We have this crystal, excited with a laser, and we monitor what's going on. With this 780-fs time resolution, we can see how a phonon is created and propagates. We can also increase the temporal resolution down to 200 fs so we can see the formation of a phonon pulse here and watch how it propagates. It actually propagates at about 15% of the speed of light, which is quite fast. So we can see the electronic response of the crystal and also the phonon formation. These phonons are actually terahertz phonons, and spectrum of each phonon pulse is centered at around 1.5 THz.

In summary, I have talked about ultrafast imaging. This helps understand the underlying laws of nature, and lots of opportunities exist for the development of new imaging methods that can circumvent the physical limits just like super-resolution fluorescence microscopy. So in my group, we basically try to develop new technology that breaks speed limits. We have eight world records for speed right now.

Reference

1. J. Kaiser, Science **327**, 1072 (2010)

Part V
Molecules and Clusters in Intense Laser Fields

Chapter 12
Classical Trajectory Models for Laser-Atom and Laser-Molecule Interactions

Erik Lötstedt, Tsuyoshi Kato, Kaoru Yamanouchi and Katsumi Midorikawa

12.1 Introduction

When an atom or a small molecule in the gas phase is exposed to an intense laser field, a complex response is generally induced. In the present context, "intense" signifies a peak-field intensity in the range between 10^{14} and 10^{16} W/cm^2, assuming a wavelength of typically 800 nm. Such a laser pulse triggers a violent rearrangement of valence electrons in the atom or molecule. Some electrons may be ejected into the continuum as a result of field ionization, while the bound electrons may be excited to higher-lying states. In the case of a molecule, electronic excitation may lead to structural changes and/or dissociation. Moreover, as a result of the oscillatory character of the electric field of the laser, an electron that is initially ejected from the atom (or molecule) may be accelerated by the laser field in such a way that the electron returns close to the atomic core with high kinetic energy. This process, in which an ejected electron absorbs energy from the laser field and comes back to the atom, is referred to as a *recollision* [1, 2] in the strong-field physics community. A recollision event may result in several outcomes, such as elastic scattering of the returning electron, emission of a high-energy photon (so-called high-order harmonic generation [3]), and inelastic scattering of the recolliding

E. Lötstedt (✉) · T. Kato · K. Yamanouchi
Department of Chemistry, School of Science, The University of Tokyo,
7-3-1 Hongo, Bunkyo-ku, Tokyo 113-0033, Japan
e-mail: lotstedt@chem.s.u-tokyo.ac.jp

T. Kato
e-mail: tkato@chem.s.u-tokyo.ac.jp

K. Yamanouchi
e-mail: kaoru@chem.s.u-tokyo.ac.jp

K. Midorikawa
RIKEN Center for Advanced Photonics, 2-1 Hirosawa, Wako, Saitama 351-0198, Japan

K. Yamanouchi (ed.), *Progress in Photon Science*, Springer Series
in Chemical Physics 115, DOI 10.1007/978-3-319-52431-3_12

electron. In the last case, if the energy transfer from the recolliding electron is large enough, one or several bound electrons may be ejected in addition to the initially ejected electron, which results in a final state with a highly-charged atom/molecule and several free electrons.

How can we simulate theoretically an atom or molecule irradiated with intense laser light? It follows from the preceding introduction that a model aiming to describe all the features of strong laser-atom/molecule interaction must satisfy the following criteria: (i) Electron-electron as well as electron-nucleus interaction should be fully included, (ii) many different channels, such as multiple ionization and different fragmentation reactions, must be allowed for, and (iii) large-amplitude motion of ejected electrons should be possible. Since an atom is an intrinsically quantum object, the first thought may be to try to solve the time-dependent Schrödinger equation (TDSE), including the coupling with the laser field as a time-dependent potential. However, to solve the TDSE for a many-electron system is extremely demanding computationally, since the large-amplitude motion of the electrons in the continuum precludes the use of localized basis sets such as Gaussian functions centered at the atomic nuclei, as is usually employed in quantum chemistry. The time-dependent Hartree-Fock approximation is inadequate to describe the correlated motion of several electrons. Therefore, we look for alternative methods to properly describe laser-atom and laser-molecule interactions.

A model which satisfies all the criteria raised above, and which is also practically feasible, is the classical trajectory model. In this model, all particles (electrons and heavy nuclei) are treated as classical point particles, interacting with each other via the Coulomb potential and with the laser field via the Lorentz force. The largest advantage of such a method is that it is easy to do the simulation: Newton's equation of motion can be straightforwardly solved on a desktop computer, even for large systems of hundreds of interacting particles. Another advantage is that a classical trajectory is easy to interpret, since we have information on both the positions and momenta of all the particles at all times. The disadvantage of a classical trajectory model is that we cannot use the bare Coulomb potential directly as the interaction potential. This is so because, in general, a collection of charged particles interacting via bare Coulomb potentials is not stable, but will spontaneously ionize or dissociate. This fact is most clearly demonstrated by an example: two classical electrons bound to a nucleus (a helium atom), as illustrated in Fig. 12.1. Even if we assume a situation where the two electrons are bound, each having negative energy, one electron may transfer energy to the other electron by the electron-electron interaction, resulting in a state where one electron is ejected, and the other is bound closely to the atomic core. Since this transition can be made in such a way that energy is conserved, the situation shown on the left in Fig. 12.1 is in general unstable. Thus, a model employing bare Coulomb potentials for the electron-nucleus interaction cannot be used, since we do not want our atom or molecule to auto-ionize before the interaction with the laser pulse.

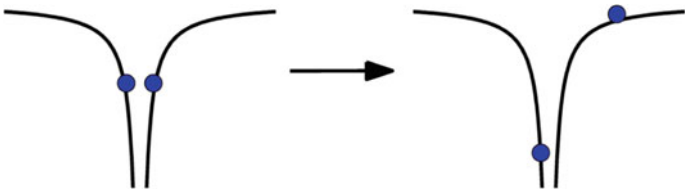

Fig. 12.1 Classical helium with a bare Coulomb potential. By the electron-electron interaction, a bound state (*left*) makes a transition to a state with one bound and one loosely bound electron (*right*). The two states have the same total energy

12.2 Theoretical Model of a Classical Many-Electron System

The example shown in Fig. 12.1 suggests a solution to the stability problem: If an electron is prevented from collapsing into the core of the nucleus, we could model a stable atom. However, we only need to prevent slow electrons from approaching the atomic core too closely. Electrons with high velocity, such as inner-shell electrons, can be allowed to be more deeply bound than valence electrons. This reasoning motivates the modification of the electron-nucleus interaction as follows:

$$V(r) = -\frac{Ze^2}{4\pi\epsilon_0 r} \rightarrow V_{\mathrm{FMD}}(r,p) = -\frac{Ze^2}{4\pi\epsilon_0 r} + g(pr), \tag{12.1}$$

where p is the momentum of the electron, and $g(pr)$ is an auxiliary repulsive potential which restricts the motion of the electron to the parts of classical phase space where the relation

$$pr \geq \hbar\xi_0 \tag{12.2}$$

is satisfied. In (12.2), ξ_0 is a constant of the order of one. To construct a model Hamiltonian for a many-electron atom, we add potential terms V_{FMD} for each electron in addition to the kinetic energies and the electron-electron repulsion. For example, a model Hamiltonian for the helium atom reads:

$$H_{\mathrm{He}} = \frac{p_1^2}{2m_e} + \frac{p_2^2}{2m_e} + V_{\mathrm{FMD}}(r_1,p_1) + V_{\mathrm{FMD}}(r_2,p_2) + \frac{e^2}{4\pi\epsilon_0 r_{12}}. \tag{12.3}$$

Even with the inclusion of the electron-electron interaction term $e^2/(4\pi\epsilon_0 r_{12})$, the helium atom defined by the Hamiltonian (12.3) has a stable ground state of minimum energy, due to the use of the modified Coulomb potential $V_{\mathrm{FMD}}(r,p)$. The model defined by the replacement of the electron-nucleus potential as in (12.1) is referred to as Fermionic Molecular Dynamics (FMD), and was first suggested in [4]. The FMD model was extensively applied to atomic and molecular collision

problems by Cohen [5, 6]. The FMD model can be extended to many-electron systems by assigning a spin direction (up or down) to each electron, and introducing an auxiliary spin-dependent potential acting between electrons with the same spin. The spin-dependent potential prevents electrons with the same spin from having the same momentum and position, effectively implementing a classical version of the Pauli principle.

12.3 Monte Carlo Simulation

After having defined the Hamiltonian of the system [in the case of helium (12.3)], we can derive the equations of motion from Hamilton's equations, adding also the Lorentz force due to the laser field. By solving the equations of motion, we would like to derive some physical observables of the laser-driven system, such as photoelectron spectra or ionization probabilities. Clearly, it is not enough to calculate only one trajectory, since the evolution of the system according to the equations of motion is deterministic. The same initial condition leads to the same outcome. Rather, we should calculate many trajectories starting from randomly selected initial conditions. The initial values are the only random elements in the calculation, and the parameters of the laser pulse, such as laser field intensity and wavelength, are fixed.

The probability distribution from which the initial values are sampled depends on the system under study. In the case of atoms, one uses the fact that the FMD ground state (the state with lowest energy) is invariant under spatial rotations of the position vectors and of the momentum vectors, so that a random initial value can be obtained by applying a random rotation to a reference ground state [7]. For molecules, initial values can be sampled from an ensemble of trajectories that are vibrationally excited, in order to mimic a certain experimental situation.

After having calculated many trajectories starting from slightly different initial conditions, we can estimate the relative yields of different dissociation or ionization channels by counting the number of trajectories with a particular final state. Energy spectra are calculated in the same way by counting the number of trajectories with a kinetic energy within a certain energy range.

12.4 Application to Laser-Driven D_3^+ and Laser-Driven C

In this section, we briefly show two examples of the application of the FMD model as defined in Sect. 2. The first example is the D_3^+ molecular ion (consisting of three deuterons and two electrons) exposed to an intense, few-cycle laser pulse [8, 9]. This research was motivated by recent experimental measurements on fragmentation and ionization of the molecular ion D_3^+ in intense laser fields [10]. D_3^+ (or H_3^+) can be said to be the simplest polyatomic molecule, and we expect that an

understanding of D_3^+ in intense laser fields will pave the way towards a general understanding of more complex molecules in intense laser fields. Despite the apparent simplicity of the molecular structure, the laser-induced dynamics of D_3^+ are rather complex. No complete quantum mechanical simulation of laser-driven D_3^+, including both the electronic and the nuclear degrees of freedom, has been published to date. After the interaction with the laser field, D_3^+ may decompose according to one of the following possibilities:

$D_3^+ \rightarrow$

1. D_3^+ (no dissociation or ionization),
2. $D^+ + D_2$ (dissociation),
3. $D_2^+ + D$ (dissociation),
4. $D^+ + D + D$ (dissociation),
5. $D^+ + D_2^+ + e^-$ (ionization and dissociation),
6. $D^+ + D^+ + D + e^-$ (ionization and dissociation),
7. $D^+ + D^+ + D^+ + e^- + e^-$ (ionization and dissociation).

The challenge for theory is to calculate the relative yields of all the seven channels as a function of the laser parameters, such as laser field intensity, pulse width, and wavelength.

Snapshots from a typical trajectory of D_3^+ exposed to a three-cycle laser pulse with a peak-field intensity of 4×10^{15} W/cm^2 and a wavelength of 790 nm are shown in Fig. 12.2. The molecule is initially in a vibrationally excited state. Through the interaction with the laser field, the electrons become excited, which eventually leads to a breakup of the chemical bond in D_3^+.

We showed in [8, 9] that in the simulation of laser-driven D_3^+ based on the FMD model, trajectories corresponding to all seven final channels as listed above could be found. We mention that all seven channels were also experimentally observed.

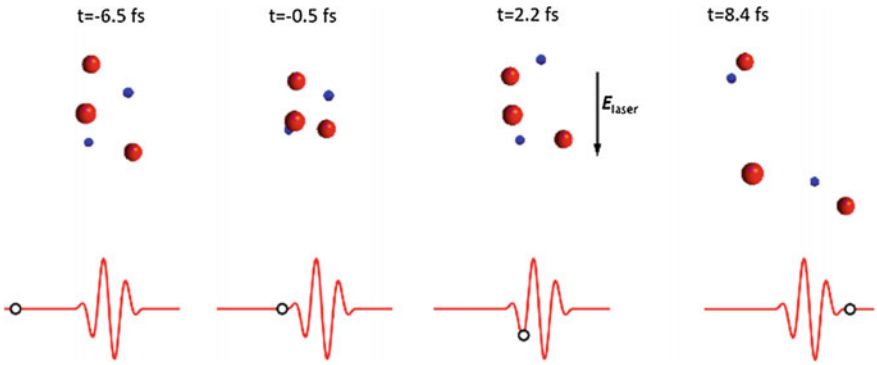

Fig. 12.2 *Upper row* D_3^+ irradiated with a few-cycle laser pulse. Deuterons are shown as *red spheres*, and electrons as *blue spheres*. After the interaction with the laser pulse, D_3^+ breaks into $D^+ + D + D$. *Lower row* Laser pulse, with the instant in time when the snapshot is taken indicated by an open circle. The total pulse width is approximately 8 fs

Although all final channels were produced in the simulation, the relative yield of each channel as a function of the laser-field intensity could not be satisfactorily reproduced as compared to the experimental observations. We also showed that the experimentally measured distributions of the kinetic energy release (defined as the sum of the final kinetic energy of all heavy fragments) could be qualitatively reproduced by the FMD simulations.

An interesting finding resulting from the FMD simulation was the high-energy part of the $D_3^+ \rightarrow D^+ + D^+ + D + e^-$ channel. We found that a small number of trajectories in this channel had the same high kinetic-energy release as the $D_3^+ \rightarrow D^+ + D^+ + D^+ + e^- + e^-$ channel. This is surprising, since the total charge of $D^+ + D^+ + D$ is smaller than $D^+ + D^+ + D^+$, and should therefore lead to a lower final kinetic energy, due to the lower initial potential energy. An analysis of the trajectories in the $D_3^+ \rightarrow D^+ + D^+ + D + e^-$ channel leading to the high-energy events revealed that the high-energy peak in the spectrum was due to incomplete electron ejection [11, 12]. An ejected electron is recaptured by a deuteron at the end of the laser pulse to form a D atom in a highly-excited Rydberg state. Since the screening effect of the excited electron is negligible, the Coulomb explosion of $D^+ + D^+ + D^*$ leads to the same kinetic-energy release as for $D^+ + D^+ + D^+$. Incomplete electron ejection in D_3^+ was later verified experimentally [13].

The second example of the application of the FMD model is the simulation of a laser-driven carbon atom [14]. This example provides a good illustration of the recollision concept discussed in the introduction. We are interested in simulating the process in which an electron is ejected from the atom by field ionization, and subsequently accelerated in the laser field so as to recollide with the residual ion with a kinetic energy large enough to knock out two or more bound electrons. This process, commonly referred to as non-sequential multiple ionization, has been experimentally investigated [15], but theoretical understanding is still lacking.

An example of a classical trajectory involving recollision is shown in Fig. 12.3. In this figure, we show the energies of the individual electrons as a function of time. Since we use a classical model, the electrons are distinguishable, and can be labelled by 1, 2, …, 6. At $t = 0$, the bound electrons in the ground-state C atom have different energies depending on how deeply bound they are. A very interesting feature of the FMD model is that the ground state of a many-electron atom has electrons paired into "shells" with different energies, which is a result of the spin-dependent potential discussed in the last part of Sect. 2.

At the beginning of the second optical cycle, the two valence electrons are ejected by absorbing energy from the laser field. Electron 5 (green line in Fig. 12.3) is accelerated by the laser field and comes back close to the C^{2+} ion, having a kinetic energy of $E_{\mathrm{kin}} \approx 3U_p$, where U_p is the average quiver energy of an electron in the laser field (usually referred to as the ponderomotive potential). Then, at $t \approx 4.6$ fs, a recollision occurs, and the recolliding electron abruptly transfers almost all of its energy to three bound electrons (electron 4 as shown with a purple line in Fig. 12.3, electron 2 shown with a pink line, and electron 3 shown with a blue line), which are ejected from the ion. Interestingly, the recolliding electron

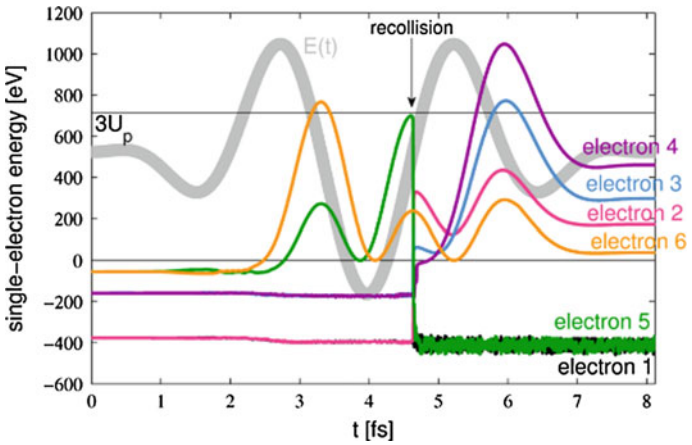

Fig. 12.3 Trajectory of laser-driven C, showing the time-dependent energies of the individual electrons. For $t \leq 4.5$ fs, the *pink curve* of electron 2 overlaps the *black curve* of electron 1, and the *purple curve* of electron 4 overlaps the *blue curve* of electron 3. For $t \leq 1$ fs, the *orange curve* of electron 6 overlaps the *green curve* of electron 5. A recollision event takes place at $t \approx 4.6$ fs. The laser field $E(t)$ is shown in the background on an arbitrary scale. U_p is the ponderomotive potential. The laser parameters used were $I_0 = 4 \times 10^{15}$ W/cm^2 and $\lambda = 800$ nm

does not scatter, but recombines with the ion and falls down into the core shell. The final result is a quadruply charged C^{4+} ion with two slightly excited electrons occupying the core shell (electrons 1 and 5), and four free electrons (electrons 2, 3, 4, and 6).

In our simulations, reported in [14], we observed non-sequential multiple ionization resulting in C^{3+}, C^{4+}, and C^{5+} ions. We found that recollision involving the ejection of core electrons is not uncommon: At a laser field intensity of 4×10^{15} W/cm^2, around 25% of all trajectories leading to quadruple ionization involve the ejection of a core electron. We suggest that this mechanism may be used to produce hollow-core atoms by the irradiation of long-wavelength (800 nm) laser light. Atoms with a core vacancy may be observed by detecting the resulting fluorescence emission.

12.5 Summary

We have discussed the requirements for a theoretical simulation model aiming to describe the interaction of gas-phase atoms and molecules irradiated with intense laser light, and argued that a good candidate satisfying these requirements is a classical trajectory model. In order to solve the problem of an unstable ground state in classical mechanics, the FMD model was introduced. In this model, an auxiliary potential is added to the classical Hamiltonian in order to prevent the electron from

collapsing into the nuclear core. The versatility of the FMD model was demonstrated by showing two examples of our recent research: simulations of laser-driven D_3^+ [8, 9], and laser-driven C [14]. For a more detailed review of these simulations, and a general discussion on classical trajectory models for describing laser-matter interaction, we refer to our review article [16].

Acknowledgments The research on D_3^+ was supported by the Ministry of Education, Culture, Sports, Science and Technology (MEXT), Japan (Grant-in-Aid for Specially Promoted Research on Ultrafast Hydrogen Migration No. 19002006), Grant-in-Aid for Scientific Research No. 21-09238, and the Global COE Program "Chemistry Innovation through Cooperation of Science and Engineering" of the University of Tokyo. The numerical calculations on laser-driven C were carried out at the RIKEN Integrated Cluster of Clusters.

References

1. M.Y. Kuchiev, JETP Lett. **45**, 404 (1987)
2. P.B. Corkum, Phys. Rev. Lett. **71**, 1994 (1993)
3. K. Midorikawa, Jpn. J. Appl. Phys. **50**, 090001 (2011)
4. C.L. Kirschbaum, L. Wilets, Phys. Rev. A **21**, 834 (1980)
5. J.S. Cohen, Phys. Rev. A **56**, 3583 (1997)
6. J.S. Cohen, J. Phys. B **39**, 1517 (2006)
7. D.A. Wasson, S.E. Koonin, Phys. Rev. A **39**, 5676 (1989)
8. E. Lötstedt, T. Kato, K. Yamanouchi, Phys. Rev. Lett. **106**, 203001 (2011)
9. E. Lötstedt, T. Kato, K. Yamanouchi, Phys. Rev. A **85**, 053410 (2012)
10. J. McKenna, A.M. Sayler, B. Gaire, N.G. Johnson, K.D. Carnes, B.D. Esry, I. Ben-Itzhak, Phys. Rev. Lett. **103**, 103004 (2009)
11. T. Nubbemeyer, K. Gorling, A. Saenz, U. Eichmann, W. Sandner, Phys. Rev. Lett. **101**, 233001 (2008)
12. H. Price, C. Lazarou, A. Emmanouilidou, Phys. Rev. A **90**, 053419 (2014)
13. J. McKenna, A.M. Sayler, B. Gaire, N.G. Kling, B.D. Esry, K.D. Carnes, I. Ben-Itzhak, New J. Phys. **14**, 103029 (2012)
14. E. Lötstedt, K. Midorikawa, Phys. Rev. A **90**, 043415 (2014)
15. A. Rudenko, T. Ergler, K. Zrost, B. Feuerstein, V.L.B. de Jesus, C.D. Schröter, R. Moshammer, J. Ullrich, J. Phys. B **41**, 081006 (2008)
16. E. Lötstedt, T. Kato, K. Midorikawa, K. Yamanouchi, *Classical Trajectory Methods for Simulation of Laser-Atom and Laser-Molecule Interaction*, Progress in Ultrafast Intense Laser Science **XII**, Chapter 2 (Springer International Publishing, Switzerland, 2015)

Chapter 13
Study of Relaxation of Multi-photon Excited Neutral Rare-Gas Molecules and Clusters in a Supersonic Jet: REMPI TOF and REMPI PES Spectroscopies of Rare-Gas Dimers and Clusters

Mikhail Khodorkovskii, Alexander Pastor and Pavel Serdobintsev

By using a pulsed nozzle and a skimmer, we can generate an ultracold molecular beam through the formation of a supersonic jet (Fig. 13.1). In the supersonic jet, we can produce van der Waals molecules and diatomic, triatomic, and clusters of rare-gas atoms. By combining the method of Resonantly Enhanced Multi-Photon Ionization (REMPI) spectroscopy, we can investigate such atomic and molecular aggregates (see Fig. 13.2).

The experimental setup is presented in Fig. 13.3. The cooled supersonic molecular beam enters the region of interaction where we can excite this beam with a tunable dye laser and collect photo ions using a reflectron, a time-of-flight mass spectrometer, and we can also ionize this molecular beam with an electron gun to determine the mass contamination in the number of atoms, molecules, dimers, trimers, and clusters in this setup. In Fig. 13.4, we can observe the detailed mass spectra of the initial part, atoms, diatomic, trimers, tetramers, and so on, and also a panoramic mass spectra which indicates that, at higher stagnation pressure before the nozzle, we obtain a broad peak of clusters with an average number, let's say, less than 100 atoms per cluster, i.e., approximately 70 atoms per cluster.

We have predecessors Dehmer et al. [1] from Argonne National Laboratory and, Lipson et al. [2]. Professor Yamanouchi [3] is also well known and studied the

M. Khodorkovskii (✉) · P. Serdobintsev
Center "Nanobiotechnology", Saint Petersburg State Technical University,
Politechnicheskaya str., 29, 195231 Saint Petersburg, Russia
e-mail: khodorkovskii@mail.ru

P. Serdobintsev
e-mail: serdobintsev@rambler.ru

A. Pastor
Physical Department, Saint Petersburg State University, Universitetskaya emb. 7/9,
199034 Saint Petersburg, Russia
e-mail: pastor273@gmail.com

K. Yamanouchi (ed.), *Progress in Photon Science*, Springer Series
in Chemical Physics 115, DOI 10.1007/978-3-319-52431-3_13

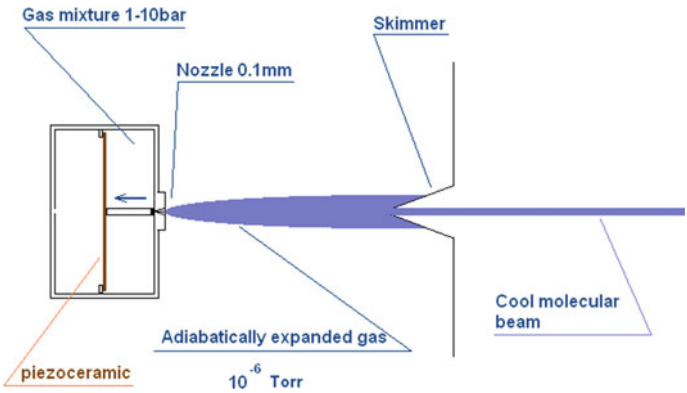

Fig. 13.1 Pulsed supersonic molecular beam

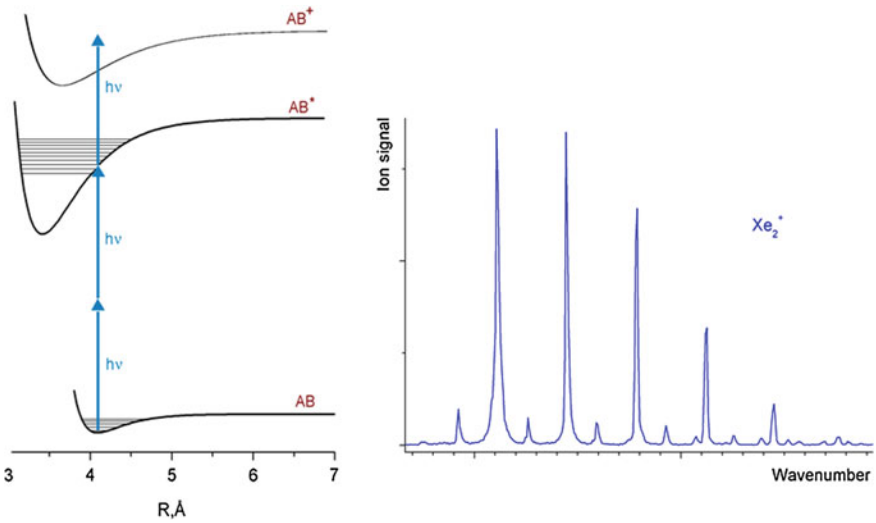

Fig. 13.2 2 + 1 REMPI laser excitation of diatomic molecules

excited states of Xe_2. The excited states of Xe_2 is quite interesting because their potentials are weakly bound and can play a role in lasing, which was suggested by one of our colleagues, Professor Gennady Gerasimov, from State Optical Institute. This weakly bound state can play a role as the upper level of lasing, and the spectral line radiated by this stimulated emission can be quite narrow. It is possible to produce a continuous wave laser in VUV spectral region. So this was an idea from Gennady Gerasimov, and he made this project work. In collaboration with Uppsala University, where I was working too, we built this second setup to study such excited states of heteronuclear molecules like XeKr, in the ESCA Laboratory of Kai Siegbahn.

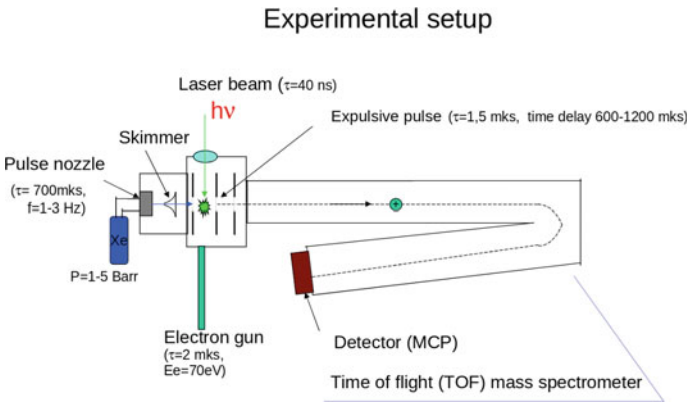

Fig. 13.3 Experimental setup with crossed supersonic flow, laser and electron beam ionized the diatomic molecules. Mass-spectra of ionic component are obtained by time-of flight mass spectrometer

We introduced quite a new method, i.e., 3 + 1 REMPI, to study such heteronuclear molecules as xenon (Xe) and argon (Ar), see Figs. 13.5 and 13.6. The advantages of 3 + 1 REMPI are that we can observe the same transition as in one-photon transition. Three photons are excited, and the fourth photon is ionized like shown in this molecule. We can study the transition by changing angular moment by large amounts. For heteronuclear molecules, we can study simultaneously 2 + 1 REMPI (red line) and 3 + 1 REMPI (blue line) because of the elimination of some selection rules, but 3 + 1 REMPI had some disadvantages that are visible.

The 3 + 1 REMPI lines of this electronic-vibrational band of molecule are very broad and shifted because the intensity that we need to realize 3 + 1 REMPI should be very high and we observed dynamical Stark broadening and shift, which is the optical Stark effect (see Fig. 13.6). This was set up in the ESCA Laboratory of Kai Siegbahn in Uppsala—a tunable dye laser, the light comes from there into the equipment, where there is a homemade TOF, time-of-flight mass spectrometer, and some electron spectrometers, which were not used at that time (see Fig. 13.7). In Fig. 13.8, the recorded 3+1 REMPI spectra are shown. For heteronuclear molecules, XeKr, XeAr, and XeNe, the bands surrounded by a green rectangular frame are those observed by the investigators mentioned above and the other bands are those observed for the first time in our work.

In some of our previous publications on 2 + 1 REMPI and 3 + 1 REMPI pectroscopy of the excited XeKr, we found that peaks in the spectra are broadened and shifted and we identified one very interesting effect. Looking at Fig. 13.9, we observed a molecular KrXe* ionization step, but we observed atomic ions too, and it is very interesting that Kr^+ is twice as intensive as Xe^+. It's very, very exciting and interesting because we need much more energy to ionize Kr than Xe. Moreover, it indicates that it is not such a simple picture. Maybe, it is not 2 + 1, but

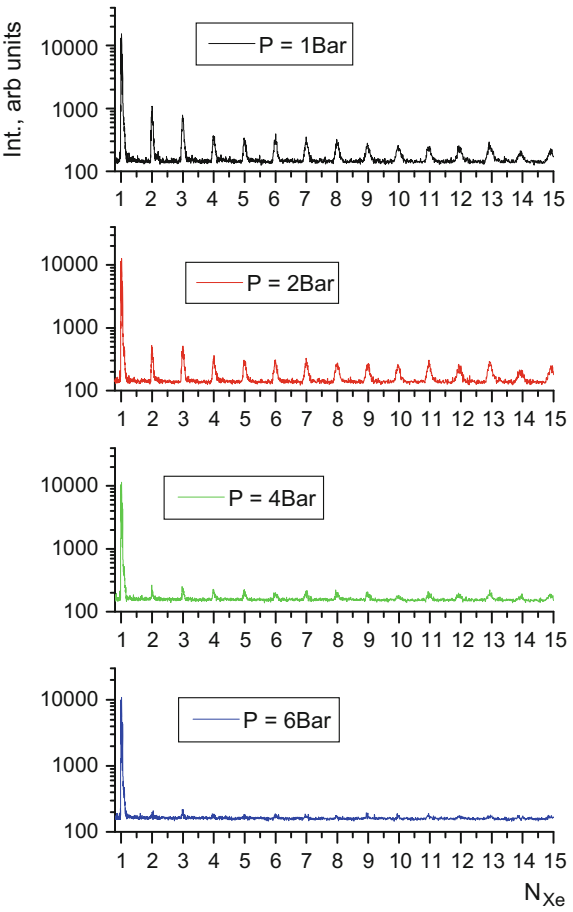

Fig. 13.4 Mass-spectra of ions obtained by electron-impact ionization of supersonic flow at various stagnation pressures

- We can see the same transitions like in case of one photon excitation without using complicate four wave mixing technique.
- Transitions with ΔJ=3 can be seen.
- For heteronuclear molecules we can see some transitions, visible in 2+1 REMPI, because of elimination of some restriction rules.

Fig. 13.5 Advantages of the 3 + 1 REMPI method

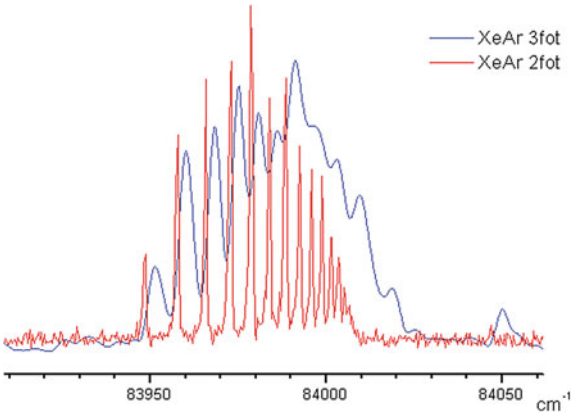

Fig. 13.6 Disadvantages of the 3 + 1 REMPI method

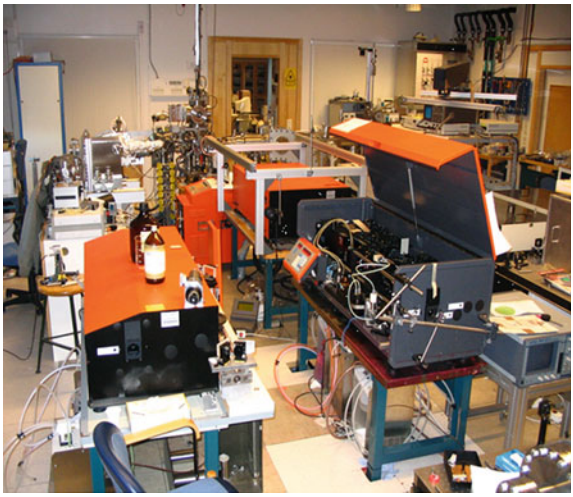

Fig. 13.7 Experimental setup used for REMPI studies in the ESCA lab at the Uppsala University

is 2 + 2 excitation, which means we need two photons in the ionization of Kr to Kr^+. It was an observation which pushed us to introduce electron spectroscopy because, without electron spectroscopy, we cannot understand what happens at the ionization stage.

There are some intermediate states of molecular ions that allows for ionization in two steps, e.g., 2 + 2 let's say, or 3 + 2 here. So we introduced a system at Saint Petersburg State University with a magnetic bottle type time-of-flight electron spectrometer.

Electrons ejected by 2 + 1 or 3 + 1 REMPI are coming into the magnetic bottle, and ions are detected by a small, homemade time-of-flight spectrometer. The main part of our result is achieved by a nanosecond tunable dye laser, pumped by the second harmonic of Nd:YAG laser radiation. Recent results we achieved were done

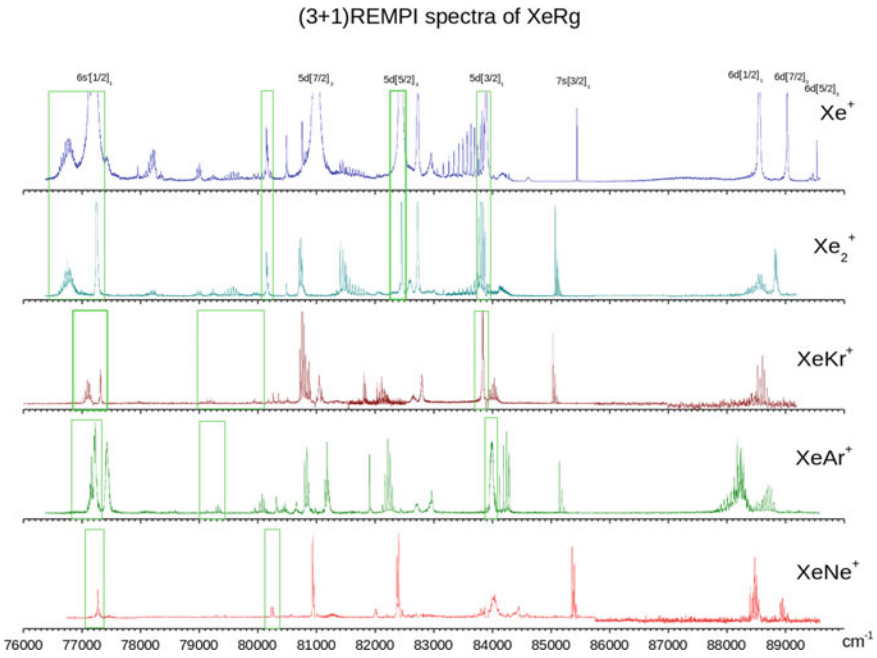

Fig. 13.8 The 3 + 1 spectra of XeRg molecules near the Xe ionization threshold. Some molecular bands (not surrounded by a green rectangular frame) are observed for the first time

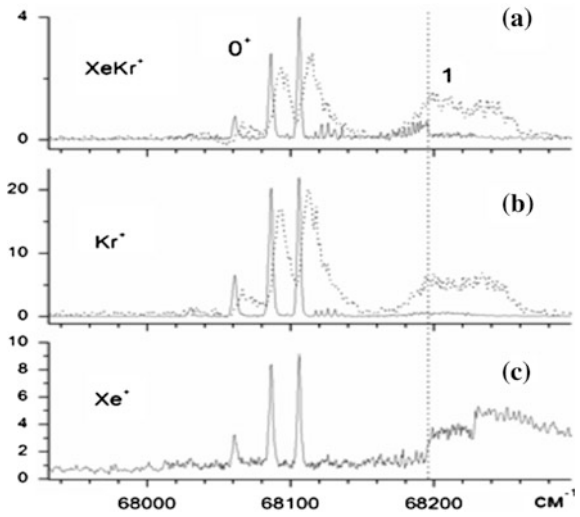

Fig. 13.9 2 + 1 (*solid line*) and 3 + 1 (*dashed line*) of the XeKr molecular bands leading to appearing and the final stage **a** $XeKr^+$ ions, **b** Kr^+ ions, and **c** Xe^+ ions

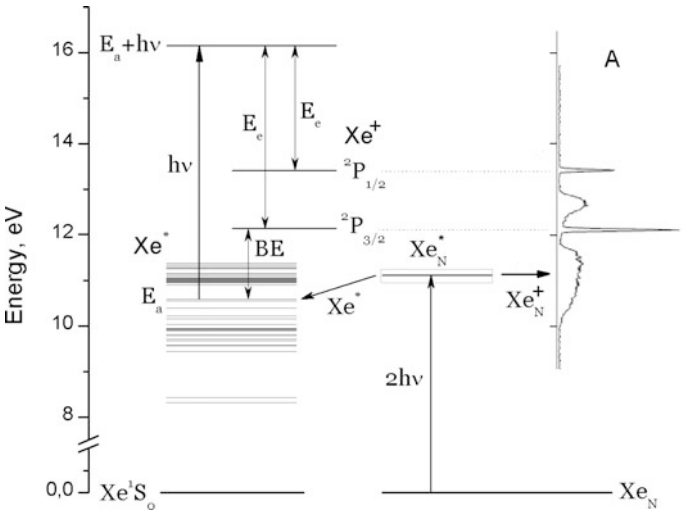

Fig. 13.10 The relaxation channels of two-photon excited Xe_N clusters. The *right side* of the figure corresponds to the two-photon ionization of Xe_N clusters. The *left side* of the figure demonstrates ionization of excited xenon atoms desorbed from the two-photon excited Xe_N clusters. These excited atoms are then ionized by one-photon transition during the same laser pulse. The part "A" is reproduced with permission from Feifel et al., Eur. Phys. J. D 30, 343 (2004). Copyright 2004 The European Physical Journal (EPJ)

with the femtosecond system PULSAR 10. So, concerning the cluster dynamics, we observed a broad band, a two-photon band of cluster excitation, and a two-photon excited cluster that can have two pathways to ionization (see Fig. 13.10). First, one is simply directed to ionization of this cluster. The second one is the process proposed by Verkhovtseva et al. [4] from the Institute of Low Temperature in Kharkov. Those are desorptions of excited atoms of xenon from two-photon excited clusters, and the third one ionized these atoms.

In Fig. 13.11, the energy levels of excited Xe atoms are marked by the red bars. The assignments of the 15 peaks are given in Table 13.1.

The last one, the slide in Fig. 13.12, presents another very interesting process. If the cluster is located in an intensive femtosecond laser field, this cluster can absorb simultaneously two quanta or more. So we get two excited centers within this excited cluster. Let us say two atoms are excited, and then, during the dipole-dipole interaction, these two excited electrons can exchange energy as the first one is coming to the ground state and second one is ionized. This process was proposed by Kuleff et al. [5] in 2010, and they calculated the relaxation time for dipole-dipole interaction, estimated as 2.8 ps. We performed direct measurements, and our measurements of the characteristic time of this process is about 3 ps.

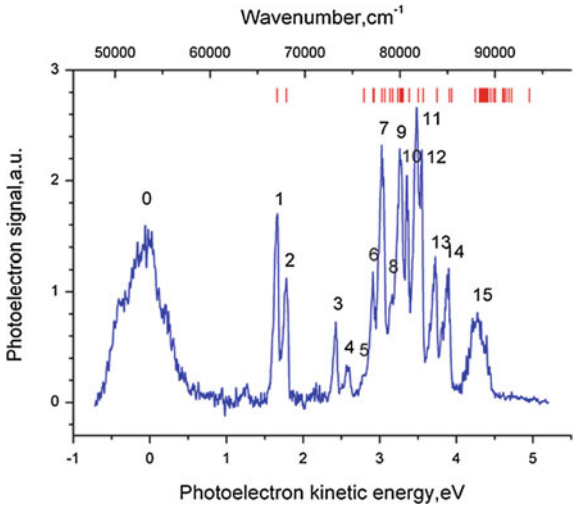

Fig. 13.11 The photoelectron spectrum of xenon clusters excited by laser radiation at the fixed wavelength $h\nu$ = 44,165 cm^{-1} (exciting photon energy −5.476 eV). *Red bars* on the top represent the energy of excited xenon atom levels responsible for production Xe^+ $^2P_{1/2}$ ions (electron peaks 1, 2, and 5–15). The energy of an ejected electron (E_e) is combined with the energy of the corresponding Xe* level (E_{exc}) according to the formula: $E_e = E_{exc} + h\nu - E_{ion}$. The same formula is valid for the peaks 3, 4 but the ionization potential for these is the other ionic state Xe^+ $^2P_{3/2}$

Table 13.1 Kinetic energies and assignments of the recorded photoelectron peaks of xenon clusters

Peak label	KE (eV)	ν (cm^{-1} [27])	Assignment, Xe* → ^2P_J Xe^+
1	1.67	67,067.547	Xe* $6s[3/2]^0_2 \rightarrow {}^2P_{3/2}$ Xe^+
2	1.79	68,045.156	Xe* $6s[3/2]^0_1 \rightarrow {}^2P_{3/2}$ Xe^+
3	2.43	83,889.971	Xe* $5d[3/2]^0_2 \rightarrow {}^2P_{1/2}$ Xe^+
4	2.60	85,188.777	Xe* $7s[3/2]^0_2 \rightarrow {}^2P_{1/2}$ Xe^+
		85,440.017	Xe* $7s[3/2]^0_1 \rightarrow {}^2P_{1/2}$ Xe^+
5	2.80	76,196.767	Xe* $6s'[1/2]^0_0 \rightarrow {}^2P_{3/2}$ Xe^+
6	2.91	77,185.041	Xe* $6s'[3/2]^0_1 \rightarrow {}^2P_{3/2}$ Xe^+
		77,269.145	Xe* $6p[3/2]_1 \rightarrow {}^2P_{3/2}$ Xe^+
7	3.03	78,119.798	Xe* $6p[5/2]_2 \rightarrow {}^2P_{3/2}$ Xe^+
		78,403.061	Xe* $6p[5/2]_3 \rightarrow {}^2P_{3/2}$ Xe^+
8	3.16	78,956.031	Xe* $6p[3/2]_1 \rightarrow {}^2P_{3/2}$ Xe^+
		79,212.465	Xe* $6p[3/2]_2 \rightarrow {}^2P_{3/2}$ Xe^+
9	3.28	79,771.267	Xe* $5d[1/2]^0_0 \rightarrow {}^2P_{3/2}$ Xe^+
		79,986.618	Xe* $5d[1/2]^0_1 \rightarrow {}^2P_{3/2}$ Xe^+
		80,118.962	Xe* $6p[1/2]_0 \rightarrow {}^2P_{3/2}$ Xe^+
		80,196.629	Xe* $5d[7/2]^0_4 \rightarrow {}^2P_{3/2}$ Xe^+

(continued)

Table 13.1 (continued)

Peak label	KE (eV)	v (cm^{-1} [27])	Assignment, Xe* → ^2P_J Xe^+
		80,322.746	Xe* $5d[3/2]^0_2$ → $^2P_{3/2}$ Xe^+
10	3.36	80,970.438	Xe* $5d[7/2]^0_3$ → $^2P_{3/2}$ Xe^+
11	3.48	81,925.514	Xe* $5d[1/2]^0_2$ → $^2P_{3/2}$ Xe^+
12	3.55	82,430.204	Xe* $5d[5/2]^0_3$ → $^2P_{3/2}$ Xe^+
13	3.73	83,889.971	Xe* $5d[3/2]^0_1$ → $^2P_{3/2}$ Xe^+
14	3.90	85,188.777	Xe* $7s[3/2]^0_2$ → $^2P_{3/2}$ Xe^+
		85,440.017	Xe* $7s[3/2]^0_1$ → $^2P_{3/2}$ Xe^+
15	4.23	87,927.131	Xe* $7p[1/2]_1$ → $^2P_{3/2}$ Xe^+ and other neighboring states

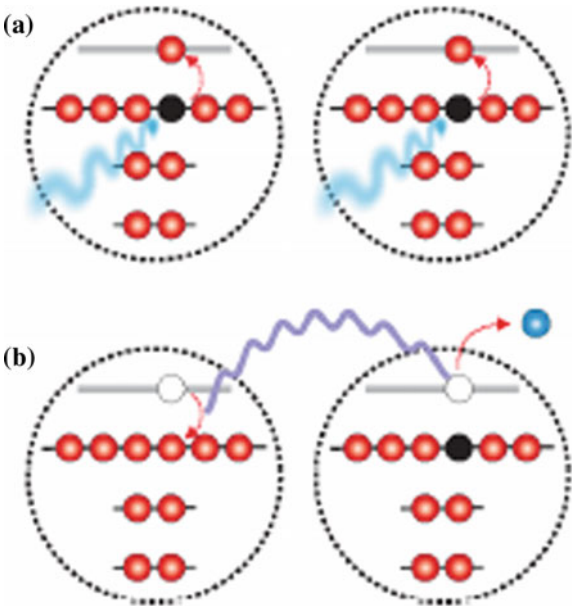

Fig. 13.12 Dipole–dipole interaction of the two excited centers within the cluster leading to an ultrafast electronic decay in multiply excited clusters

References

1. P.M. Dehmer, S.T. Pratt, J.L. Dehmer, J. Chem. Phys. **91**, 2593 (1987)
2. X.K. Hu, D.M. Mao, Y.J. Shi, S.S. Dimov, R.H. Lipson, J. Chem. Phys. **109**, 3944 (1998)
3. C.D. Pibel, K. Ohde, K. Yamanouchi, J. Chem. Phys. **105**, 1825 (1996)
4. E.T. Verkhovtseva, E.A. Bondarenko, Y.S. Doronin, Low Temp. Phys. **30**, 34 (2004)
5. A.L. Kuleff et al., Phys. Rev. Lett. **108**, 043004 (2010)

Chapter 14
Broadband Electromagnetic Wave Emission from an Atomic Cluster Plasma Produced by Femtosecond Laser Pulses: From X-Ray to Terahertz Wavelengths

Alexander Shkurinov

14.1 Introduction

Simultaneous generation of intensive pulsed electromagnetic radiation with various different wavelengths is a very important subject of research now. One of the prospective problems where such kinds of radiation may be applied is a pump-probe experiment in which one pulse excites the system under study and the other pulse probes it in order to deliver the required information about it. Such experiments using the terahertz radiation are already planned in laboratories in the United States and Japan as well as in Russia. For such experiments it is necessary to produce not only terahertz wavelength but several electromagnetic beams with different wavelengths, several pulses of electromagnetic radiation of different pulse durations, delayed relative to each other. The main aim of the present work is to progress to the field of the generation of multiwavelength high power radiation, including the terahertz waves.

The motivation of our work may be expressed as to develop the methods of generation of intense sub-picosecond pulses in the spectral range from X-ray up to terahertz (0.1–10 THz). There are several main reasons for that:

- Commercially available sources of femtosecond laser pulses with energies of mJ/pulse are very attractive for applications to develop efficient nonlinear emitters of intense sub-picosecond pulses in the wide spectral range.
- Solid-state optoelectronic emitters (e.g., semiconductors, nonlinear crystals) that are conventional for pulsed THz generation reach a saturation (or damage) threshold under excitation with high-power femtosecond laser pulses. Moreover,

A. Shkurinov (✉)
Department of Physics and International Laser Center, Lomonosov Moscow State University, Leninskie Gory, Moscow 119992, Russia
e-mail: ashkurinov@gmail.com

K. Yamanouchi (ed.), *Progress in Photon Science*, Springer Series in Chemical Physics 115, DOI 10.1007/978-3-319-52431-3_14

the achievable bandwidth is limited not only by the duration of the input optical pulse, but also by the carrier dynamics or phase-matching requirements.
– High-temperature plasmas initiated by irradiation of the target with high-power femtosecond laser pulses (10^{15}–10^{16} W/cm^2) are sources of high-energy particles and possess strong nonlinear optical properties. Moreover, they are sources of electromagnetic radiation in a wide range of wavelengths and intensities.

In fact, the first idea that a free moving electron in plasma may emit the terahertz radiation, was put forward by Professor Askaryan from P.N. Lebedev Physics Institute, U.S.S.R. Academy of Sciences in 1962 [1]. He published a paper in 1962 in which he stated that "… the plasma has a low threshold of nonlinearity and its dispersion may be changed by magnetic fields. The frequency range of radiation may be fairly large, i.e. from radio and light waves up to X-rays".

However, the laser pulse as a source of THz radiation was not very useful until the fundamental publications of D.H. Auston. In 1984, he published a paper about the experiments of the terahertz wave radiation and rectified radiation in semiconductor devices. Since that time, there is real competition between two ideas: electrons in semiconductors and free electrons in plasma. In 1991, Professor Falcone [2] published a paper in which he reported that he had measured the emission of the terahertz radiation from the laser-breakdown plasma created by a femtosecond laser pulse. In this paper, it is shown that a strong emission of pulsed radiation at terahertz frequencies was observed from the resulting plasmas. Results indicate that radiative processes in such a plasma are driven by ponderomotively induced space-charge fields. However, not only plasma may be a source of THz radiation, but also a non-ionized gas consisting of neutral molecules [3]. In this paper, the authors describe a new four-wave rectification method of four-wave mixing for the generation of intense, ultrafast terahertz (THz) pulses from gases.

14.2 THz Generation from Clusters

An important effect which limits optical to terahertz conversion efficiency is a screening of terahertz radiation in a dense plasma. With the use of terawatt-power laser systems very high light fields can be obtained and high electron density in the laser-produced plasma results in screening of the low-frequency terahertz radiation. Another work that we use was published by Professor M. Hangyo from Osaka University [4]. In his experiments, he studied the generation of terahertz radiation from the cluster beam, and he observed more than a one-order increase of magnitude of the terahertz pulse energy as compared to that in the bulk gas medium. Perhaps this was due to a decrease of the screening of terahertz waves by the surrounding plasma. He also observed that the spatial distribution of the output emission has conical structure, and there is no forward emission.

The main goal of the present work is observation of the simultaneous generation of X-ray and terahertz pulses produced by the laser-cluster interaction in the case of two-frequency excitation.

The clusters were formed in the supersonic jet that is shown in Fig. 14.1. There is no distraction of the target after the irradiation, and, since the target recovers its properties from each act of interaction with the laser pulse, there is no accumulation of electron density between pulses. There are several parameters which are important for the formation of clusters: temperature and pressure of the gas and some parameters of the nozzle. In our experiments, we used argon clusters. In this case, we achieve a number of atoms in the cluster, approximately 10^6, and the radius of the cluster is approximately 22 nm. If we talk about the mechanism that could be used to describe the electromagnetic-wave emission, firstly we need to take into account ionization because, after the pulse strikes the cluster, there occurs immediately ionization of the atoms inside, and many electrons should be in a localized area. Then, there follows the heating and expansion processes (Fig. 14.2). In the present work, we assume a very simple model of expansion of the cluster and will show that it agrees well with the experiment. When the laser frequency matches a Mie-resonant frequency, this results in the high absorption of the pulse energy. The model that we used to describe the terahertz generation is quite simple. During laser-cluster interaction, some portion of the electrons are expelled from the cluster, and expansion of the charged cluster results in emission of the electromagnetic waves. If we make a Fourier transform of the temporal solution of the cluster expansion, we can estimate the frequency spectrum of the electromagnetic waves. Moreover, we can find that the maximum of the spectrum is near one terahertz.

Scheme of our experimental setup is shown on the Fig. 14.3. We used a terawatt laser system with following parameters: maximum pulse energy 25 mJ, pulse duration 50…1000 fs, central wavelength 810 nm, beam diameter 1.5 mm, repetition rate 10 Hz. Two color excitation scheme was used: laser beam combined the fundamental frequency and the second harmonic, and thus we had $\omega + 2\omega$

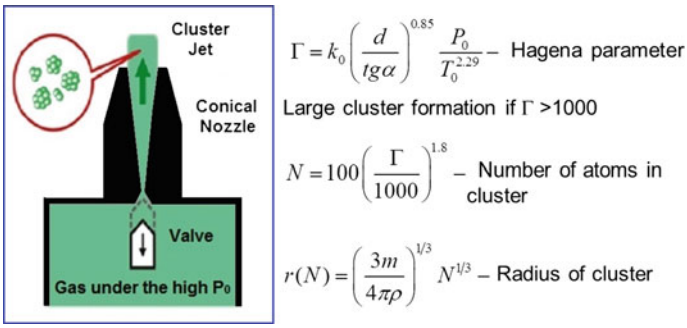

Fig. 14.1 Generation of clusters using a conical nozzle

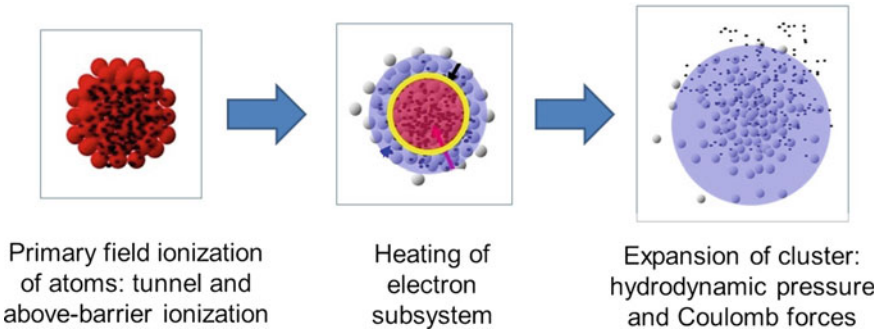

Fig. 14.2 Mechanism of the cluster expansion

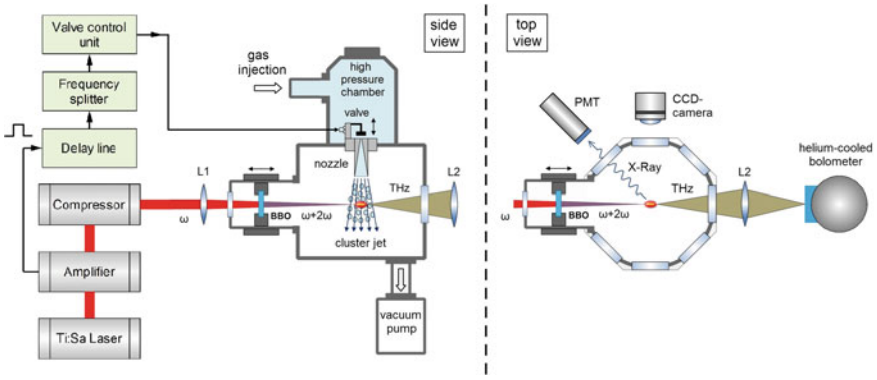

Fig. 14.3 Experimental setup for the generation of THz waves and X-rays using clusters

interaction in the cluster jet. We used the liquid-helium cooled bolometer to measure the intensity of the THz emission.

The results of the experiments are shown on the Figs. 14.4–14.6. THz and X-Ray signals as a function of the gas pressure inside the jet are shown on the Fig. 14.4. We observed that THz emission intensity is saturated at pressure above 7–8 atm, unlike the X-Ray signal. If we change the pressure, we may also change the relative intensity of the radiations. One of the problems of the experiment is the low concentration of clusters relative to the buffer gas because only 10% normally argon gas should be presented as a cluster form, but 90% is simply buffer gas. Scaling of the THz signal with excitant laser pulse energy is presented on the Fig. 14.4. As can be seen from the graph, intensity of the THz emission grows nonlinearly without saturation with increase of the laser pulse energy up to its maximum value of 25 mJ (which corresponds to the vacuum intensity $\sim 10^{17}$ W/cm^2).

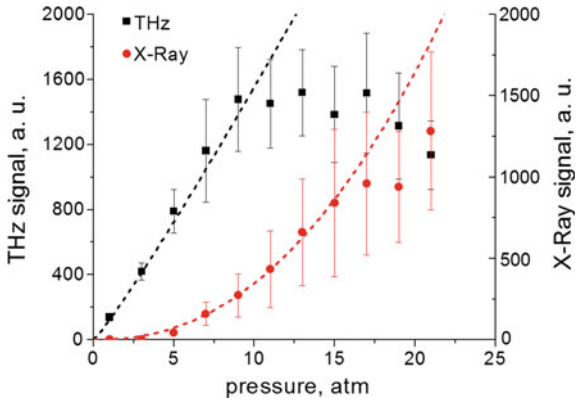

Fig. 14.4 THz and X-ray signal intensities as a function of the stagnation pressure at the nozzle

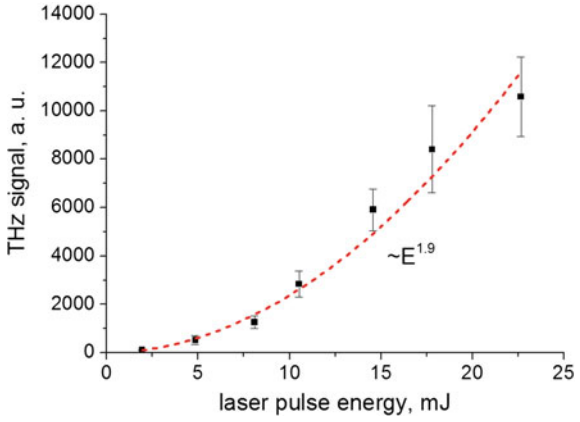

Fig. 14.5 THz signal as a function of the laser pulse energy

Also we studied variation of THz and X-Ray signals during evolution of the cluster jet. In our experiments laser pulse was delayed relative to the opening of the valve and delay time could be varied (valve opening duration was 0.4 ms). We measured how THz and Xray yield scales with delay time (see Fig. 14.6). Both THz

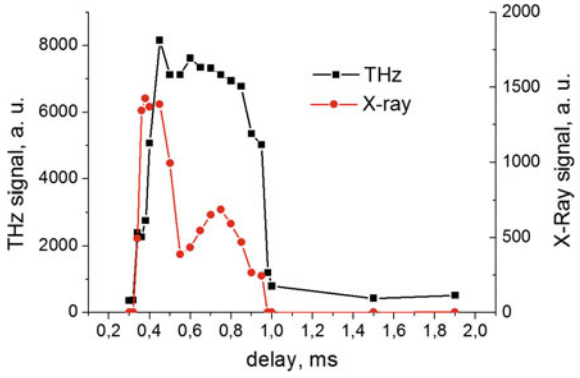

Fig. 14.6 THz and X-ray signals as a function of the time delay between laser pulse and the opening of the nozzle valve

and X-Ray signal appears at delay time above 0.3–0.4 ms: this time is required for clustering of gas flow and its propagation to the interaction point. Maximum of X-Ray yield is achieved at 0.4–0.45 ms delay, while the THz signal is nearly unchanged in the range of 0.45…0.8 ms.

14.3 Conclusion

In conclusion, we have successfully observed simultaneous generation of X-ray and THz pulses in the laser-cluster interactions. Two color (ω+2ω) excitation scheme of the cluster jet was used in our experiments. We have found that THz yield grows without saturation with increase of the excitant laser pulse energy up to its maximum value of 25 mJ. The experimental conditions for the effective generation of the X-ray and THz radiation are different.

References

1. G.A. Askar'yan, JETP **15**(5), 943 (1962)
2. H. Hamster, A. Sullivan, S. Gardon, W. White, R.W. Falkone, Phys. Rev. Lett. **71**(17), 2725 (1993)
3. R.M. Hochstrasser, Opt. Lett. **25**(16), 1210 (2000)
4. F. Jahangiri, M. Hashida, T. Nagashima, S. Tokita, M. Hangyo, S. Sakabe, Appl. Phys. Lett. **99**, 261503 (2011)

Part VI
New Methods in Spectroscopy

Chapter 15
High-Resolution Femtosecond Comb Spectroscopy

Sergey Pulkin

Today, I will talk about non-linear comb spectroscopy. What are the advantages of comb spectroscopy? They span a very wide spectrum, making simultaneously possible detection of a large number of spectral lines, with high-field intensity, high resolution, and high spectral brightness. For example, if you use a usual Fourier spectrometer, you will spend a few hours to make some spectrum, but, in the case of comb spectroscopy, you can make it in a matter of seconds. The spectral resolution of normal linear comb spectroscopy is restricted by inhomogeneous (Doppler) broadening. The new field we are starting is non-linear comb spectroscopy—Doppler free comb spectroscopy. Comb spectroscopy and holographic microscopy (CARS), i.e., an optical clock with comb spectroscopy, are the other fields of our interest. I will also talk about Doppler-free comb spectroscopy today.

What is the comb? Its research began in the early part of the twenty-first century. Comb was obtained from the femtosecond train that passed from the micro-structured fiber, and broadening of spectrum took place. We can see the spectrum from the ultraviolet to the red side, and there was a revolution in the measurement of optical frequency. Now, it is possible to measure optical frequency directly, not using the frequency chain as before, and this revolution was made by two scientific groups: Prof. John Hall's group and Prof. Hänsch's group.

John Hall won the Nobel Prize in 2002. His group worked in the field of direct optical-frequency measurements. I worked with some of people e.g., Professor Yoon who is affiliated with a Korean university now. When I began to work with him in 1998, we started to study quantum mechanics. We wrote several interesting papers about polychromatic field interactions with atoms. After that, he defended a PhD thesis and John Hall invited him to his lab where he worked very effectively on frequency measurements. Our paper on theoretical analysis of resonances in

S. Pulkin (✉)
Department of General Physics 1, Physical Faculty, Saint-Petersburg State University, Universitetskaya nab., 7-9, Saint-Petersburg 199034, Russia
e-mail: spulkin@mail.ru

K. Yamanouchi (ed.), *Progress in Photon Science*, Springer Series in Chemical Physics 115, DOI 10.1007/978-3-319-52431-3_15

polarization spectrum of a two-level atom is the basis of our future work. What does it mean?

If we have a two-level system and if we have a comb, here you have no comb (only five components), but it is enough when one understands how a comb works. If we have polychromatic fields, then the two-level system became a multi-level system.

There are multi-, sub-, and quasi-energy levels, and there are some manifolds of quasi-energy levels. Transitions between manifolds are possible, or, in a similar manner, intersections between these quasi-energy levels take place. The intersections give you the position of new components of polarization in spectrum. The polarization is a source of new waves, and we can see in the polarization spectrum that there are the new components of the frequency. This problem is possible to solve analytically, and, if it is solved, we can solve the system of equations for the density matrix. Then we can see the analytical results. For comb, it is possible to have components of fields, and what is the structure of polarization?

We can analyze, from the form of the denominator, the conditions of resonances. We named them as "super-narrow resonances". The main idea behind using it for Doppler-free comb spectroscopy is replacing the detuning δ by kv, i.e., the product of the wave number k and the velocity v.

There is an interaction between counter-propagating waves and a medium of moving atoms. Each molecule moving with velocity v "sees" not one field, but two fields, which detune one from each other at the frequency of $2kv$. The first field with frequency ω_1 always is in resonance at the transition frequency; then, at the frequency $\omega_{21} + 2kv$ in the frame of the moving atom coordinate, the second field acts. If both fields are strong, the system converts from two-level to multi-level, one consisting of manifold quasi-energy levels. The transitions between quasi-energy levels are possible [1]. Two manifolds shifted to frequency $2kv$ arise in the case of moving atoms with velocity v. The narrow coherent peaks in the polarization and susceptibility spectrum arise. This work is a prolongation of our previous work [2], where we considered the interaction of two counter propagating waves with a two-level system—a bi-harmonic (strong modulated) and a weak counter-propagated monochromatic field. It was shown that, in the polarization spectrum, the additional narrow resonances arise at the frequencies that satisfy the conditions of multi-photon resonances. We can explain the result of present research activities using results of papers [1, 2]. The possibility of Doppler-shift compensation was firstly proposed in our previous work [3], when direct integration of density-matrix equations was made. We showed there that the mechanism of Doppler-shift compensation in two-photon comb spectroscopy and the method described here are different. In the case of two-photon comb spectroscopy, one photon comes from the low-frequency side of the comb spectrum with frequency $\omega_0 - \Omega$, and second photon with frequency $\omega_0 + \Omega$ comes from the high-frequency side. The effective two-photon transition at transition frequency $\omega_{21} = 2\omega_0$, where ω_0 denotes the carrier-laser frequency, which coincides with the center of Doppler counter, will arise for the group of atoms when the resonant condition is satisfied: $kv = \Omega$. (Ω—is the frequency interval between comb components). The other cause

is in the case of counter-propagated combs acting near one-photon transitions [3]. The effective interaction for multi-photon transitions between quasi-energy levels at the frequency of a one-photon transition takes place for groups of atoms with velocity v. This group of atoms interacts effectively with comb components at the frequencies $\omega_0 - p\Omega$ and $\omega_0 + n\Omega$. (n and p are integers and zero) For $n = -p$ and when $2kv = n\Omega$.

Thus, as it follows from [3], the physical nature of the narrow peaks in the existing multi-photon transitions between manifolds of quasi-energy levels arises for various groups of atoms moving with velocities that satisfy the resonant conditions $2kv = (n + l)\Omega$, where n, l are integers and Ω is the frequency difference between comb teeth.

There is a partial case when the strong modulated field and counter-propagating weak-probe field act on the Doppler-broadened medium. This is realized in the method of modulated transfer spectroscopy (MTS) [4, 5]. Thefour-wave mixing in a medium leads to the emergence of modulation of the probe field on the exit of cells with atoms. The order of nonlinearity is determined in this case by nonlinear susceptibility $\chi(3)$. The condition of phase synchronism is satisfied in this case. The condition of phase control and synchronism is necessary to satisfy the conditions for multi-photon interactions in our case, too.

The two-row Fourier-expansion method for density matrix elements [6] for the case of moving atoms was applied for solving the density-matrix equations. My student Alexey Kalinichev solved analytically the density-matrix equations for two-level moving atoms in counter-propagating comb fields:

The field member has the form:

$$E(t) = \frac{1}{2}\left\{W_{1m}e^{i(\omega_{s0}-kv)t} + W_{2m}e^{i(\omega_{p0}+kv)t} + c.c\right\} \tag{15.1}$$

where, W_{1m}, W_{2m}—the comb amplitudes of counter-propagating waves:

$$W_{1m} = \sum_{m=-n}^{n} E_{1m}e^{im\Omega t}, \tag{15.2}$$

$$W_{2m} = \sum_{m=-n}^{n} E_{2m}e^{im\Omega t}, \tag{15.3}$$

where Ω—frequency differences between neighboring comb components.

The density-matrix element in the rotation wave approximation has the form:

$$\rho_{12} = \tilde{\rho}_{12}e^{i(\omega_{p0}+kv)t} \tag{15.4}$$

The density matrix equations are (we omit tilde for slow parts of density matrix elements):

$$\frac{\mathrm{d}\rho_{22}}{\mathrm{d}t} = \lambda_2 - \gamma_2\rho_{22} + i\frac{d}{2\hbar}\left((W_{1m}\mathrm{e}^{i(-2kv)t} + W_{2m})\tilde{\rho}_{21} - (W_{1m}^{*}\mathrm{e}^{i2kvt} + W_{2m}^{*})\tilde{\rho}_{12}\right) \tag{15.5}$$

$$\frac{\mathrm{d}\tilde{\rho}_{21}}{\mathrm{d}t} + (i(\delta - kv) + \gamma_{21})\tilde{\rho}_{21} = i\frac{d}{2\hbar}(W_{1m}^{*}\mathrm{e}^{i2kvt} + W_{2m}^{*})(\rho_{22} - \rho_{11}) \tag{15.6}$$

$$\frac{\mathrm{d}\rho_{11}}{\mathrm{d}t} = \lambda_1 - \gamma_1\rho_{11} - i\frac{d}{2\hbar}\left((W_{1m}\mathrm{e}^{i(-2kv)t} + W_{2m})\tilde{\rho}_{21} - (W_{1m}^{*}\mathrm{e}^{i2kvt} + W_{2m}^{*})\tilde{\rho}_{12}\right) \tag{15.7}$$

We used the two-row Fourier-expansion method for density matrix elements [6] for the case of moving atoms. Let us write this as an expansion as it was done in [7]:

$$\rho_{ii} = \sum_{l=-\infty}^{\infty}\sum_{p=-\infty}^{\infty}\rho_i^{(l,p)}\mathrm{e}^{ilkvt}\mathrm{e}^{ip\Omega t} \tag{15.8}$$

$$\rho_{22} - \rho_{11} = \sum_{l=-\infty}^{\infty}\sum_{p=-\infty}^{\infty}d^{(l,p)}\mathrm{e}^{ilkvt}\mathrm{e}^{ip\Omega t} \tag{15.9}$$

From these equations, using the condition of reality of diagonal elements $d^{(-l,-p)} = (d^{(l,p)})^{*}$, we obtain a relation in which as unknown's values remain $d^{(l,p)}$—Fourier components of population differences.

As can be seen from this expression, only even members $d^{(l,p)}$ are interconnected. To find $d^{(l,p)}$, it is necessary to solve an equation of the form **Ad = G**. In this equation, the vector **d** is given by the expression:

$$\mathbf{d} = \begin{pmatrix} d^{(-k_1,-k_2)} \\ \vdots \\ d^{(-k_1,k_2)} \\ d^{(-k_1+2,-k_2)} \\ \vdots \\ d^{(0,-1)} \\ d^{(0,0)} \\ d^{(0,1)} \\ \vdots \\ d^{(k_1-2,k_2)} \\ d^{(k_1,-k_2)} \\ \vdots \\ d^{(k_1,k_2)} \end{pmatrix} \tag{15.10}$$

A matrix **A** is a matrix of coefficients as before with the appropriate components $d^{(l,p)}$. Vector **G** is a column vector $G_i = \bar{N}\delta_{i,((2k_1+1)(2k_2+1)+1)/2}$ with $(2k_1+1)(2k_2+1)$

We write the atomic polarization in the form:

$$\tilde{\rho}_{21} = \sum_{l=-\infty}^{\infty}\sum_{p=-\infty}^{\infty} r^{(l,p)} e^{ilkvt} e^{ip\Omega t}, \tag{8.11}$$

$$\tilde{\rho}_{12} = \sum_{l=-\infty}^{\infty}\sum_{p=-\infty}^{\infty} r^{*(-l,-p)} e^{ilkvt} e^{ip\Omega t}. \tag{8.12}$$

Substituting these expressions in our system of equation and equating coefficients of like powers, we find:

$$\begin{aligned} d^{(l,p)} &= \bar{N}\delta_{l,0}\delta_{p,0} + i\frac{d}{2\hbar}D_1^{(l,p)} \\ &\times \left(\sum_{m=-n}^{n} E_{1m} r^{(l+2,p-m)} + \sum_{m=-n}^{n} E_{2m} r^{(l,p-m)} \right. \\ &\left. - \sum_{m=-n}^{n} E_{1m} r^{*(-l+2,-p-m)} - \sum_{m=-n}^{n} E_{2m} r^{*(-l,-p-m)} \right) \end{aligned} \tag{8.13}$$

$$r^{(l,p)} = i\frac{d}{2\hbar}D_2^{(l,p)} \left(\sum_{m=-n}^{n} E_{1m} d^{(l-2,p+m)} + \sum_{m=-n}^{n} E_{2m} d^{(l,p+m)} \right) \tag{8.14}$$

Here we introduce the function

$$D_1^{(l,p)} = \frac{1}{2}\left(\frac{1}{i(p\Omega + lkv) + \gamma_2} + \frac{1}{i(p\Omega + lkv) + \gamma_1} \right) \tag{8.15}$$

$$D_2^{(l,p)} = \frac{1}{i(\delta + kv(l-1) + p\Omega) + \gamma_{21}} \tag{8.16}$$

$$\begin{aligned} P(t) &= d(\rho_{21} + c.c.) \\ &= d\left(\sum_{l=-\infty}^{\infty}\sum_{p=-\infty}^{\infty} r^{(l,p)} e^{ilkvt} e^{ip\Omega t} e^{i\left(\omega_{p0} + kv\right)t} + c.c. \right) \end{aligned} \tag{8.17}$$

Then, for the polarization components at the frequency $\omega_{p0} + kv$, the condition $lkv + p\Omega = 0$ must be satisfied. This condition is satisfied when $l = 0$ and $p = 0$. So, in order to find the polarization at the frequency of interest, $r^{(0,0)}$ must be found.

In an isotropic medium, the direction of the polarization vector of the medium coincides with the orientation of the field, and, for the susceptibility, it can be written:

$$\chi_{\omega_{p0}} = -\frac{P(\omega)d}{\Omega_{\omega_{p0}}\hbar} \tag{8.18}$$

The absorption coefficients of the probe-field component are determined by the imaginary part of the susceptibility:

$$\frac{K_{\omega_{p0}}}{K_\Lambda} = -\frac{2\omega_{21}d}{K_\Lambda} Im\left(\chi_{\omega_{p0}}\right) \tag{8.19}$$

where $K_\Lambda = \frac{\omega_{21}d^2}{\hbar\gamma\Gamma}$—the linear absorption coefficient at the center of the line in the absence of a strong field ($\gamma = \Gamma = 0.5\gamma_{21}$).

We scanned the carrier frequency ω_{p0} and found that the dependence of the absorption coefficient is from the detuning.

Figure 15.1 is obtained when the shape of the inhomogeneous counter is rectangular and the width of the counter is equal to 10 γ_{12}. When the shape of the Doppler counter is the Gaussian function, Fig. 15.2 is obtained. The width of Doppler counter in this case is 10 γ_{12}.

For the case of strong fields the field broadening of homogeneous line was found. In an absorption spectrum, the dips with homogeneous width of the line broadened by a strong field are shown in Fig. 15.2. The contrast of the homogeneous dip for strong fields is larger than for the weak fields.

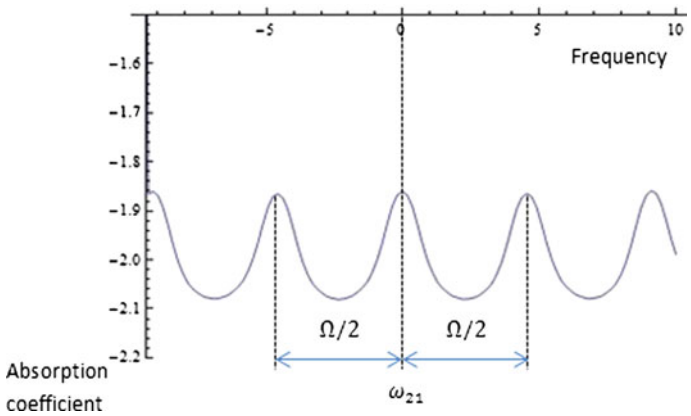

Fig. 15.1 Absorption coefficient in the case of inhomogeneous broadening with rectangular distribution on the velocity. The width of counter is equal to 10 γ_{12}. $E_{1m} = E_{2m} = 1, \Omega = 10, n = 5$

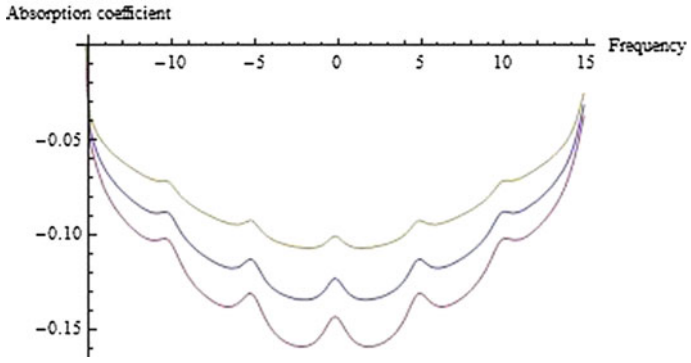

Fig. 15.2 Absorption coefficient in the case of Doppler broadening ($E_{1m} = E_{2m} = 1; 0.7; 0.5, \Omega = 10, n = 5$). The amplitude of the field decreased from the *lower* to the *upper curves*. The width of the Doppler counter for this case is equal to 10 γ_{12}

We checked the validity of proposed approach by using direct numerical integration of density matrix equations [3] and found excellent coincidence.

It is shown that the spectral range is defined by the spectral range of radiation of the comb generator. The spectral range of the comb generator can be made wide enough for simultaneous registration of a considerable quantity of homogeneously-widened spectral lines. It is the big advantage of the proposed method of comb spectroscopy in comparison with existing methods of Doppler-free spectroscopy.

All the components of the spectrum of a mixture of gases appear in the spectrum of polarization simultaneously. Doppler shifts that satisfy the conditions of resonance, i.e., the Doppler shift must be a multiple of the intermodal frequency (difference between adjacent frequency-comb spectrum) or its subharmonics. Thus, the proposed study will have all the advantages of Doppler-comb spectroscopy, e.g., high brightness, simultaneous recording over a wide spectral range of a large number of lines of various gases, and (the new thing) the resolution within the Doppler contour. These resonances “draw” thesusceptibility spectrum when the carrier frequency of the probe comb is scanned along the Doppler shape.

These are the field members, and this is the comparison between the numerical and analytical solution. The theory is right if the equation is right and it works well.

We can use this result for the measurements of components, i.e., the molecular structure of biomarkers, but how does one increase resolution? If we decrease pressure, then we can see, after decreasing the collisional broadening, Doppler broadening and, after interactions with counter-propagating comb, one can see the natural shape. We decrease the pressure by a factor of 100, but the absorption coefficients do not change so large. It is a well-known phenomenon that, when the collisional shape is larger than the natural one, then the amplitude is not dependent on concentration.

The concentration of nitric oxide is 20 ppb, which means a very small concentration. The concentration for other components is very large. For example, for high pressure, the broadening is mainly determined by the collisional broadening: if we decrease the pressure, then we can resolve the natural line. All these parameters are available for prospective experiments, and we will try to perform them.

References

1. T.H. Yoon, S.A. Pulkin, J.R. Park et al., Phys. Rev. A **60**, 605 (1999)
2. S.A. Pulkin, T.H. Yoon, A.I. Kuzmin, S.V. Uvarova, Opt. Spectr. **105**, 288 (2008)
3. S.A. Pulkin, K. GuangHoon Kim, U.K. Kang, V. Arnautov, S.V. Uvarova. Am. J. Mod. Phys. **2**(4), 223–226 (2013)
4. J.H. Shirley, Opt. Letters. **7**, 537 (1982)
5. G. Camy, C.J. Borde, M. Ducloy, Opt. Com. **41**, 325 (1982)
6. M.S. Yoon, H.V. Chang, J.R. Lee, Park. Phys. Rev. A **60**, 2547 (1999)
7. S. Stenholm, *Foundations of Laser Spectroscopy* (Wiley, New York, 1984; Mir, Moscow, 1987)

Chapter 16
Laser Synthesis of Ultra-Cold Molecules: From Design to Production

Andrey Stolyarov

16.1 Introduction

I will talk how high-resolution laser spectroscopy and comprehensive deperturbation treatment of the spin-orbit coupled diatomic states can help us assemble diatomic molecules from ultra-cold atoms, and show the practical importance of producing the stable molecular ensembles under low-temperature conditions.

First of all, this leads to a new type of physics since a matter under very-low internal temperature demonstrates the dual "particle-wave" property simultaneously. From the practical view point, if we have got a very cold ensemble of molecules, we deal with very narrow and stable lines. Therefore we have unique opportunity to perform ultimately high-precision energy measurements. In particular, this opens a window to measure possible variations of fundamental physical constants (e.g., a ratio of electron mass to proton mass m_e/m_p and a fine structure constant α) over a cosmologic time scale. Then, of course, we can design a new metrology application: a new standard for time and frequency. This stuff is in progress now. From the chemical viewpoint, we have also new horizons to control a chemical reaction since the kinetic energy of the cold colliding particles is comparable with the energy of the external electro-magnetic field of conventional laboratory strength. So we have a good opportunity to monitor an elastic collision rate or even to change the mechanism of chemical reactions.

The problem now is to produce the ultra-cold molecules in sufficient amounts and to be able to maintain them for a relatively long time. Of course, there are many ways to realize this, and now I just would like to introduce one of them. The general way is to assemble molecules from cold atoms by means of a multi-step optical cycle.

A. Stolyarov (✉)
Department of Chemistry, Lomonosov Moscow State University, GSP-2, Leninskie gory 1/3, Moscow 119991, Russia
e-mail: avstol@gmail.com; avstol@phys.chem.msu.ru

K. Yamanouchi (ed.), *Progress in Photon Science*, Springer Series in Chemical Physics 115, DOI 10.1007/978-3-319-52431-3_16

16.2 Experimental Procedure

So we will start from ultra-cold atoms which already are a common thing in the laboratory. An advantage of the photo-association method is that we already have the colliding particles possessing ultra-low kinetic energy. However, due to cold atom collisions, we deal with the very weak bound and highly excited vibronic molecular states which are not stable. In this case, we have to transfer them to the so-called absolute ground state ($v = 0$ and $J = 0$) which lives much longer than the initial one. The optical transformation is not feasible process, and we have to employ excited states using them as intermediate ones in multi-step excitation and dumping schemes (see Fig. 16.1). Hereafter, I wish to focus on the robrivonic structure of the ground and/or excited states of several alkali dimers.

From atomic physics, we know that the Stimulated Raman Adiabatic Passage (STIRAP) method [1] could be useful for laser *transformation* from the initial level to the excited level (PUMP), and, then, to the ground one (DUMP) with almost 100% efficiency. However, to find out the most efficient STIRAP pathway, we need to know precisely the energy and radiative properties of all the states involved in the cycle.

In order to get the required information, one needs to study first the ground states, which are singlet and triplet sigma states for alkali-metal dimers. Then we can move to the higher-energy region with the eventual aim to investigate excited states as well. Of course, different kinds of spectroscopic data could be useful, and, hence, be welcome. Among them, the comprehensive term value sets come from analyses of laser-induced fluorescence (LIF) spectra (see Fig. 16.2) and the

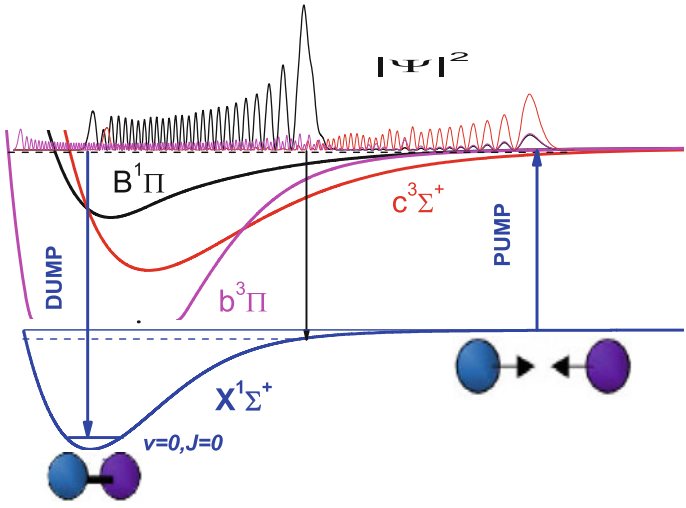

Fig. 16.1 The example of the two-step pump-dump optical cycle used to transform alkali metal pairs to the absolute ground state

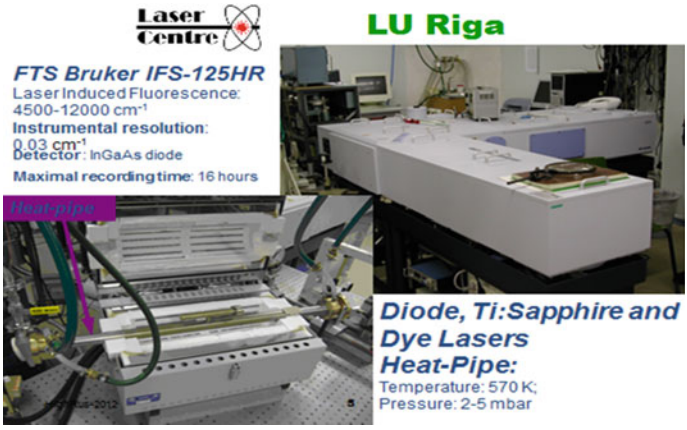

Fig. 16.2 The experimental setup that is exploited in the Laser Center of University of Latvia and Institut für Quantenoptik, Gottfried Wilhelm Leibniz Universität Hannover with outstanding laser facilities combined with very high-resolution Fourier spectrometers. The setup enables one to record LIF spectra with instrumental resolution comparable to Doppler width in the visual and infrared region of spectra [2]

polarization-labelling spectroscopy technique. The high-resolution spectra assignments are apparently very long and hard work, and we try to have close collaboration with many experts in this field to simplify the process.

So what do we expect from the experimental work? We get a spectral database containing robrivonic term values for different states—here are the excited states belonging to the so called spin–orbit A–b complex of NaRb dimer. We have got at our disposal thousands of lines, most of them obtained by the Riga's and Hannover's groups (see Fig. 16.3), some by another one, and we pick up all of them together to analyze. The overall set always is not sufficient to make the total picture because the empirical data set is fragmented, as usual.

16.3 Coupled Channel Deperturbation Analysis

In order to analyze the strongly-perturbed molecular structure, we used the rigorous coupled-channel (CC) method (see Fig. 16.4).

$$\left(-\mathbf{I}\frac{\hbar^2 d^2}{2\mu dR^2} + \mathbf{V}(R;\mu;J;a_p) - \mathbf{I}E_j^{cc}\right)\mathbf{\Phi}_j^{cc} = 0 \tag{16.1}$$

Basically we started from an ab initio calculations that provide us the initial parameters of the potential-energy curve (PEC), transition dipole moments, and the non-adiabatic spin-orbit coupling-matrix elements. Then, we construct the potential-energy matrix, which is an explicit function of the internuclear distance R,

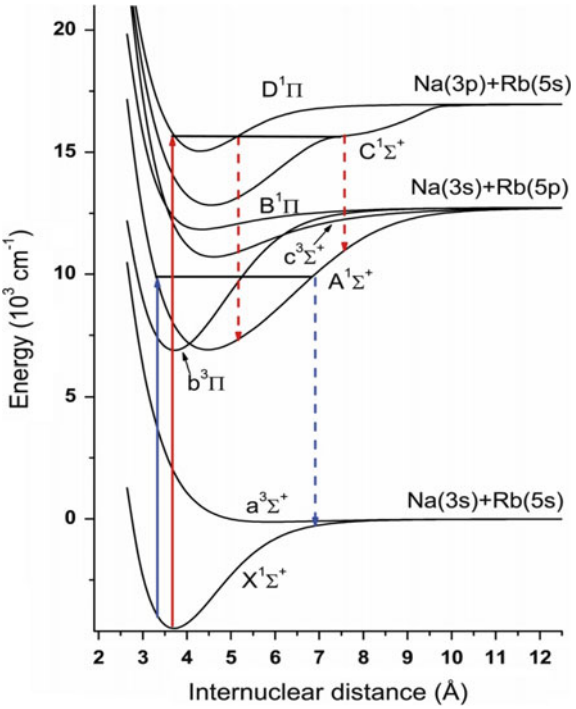

Fig. 16.3 The LIF spectra used to study the spin–orbit A–b complex of a NaRb molecule at the Laser Center of University of Latvia and Institut für Quantenoptik, Gottfried Wilhelm Leibniz Universität Hannover, [2, 3]

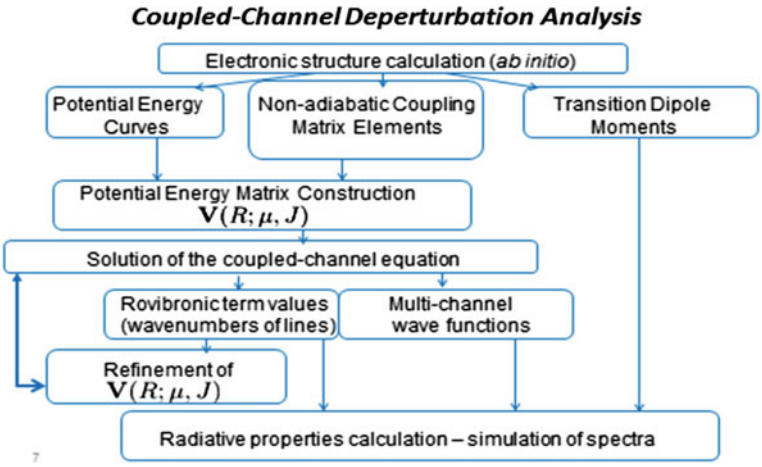

Fig. 16.4 Coupled-channel (CC) approximation used to deperturb the fully mixed (non-adiabatic) diatomic states

rotational quantum number *J,* and reduced mass. We numerically solve the CC equation by homemade program to yield the term values, which can directly compare with their experimental counterparts. The resulting vibrational wave functions are involved in the calculation of radiative properties, such as lifetimes, branching ratios, and Einstein coefficients, which are used for spectrum simulation.

If the current accuracy of the calculated term values are not sufficient to reproduce the experimental data, we have to refine the model iteratively in the framework of non-linear least-squares fitting procedure. This is rather tedious work. Furthermore, the convergence of non-linear optimization becomes ambiguous if the initial molecular parameters are too far from the real ones. To fit the PECs, we use the advanced analytical forms (Extended Morse Oscillator (EMO) and Morse-Long-Range (MLR) forms [4]):

$$U_{\mathrm{EMO}}(R) = D_e\left[1 - \mathrm{e}^{-\beta(R)(R-Re)}\right]^2 \tag{16.2}$$

$$U_{\mathrm{MLR}}(R) = D_e\left[1 - \frac{u_{\mathrm{LR}}(R)}{u_{\mathrm{LR}}(Re)}\mathrm{e}^{-\beta(R)\cdot y_p^{\mathrm{eq}}(R)}\right]^2 \tag{16.3}$$

For example, the compact and physically-justified MLR function predicts correct long-range behavior near the dissociation limit. From another point, both EMO and MLR models are still flexible enough to represent energy in the very wide energy region with the desirable spectroscopic accuracy.

The more complicated tasks are to approximate both the diagonal and off-diagonal spin–orbit (SO) matrix elements as functions of *R*. The ab initio calculations highlighted that the SO functions between different electronic states (see Fig. 16.5) can have very complicated forms in order to be approximated analytically. In this case, we imply the so-called "morphed" form of:

$$\xi_{\mathrm{so}}^{\mathrm{emp}}(r) = \xi_{\mathrm{Cs}}^{\mathrm{so}} + \tilde{a}\left[\xi_{\mathrm{so}}^{\mathrm{ab}}(\tilde{b}r) - \xi_{\mathrm{Cs}}^{\mathrm{so}}\right], \tag{16.4}$$

which simply is the scaling of the initial ab initio data.

We also often involve ab initio data in the fitting process simultaneously with experimental data. We do it because experimental data are always limited. In order to propagate our empirical functions outside the experimental region, we fit ab initio potential energy curves and spin–orbit coupling functions at small and large internuclear distances where the experimental data is absent. On the way, we try to improve extrapolation properties of the deperturbation model used.

16.4 Applications

In Fig. 16.6, you see our recent results of the fitting procedure for a lithium–cesium molecule [6]. This is the residual between the calculated energies and their experimental counterparts. The deviation is very strong and comparable to the

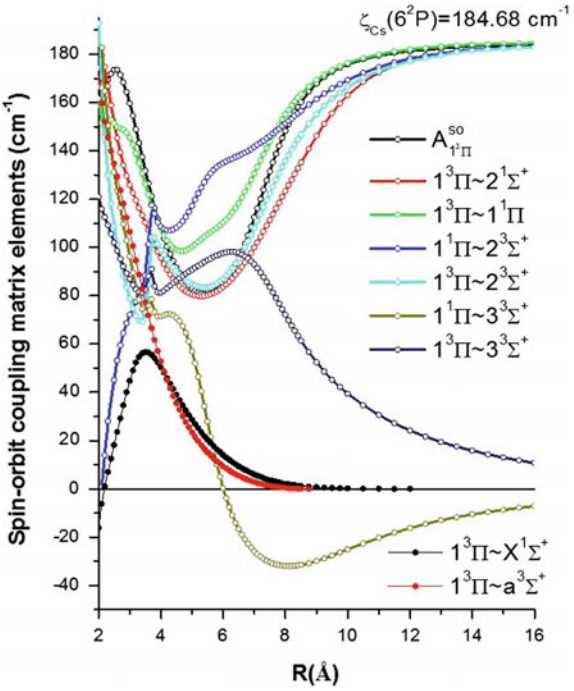

Fig. 16.5 The ab initio spin–orbit coupling matrix elements calculated between low-lying states of KCs molecule [5]

vibrational quanta, and, hence, the conventional adiabatic approximation is definitely not sufficient to make reliable predictions at all. A more complicated approach, which is often used for polyatomic molecules (the so-called effective Hamiltonian approach) improves the situation and decreases the residual up to 1 cm^{-1}. However, it is still too far from spectroscopic accuracy. Only the very tedious coupled-channel approach mentioned above yields the satisfactory results: the four channels deperturbation model provides the experimental accuracy of the spectroscopic data.

The initial test is to check the mass-invariant properties of the deperturbed parameters obtained. During the fit, we have used only term values of the single isotopologue. So, we obtained fitting parameters formally suitable to represent term values of the particular isotopologue. Now, we just have changed the reduced mass in the CC equation (16.1) to predict the term value positions of another isotopologue. The observed residuals are comparable to the accuracy of measurements. A more rigorous test is the extrapolation outside the experimental region. It means that we have fitted the data in some local energy region where the experimental data exist. Then we have predicted term values in the low-energy region, and, after that, we measure them. We see in Fig. 16.7 that the residual exponentially grows as the energy decreases. Nevertheless, the change energy by 500 cm^{-1} leads to the residuals of about 0.2 cm^{-1}. So, this is indeed a very good extrapolation. We also could reproduce the relative intensity distribution in LIF spectra with experimental accuracy. Thus we trust in the present deperturbation CC model. Furthermore, we

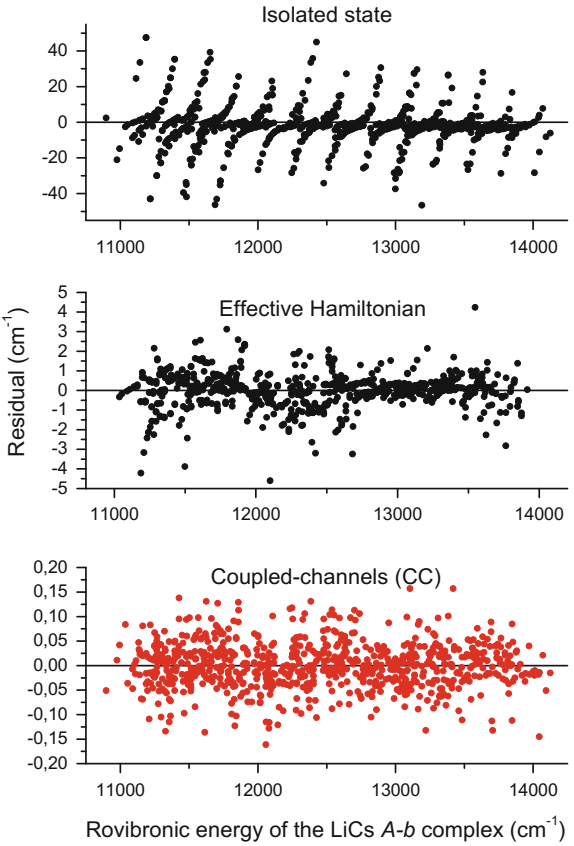

Fig. 16.6 The residual between the experimental and calculated term values of the spin–orbit A–b complex $^{7}Li^{133}Cs$ molecule [6]

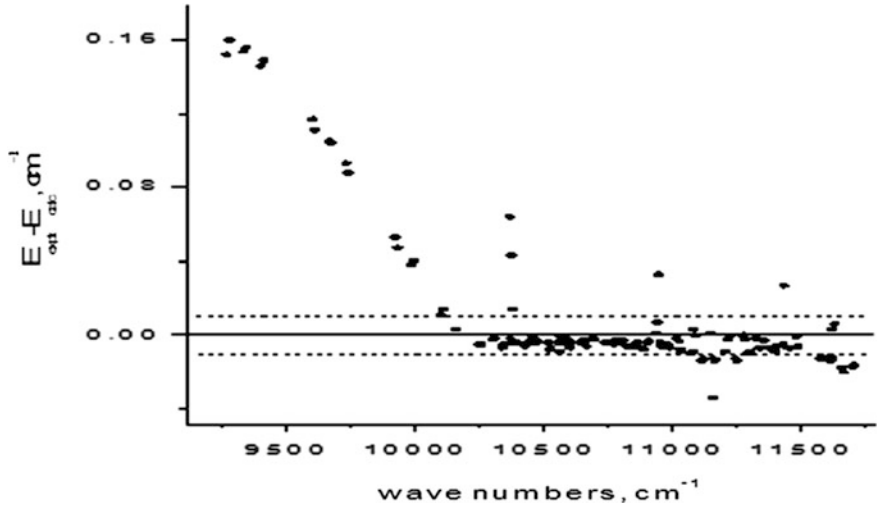

Fig. 16.7 The extrapolation error observed in low-energy terms of the spin–orbit A–b complex of the KCs molecule

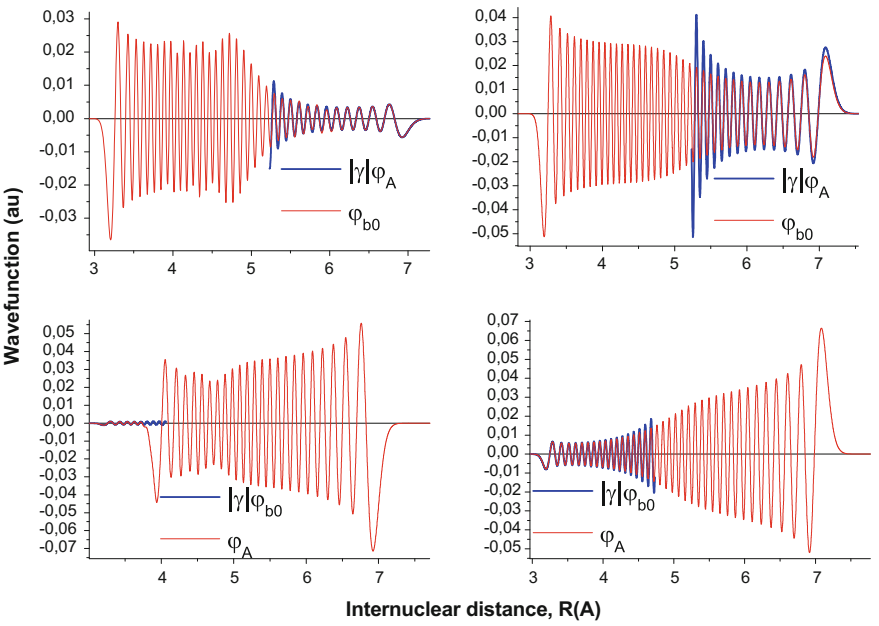

Fig. 16.8 Nodal structure of the multi-channel vibrational wave functions

could estimate the probabilities not only for the spin-allowed transitions, but also for spin-forbidden transitions.

Now, there is very interesting point which I wish to show you. This is the effect of local perturbations on a nodal structure of the multi-channel vibrational functions. The influence is not trivial one because we can observe only the energy, while the strong perturbation can change dramatically wave functions as well. In particular, we should expect absolutely different forms and shapes of the perturbed wave functions. The perturbations can even modify a nodal structure of vibrational wave functions. For example, you can see in Fig. 16.8 the loop structure of the non-adiabatic vibrational wave functions modified by the pronounced spin-orbit interaction between the singlet A and triplet b states of the KCs molecule.

16.5 Conclusion

So, we can finally conclude that the developed CC deperturbation model enables us to reproduce the high resolution spectroscopic data within experimental uncertainty. We can also predict the radiative properties and energy of the assembling molecules in a wide excitation energy region and select the most efficient way for laser cooling and laser transfer of molecules from the initial weakly-bound state (which is non-stable enough) to the absolute ground state (which has the lowest energy and, hence, an infinite lifetime).

References

1. K. Bergmann, N.V. Vitanov, B.W. Shore, J. Chem. Phys. **142**(17), 170901–170920 (2015)
2. E.A. Pazyuk, A.V. Zaitsevskii, A.V. Stolyarov, M. Tamanis, R. Ferber, Russ. Chem. Rev. **84** (10), 1001–1020 (2015)
3. O. Docenko, M. Tamanis, R. Ferber, E.A. Pazyuk, A. Zaitsevskii, A.V. Stolyarov, A. Pashov, H. Knoeckel, E. Tiemann, Phys. Rev. A **75**, 042503 (2007)
4. R.J. Le Roy, in *Determining Equilibrium Structures and Potential Energy Functions for Diatomic Molecules* (Chapter 6), ed. by J. Demaison, A.G. Csaszar (Taylor & Francis, London, 2011), pp. 159–203
5. J.T. Kim, Y. Lee, A.V. Stolyarov, J. Mol. Spectrosc. **256**, 57–67 (2009)
6. P. Kowalczyk, W. Jastrzebski, J. Szczepkowski, E.A. Pazyuk, A.V. Stolyarov, J. Chem. Phys. **142**, 234308 (2015)

Chapter 17
Ultracold Molecules: Production and Application

Shin Inouye

17.1 Introduction

First, I would like to introducet ultracold molecules. The motivation for studying ultracold molecules was nicely introduced in the previous chapter. I just would like to emphasize that a cold molecular gas is one of the biggest frontiers left for us [1]. Figure 17.1 shows my simplified view of the relevant fields. Imagine you want to do a precision measurement based on particles in the gas phase. Natural candidates are atoms, ions, and molecules. Cold atoms have been already produced by laser-cooling, and the properties of the ultracold atomic gas have also been well studied—as you know, these studies led to the Nobel Prize in Physics in 1997 and 2001. Cold ions have been laser-cooled before atoms were laser-cooled. The study on the interaction between cold ions enabled the manipulation of entangled states with ions, and the experimental study on cold-trapped ions led Dr. Wineland to receive a Nobel Prize in Physics (2012). Compared to these, there are not so many clear results on cold molecules: ultracold molecular gas is still in its infancy.

Cold molecules are difficult to make. One cannot use laser-cooling for producing ultracold molecules. Let me explain why by comparing atoms and molecules. Just by shining laser beams into a glass cell, one can cool atoms in the cell to 100 μK or less. This is possible because the same atom can scatter a lot of photons. For laser-cooling atoms to an ultracold temperature, one needs a large number of photon scatterings, since momentum transfer per one photon scattering is quite small. The common number of photon scattering needed to reach an ultracold temperature is on the order of 10,000 or more.

S. Inouye (✉)
The University of Tokyo, Bunkyo, Japan
e-mail: inouye@sci.osaka-cu.ac.jp

S. Inouye
Graduate School of Science, Osaka City University, 3-3-138 Sugimoto, Sumiyoshi-ku, Osaka 558-8585, Japan

K. Yamanouchi (ed.), *Progress in Photon Science*, Springer Series in Chemical Physics 115, DOI 10.1007/978-3-319-52431-3_17

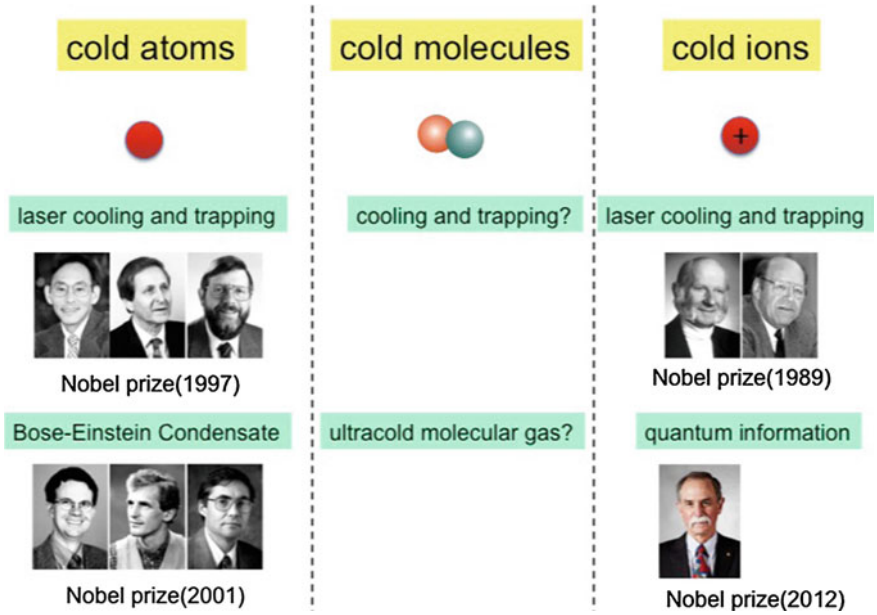

Fig. 17.1 Motivation behind studying ultracold molecules [2]

On the other hand, molecules do not scatter many photons. More precisely, molecules tend to go into different ground states after scattering one photon. Atoms and ions have only one electronic ground state. Therefore, after the photon scattering, they always move to the same ground state. However, molecules have a lot of rotational or vibrational degrees of freedom. Thus, after scattering one photon, molecules tend to go into different vibrational and rotational states. Once the molecules join other vibrational and rotational levels, they do not absorb the same laser light anymore. This is the reason why laser-cooling, which is a strong technique for cooling atoms and ions, does not work for molecules.

However, if you are dealing with simple molecules like diatomic molecules, there is a way around it: if one can develop a way to combine ultracold atoms into molecules without heating them up, then you should be able to produce ultracold molecules. This was the experiment we started ten years ago.

17.2 Preparation of Ultracold Molecules

How should we combine ultracold atoms into molecules? There is a special technique called "Feshbach resonance" [3]. Let me explain. Originally, "Feshbach resonance" was invented as a method to manipulate the interaction between ultracold atoms [4]. By applying an external magnetic field, one can bring another

spin state into resonance, modifying the scattering process dramatically. This process was not only effective in modifying the amplitude of the scattering wave-function, but also enabled us to transform ultracold atoms into ultracold molecules. By just sweeping an external magnetic field, one can adiabatically transform the wave-function of atomic pairs into that of molecules.

However, molecules produced in this method have a serious drawback: they are fragile. Typical binding energies of those "Feshbach molecules" are only $\sim 10^{-8}$ eV, or 100 μK. Any type of interaction with the environment will either break up these molecules or induce vibrational quenching that transfers molecules into lower vibrational levels.

Our plan was to use light. We planned to use a two-photon transition to transfer loosely bound molecules into the ro-vibrational ground state. Once in their ground states, molecules are tightly bound, and they have a large electric-dipole moment. The molecules can interact with each other through dipole-dipole interaction, which is anisotropic and long range. This new type of interaction should allow us to explore physics in a wider range.

However, these two-photon transition are not easy to realize. In order to avoid heating, we cannot allow absorption of a single photon. Thus, the population is always hidden in the "dark state". This transferring process is based on mutual coherence between the two lasers and called "STimulated Raman Adiabatic Passage (STIRAP)". The necessary condition for realizing this process is to have large Rabi frequencies compared to laser line-widths and any other source of de-coherence. So this project requires lot of molecular spectroscopies to study the Franck Condon Factors, and lot of laser work to stabilize the laser line-widths. We used Resonance-Enhanced Multi-Photon Ionization (REMPI) to detect the molecules that went to the right rotational and vibrational levels.

After all the molecular spectroscopy, we found out that the best transition for STIRAP is the combination of 875 and 641 nm. We prepared light sources. We did not use a frequency comb, but instead we locked diode lasers to a highly stable cavity, which is made of Ultra Low Expansion (ULE) glass. The lasers were stabilized to kilohertz level. By just sweeping the intensities of those two laser beams, we have succeeded in transferring loosely bound molecules into tightly bound molecules [5] (Fig. 17.2).

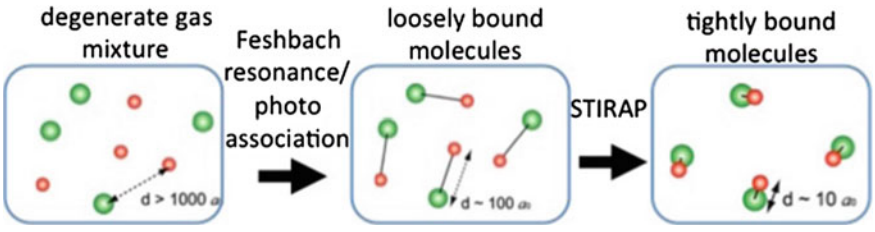

Fig. 17.2 How we produce ultracold molecules [5]

Here is a summary of the experiment for producing ultracold molecules: we start with Rubidium (Rb) and Potassium atoms in a vacuum chamber. Those atoms were laser-cooled and trapped in the magneto-optical-trap (MOT). We shine a cw-laser beam into the magneto-optical trap to photo-associate those atoms into loosely-bound KRb molecules. Here, we have to mention that, instead of Feshbach resonance, we used photo-association, because we could not suppress the inelastic loss at the Feshbach resonance. Due to this change, the density of the molecule was lower, and the temperature of the molecule was higher than we planned. However, the repetition rate of the experiment became higher. After that, the loosely bound molecules are converted into tightly bound molecules in the ro-vibrational ground state by STIRAP.

So now, we produced ultracold KRb molecules in the ro-vibrational ground state. Actually we can produce ultracold molecules in any rotational or vibrational level we want. Is there any advantage to producing ultracold molecules in a desired state? In the next experiment, we show that we can improve the accuracy of the measurement of the variation of fundamental constants by preparing molecules in a desired state. We succeeded in improving the world record by a factor of two [6].

17.3 Variation of Fundamental Constants

Let me explain the motivation for measuring the variation of fundamental constants. Currently, one of the biggest mysteries in physics is the accelerated expansion of the universe [7]. Although the observation of the accelerated expansion is established, there is a big controversy in understanding the origin. Especially, the source for energy needed to support the expansion is unknown. People named the energy "dark energy". The density of the "dark energy" is so low that it is quite difficult to detect the energy directly. There are so many theories on "dark energy". There are theories ("quintessence") that predict that the energy is stored in the form of fluctuations of a new scalar field [8]. The field can couple with other fields (e.g., the electromagnetic fields), causing fundamental constants to fluctuate. The fluctuation is expected to be of a low frequency.

Thus, it is very important to measure the fluctuation of fundamental constants. For this purpose, we can measure dimensionless fundamental constants like a fine-structure constant, electron-to-proton mass ratio, or proton g-factor. We decided to look into the electron-to-proton mass ratio.

There are two ways to look into the variation of fundamental constants. One is called "astronomical observations" where people investigate with an observatory and compare the spectra observed in the early universe with those measured in the laboratory. One of the astronomical observations based on microwave transition of alcohol shows that electron-to-proton mass ratio is stable at 10^{-7} in 7 billion years [9]. The other approach is to pursue the high-precision frequency metrology in the lab. You can measure the frequency of a molecular transition with better than 10^{-14} accuracy and compare the result with the one you obtained the day before.

The reason why molecular spectroscopy is needed for measuring the stability of electron-to-proton mass ratio is as follows. If you assume the Born-Oppenheimer approximation, the potential energy curve for a nucleus is determined by the electron mass and the fine-structure constant. If the properties of electron are stable, there is no chance for the potential-energy curve to change.

However, what we measure is the frequency caused by the motion of the nucleus, and that is sensitive to the mass of nucleus. Suppose that the electron mass stays the same, but the proton mass changes: Then, the vibrational frequency of the molecule changes because the frequency is inversely proportional to the square root of the mass of the nucleus. So by measuring the transition frequency between vibrational levels of molecules precisely, one can tell the stability of the electron-to-proton mass ratio.

Currently, the most precise lab measurement was done by a French group, who worked on the molecular spectroscopy of SF_6. They achieved a 5×10^{-14} level of accuracy by combining an optical spectroscopy of thermal SF_6 beam, a frequency comb, and an atomic clock [10]. Since the atomic clock sits in a different city ($\sim$40 km away), they had to use an optical-fiber link. What I would like to show you is that you can surpass this measurement by using ultracold molecules. The experiment can be contained on a single optical table. By using ultracold molecules, one can: (i) eliminate Doppler broadening, (ii) increase the interaction time, and (iii) eliminate signals from other transitions since one can prepare ultracold molecules in any target state.

Theoretical predictions showed that bi-alkali molecules have a microwave transition whose frequency is quite sensitive to electron-to-proton mass ratio. We scrutinized the molecular potential of KRb and found a good candidate: the fractional change in the frequency of this transition is about 14,890 times the fractional change in the electron-to-proton mass ratio. This is a huge gain compared to the experiments using thermal beams, where this factor is only on the order of one.

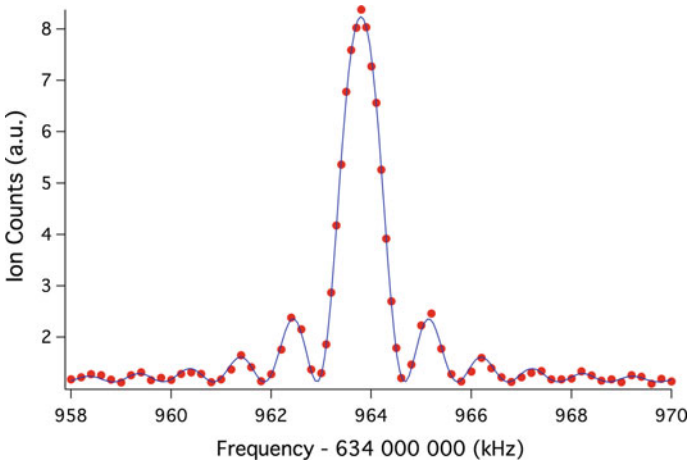

Fig. 17.3 Typical excitation spectra for measuring the stability of the electron-to-proton mass ratio [6]

In order to transfer ultracold molecules into this target state, we prepared another ULE cavity, locked two diode lasers for Raman transition. Using those two new laser beams, we succeeded in realizing STIRAP to the target state. We made an excitation spectra of the ultracold molecules, and measured the drift of the peak of the spectra over a year.

Even if the fundamental constants are stable, any fluctuations of experimental conditions can cause drifts in the spectra. Fluctuation of the magnetic field is one of them. In order to minimize the effect, we used a transition that does not have a linear Zeeman effect. Still there is a second-order Zeeman effect, but we also eliminated the effect from that by simultaneously taking excitation spectra of magnetic-field-sensitive microwave transitions and subtracting the second-order Zeeman shift from the measured peak frequencies.

As shown in Fig. 17.3, the result shows that the electron-to-proton mass ratio is constant within 2.8×10^{-14} [6]. This result is a factor of two improvement in accuracy over the previous world record.

The major part of the work has been done by Dr. Kobayashi and Mr. Ogino, who was a master course student.

References

1. L.D. Carr et al., New J. Phys. **11**, 055049 (2009)
2. Photos from Nobelprize.org
3. C. Cheng et al., Rev. Mod. Phys. **82**, 1225 (2010)
4. S. Inouye et al., Nature **392**, 151 (1998)
5. K. Aikawa et al., Phys. Rev. Lett. **105**, 203001 (2010)
6. J. Kobayashi et al., in preparation
7. P.J.E. Peebles, B. Ratra, Rev. Mod. Phys. **75**, 559 (2003)
8. E.J. Copeland, M. Sami, S. Tsujikawa, Int. J. Mod. Phys. D **15**, 1753 (2006)
9. J. Bagdonaite et al., Science **339**, 46 (2013)
10. A. Shelkovnikov et al., Phys. Rev. Lett. **100**, 150801 (2008)

Chapter 18
Spectroscopy of Flavin-Containing Proteins: Theoretical Insights

Maria Khrenova

This chapter is devoted to the theoretical insights of the spectroscopy of flavin-containing proteins[1–4]. The main part of a flavin molecule is the isoalloxazine ring that can be found in various biological systems. Flavin may exist in different redox states, but, normally in water solution, flavin exists either in an oxidized form or, if two electrons and two protons are added, it turns to the fully reduced state. But in biological systems, there is another state that is formed if one adds one electron and one proton— the semiquinone radical state that is responsible for the functioning of some proteins (Fig. 18.1).

As for the photochemical properties, flavin can absorb in the visible part of spectrum. It has a broad band with a maximum at around 450 nm in water solutions and emits with a maximum at 520 nm. From the theoretical studies, as well as from experimental data, we find that its excitation results in huge redistributions of electron density, and it increases on N5 and C4A, which is responsible for photo-induced redox properties (Fig. 18.2).

LOV is the photoreceptor protein, and, upon excitation, the sidechain of Cys interacts with N5 and C4A atoms of the chromophore forming covalent adduct, which recovers to the initial dark state after some time. Now it is popular to design new biological fluorescent compounds, several groups have proposed point mutations to abolish the photo-induced reaction and to introduce fluorescent properties to this system. They started with the substitution of Cys with other amino acids. After that, they made some additional mutations to enhance properties. The most prominent member of this family is the so-called iLOV protein. We try to understand the origin of these properties and to introduce new colors to the LOV fluorescent-protein family by introducing additional mutations.

M. Khrenova (✉)
Moscow State University, Moscow, Russia
e-mail: wasabiko13@gmail.com

K. Yamanouchi (ed.), *Progress in Photon Science*, Springer Series in Chemical Physics 115, DOI 10.1007/978-3-319-52431-3_18

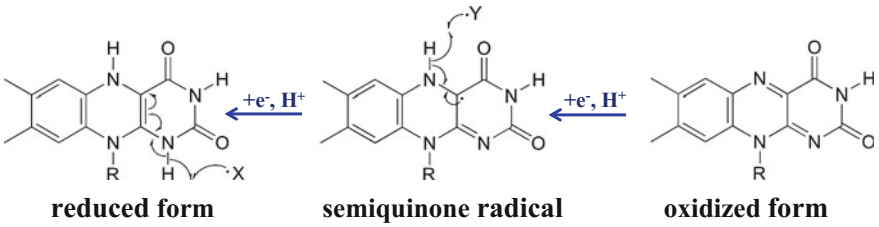

Fig. 18.1 Redox states of flavin

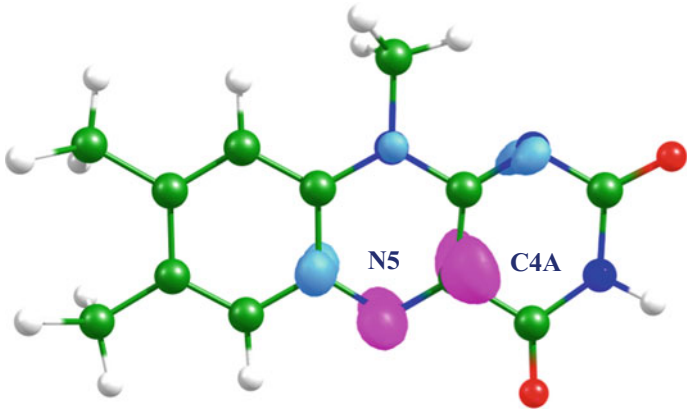

Fig. 18.2 Charge redistribution upon excitation of flavin; *pink* corresponds to the increase of electron density and *blue* to the decrease upon S_0-S_1 excitation. Color code: carbon in *green*, nitrogen in *blue*, oxygen in *red*, hydrogen in *white*

Our calculations are mainly based on the combined quantum mechanics/molecular mechanics approaches (QM/MM) [4]. If we deal with a huge protein system, we cannot treat it with quantum-chemical approaches, therefore, we take a chromophore group and neighboring residues that interact with the chromophore and treat them at the quantum-chemical level of theory. Usually we utilize the density functional theory, which is well-known nowadays. The rest of the system is treated through classical approaches, i.e., conventional force fields for proteins. First, we take crystal structure of the iLOV protein and perform molecular dynamics simulation to understand the flexibility of the neighboring residues in the chromophore-containing pocket. We found that the glutamine side chain is very flexible: It has two different conformations, one of them is inside the chromophore-binding pocket and another is exposed outside the protein. When returning to the static consideration, we use crystal structure and modify it to get two different equilibrium geometry configurations (Fig. 18.3).

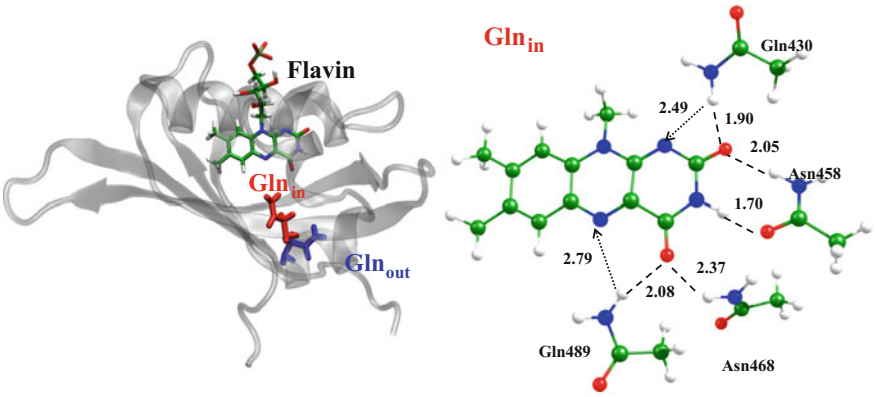

Fig. 18.3 Two conformations observed in MD simulations (*left*) and equilibrium geometry configuration of Gln_{in} conformation (*right*). Distances are shown in angstroms

We calculated the vertical excitation and emission energies for both of these structures and found them to be quite similar. If we introduce an additional hydrogen bond to this region, it stabilizes the excited state and results in a redshift of the vertical excitation and emission energies. Thus, the addition of a hydrogen bond influences the properties, and we modified the glutamine side chain with positively charged lysine, which can form two hydrogen bonds with flavin. This modification shifts the absorption band to 500 nm and the emission band to 583 nm, introducing new color to the LOV family of fluorescent proteins.

BLUF is another flavin-containing protein. Upon irradiation, it turns to the light state, and, then, after some time, it recovers. The spectral shift between these two states is 10–15 nm.

The main difference between light and dark states is in positions of Trp104 and Met106: The side chains are either exposed to the solution or located in the chromophore-binding pocket. Another uncertainty is due to the resolution of the X-ray spectroscopy of large molecules like proteins. It is difficult to find a difference between the electron densities of oxygen and nitrogen atoms, as those are similar. Moreover, protons are not visible in these studies, therefore, we cannot distinguish amide or imide forms of the side chain of glutamine that maybe critical because this residue is close to the chromophore.

We performed QM/MM modeling and found that the structure that is better attributed to the dark state has glutamine in amide form, and its NH_2 group forms a hydrogen bond with the N5 atom of flavin while methionine is inside the chromophore-binding pocket [1–3]. In the light state, glutamine is in tautomeric-imide form and tryptophan substitutes methionine in the chromophore-binding pocket. We suggest that the photoreaction mechanism assumes flip and the tautomerization of glutamine and the substitution of methionine with tryptophan (Fig. 18.4).

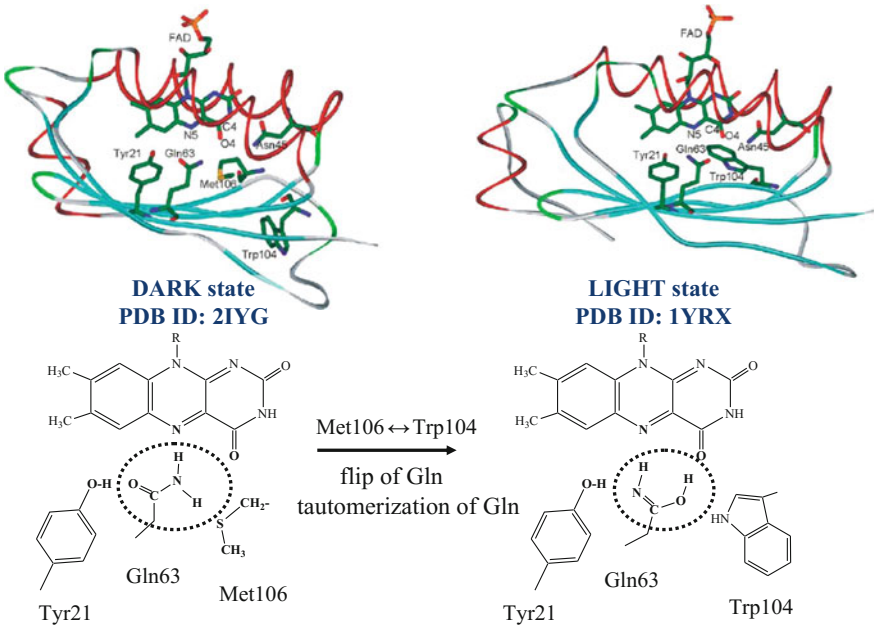

Fig. 18.4 Dark and light states of BLUF

References

1. M. Khrenova, A. Nemukhin, T. Domratcheva, J. Phys. Chem. B. **117**, 2369–2377 (2013)
2. M.G. Khrenova, T. Domratcheva, I. Schlichting, B. Grigorenko, A.V. Nemukhin, Photochem. Photobiol. **87**, 564–573 (2011)
3. M.G. Khrenova, T. Domratcheva, B. Grigorenko, A.V. Nemukhin, J. Mol. Model. **17**, 1579–1586 (2011)
4. M.G. Khrenova, A.V. Nemukhin, T. Domratcheva, J. Phys. Chem. B. **119**, 5176–5183 (2015)

Part VII
Photochemistry of Novel Materials

Chapter 19
Photo-Excited State Chemistry of 4-Diazo-2,2-Dimethyl-5, 5-Dihydrofun-3-One

Alexey Povolotskiy

The main reaction which was under study is the photo-excited reaction of diazoketone, which is called the Wolff Rearrangement, accompanied by narrowing of the cycle.

The earliest work was done with a mercury lamp as a light source with an average power about 100 W and a filter to remove wavelengths of less than 210 nm. Elimination of the diazoketone in a solution of tetrahydrofuran leads to formation of the products presented in Fig. 19.1.

The kinetics of photolysis showed the continuous formation of the Wolff rearrangement product, while the precursor—the initial diazoketone was gone. This argued for the possible presence of the diazoketone's isomer—the corresponding diazirine in the reaction mixture which can take part in Wolff rearrangement. The aim of the present study was to establish the conditions of diazoketone 1 photoisomerisation into the corresponding diazirine, to identify it, and to find out its role in the photochemical reactions under study.

For diazoketone 1, absorption, luminescence, and phosphorescence spectra were obtained. Based on these data, the energy-level diagram was built, and corresponding excited state lifetimes were measured (Fig. 19.2). To study the photochemical processes occurring from each specific excited state, we have chosen monochromatic light sources with the following emission wavelengths: 266, 308, and 405 nm.

The reaction was controlled by taking an aliquot of the reaction mixture during specific periods of time and analyzing it by IR spectroscopy. By overlapping the obtained IR spectra, we built the kinetics of photolytic processes for three excitation wavelengths. For each of these three wavelengths, the dynamics looked similar, besides some peculiarities which will be discussed further.

A. Povolotskiy (✉)
Institute of Chemistry, Saint Petersburg State University,
Ulianovskaya 5, Saint Petersburg 198504, Russia
e-mail: alexey.povolotskiy@spbu.ru

K. Yamanouchi (ed.), *Progress in Photon Science*, Springer Series in Chemical Physics 115, DOI 10.1007/978-3-319-52431-3_19

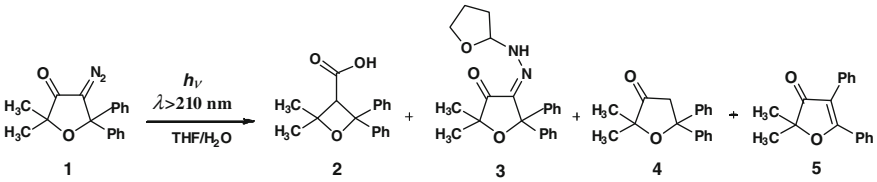

Fig. 19.1 Photo-excited reactions of diazoketone 1 [1]

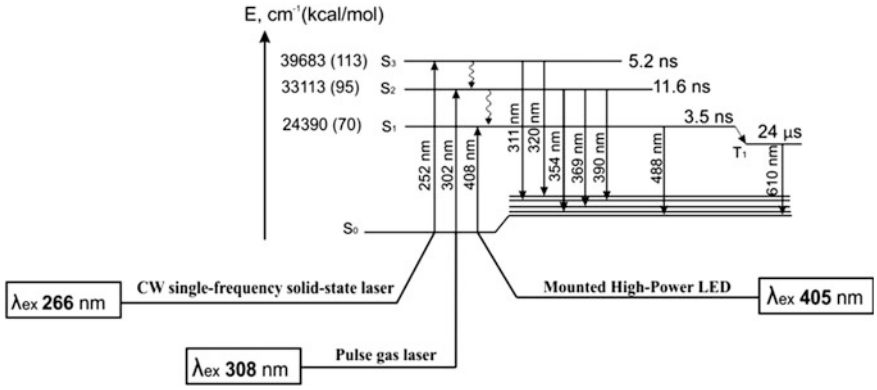

Fig. 19.2 Energy levels of diazoketone 1

We observed the subsequent decrease in intensity of the absorption band corresponding to diazoketone. At the same moment, we can observe the growth of three new absorption bands, which can be assigned to the subsequent products. Now let us consider each of them in more detail.

If we closely compare the IR spectra of the reaction mixtures obtained by irradiation on 266 and 405 nm wavelengths, we will see that the absorption band at 1535 cm^{-1}, which is assigned to deformation stretches of hydrazone, exists only in the spectra of the reaction mixture irradiated by the 266-nm laser, while, in the spectra of the reaction mixture irradiated by the 405-nm laser, we can observe the weak growth of the band centered at 1557 cm^{-1}. In the absence of irradiation, this band shifts to the longer wavelengths and centers at 1535 cm^{-1}. If we repeat the irradiation for a short period of time, the reverse shift to 1557 cm^{-1} occurs.

Probably, this happens due to the Z-E photoisomerisation of hydrazone. We established that this process takes place only in case of 405-nm irradiation and not in the case of 266 nm, because the hydrazone absorbs irradiation in the region 385–440, while no absorption exists around 206 nm.

Let us consider the origin of the band at 1812 cm^{-1}. In the absence of sufficient amounts of water in the reaction mixture, i.e., the product of the Wolff rearrangement, the corresponding ketene interacts with the acid, which is nevertheless formed in presence of water traces. This reaction proceeds as a nucleophilic addition and

yields anhydride, which tends to hydrolyze, while the work up forms oxetancarboxylic acid, whose signals can be further observed in the proton spectra of the reaction mixtures. It is known from the literature [2] that the anhydride-motive-characteristic vibrations lay in the region 1800–1840 cm^{-1}. Thus, based on our argumentation and the literature data, the band at 1812 cm^{-1} can be assigned to the anhydride and used as a reference band to track the Wolff- rearrangement product.

Diasirine was isolated, and its IR spectrum was obtained. In this spectrum, the intensive band centered at 1754 cm^{-1} was revealed. Furthermore, we calculated the IR spectrum of diazirine whose band position was in good accordance (within the margin of error) with experimental spectrum.

To confirm the structure of the diasirine, the crystal was grown and submitted to X-ray analysis. The obtained data proved the diazirine structure. This substance was characterized with several methods.

To get more information about the reaction pathway, and to study the dynamics of products formation, we built kinetic curves for the photolysis of diazoketone and diazirine. From these kinetic curves, we can observe that, in the case of 266-nm excitation of diazoketone starting at some moment of time, decomposition of diazirine begins. However, while being excited with 405-nm light, diazirine remains stable. That is why we can deduce that, in this case, the Wolff rearrangement results exclusively from the excited states of diazoketone.

If we look at the kinetic curves to explain why this is obtained for diazirine, we can see that, during the first 15 min of photolysis, its decomposition along with the formation of diazoketene occurs. Formations of any other products were not observed. However, starting with the 20th minute, diazoketone decomposition and the simultaneous formation of hydrazone and anhydride occurs. This testified to the fact that the Wolff rearrangement and hydrazone formation take place from the excited state of diazoketone, however, for diazirine, the only observed transformation was its photoisomerisation.

Finally, I have a suggestion for cooperation. We are extremely interested in the determination of the mechanism of chemical reaction, i.e., photo-excited chemical reactions, and we are looking for the possibility to study the *photolysis in* femtoseconds and picosecond regions reduce of femtoseconds pump probe.

References

1. V.A. Nikolaev, O.S. Galkina, J. Sieler, L.L. Rodina, Tetrahedron Lett. **51**, 2713–2716 (2010)
2. G.V. Saydov, O.V. Sverdlova, Professional NGOs. pp 227 (rus.)(2006)

Chapter 20
Novel Porphyrin–Fullerene Covalent Dyads Capable of Forming Charge-Separated States on a Microsecond Lifetime Scale

Alexander Konev

Porphyrin–fullerene dyads, among other donor-acceptor systems, evoke interest as prospective materials for the conversion of solar energy. The principle of their action can be envisioned as depicted in Fig. 20.1.

First, the donor-acceptor molecule consumes a photon quantum to form an excited state. From that excited state, it can relax to a specific lower excited state where the electron density is redistributed, resulting in formal relocation of an electron from the donor part of the molecule, which has now a positive charge, to the acceptor part, which acquires a negative charge. If this charge-separated state has lasted enough, these molecules can then interact intermolecularly and act either as a photoredox catalyst or as a photoactive material in organic solar cells.

When we talk about porphyrin–fullerene dyads, in this case, the fullerene is an acceptor fragment while porphyrin is a donor counterpart. A survey of the literature on these compounds presented in our recent work [1] shows that the charge-separated-state lifetime depends strongly on the bridge (denoted in Fig. 20.1 as X) that connects the chromophores. When this bridge is such that it fixes the chromophores together in close contact, i.e., with the porphyrin face oriented towards the C_{60} sphere, let us call it a face-to-face contact, then the charge-separated state has a very short lifespan of 3.5 ns at the most [2]. A similar picture is observed when the bridge is long and flexible, so that the chromophores can achieve a close face-to-face contact [3]. The reported lifespan of the charge-separated state in this case does not exceed 650 ns. Only when the bridge keeps the chromophores apart, or fixes them in such an alignment that the porphyrin edge (and not the face) is oriented towards C_{60} sphere, what we shall call a "face-to-edge" alignment, only then does the lifetime of the charge-separated state

A. Konev (✉)
Department of Organic Chemistry, Institute of Chemistry,
St. Petersburg State University, Universitetskiy pr. 26, Petrodvorets,
St. Petersburg 198504, Russia
e-mail: a.konev@spbu.ru

K. Yamanouchi (ed.), *Progress in Photon Science*, Springer Series in Chemical Physics 115, DOI 10.1007/978-3-319-52431-3_20

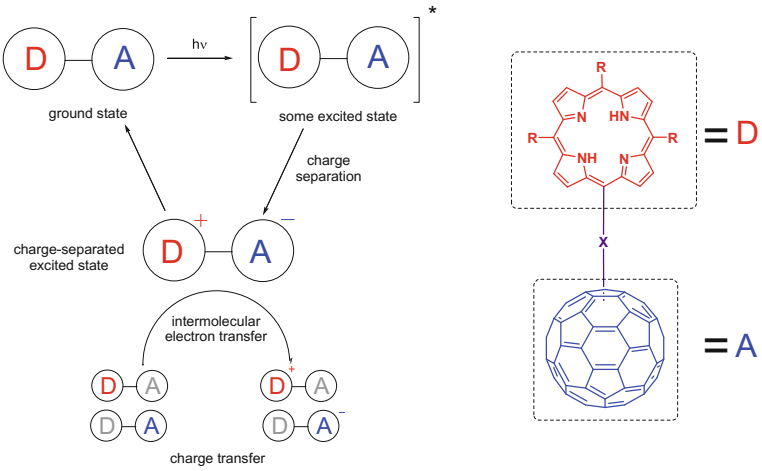

Fig. 20.1 Schematic representation of the principle of solar-energy transformation by donor-acceptor dyads

reach several microseconds. There are only eight examples of such systems with lifetimes of the charge-separated state in the microsecond range [4].

However, it should also be mentioned that the large distance between porphyrin and fullerene fragments is not a sufficient condition to achieve a long lifetime of the charge-separated state. When the bridge enables continuous conjugation of the π-systems of the chromophores, the lifespan of the charge-separated state is significantly reduced.

Based on this analysis, we proposed three criteria to be met to construct a molecule that would be able to form charge-separated state with a long lifetime: the molecule should have fixed and large inter-chromophore distance, conjugation of the chromophores should be avoided, and the alignment of the chromophores should be face-to-edge like.

We proposed porphyrin–fullerene dyad connected by a pyrrolo[3,4-c]–pyrrole bridge (Fig. 20.2) as a compound that should meet all the criteria above, so let us check it. It has a rigid bridge that fixes the chromophores at a large distance, the sp^3-carbons that keep the π-systems apart, and *N*-substitution plus-linear linker that ensures face-to-face orientation of the π-systems. We also added some additional components: the ester groups in the bridge are solubilizing groups. They are added to make the molecule soluble in conventional organic solvents. Another supplement is the aryl groups in the porphyrin core: they are added to enable electronic-structure modulation. Let me refer you to our papers mentioned at the beginning of my talk for the story of the synthesis of these compounds. I will note here that the three compounds we shall discuss now differ only in the aryl substituents, which are phenyl (**1a**), 4-bromophenyl (**1b**), and 4-methoxyphenyl (**1c**). R-substituent is ethyl for every compound.

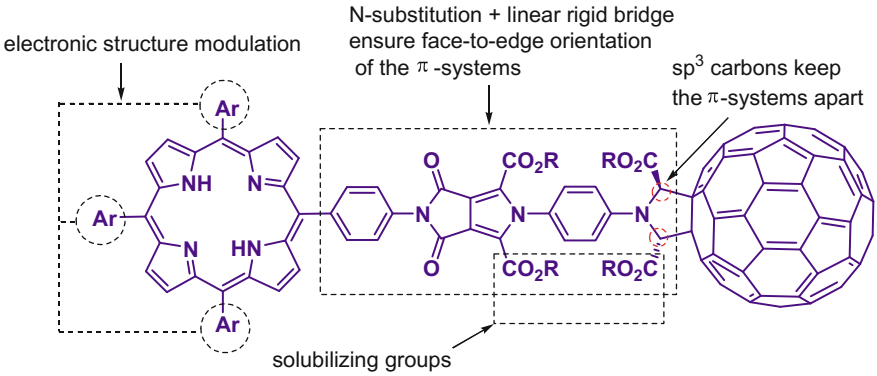

Fig. 20.2 Designed porphyrin–fullerene dyads for solar-energy conversion

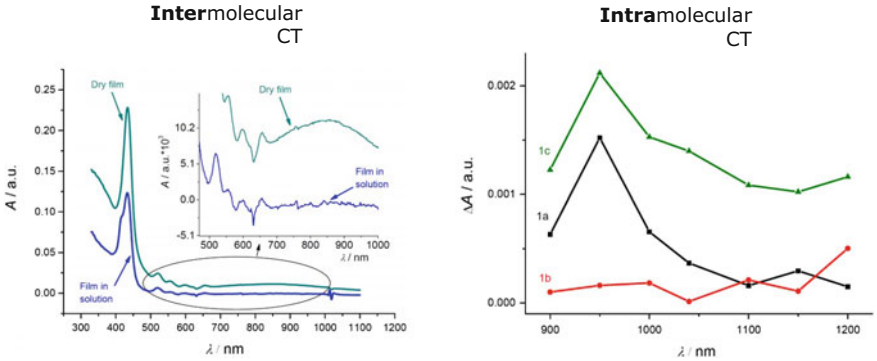

Fig. 20.3 Inter- versus intramolecular charge transfer. Absorption spectra of a thin film of compound **1a** on ITO/glass support in dry form and immersed in MeCN (*left*). Transient absorption 500-ns ΔA spectra (Near-IR range) (*right*) [1]

Now, to the photophysical properties. Let us check if these products indeed can form a charge-separated state with a long lifespan.

The absorption spectra of the synthesized porphyrin–fullerene dyads represent the typical porphyrin spectra with Soret band at 415 nm and Q bands in the region of 500–700 nm. Fluorescence spectra with emission close to 650 nm are quite common for porphyrins, as well. So, there is no interaction of the chromophores in the ground state and no charge-separated state so far.

An interesting result was obtained when recording the absorption spectra of a thin film of one of these compounds on a glass support in a dry form (Fig. 20.3, left). On the insert here, you can see a very weak and very broad band that we attributed to the intermolecular charge transfer band. The evidence for that is that this band disappears when we immerse this film in an acetonitrile medium. Still,

even should this band correspond to a charge transfer process, this is an intermolecular process, not the intramolecular one we were looking for.

So, we proceed further. To locate the charge-separated state resulting from intramolecular charge transfer, we performed a transient-absorption and emission-spectroscopy study of the synthesized dyads (Fig. 20.4). According to this study, when we irradiate the porphyrin-fullerene dyads, they are excited to the first excited-singlet state, which has quite a short lifespan of 2 ns. This excited state can then either relax back by a radiative or irradiative transition, or it can undergo intersystem crossing, giving us a triplet state which has a much longer lifetime of several microseconds. The latter was detected by transient absorption at around 450 nm. Either from this new triplet state or from the initially formed first excited singlet state, another intersystem crossing leads to a lower excited state, which is detectable by transient absorption at ca. 950 nm (Fig. 20.5), which is within the characteristic region of the fullerene radical-anion absorption. The lifespan of the charge-separated state corresponding to this band was found to be 4 μs for

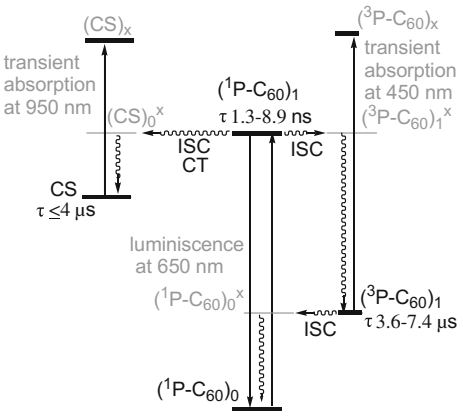

Fig. 20.4 Schematic representation of photo dynamics in porphyrin–fullerene dyads **1** according to transient absorption and emission spectroscopy data

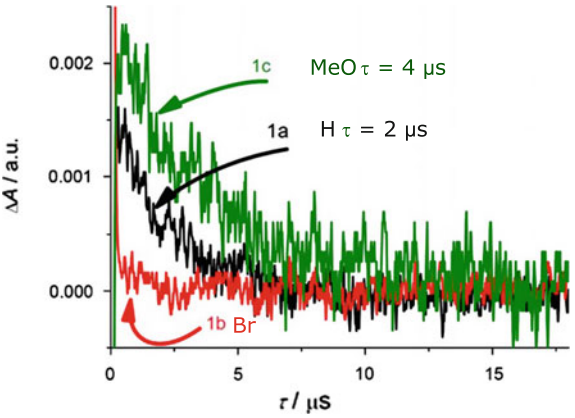

Fig. 20.5 950-nm kinetic traces of the porphyrin–fullerenes **1a–c** in deoxygenated $(CH_2Cl)_2$ upon 532-nm excitation [1]

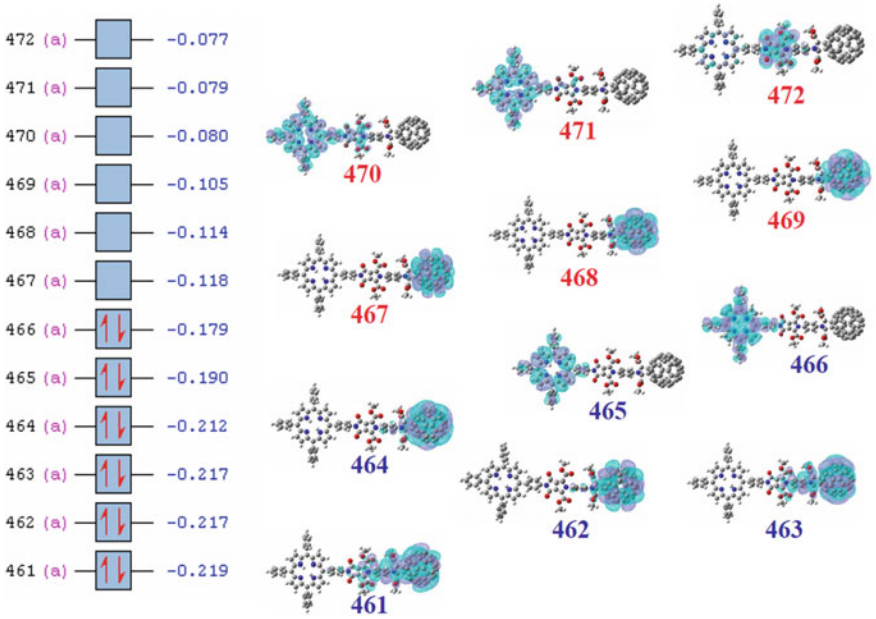

Fig. 20.6 Fragment of the energy diagram of molecular orbitals of compound **1′a**

methoxy-substituted compound **1c** and 2 μs for the benchmark compound **1a**. Surprisingly, no charge-separated state (denoted on the scheme as CS) was observed for bromine-substituted compound **1b**.

We supposed that the reason might lie in the electronic structure of the dyads. To obtain insight into that, we performed DFT calculations (B3LYP 6-31G(d)) on the model dyads **1′** that differ from the real objects by an R-substituent in the ester group, which is methyl instead of ethyl. In Fig. 20.6, you can see the fragment of the energy diagram of molecular orbitals of model compound **1′a**. What is interesting is that almost all the orbitals here are mostly located either on fullerene or porphyrin fragments, with HOMO being located on porphyrin and LUMO located on the fullerene part.

Now, we can visualize the photo dynamics occurring in porphyrin–fullerene dyads **1a–c**. When the molecule in the ground state is excited with visible light, the electron from, for example, the highest occupied molecular orbital (MO 466) goes to the appropriate level in terms of energy and symmetry-vacant molecular orbital, e.g., to MO 471, giving us the first singlet-excited state, which has a short lifespan as we have already seen, and it can undergo inter-system crossing, giving us the first triplet state. Alternatively, the first singlet-excited state can undergo another process with the electron falling from MO 471 to MO 467. MO 471 is mostly located on porphyrin while MO 467 is mostly located on fullerene. Hence, this transition gives us the charge-separated state. Of course, this is a simplification of the real process, yet it helps to understand what is going on upon interaction of the

dyad with light and to formulate the working hypothesis that explains the absence of the charge-separated state in the case of bromine-substituted dyad **1b**. We suppose that the processes discussed above compete with each other. The absence of the charge-separated state, in case of the bromine- substituted dyad **1b,** means that either formation of the triplet state is accelerated, for example due to the heavy-atom effect, or formation of the charge-separated state is decelerated, or both these effects take place.

To find possible reasons for deceleration of the charge-separated state formation in the case of the bromine-substituted compound **1b**, we performed time-dependent DFT calculations that provided us with information about the first lowest 50 excited states; the diagram of the energy of the states is presented on Fig. 20.7. You can see that all the excited states can be separated into several groups: the first two columns are composed of the states that involve the transition between orbitals located mostly on porphyrin moiety, giving us either singlet- (first column) or triplet-excited (second column) states. In the next two columns, there is the same story, but the orbitals are located mostly on the fullerene core. Finally, the last column gives us the formal transitions from the orbitals located on porphyrin to the orbitals located on fullerene. The first four columns are pairs of singlet and triplet states. In the fifth group of states, there are also singlet and triplet states, but we

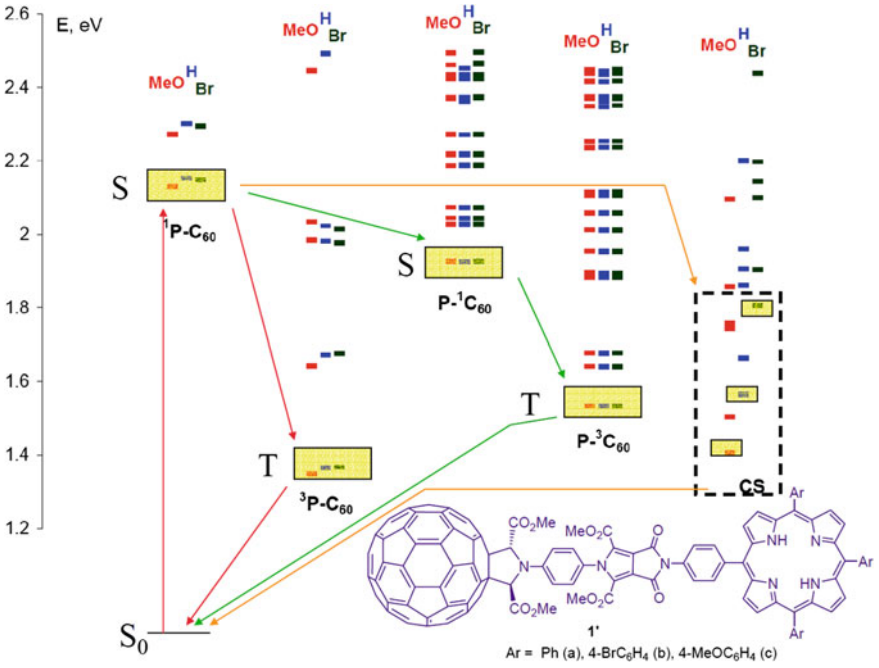

Fig. 20.7 Energy diagram of the excited states of compounds **1′a–c**. The graphics are based on a fragment of the diagram [1]

could not see any difference in energy between them, so we combined them into one column.

Now we can discuss the possible reason for deceleration of the process of the charge- separated-state formation in the case of the bromine-substituted compound **1b**. As you can see from this diagram, the driving force for the electron transfer, which is the difference between the first excited-singlet state and the charge-separated state, is the lowest one for the bromine-substituted compound **1b** and the largest one for methoxy-substituted compound **1c**. Yet, the effect that this difference should have on the electron-transfer rate (20.1) depends on the ratio between the Gibbs energy of the reaction (which includes the difference in the electron energy of the two states as the main term) and the reorganizational energy, according to Marcus theory [5].

$$k_{ET} \sim \exp\left(-(\Delta G_{ET} + \lambda)^2 \Big/ (4\lambda k_B T)\right) * \lambda^{-1/2} \tag{20.1}$$

If the absolute value of the Gibbs energy of the electron transfer is less than the reorganizational energy, then we are in what is called the normal Marcus parabola region where the larger the driving force, the larger the rate constant or the smaller the driving force, the smaller the rate constant. However, if the absolute value of the Gibbs energy is larger than the reorganizational energy, then we turn to the inverted Marcus parabola region where the larger the Gibbs energy the slower the process.

So we have to check in which region we are. We had to estimate the Gibbs energy and the reorganizational energy. The formulae that we used for these estimations are given in (20.2) and (20.3). The one given in (20.2) is based on the Rhem-Weller approach [6], while the assessment in (20.3) estimates Gibbs energy as just the electronic energy difference between the two states. The last estimation can be justified by a notion that the main contribution to the Gibbs energy of a reaction is given by the electronic energy term.

$$-\Delta G_{\mathrm{ET}} \approx E_{\mathrm{S0}\rightarrow\mathrm{S1}} - \left(E_{\mathrm{ox}}^{1/2} - \mathrm{E}_{\mathrm{red}}^{1/2}\right) (\text{for } 1\bar{\mathrm{e}}) \tag{20.2}$$

$$-\Delta G_{\mathrm{ET}} \approx -\Delta E_{\mathrm{el}} = E\left({}^1\mathrm{P} - \mathrm{C}_{60}\right) - E(\mathrm{CS}) \tag{20.3}$$

The results are given in Table 20.1. The estimation of Gibbs energy in the fourth column is obtained through the experimental data on cyclic voltammetry and absorption spectrum (20.2), while the estimation given in the seventh column is the one based on the electronic energy of the states (20.3). Though there are some differences between the absolute values, we have the same trend in both cases: the Gibbs energy of the forward electron transfer decreases in the sequence: **1c > 1a > 1b**, that is, the Gibbs energy is the largest for the methoxy-substituted compound and the smallest for the bromine-substituted dyad.

Next, we have estimated the reorganizational energy λ. This value has two terms: the outer reorganizational energy λ_{out} and the inner reorganizational energy λ_{in}. The last one is quite difficult to calculate, so we used the literature estimation

Table 20.1 Estimations of the gibbs energy for a charge-separation process

1	$E_{S0\rightarrow S1}$, eV (nm)[a]	$E^{1/2}{}_{ox} - E^{1/2}{}_{red}$, V[b]	$-\Delta G_{ET}$, eV[c]	$E(^1P-C_{60})$, eV	E (CT), eV	$-\Delta G_{ET}$, eV[d]
1a (H)	1.92 (645)	1.77	0.15	2.153	1.565	0.59
1b (Br)	1.92 (645)	1.79	0.13	2.148	1.805	0.34
1c (MeO)	1.92 (645)	1.69	0.24	2.130	1.406	0.72

[a]Based on the absorption spectra of 1,2-dichloroethane solution of **1**. [b]Based on cyclic voltammograms of film of **1** immersed in 0.1 m Et_4NBF_4 solution in MeCN, scan rate 500 mV/s. [c]Estimated based on experimental data. [d]Estimated based on quantum-chemical calculations [1]

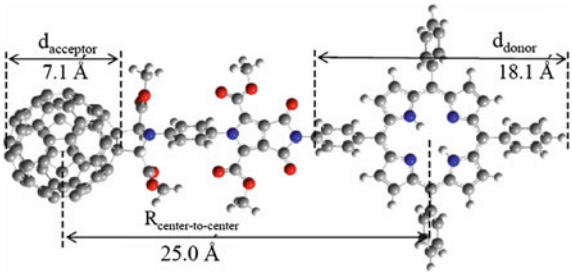

Fig. 20.8 Structural parameters in DFT (B3LYP/6-31G(d)) optimized structure of compound **1′a**

reported in the work of Williams [7]. According to that report, the inner reorganizational energy falls within 0.2–0.7 electron volt. The outer reorganizational energy (20.4) can be easily calculated [5] with the geometrical parameters of our compounds that we obtained from the DFT optimized structure (Fig. 20.8). Using these data, we calculated reorganizational energy in a number of solvents (Table 20.2) and found that, in a polar solvent like dichloroethane, the reorganizational energy should fall within the range 1.1–1.6 electron volts. Now let us compare it with the estimations for the Gibbs energy:

$$\lambda_{out} = e^2 \cdot (4\pi\varepsilon_0)^{-1} \cdot \left(d_{donor}^{-1} + d_{acceptor}^{-1} - R_{center-to-center}^{-1} \right) \cdot (n^{-2} - \varepsilon^{-1}) \qquad (20.4)$$

You can see that, in each case, both for estimation of Gibbs energy based on experimental data and on DFT calculations, the absolute value of the Gibbs energy is less than the reorganizational energy. That means we are in the normal Marcus-parabola region, and the trend for the rate constant must be the same as the trend for the driving force. So, unlike compounds with proton and methoxy substituents, the rate of charge-separated state formation in the bromine-substituted compound might not be sufficient for a successful competition with other relaxation processes.

Table 20.2 λ_{out} for compound 1′a in various solvents according to (20.4) [8]

Solvent	n_D^{20}	ε	λ_{out}, eV
Benzene	1.5011	2.27	0.007
Toluene	1.4969	2.38	0.058
Dichloromethane	1.4241	8.93	0.857
o-dichlorobenzene	1.5514	9.93	0.708
1,2-dichloroethane	1.4448	10.36	0.861

So, we have designed, synthesized, and studied novel porphyrin–fullerene dyads. We found that, in favorable cases, we have a lifespan of the charge-separated state in a microsecond range, a range which is quite good. Yet, we also found that the structural criteria that we formulated were not sufficient, and another factor should be also taken into account: the energy of the charge-separated state should be lowered to reduce the relative rate of the competitive processes.

Acknowledgements I would like to acknowledge Dr. A. V. Povolotskiy and Dr. A. S. Mereschenko who performed the transient absorption experiments, my colleagues, and collaborators whose contribution to this work is greatly appreciated: Prof. A. F. Khlebnikov, Mr. P.I. Prolubnikov, Dr. O. V. Levin, and Prof. A. Hirsch, and of course thank you for your kind attention.

References

1. A.S. Konev, A.F. Khlebnikov, P.I. Prolubnikov, A.S. Mereshchenko, A.V. Povolotskiy, O.V. Levin, A. Hirsch, Chem. Eur. J. **21**, 1237–1250 (2015)
2. D.I. Schuster, P. Cheng, P.D. Jarowski, D.M. Guldi, C. Luo, L. Echegoyen, S. Pyo, A.R. Holzwarth, S.E. Braslavsky, R.M. Williams, G. Klihm, J. Am. Chem. Soc. **126**, 7257–7270 (2004)
3. M.E. El-Khouly, J. Hasegawa, A. Momotake, M. Sasaki, Y. Araki, O. Ito, T. Arai, J. Porph. Phthalocyan. **10**, 1380 (2006)
4. Y. Kobori, Y. Shibano, T. Endo, H. Tsuji, H. Murai, K. Tamao. J. Am. Chem. Soc. **131**, 1624–1625 (2009)
5. R.A. Marcus, N. Sutin, Biochim. Biophys. Acta **811**, 265–322 (1985)
6. D. Rehm, A. Weller, Isr. J. Chem. **8**, 259–271 (1970)
7. R.M. Williams, Fullerenes as electron accepting components in supramolecular and covalently linked electron transfer systems. Ph.D. thesis, Faculty of Science, Van't Hoff Institute for Molecular Sciences, The Univeristy of Amsterdam, Amsterdam, (1996)
8. A.S. Konev, A.F. Khlebnikov, T.G. Nikiforova, A.A. Virtsev, H. Frauendorf, J. Org. Chem. **78**, 2542–2552 (2013)

Chapter 21
Optical Properties of Ultra-Small Gold Nanostructures

Tatsuya Tsukuda

21.1 Introduction

I will talk about the optical properties of very small gold (Au) nanostructures. Before talking about the main topic, let me briefly introduce our research activity. Figure 21.1 shows the difference between nanoparticles and clusters. The fundamental properties of nanoparticles are more or less scalable as a function of the diameter. However, when you reduce the diameter smaller than two nanometers (nm) and the number of constituent atoms is smaller than 100 atoms, they start to exhibit non-scalable properties and structures. For example, clusters show very different atomic packing, such as icosahedral and decahedral structures, and their energy levels are well quantized like conventional molecules. Thus we focus on such small clusters for future application as novel materials.

The first project is about the synthesis and catalytic application of two types of metal clusters, homogeneous and heterogeneous systems (see Fig. 21.2) [1]. We studied the effect of size and elements on the catalytic activity and selectivity for both systems. In heterogeneous systems, we can now change the number of atoms precisely with atomic precision [2], and we also can dope a single atom into well-defined clusters [3].

Another project is to establish the relationship between the structures and properties of small clusters. Figure 21.3 shows an overview of the optical properties of Au nanostructures as a function of diameter and morphology. As you may know, Au nanospheres larger than 2 nm show surface-plasmon resonance at 520 nm [4]. Au nanorods exhibit an additional plasmon band in the IR region [5, 6]. Today I will talk about the optical properties of small clusters less than 2 nm and nanorods and nanowires with a diameter of smaller than 2 nm. The first topic relates to the

T. Tsukuda (✉)
Department of Chemistry, School of Science, The University of Tokyo,
7-3-1 Hongo, Bunkyo-ku, Tokyo 113-0033, Japan
e-mail: tsukuda@chem.s.u-tokyo.ac.jp

K. Yamanouchi (ed.), *Progress in Photon Science*, Springer Series
in Chemical Physics 115, DOI 10.1007/978-3-319-52431-3_21

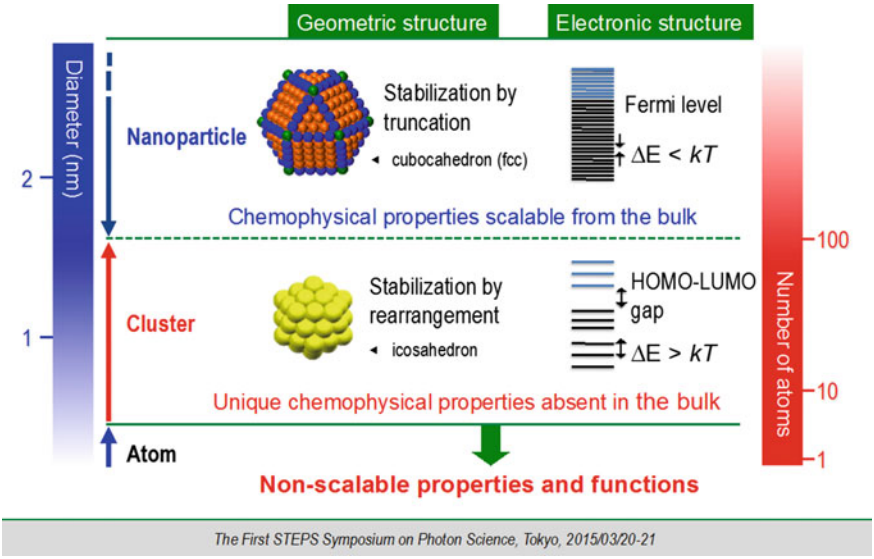

Fig. 21.1 Metal clusters as novel functional units

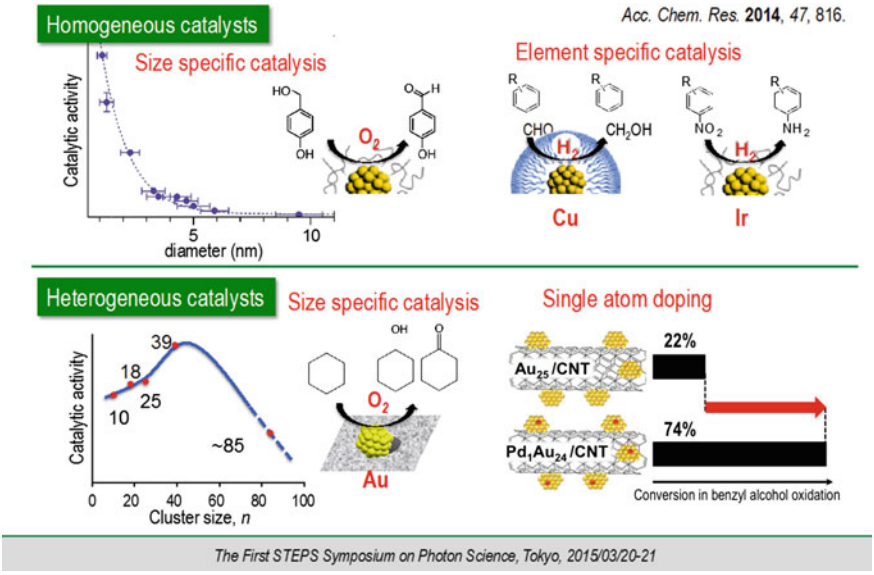

Fig. 21.2 Development of metal-cluster catalysts

surface-plasmon resonance of Au ultrathin nanorods and nanowires. The other part is about the optical properties of very small clusters that we call superatoms, superatomic molecules [7], and superatomic oligomers.

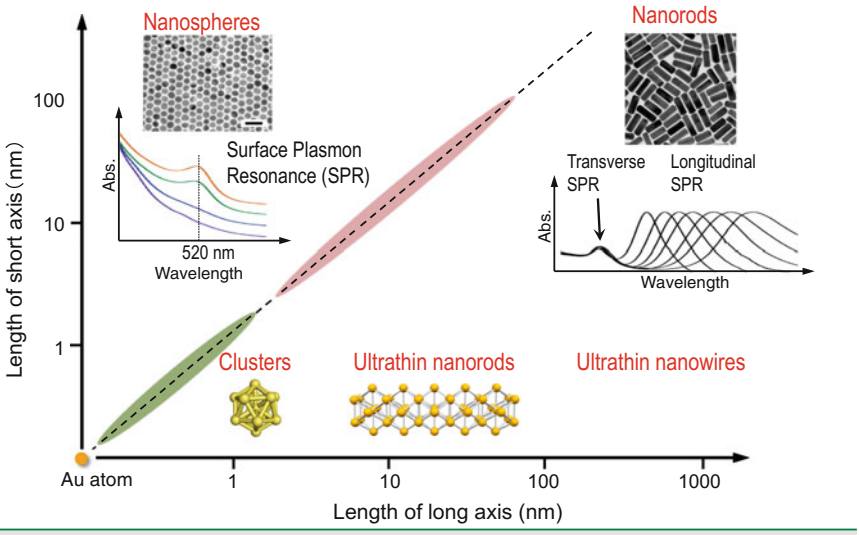

Fig. 21.3 Understanding structure-properties correlation

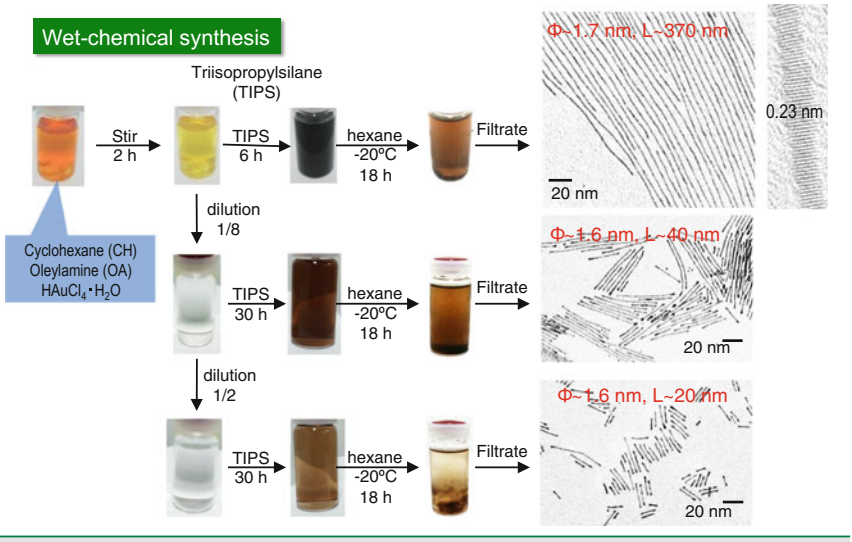

Fig. 21.4 Au ultrathin nanowires and nanorods (Au UTNWs and UTNRs)

We synthesized nanowires and nanorods with the diameter of less than 2 nm by reducing Au ions slowly in the presence of oleylamine [8] (see Fig. 21.4). I will not go into the details of the synthesis, but the key for the synthesis of anisotropic

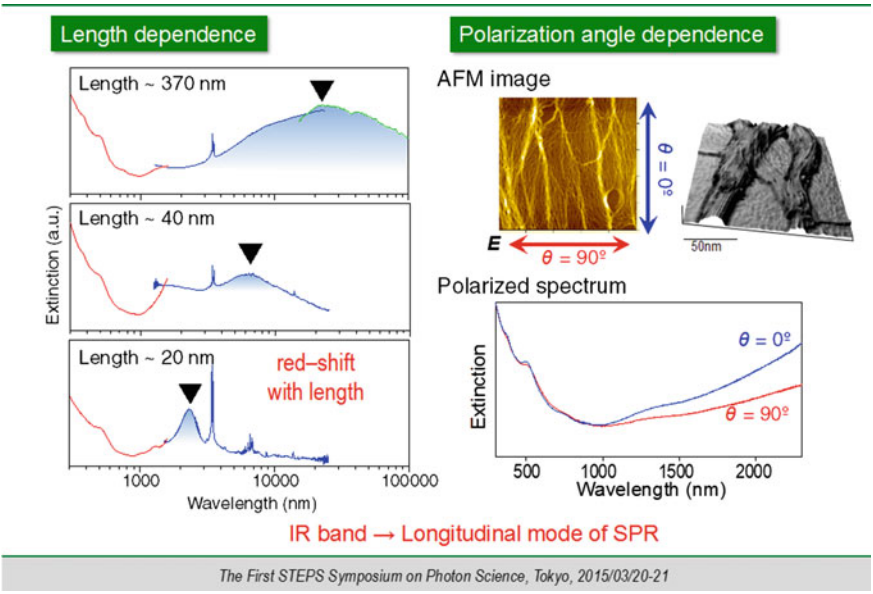

Fig. 21.5 Intense IR bands in Au UTNW and UTNR

structures is to reduce Au ions using the weak reducing agent triisopropylsilane (TIPS). The lengths were controlled while keeping the diameter constant by changing the concentration of the mother solution.

Then we measured the optical spectra of these wires and rods. New bands were observed in the IR region, and the peak position was red-shifted with an increase of the lengths (see Fig. 21.5). In order to assign the IR bands, we aligned the wires on the glass plate and conducted polarized spectroscopy. This result indicates this IR band is due to surface-plasmon resonance along the longitudinal axis of these unique structures. However, the wire does not show any plasmon-resonance band at 520 nm due to the small diameter (1.6 nm).

21.2 Optical Properties of Au Clusters

Let me move on to the optical properties of smaller Au clusters. The technical problem in their synthesis is to control the size of Au clusters with atomic precision. For this, we developed a synthetic method as shown in Fig. 21.6 [9, 10]. The first step is to prepare a mixture of small Au clusters by the conventional chemical method. The second step is to separate the mixture by size using these methods. For example, the crude mixture with brownish color was fractionated into a series of solutions with different colors as shown in the middle of Fig. 21.6. The final step is

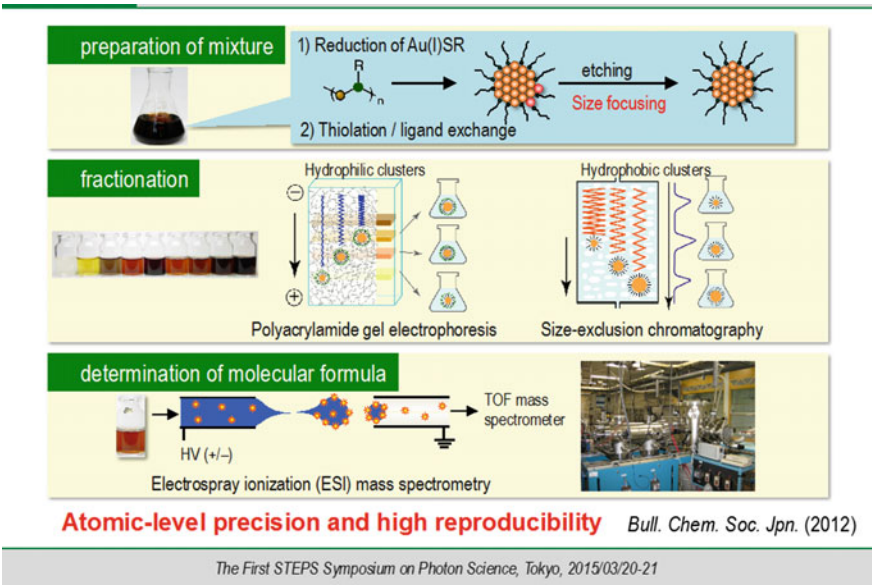

Fig. 21.6 Synthetic method of thiolated Au clusters

to determine the molecular formula in each fraction by using mass spectrometry; this is a home-made apparatus.

By using this approach, we can synthesize thiolate-protected Au clusters with the sizes ranging from several tens of atoms up to 500 atoms [11]. The left panel shows typical mass spectra of the thiolated Au clusters that we isolated. We can probe the evolution of the optical spectra as shown in Fig. 21.7. The surface plasmon band disappears, and sharp peaks become more prominent when the size becomes smaller than 187 atoms. The powder XRD-diffraction pattern indicates the atomic-packing changes from face-centered cubic (FCC) to non-bulk structures on going from Au_{187} to Au_{144} [11]. In the following, let me focus on the smaller region.

This is the first successful report of the precise synthesis of thiolate-protected Au clusters [9]. We can synthesize a series of clusters with various sizes as listed here. The numbers of Au atoms and the thiolate are shown in Fig. 21.8. The absorption spectra are shown in green. You can see the quantized nature of the electronic structures, and they show photoluminescence in sharp contrast to the bulk Au.

Among these series of clusters, we found that $Au_{25}(SR)_{18}$ clusters are very stable under harsh conditions in solution. 25–18 clusters survived, and all the other clusters were converted to 25–18 clusters in the presence of an excess amount of thiol [12]. We can easily synthesize 25–18 clusters on a large scale by a kinetic control of growth and etching [13]. These results indicated that 25–18 cluster is really a magic cluster (see Fig. 21.9).

Why are the 25–18 clusters so stable? There are two reasons (see Fig. 21.10). One is the geometrical structure. Among 25 Au atoms, 13 Au atoms form an icosahedral core, and their surface Au atoms are completely protected by the

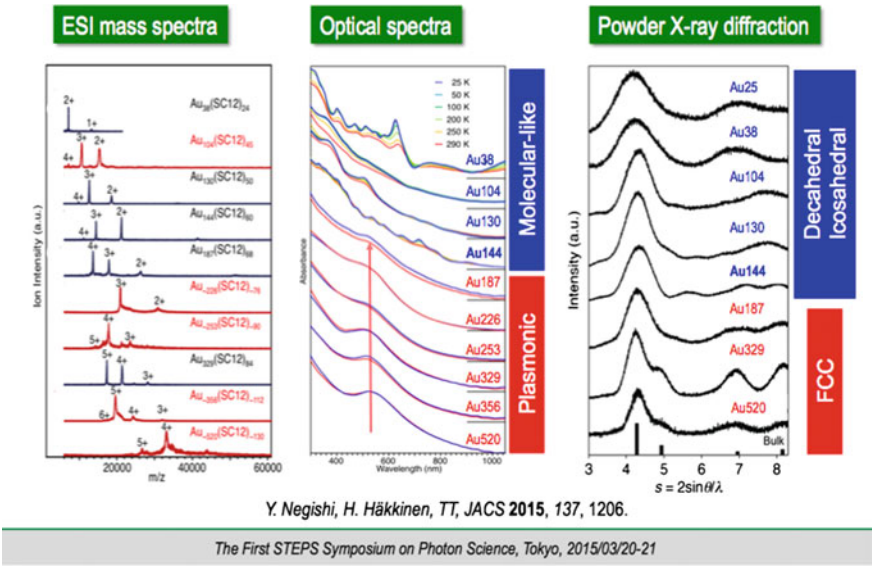

Fig. 21.7 Emergence of non-bulk structures

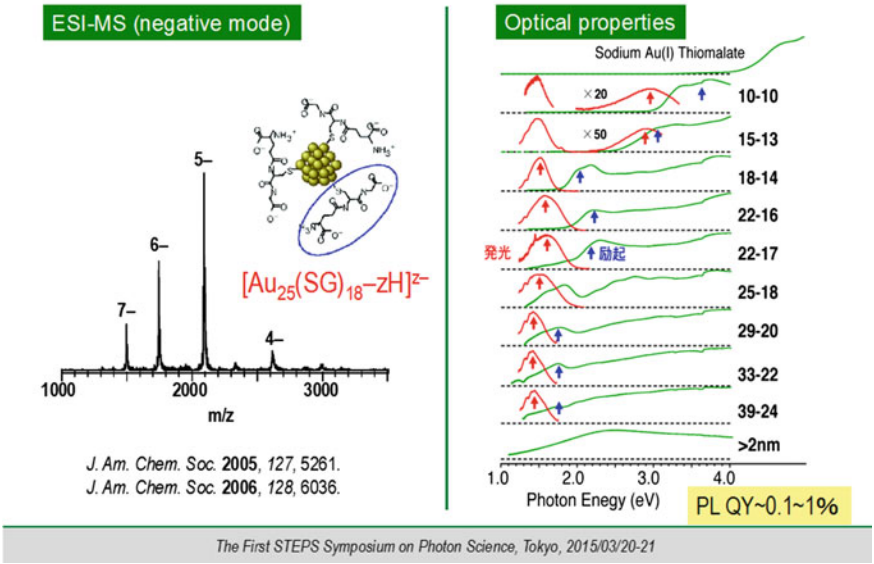

Fig. 21.8 Glutathione-protected Au_n clusters

Au-thiolate oligomers [14, 15]. The second reason is the electronic structure: the number of valence electrons in the Au_{13} core can be calculated to be 8 [16]. This number indicates the electronic shell is closed in this cluster core. These

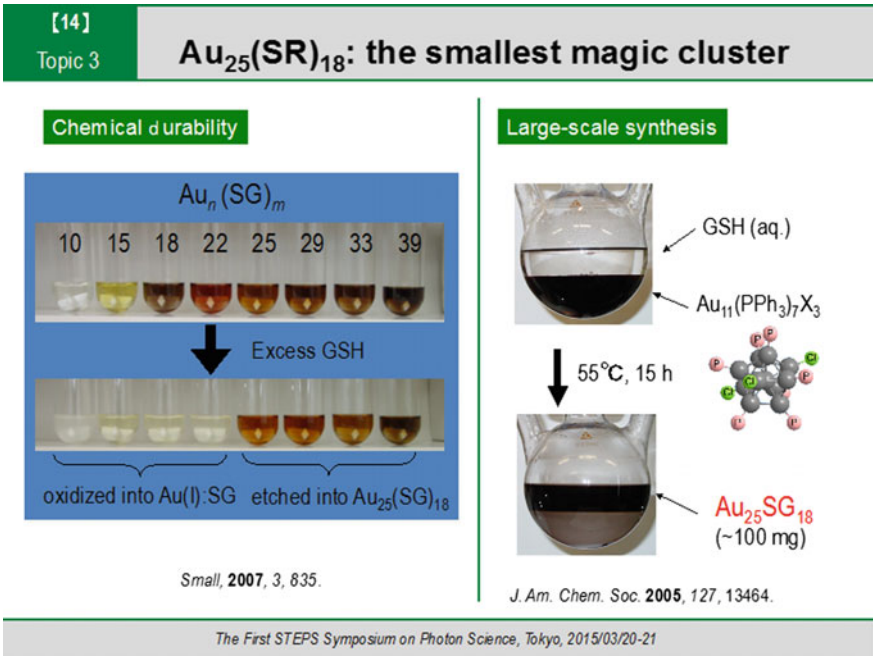

Fig. 21.9 $Au_{25}(SR)_{18}$: the smallest magic cluster

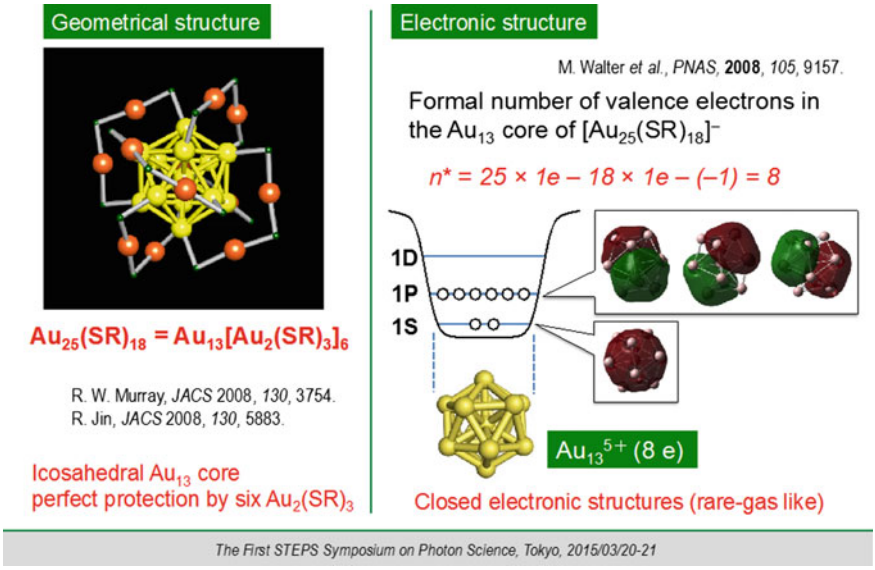

Fig. 21.10 $Au_{25}(SR)^{-}_{18}$: origin of magic stability

considerations lead us to conclude that this magic cluster can be viewed as a superatom with the closed electron configuration like that of a rare gas.

Now we can synthesize superatoms. Then what about quasi-molecules made of superatoms? I will talk very briefly about the optical properties of these dimers of superatoms (see Fig. 21.11) [7].

The upper left of Fig. 21.12 is the first example of dimers of Au_{13} superatoms published in 2008 [17]. We succeeded in synthesizing clusters composed of 38 Au atoms and 24 thiols. We proposed the structure with a bi-icosahedral Au_{23} core based on powder XRD and DFT calculations [18]. This structure was proved by single-crystal XRD experiment soon after our proposal [19]. This is the optical spectrum of this cluster compound. You can see many sharp peaks there, and the theory can explain these optical transitions [18].

Figure 21.13 is a theoretical predicted electronic structure of Au_{23} core [20]. It was found that the molecular orbital of an Au_{23} core looks very similar to F_2 molecule. The energy order is slightly different, but the morphology of the orbital is very similar. So we can consider the bonding scheme like this. We consider two Au_{13} superatoms with halogen-like electron configuration and combine them by removing three atoms. Namely, the Au_{23} core can be viewed as a halogen molecule version of superatoms.

The second example of the superatomic dimer is Au_{25} clusters protected by thiolates and phosphines. This is the structure of the Au_{25} core determined by single-crystal XRD (see Fig. 21.14) [21]. Interestingly, the Au_{25} core is formed by sharing one atom between two icosahedral Au_{13} superatoms. This Au_{25} cluster shows a very similar optical spectrum with that of Au_{13} moiety. But additionally, it

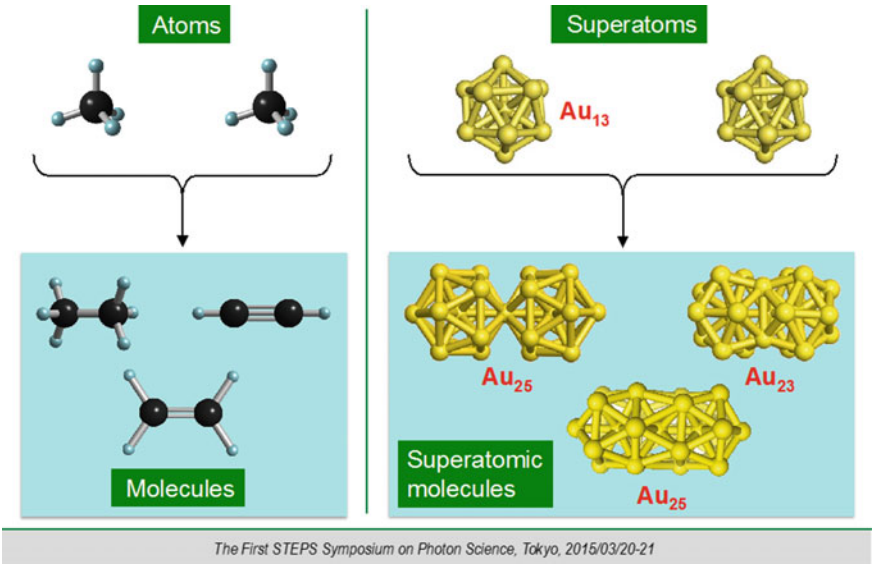

Fig. 21.11 Superatomic molecules?

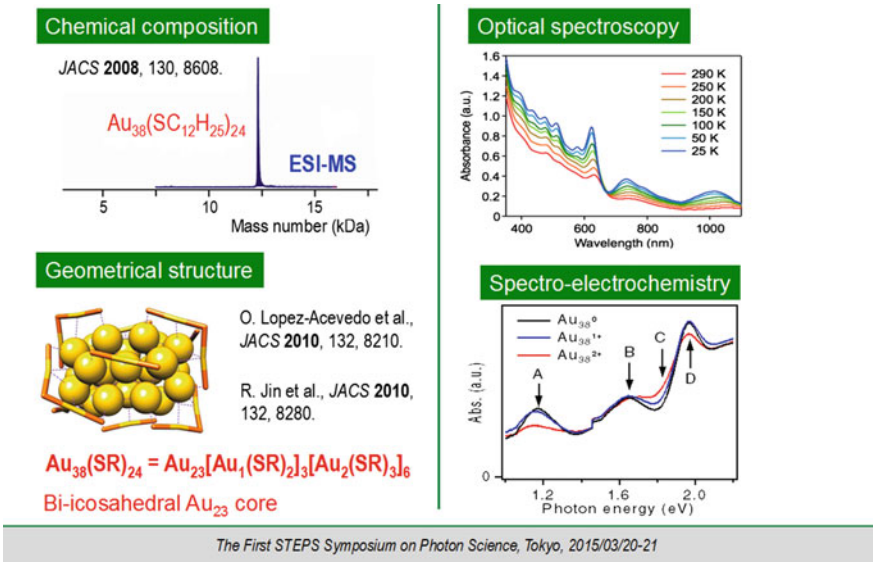

Fig. 21.12 Superatomic molecule, Au_{23}^{9+}(14e)

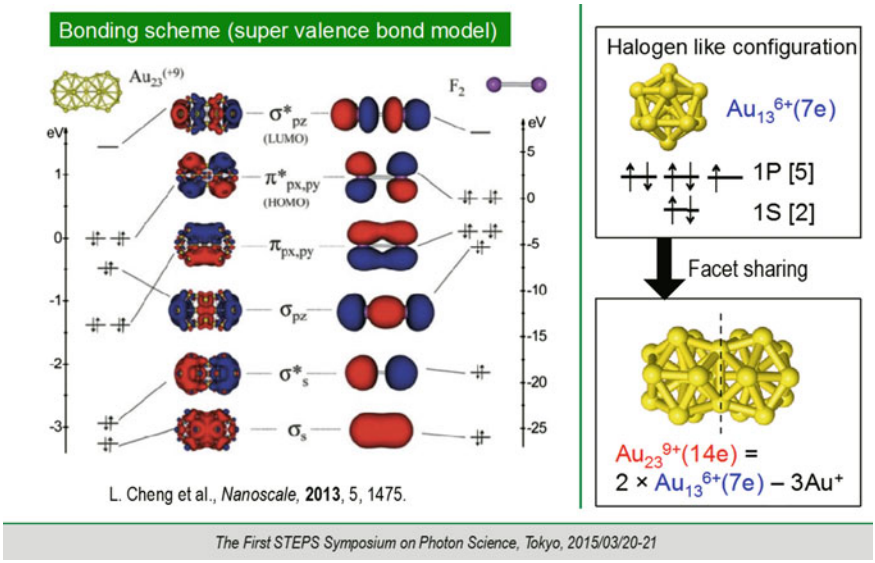

Fig. 21.13 Superatomic molecule, Au_{23}^{9+}(14e)

exhibits a new absorption peak and exhibits photoluminescence. Namely, the Au_{25} cluster not only retains properties of the icosahedral constituents, but also exhibits new properties due to the bonding. The bonding scheme of Au_{25} can be explained

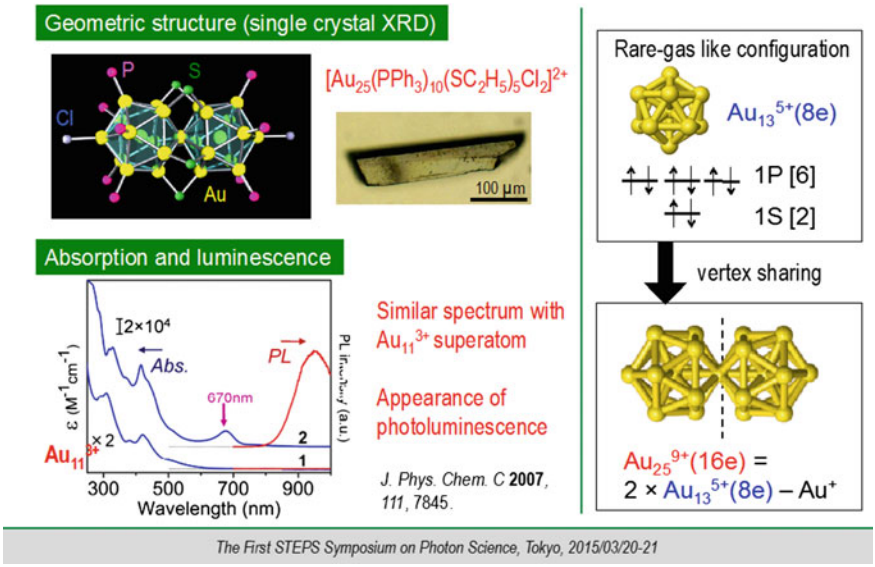

Fig. 21.14 Superatomic molecule, $Au_{23}^{9+}(16e)$

as follows. We consider superatoms with rare-gas like electron configuration as the building units, and then they are connected by removing a single atom shared by the two superatoms.

This is the third type of superatomic dimers (see Fig. 21.15). We obtained Au_{25} clusters protected by eleven bulky ligands [22]. Based on structure characterization by high-energy XRD, EXAFS and TEM, we conclude that eleven thiolates are directly bonded to the surface of Au_{25} core. The optical spectrum of this cluster has a less-structured profile as compared with the bi-icosahedral Au_{25} introduced in the previous slide. This suggests that the two superatoms are fused together more strongly than in the previous one. We proposed that the core has a twisted bi-icosahedral structure as shown here. This structure can be constructed by icosahedral Au_{13} with halogen-like electron configuration.

In summary, we can synthesize a variety of superatomic molecules—made of two superatoms with different electron configurations (see Fig. 21.16). Then what about trimers and oligomers?

There is no experimental report for the synthesis of this class of higher superatomic molecules, but the theory predicts that trimers [23] and polymers [24] can be synthesized (see Fig. 21.17). More interestingly, the theory predicts that conductance depends strongly on how the superatoms are connected [24].

In the final Fig. 21.18, let me introduce our recent results toward the synthesis of larger superatomic molecules [25]. Slow reduction of Au ions in the presence of this ligand yielded greenish Au nanostructures. By using mass spectrometry and thermogravimetric analysis, we conclude that the cluster is composed of 76 Au atoms and

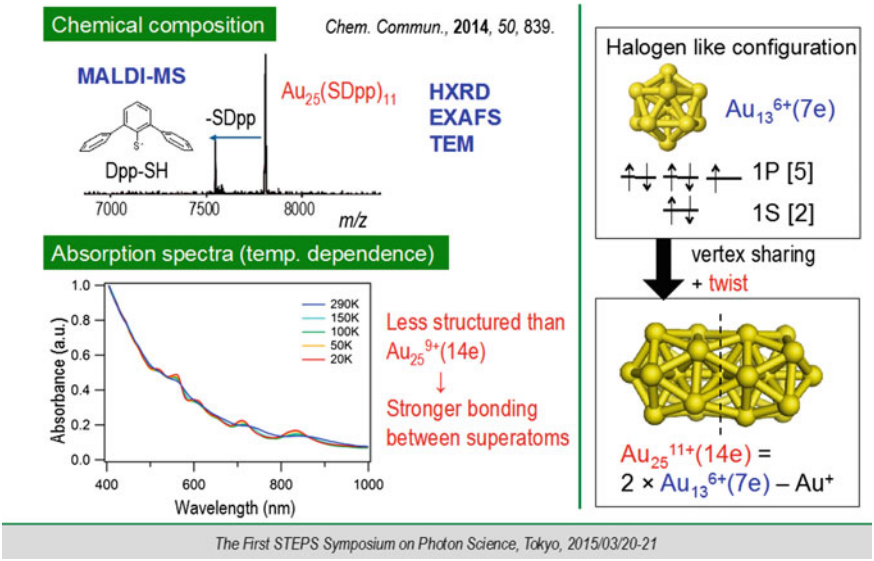

Fig. 21.15 Superatomic molecule $Au_{25}^{11+}(14e)$

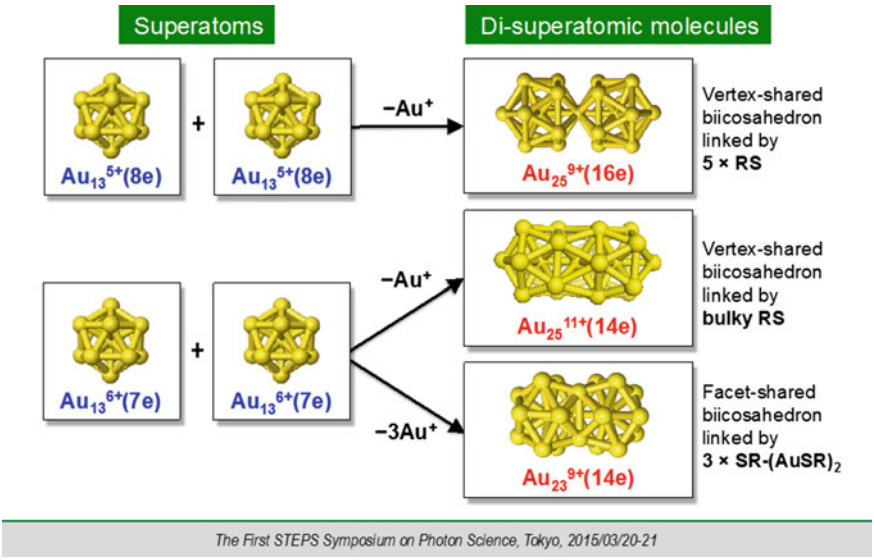

Fig. 21.16 Di-superatomic molecules

44 thiolate. We propose, based on the powder XRD analysis, that the cluster has an oligomeric structure made of the cuboctahedral Au_{13} units. This cluster shows a strong absorption in the IR region which may be assigned to a HOMO-LUMO transition.

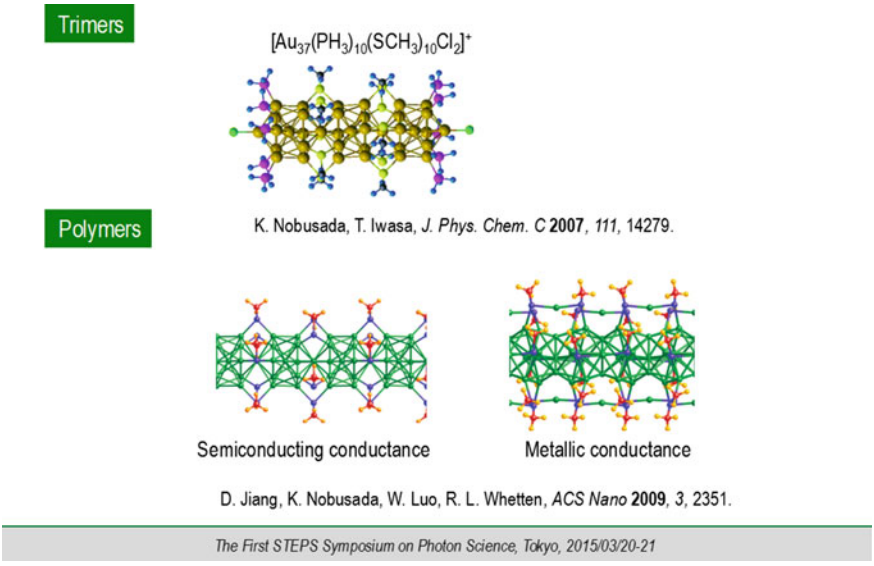

Fig. 21.17 Superatomic oligomers/polymers?

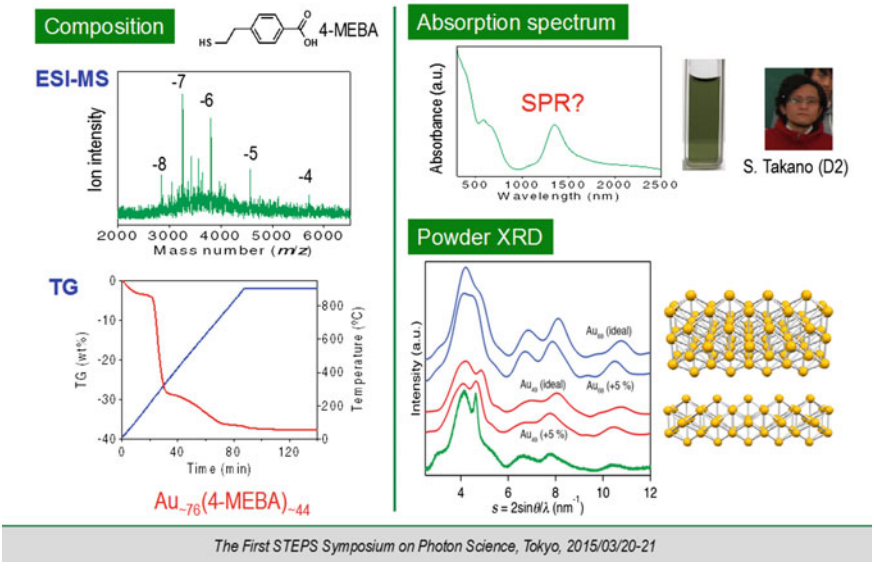

Fig. 21.18 Superatomic oligomers/polymers

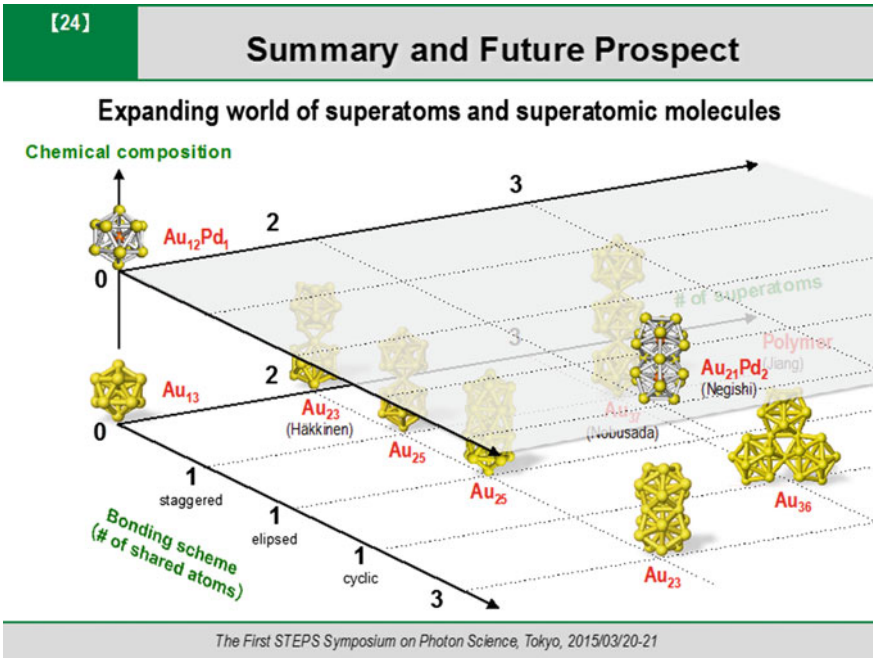

Fig. 21.19 Summary and future prospect

21.3 Summary

As demonstrated in my talk, we can synthesize a variety of superatoms and their dimers with various bonding schemes. I believe that larger superatomic molecules can be synthesized in the future (see Fig. 21.19). Another interesting structure parameter is the chemical composition. I cannot tell you about it today, but we can now synthesize a variety of alloy clusters that contain Pd, Pt, Ag, and Cu [26]. I hope that we can expand the world of superatoms and superatomic molecules.

References

1. S. Yamazoe, K. Koyasu, T. Tsukuda, Acc. Chem. Res. **47**, 816 (2014)
2. Y. Liu, H. Tsunoyama, T. Akita, S. Xie, T. Tsukuda, ACS Catal. **1**, 2 (2011)
3. S. Xie, H. Tsunoyama, W. Kurashige, Y. Negishi, T. Tsukuda, ACS Catal. **2**, 1519 (2012)
4. K.L. Kelly, E. Coronado, L.L. Zhao, G.C. Schatz, J. Phys. Chem. B **107**, 668 (2003)
5. C.J. Murphy, T.K. Sau, A.M. Gole, C.J. Orendorff, J. Gao, L. Gou, S.E. Hunyadi, T. Li, J. Phys. Chem. B. **109**, 13857 (2005)
6. J. Pérez-Juste, I. Pastoriza-Santos, L.M. Liz-Marzán, P. Mulvaney, Coord. Chem. Rev. **249**, 1870 (2005)

7. J. Nishigaki, K. Koyasu, T. Tsukuda, Chem. Rec. **14**, 897 (2014)
8. R. Takahata, S. Yamazoe, K. Koyasu, T.J. Tsukuda. Am. Chem. Soc. **136**, 8489 (2014)
9. Y. Negishi, K. Nobusada, T. Tsukuda, J. Am. Chem. Soc. **127**, 5261 (2005)
10. T. Tsukuda, Bull. Chem. Soc. Jpn. **85**, 151 (2012)
11. Y. Negishi, T. Nakazaki, S. Malola, S. Takano, Y. Niihori, W. Kurashige, S. Yamazoe, T. Tsukuda, H. Häkkinen, J. Am. Chem. Soc. **137**, 1206 (2015)
12. Y. Shichibu, Y. Negishi, H. Tsunoyama, M. Kanehara, T. Teranishi, T. Tsukuda, Small **3**, 835 (2007)
13. Y. Shichibu, Y. Negishi, T. Tsukuda, T. Teranishi, J. Am. Chem. Soc. **127**, 13464 (2005)
14. M.W. Heaven, A. Dass, P.S. White, K.M. Holt, R.W. Murray, J. Am. Chem. Soc. **130**, 3754 (2008)
15. M. Zhu, C.M. Aikens, F.J. Hollander, G.C. Schatz, R.J. Jin, Am. Chem. Soc. **130**, 5883 (2008)
16. M. Walter, J. Akola, O. Lopez-Acevedo, P.D. Jadzinsky, G. Calero, C.J. Ackerson, R.L. Whetten, H. Grönbeck, H. Häkkinen, Proc. Natl. Acad. Sci. USA **105**, 9157 (2008)
17. N.K. Chaki, Y. Negishi, H. Tsunoyama, Y. Shichibu, T. Tsukuda, J. Am. Chem. Soc. **130**, 8608 (2008)
18. O. Lopez-Acevedo, H. Tsunoyama, T. Tsukuda, H. Häkkinen, C.M. Aikens, J. Am. Chem. Soc. **132**, 8210 (2010)
19. H. Qian, W.T. Eckenhoff, Y. Zhu, T. Pintauer, R. Jin, J. Am. Chem. Soc. **132**, 8280 (2010)
20. L. Cheng, C. Ren, J. Zhang, X. Yang, Nanoscale **5**, 1475 (2013)
21. Y. Shichibu, Y. Negishi, T. Watanabe, N.K. Chaki, H. Kawaguchi, T. Tsukuda, J. Phys. Chem. C **111**, 7845 (2007)
22. J. Nishigaki, S. Yamazoe, S. Kohara, A. Fujiwara, W. Kurashige, Y. Negishi, T. Tsukuda, Chem. Commun. **50**, 839 (2014)
23. K. Nobusada, T. Iwasa, J. Phys. Chem. C **111**, 14279 (2007)
24. D. Jiang, K. Nobusada, W. Luo, R.L. Whetten, ACS Nano **3**, 2351 (2009)
25. S. Takano, S. Yamazoe, K. Koyasu, T. Tsukuda, J. Am. Chem. Soc. **137**, 7027 (2015)
26. T. Tsukuda, H. Häkkinen, *Protected metal clusters: from fundamentals to applications* (Elsevier, Amsterdam, 2015)

Part VIII
Light Propagation and Its Applications

Chapter 22
Femtosecond Filaments and Their Plasma Channels in a Focused Laser Beam in Air

Svyatoslav Shlenov

It will be a short introduction to the physics of filament and plasma channels in the air and a few words about numerical simulations of pulse propagation in the regime of filamentation. Then I will be speaking about comparative analysis of infrared and ultraviolet filaments in focused beams, filamentation of the pulse with wave-front astigmatism of the beam, and the influence of dynamic wave-front aberration on filamentation.

If we are talking about filamentation in air, we consider pulses at wavelengths around 800 nm in infrared and 248 nm in ultraviolet. Since we want to obtain filamentation, the pulse-peak power should be higher than the critical power for self-focusing in air. This means the peak power should be higher than 6 GW in infrared and higher than 70 MW in ultraviolet. We will consider pulse durations from 10^{-14} s and up to one picosecond, and this means that the energy should be higher than 1 mJ in infrared.

Figure 22.1 actually was taken from the presentation by Olga Kosareva. She explained about the physics of filamentation in detail. So I would just like to remind you that the fundamental mechanism of the filamentation process is the dynamical balance between self-focusing induced by the optical Kerr effect and defocusing due to self-generated plasma in this self-focal region. So, the filamentation is accompanied by formation of a conducting plasma channel in air.

The plasma electron concentration is not very high: It reaches approximately 0.1% of neutrals, and these electrons remain free for a few nanoseconds after each laser pulse. So, the instant length of the plasma channel is around 1 m, or a little bit longer, and this plasma channel arises in the wake of the pulse and propagates with the pulse.

S. Shlenov (✉)
Department of Physics and International Laser Center, Lomonosov Moscow State University, Leninskie Gory 1, GSP-1, Moscow 119991, Russia
e-mail: shlenov@physics.msu.ru

K. Yamanouchi (ed.), *Progress in Photon Science*, Springer Series in Chemical Physics 115, DOI 10.1007/978-3-319-52431-3_22

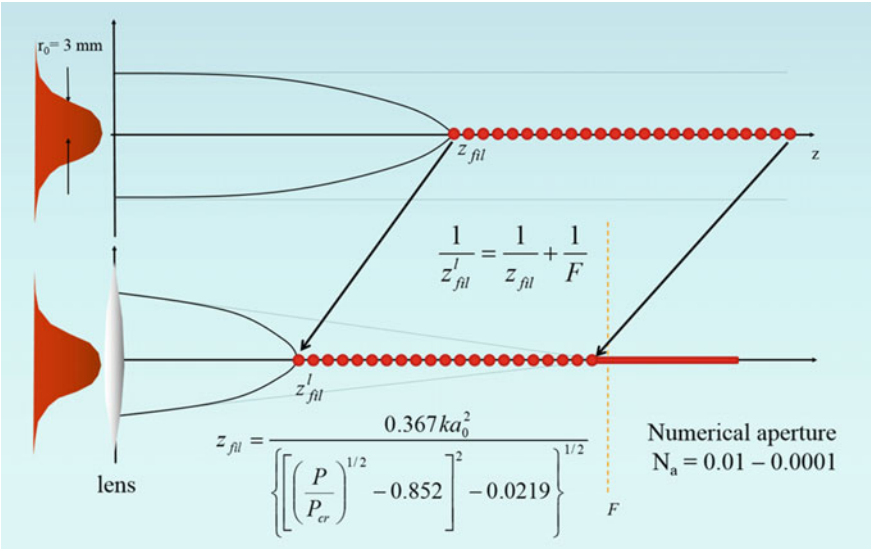

Fig. 22.1 Laser-induced filamentation in a focused pulsed beam

These plasma channels could be applied to create a wave guide in the air for directed propagation of other pulses, for example, microwave pulses. So it is important to study the characteristics of such plasma channels and to be able to control the position, length, and concentration of electrons in them. In a laboratory experiment, it is easier and more convenient to deal with focused beams. In this case, the start of the filamentation is shifted closer to the laser system. The distance to the start of the filamentation can be calculated using just a simple formula for a thin lens (Fig. 22.1).

Here in the picture, the dashed line shows the position of the focal plane, and F is the focal length of an external focusing system. The distance z_{fil} to the start of filamentation of the collimated beam can be estimated using the Marburger formula. The result is the distance to the filament in focused beams. We considered the beams with numerical aperture varying from 0.01 (which is relatively tight focusing) to 0.0001 (loose focusing).

The numerical simulation of pulse propagation is based on the self-consistent system of the equations: the propagation equation for the slowly varying envelope of the electrical field, which takes into account diffraction, dispersion, Kerr nonlinearity (both terms: instantaneous and delayed one), plasma refraction and losses due to ionization, and the kinetic equation for the concentration of free electrons (Fig. 22.2).

There are actually two kinetic equations for the main components of air: molecules of oxygen and nitrogen. The coefficient '*R*' here is the free-electron generation rate. We calculated this coefficient using different models for ultraviolet and infrared pulses.

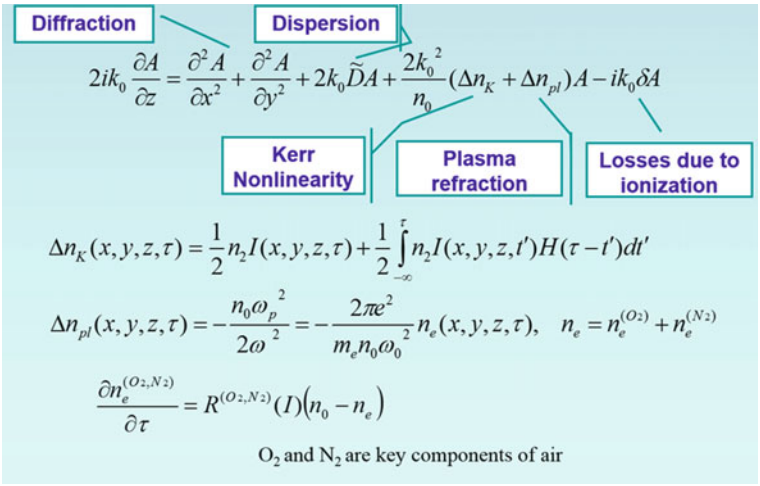

Fig. 22.2 Numerical simulation of pulse propagation

In the case of multiphoton ionization, the Keldysh parameter 'γ' is much higher than unity, and the electron generation rate is described by the power dependence on intensity. For example, for molecules of oxygen, the multiphoton order is 3 for ultraviolet and 8 for infrared. But, inside an infrared filament, the Keldysh parameter is approximately unity. So in this case, the multiphoton ionization model is not the best one, and we used the so-called PPT or Perelomov, Popov, Terentev model, which actually saturates MPI rates at high intensities.

To compare infrared and ultraviolet filamentations, we considered Gaussian pulses of an identical pulse duration (60 fs), beam radius (3 mm), and focal length F. The excess of the pulse peak power P over critical power P_{cr} was also the same at the two wavelengths and equal to 5, which ensured the formation of a single filament. It resulted in the difference of the other pulse parameters: pulse energy, initial peak intensity, diffraction, dispersion length, and the distance to the filament start z_{fil}.

After numerical solutions of these equations, we calculated such pulse characteristics such as fluence, peak on-axis intensity, plasma density in the wake of the pulse, linear plasma density, which is actually the integral of the electron concentration over the beam cross section, and the total number of free electrons in the plasma channel.

This is the peak electron concentration obtained in numerical simulations as a function of the external focal length (Fig. 22.3). In Figs. 22.3, 22.4 and 22.5, the red color denotes infrared pulses and the blue color denotes ultraviolet pulses. The peak electron density in the plasma channel of UV filament in a weakly focused beam is almost an order of magnitude smaller than in the channel of IR filament. The peak electron density in a relatively-tightly focused UV pulse, vice versa, may exceed the electron density in the plasma channel of an IR pulse.

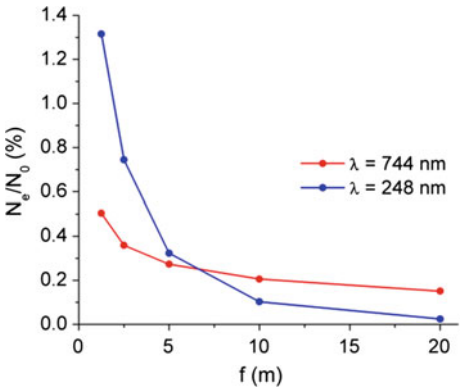

Fig. 22.3 Peak electron concentration as a function of the external focal length

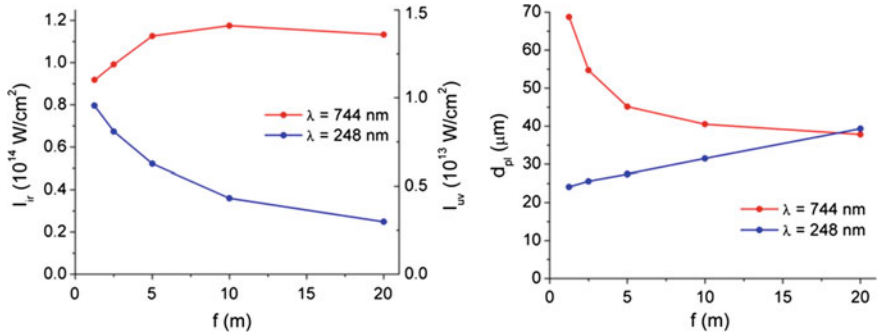

Fig. 22.4 The maximum laser-field intensity (*left*) and the diameter of the plasma (*right*) as a function of the external focal length

Fig. 22.5 Ionization model (indicated in parentheses) dependence of the laser-field intensities

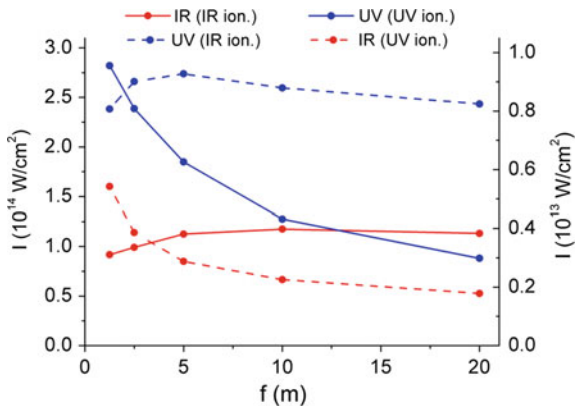

The peak intensity (Fig. 22.4 (left)) and the diameter of the plasma channel (Fig. 22.4 (right)) in the UV and IR pulses exhibit a qualitatively different behavior with the change of the focal length. For example, the peak intensity in the infrared pulse drops if the focusing is tight, while in the ultraviolet pulse it increases. The diameter of the plasma channel decreases in ultraviolet pulses and increases in infrared ones in a tight-focusing regime.

The difference in behavior of these dependencies can be explained by the different multiphoton order for these two wavelengths. To verify this assumption, we made a series of numerical simulations in which the model of the ultraviolet multiphoton ionization was used for infrared pulses and, vice versa, the model of infrared ionization was used for ultraviolet pulses.

The resulting peak intensities in the filament are shown on Fig. 22.5. The solid curves were obtained with the correct model. The dashed curves indicate the peak intensity in the simulations with the "vicarious" model. We can see that the behavior of the curves is very similar for infrared and ultraviolet pulses with the same model of ionization. So, it allows us to say that the main reason for the difference between the behavior of the characteristics of the infrared and ultraviolet pulses under filamentation is the order of multiphoton ionization, which is different for these pulses.

The experimental study of the filamentation under a similar condition was carried out by our colleagues in Lebedev Physical Institute of Russian Academy of Science in Moscow, in the laboratory headed by Professor Ionin. In the experiment, they used a Ti:Sapphire laser system, which produced 100 fs pulses with energy of 6 mJ at a wavelength around 744 nm. The third harmonic at the wavelength of 248 nm was used to study UV filamentation.

After focusing the lens or, in some experiments, the mirror, the convergent beam formed a filament at some distance in air. To measure the linear plasma density, they used two metallic hemispheres with the gap of around several mm. The voltage between them was 300 V. When the propagating pulse generates plasma, the conductivity between the electrodes changes. This could be detected by an oscilloscope measuring the recharging current and the variation of voltage.

The results of the experiment (dots) and numerical simulations (solid curves) are shown in the next slide for various pulse energies (Fig. 22.6). Lower energy on the top and higher energy at the bottom; infrared pulses to the left and ultraviolet pulses to the right. Both in the numerical simulation and in the experiment, the length of the plasma channel increases with increases of the pulse energy, and its start is shifted closer to the laser system.

The peak values of the linear electron concentration obtained in the numerical simulation are consistent with the values obtained in the experiment in the sense, i.e., doubling of the pulse energy results in doubling of the signal recorded in the experiment for both wavelengths, as it is in the numerical simulations. The main difference between the calculations and the experimental data is that the plasma channels in the experiment are nearly twice as long as in the computer simulations.

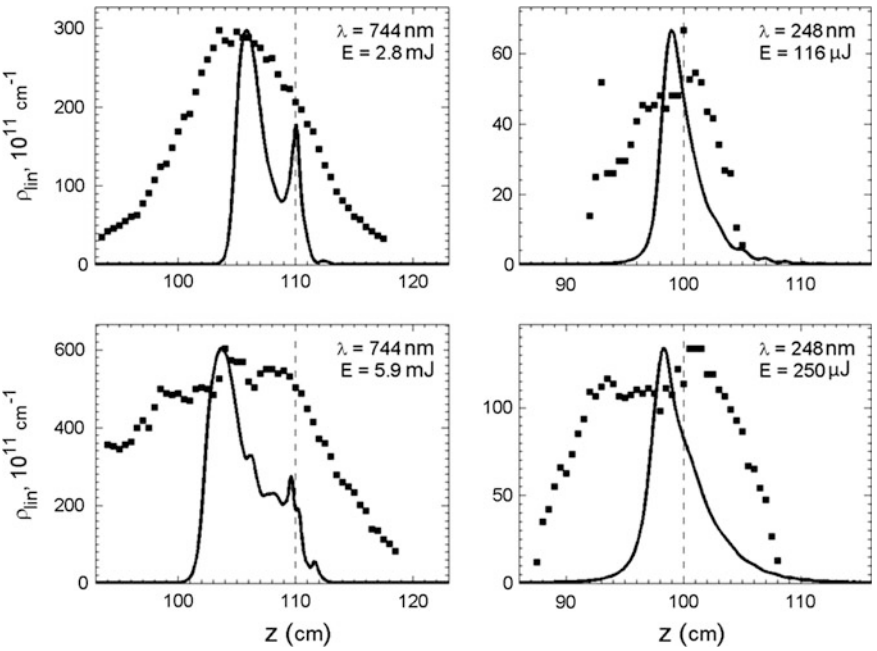

Fig. 22.6 The linear density of the plasma obtained in the experiment (*dots*) and numerical simulations (*solid curves*) for various pulse energies [1]

One of the reasons for that could be aberrations of the beam wave front, for instance, wave-front astigmatism. The phase in this case can be written as having two terms, which correspond to two foci at different distances along the propagation direction, e.g., the front focus on the horizontal plane and back focus in the perpendicular plane. Since there are differences between the two foci, we can introduce the astigmatism parameter to characterize these aberrations. Actually, this is a difference between the two foci divided by average focus.

Figure 22.7 an increase in astigmatism of the wave front leads to a monotonic decrease in the peak intensity inside the filament and a decrease in plasma density, both for infrared and ultraviolet pulses [2]. Under the strong astigmatism beam, focusing actually occurs initially only in one of the transverse directions. This kind of focusing prevents quick formation of the nonlinear focus. The focus only in one plane requires a weaker negative lens, formed by the self-induced plasma, to arrest beam collapse. Therefore, the peak intensity can be less than in the case of aberration-free beam.

A decrease in intensity causes a sharp drop in the rate of ionization according to both models that we used in our simulation and therefore in the electron density in the laser plasma. At the same time, the transverse size of the plasma channel of the infrared pulse remains almost unchanged. This eventually leads to a rather sharp decrease of the total number of electrons in the plasma channel (Fig. 22.8). The transverse size of the plasma channel of ultraviolet pulses increases with the increase

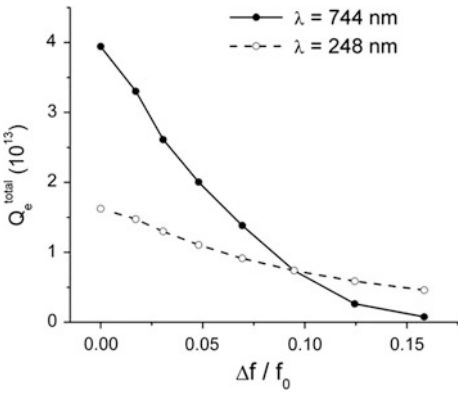

Fig. 22.7 Total number of electrons in the wake of IR and UV pulses as functions of the astigmatism parameter

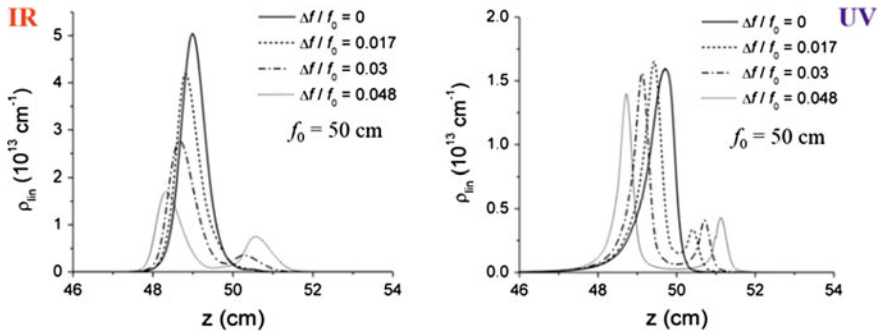

Fig. 22.8 Linear plasma density profiles along the propagation path for various parameters of astigmatism for infrared (left) and ultraviolet (right) pulses

of the astigmatism parameter. As a result, the linear-plasma concentration and the total number of electrons decrease more slowly than in the case of infrared pulses.

These are linear plasma-density profiles along the propagation path for various parameters of astigmatism (Fig. 22.9). Again, infrared pulses to the left, ultraviolet pulses to the right. Analyzing linear plasma density profiles along the propagation direction (Fig. 22.9) we can see that an increase in the astigmatism leads to the formation of a slightly longer plasma channel. The peak values of the linear electron concentration are significantly reduced in the case of infrared pulses, while, in the case of ultraviolet pulses, the peak values decrease much less with increasing astigmatism parameter. What is more interesting is that stronger astigmatism causes splitting of a single channel into two regions near the front and the back foci.

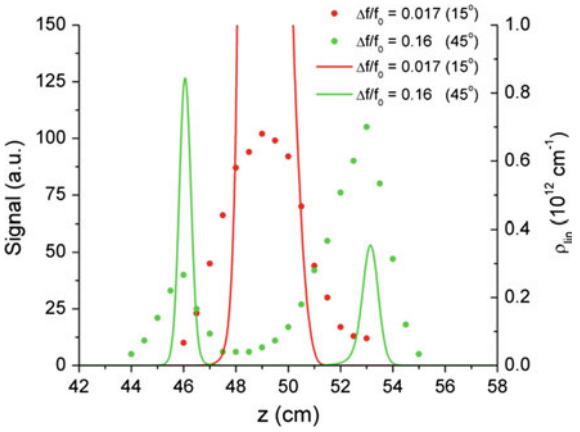

Fig. 22.9 Linear plasma-density profiles along the propagation path for various parameters of astigmatism obtained in the experiment (dots) and numerical simulations (solid curves) [2]

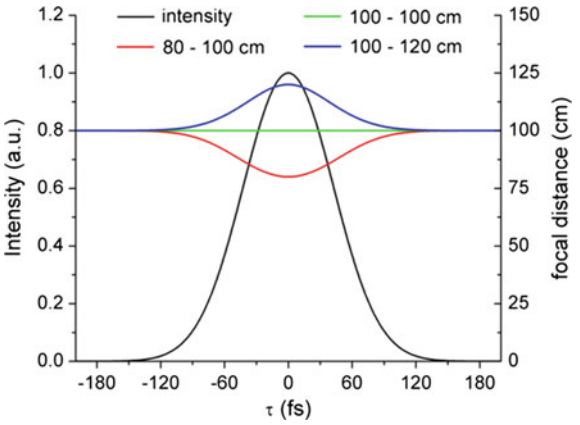

Fig. 22.10 Schematic picture of the change in focal length during the pulse in the case of positive (red curve) and negative (blue curve) nonlinearity. Initial focal length (green line) and the pulse temporal profile (black curve) are also shown

The wave-front astigmatism occurs when the incident beam hits the focusing mirror at some angle. In the experiment, which was done by Professor Ionin's group, the incident beam after focusing by the mirror formed a filament. The astigmatism parameter can be calculated if we know the incident angle 'α'. The plasma channel of the laser filament with weak astigmatism (angle 'α' is 15°) is continuous. With increase in astigmatism (angle 'α' is 45°), it is torn into two separate regions (Fig. 22.9).

Another reason to stimulate longer plasma channels is so-called dynamic wave-front aberrations, which can occur in solid-state pass-through optics. Since the nonlinearity in the solids is much higher than in gases, even a thin lens or a plate can influence subsequent filamentation of the pulse. Even if a so-called B integral is less than a unit, which means that the small-scale self-focusing does not occur in pass-through optics, the pulse self-phase modulation acquired in solids can influence the pulse filamentation afterwards, even in air.

The phase shift after propagating through a solid-state plate can be estimated using a simple formula with the assumption that the plate is thin enough. Then we can estimate the focal length of a nonlinear lens that arises in this case. This focal length depends on time during the pulse itself. Therefore, there is an addition to the focal length of the external lens, which depends on the time. If the nonlinearity is positive (as in fused silica or other materials), the focal length of the resulting lens becomes smaller in the central part of the pulse. On the leading and trailing edges of the pulse, where power is less than in the central part, nonlinear focusing is weaker. The difference in instant focal length can reach, for example, 20% for a fused silica plate of 1-mm thickness (Fig. 22.10).

The fluence distribution in air obtained in numerical simulations, after pulse propagating in fused silica plate, is presented in the lower image in Fig. 22.11. For comparison, the upper figure shows fluence in the absence of the plate. Self-phase modulation in a fused silica plate leads to the increase in the filament length. Due to the greater wave-front curvature, the central time slices of the pulse are focused closer to the focusing mirror, thus stimulating earlier filament start and plasma-channel onset.

Figure 22.12 shows plasma channels of the pulse after dynamic wave-front aberrations. Here the green color stands for the no-aberration case, when the focal length is constant. The red curve stands for positive nonlinearity and the blue color for negative nonlinearity. We can see that the positions of the start of the filament differ, but the end of the filament is at the same distance for each case. Positive nonlinearity means the additional focusing of the central time slices of the pulse due to the self-focusing in the plate. The plasma channel in this case starts earlier than without a plate but ends at practically the same distance. The channel therefore becomes longer. The negative nonlinearity, for the same reason, would shorten the plasma channel.

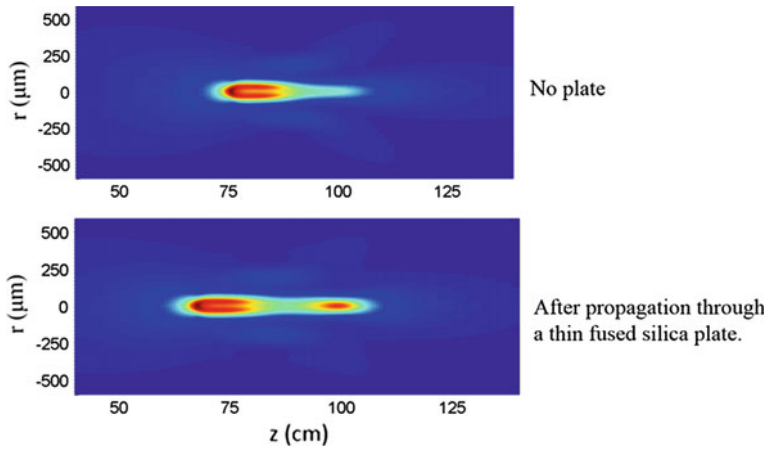

Fig. 22.11 Fluence distribution in air after propagating in the fused silica plate

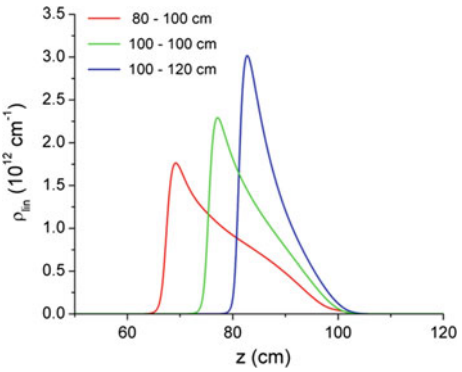

Fig. 22.12 Linear concentration of electrons in the plasma channels of the pulse after dynamic wave-front aberrations

In conclusion, we studied the characteristics of a single, femtosecond filaments in focused beams at wavelengths of 744 and 248 nm. The peak intensity and the diameter of the plasma channel in ultraviolet and infrared pulses exhibit a qualitatively different behavior. Weak wave-front astigmatism increases the length of the plasma channel compared with an aberration-free focusing. Strong astigmatism leads to the formation of two separate regions of the plasma column near the front and back foci. Self-phased modulation after high-power pulse propagation through the transparent solid dielectrics can shift the filament closer to the laser system, making the plasma channel of the filament longer.

References

1. A.A. Dergachev, A.A. Ionin, V.P. Kandidov, et al. Quantum Electron. **43**, 29–36 (2013)
2. A.A. Dergachev, A.A. Ionin, V.P. Kandidov, et al. Quantum Electron. **44**, 1095–1090 (2014)

Chapter 23
Coherent Photon Technology: Science to Innovation

Junji Yumoto

I will talk about coherent photon technology, especially, we are now working on coherent addition for generation of short pulses with a high peak intensity. The development of Coherent Photon Ring aiming at the generation of high-power and short laser pulses covering soft-UV, visible, IR and THz region is also presented.

The second topic addresses some activities about the technological transfer of cutting-edge knowledge to industry. That is the reason the title of my talk includes the subtitle "Science to Innovation". Actually, we started a new program supported by the Ministry of Education in 2013. Our project name is Innovative Center for Coherent Photon Technology. I will give some explanations of our activities connected to this project.

Figure 23.1 shows the evolution of laser technology. The first laser was demonstrated in 1960, and Charles H. Townes, Nicolay G. Basov and Aleksandr M. Prokhorov were awarded the Nobel Prize in 1964. So we already have a history of more than 60 years of laser technology, but, in the last decade, we have had great progress in coherence control using mode-locked laser pulses.

The first demonstration of the carrier-envelope phase (CEP) control using a femtosecond mode-locked laser was carried out by Professors John Hall and Theodor Hänsch in 2000, and they were awarded the Nobel Prize in 2005.

Figure 23.2 explains the concept of CEP control using a mode-locked laser. We can control the carrier phase in each pulse envelope, and this technique enables us to add each pulse constructively. The phase of the optical pulses in the cavity is also completely matched with the input pulses, so we can add each pulse coherently in the cavity. This enables us to accumulate the input pulses coherently and to obtain femtosecond optical pulses with a large pulse energy.

J. Yumoto (✉)
Institute for Photon Science and Technology, Faculty of Science,
The University of Tokyo, 7-3-1 Hongo, Bunkyo-ku, Tokyo 113-0033, Japan
e-mail: yumoto@ipst.s.u-tokyo.ac.jp

K. Yamanouchi (ed.), *Progress in Photon Science*, Springer Series
in Chemical Physics 115, DOI 10.1007/978-3-319-52431-3_23

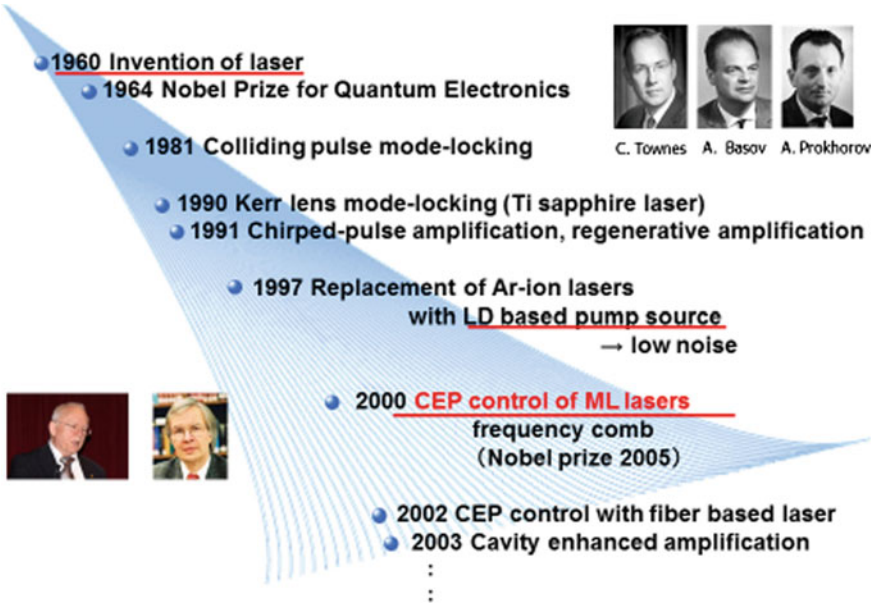

Fig. 23.1 Evolution of laser technology

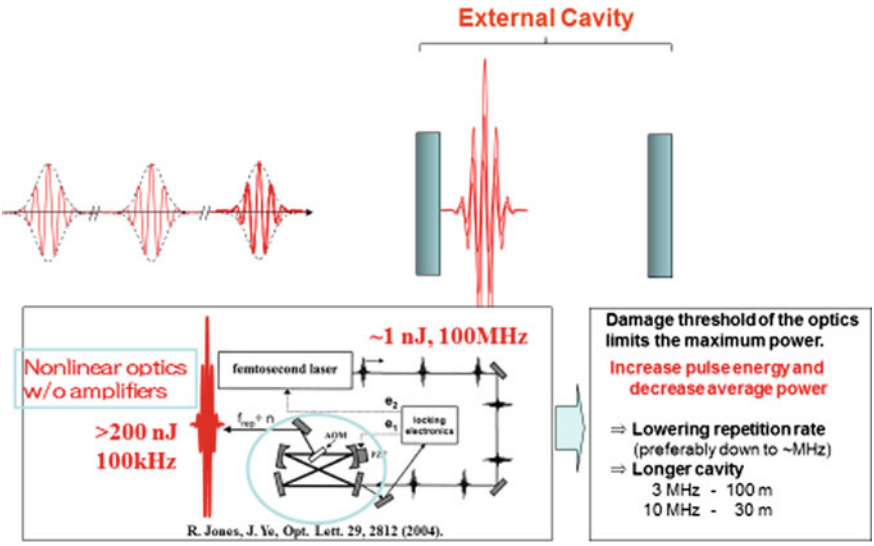

Fig. 23.2 Enhancement cavity: coherent addition of CEP controlled pulses

In 2004, two researchers in JILA, at the University of Colorado, demonstrated a coherent addition [1]. They used a mode-locked laser with a pulse energy of 1 nJ at a repetition rate of 1 MHz for a seeding source, and the pulse train is coupled to the cavity. Each input pulse is CEP-controlled, and the cavity is also controlled so that the optical field in the cavity interacts with each input pulse constructively as shown in Fig. 23.2. Coherently-added optical pulses in the cavity are extracted by an acousto-optic modulator (AOM) at a repetition rate of 100 kHz. The intensity achieved by the coherent addition is 200 times larger than the input seeding pulses without any gain media.

However, the problem in this case is the optical damage to the optical components composing the cavity. The optical-damage threshold is strongly dependent on the average power in the cavity. Our purpose is to obtain short optical pulses with a large peak intensity, and we have to balance the competing factors for a high-peak intensity and a low-average power.

Our idea to satisfy a higher output power without any optical damage to the optics is that we decrease the repetition rate to decrease the average power in the cavity. For example, if we decrease the repetition rate from 100 to 10 MHz, the output power can be increased ten times while keeping the average power lower than the optical-damage threshold. The repetition rate of the mode-locked operation is inverse-proportional to the cavity length. That means it is a key technology to realize stable operation of an optical cavity with a long cavity length.

Professor Kobayashi and his colleagues in our group demonstrated the coherent addition using a 30-m cavity [2]. Figure 23.3 is a schematic of the cavity design by Prof. Kobayashi. The input pulse has an energy of 1 μJ, and it is extended to 0.1 mJ by coherent addition. Optical pulses in the cavity is focused on Ar gas injected into the

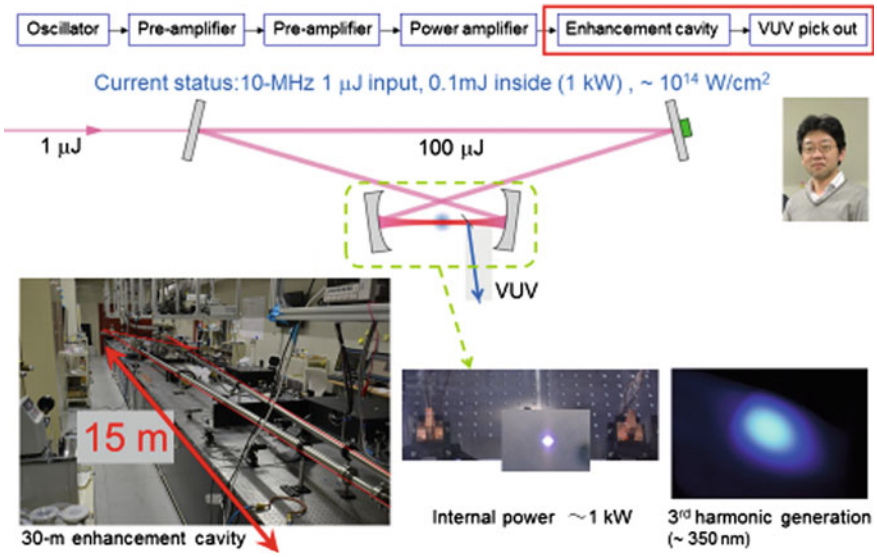

Fig. 23.3 High-power XUV light source by 30-m enhancement cavity

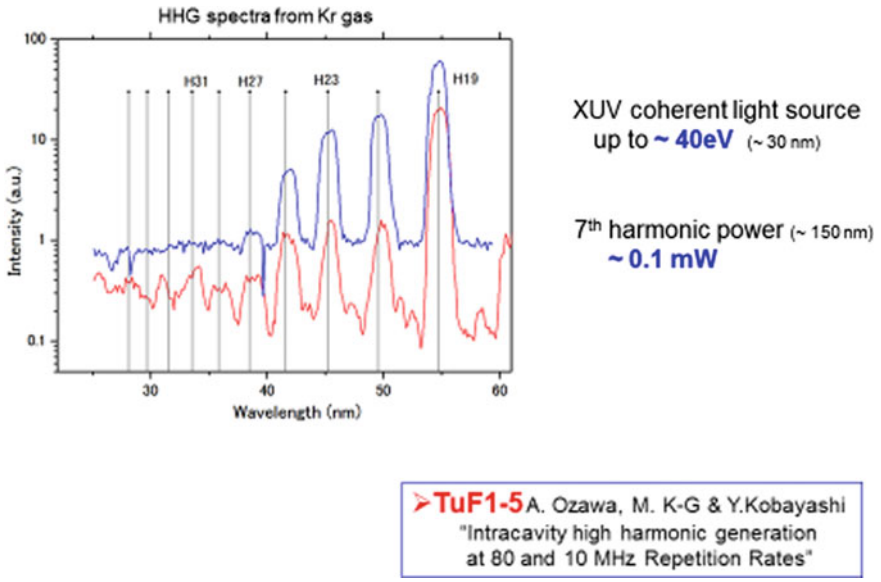

Fig. 23.4 High-order harmonics generation

cavity to generate high harmonics. Vacuum ultraviolet (UV) light was generated due to the interaction between Ar atoms and the enhanced short pulses. The photo at right-bottom of Fig. 23.3 shows third-harmonic generation in the cavity.

Figure 23.4 shows the spectrum of High Harmonics Generation (HHG) from Ar gas in the 30-m enhanced cavity. The pump wavelength is 1030 nm, and the HHG spreads to 30 nm, 40 eV. The output power of the seventh harmonic generation is about 0.1 mW.

The mechanism of HHG is explained by a three-step model as shown in Fig. 23.5 [3, 4]. The potential in which an electron is trapped is modified by the optical field as shown on the right-hand side of the figure. The electron is detached from the Coulomb potential of an atom by the tunnel effect. This electron is accelerated by the optical field shown by a yellow line, comes back to the original position, and recombines. The accumulated energy in the electron is converted to HHG.

To get intense short pulses, we have another idea. The right-bottom of Fig. 23.6 shows an enhancement cavity HHG as mentioned above, and the left-bottom is an intra-cavity HHG. The latter has a gain media in the cavity, and it is expected the pulse energy is much larger than that generated by the enhancement cavity. To obtain much larger pulse energy without any damage to optical components, the average power in the cavity should be kept below the optical-damage threshold. Therefore, the optical cavity with a cavity length of 100 m was employed to reduce the repetition rate to 3 MHz.

Femto-second lasers with high-peak intensity are expected to expand their feasibility to many applications. We proposed the concept of Coherent Photon Ring as shown in Fig. 23.7. The ring cavity shown by a green line has a cavity length of

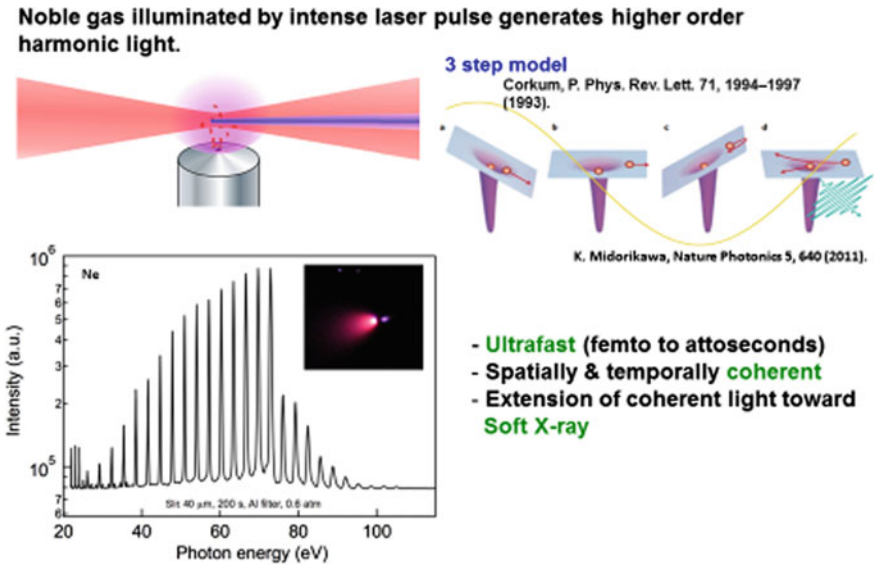

Fig. 23.5 High-harmonic generation

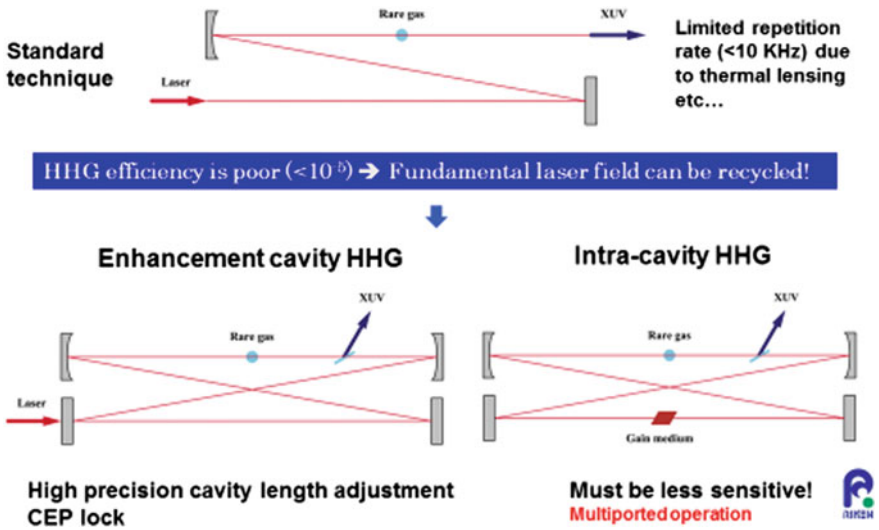

Fig. 23.6 Ultrahigh-repetition rate HHG

100 m, and femto-second pulses with a high peak intensity are generated as mentioned above. Some wavelength-conversion elements are also placed in the cavity and indicated by dark green boxes. Soft X-ray and terahertz emission will be generated from each element.

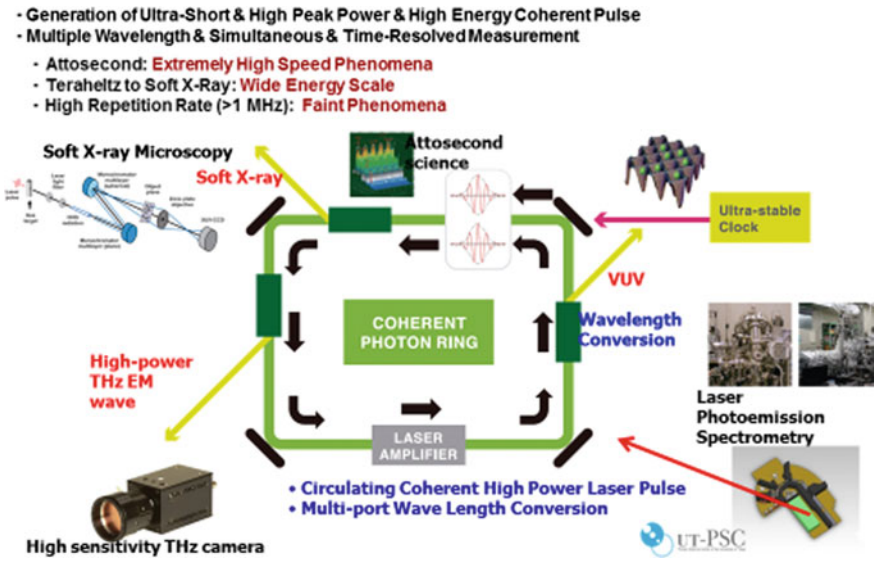

Fig. 23.7 "Photon Ring" concept

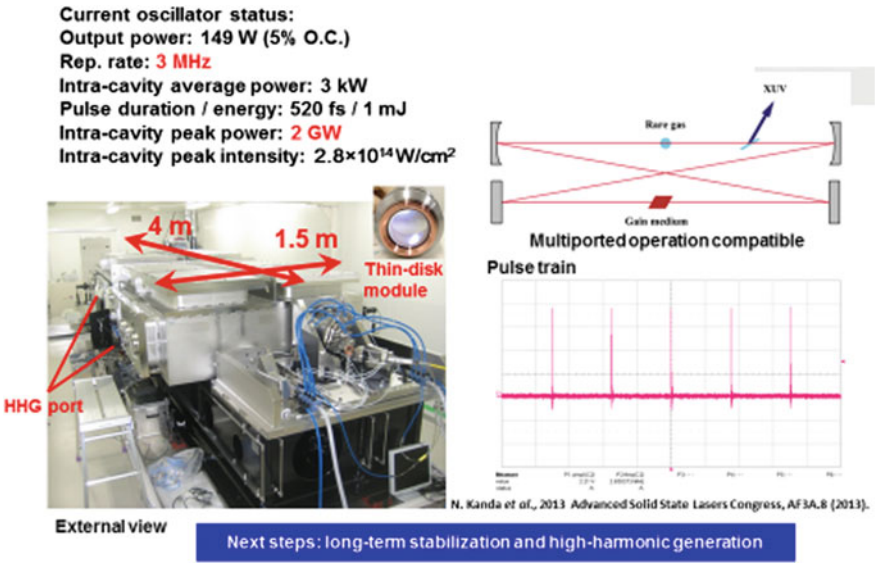

Fig. 23.8 Intra-cavity HHG system "Coherent Photon Ring"

In Fig. 23.8, the left-side hand photo shows the photon ring demonstrated by Professor Midorikawa's group, at RIKEN in Tokyo. It consists of a vacuum chamber with dimensions of 1.5 × 4 m. The gain media of Yb:YAG is in a thin

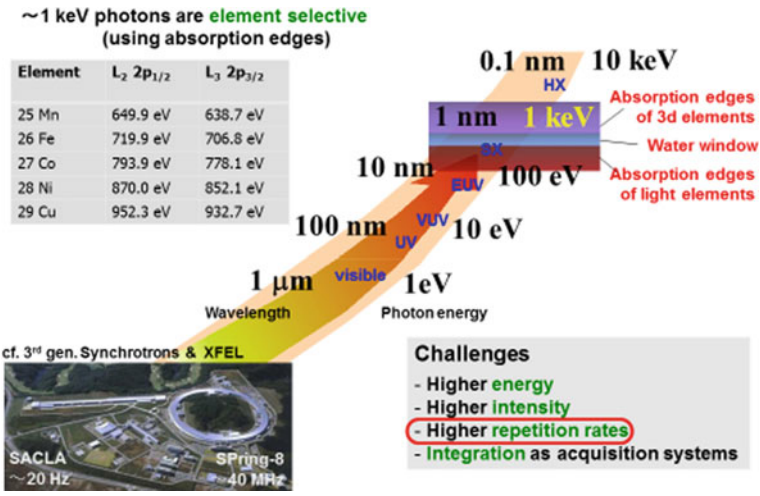

Fig. 23.9 Extension of coherent light towards 1-keV

disc pumped by laser diodes. Stable unidirectional operation in this cavity has been demonstrated as shown in the left-bottom of Fig. 23.8. A pulse duration of 520 fs and intra-cavity peak intensity of 2.8×10^{14} W/cm^2 have been demonstrated as summarized in Fig. 23.8 [5].

Synchrotron radiation and free-electron lasers are also candidates to generate soft X-ray light as shown in Fig. 23.9. They require big facilities and cost a lot of money. In our laboratory, soft X-ray generation has already been demonstrated, and our photon ring is expected to become a compact and low-cost light source for "coherent" soft-X-rays in future. It is expected that it will be used to explore the wide range of novel applications, such as ultrafast XUV spectroscopy and photon-electron spectroscopy.

The right-hand figure in Fig. 23.10 shows brilliance versus photo energy for our photon ring and SPring-8. The red line shows outputs of "coherent" XUV from the synchrotron radiation. These blue areas are our expectation of the soft-X ray output from the photon ring for the average and peak power, respectively. The actual output from Spring-8 is two or three orders of magnitude higher than the red lines shown in Fig. 23.10, but the coherence of the output is much poorer than the output from the photon ring. In consequence, the photon ring will be able to generate "coherent" soft X-ray radiation two or three-orders of magnitude better than the synchrotron radiation, depending on having the same coherence. In the next step, we are now trying to get THz radiation from the photon ring, and we are also trying to get emissions in other wavelength regions. We just talked about the soft X-ray generation today, and I hope we can show the new results in the next meeting. I will move to the second topic of the transfer of cutting-edge technology to industry.

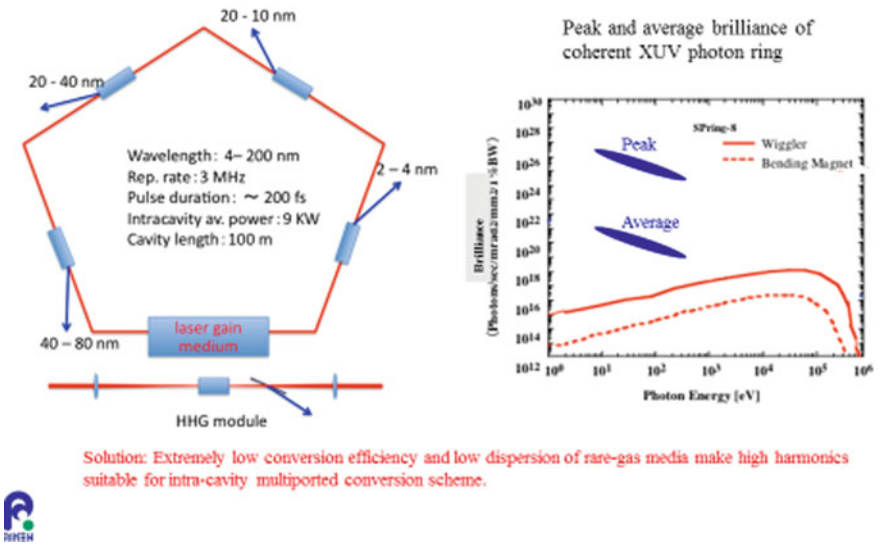

Fig. 23.10 MHz-coherent XUV photon ring

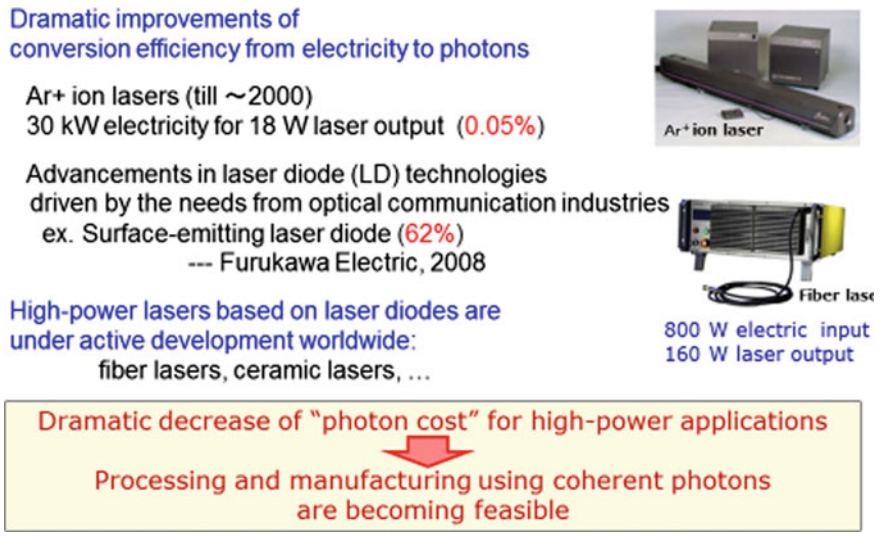

Fig. 23.11 Dramatic decrease of "photon cost"

As shown in Fig. 23.11, lasers consumed huge amounts of energy before the year 2000. For example, Argon-ion lasers have a conversion efficiency of 0.05%, and most of the electrical input is transferred to the hot water. But in last decade, the conversion efficiency of semiconductor lasers improved to 60 or 70%. This means the cost of a photon has been dramatically reduced. So many people are trying to use

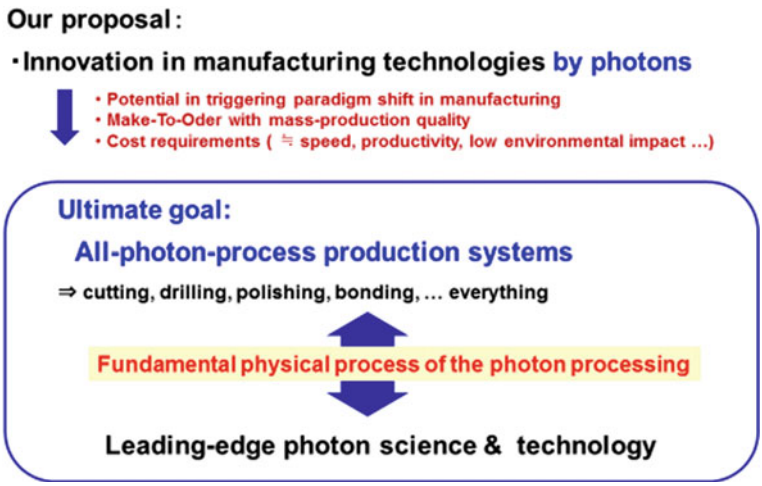

Fig. 23.12 MEXT-COI Program: fulfilling the needs of society

lasers for material processes, for example, laser cutting and laser welding. Actually, a 100 kW fiber laser system was commercialized last year. It is a very huge one, but it is suitable to cut metals or other materials.

Next, I will talk about our project which started in 2013. This project aims to create innovations for manufacturing technology by photons as shown in Fig. 23.12. As mentioned before, the cost of a photon has reduced dramatically, so we are expecting to change the scheme of laser manufacturing. So far, most of the lasers for manufacturing applications are developed at wavelengths of around 1 μm and 10 μm. Despite that each material has a different absorption spectrum, we cannot adjust the laser wavelength to the absorption peak of each material. However, we believe it is crucial to match the laser wavelength to the absorption peak of each material, so one of our targets is to develop lasers operating at the best wavelength for the material processing for each material. We are also aiming to develop non-thermal laser processing using a femtosecond laser system at a UV wavelength with a high fluence.

We are now approaching the paradigm shift of manufacturing by taking advantage of scientific achievements. One of our targets is to develop laser-cutting technology for Carbon Fiber Reinforced Plastics (CFRP). CFRP is a composite material of carbon fiber and resin, and the specific strength and elasticity-per-unit-weight is ten times and seven times higher than those of iron. CFRP featuring light weight and high strength is getting popular in the aircraft and automobile industries. Carbon fiber (CF) does not have a melting point, and just sublimates at a temperature of 3600 °C. But resin melts at around a temperature of 200 °C. It is very difficult to manage this big gap in temperature of 200–3600 °C. So far, a fiber laser at the wavelength of around 1 μm and a CO_2 laser at the wavelength of 10.6 μm are employed for laser cutting of CFRP using a thermal process. CF and resin, however, have an absorption peak around 230 or 240 nm. It is expected that we can cut CFRP

more effectively using short pulse lasers at the wavelength around 230–240 nm. Unfortunately, high-power and short- pulse lasers at wavelengths of 200 or 300 nm have not developed yet, and so we need further developments of lasers to launch the next generation of manufacturing technology. We are thinking that UV-femtosecond lasers with a high fluence will be able to surmount the obstacles to create a new world of laser processing. And the combination of science and technology will create new innovations. This activity also expected to stimulate science.

References

1. R. Jones, J. Ye, Opt. Lett. **29**, 2812 (2004)
2. A. Ozawa et al., Opt. Express **23**, 15107 (2015)
3. P. Corkum, Phys. Rev. Lett. **71**, 1994–1997 (1993)
4. K. Midorikawa, Nat. Photonics **5**, 640 (2011)
5. N.Kanda, et al. Yb:YAG thin disk mode-locked oscillator with high pulse energy for intra-cavity high harmonic generation, in *IEEE Photonics Conference 2014*, WG1.3, San Diego, USA (2014)

Part IX
Material Synthesis

Chapter 24
Laser-Inspired Chemical Transformations

Alina Manshina

When we discuss the concept of laser-induced phenomena, we refer to several different processes such as laser ablation, optical breakdown, laser pyrolysis, and laser-induced reduction reactions. In our recent study, we discovered a new phenomenon, which can be called "laser-inspired chemical transformations".

The experimental realization of this process is simple. We put just a small amount of yellow liquid into a cuvette and cover it with substrate (Fig. 24.1). We have He–Cd laser as a light source. The cuvette with substrate and liquid is placed under the laser beam, and after 10 min, we can see that a new phase (this black spot) has appeared on the surface of the substrate.

I would like to draw your attention to the deposition process that took place only in the laser-affected area (Fig. 24.1). The second important factor is that, in our experiments, we used a laser with very small laser intensity, 0.1 W/cm^2. We can use various substrates having different surface structures, such as microscope-cover glass, microscope-cover glass with ITO film, monocrystalline substrates, or nanostructured crystals (silicon nanowires).

It is clear that the main trick in our experiments is the liquid-phase composition. In our experiments, we use the solution of organometallic precursors. In particular, we use the family of heterometallic supramolecular complexes synthesized for us by Professor Tunik's laboratory. The structure and composition of complexes can vary. You can see an example in Fig. 24.2.

The special features are as follows. There is a heterometallic cluster core surrounded by phosphine and alkyl ligands, and it is very important that the size and composition of this core varies. It could possibly be Au–Ag, Au–Cu, or even Ag–Cu. Also the complexes are photosensitive. They have specific absorption bands in the UV region and luminescence emission in visible region. We can

A. Manshina (✉)
Institute of Chemistry, St. Petersburg State University,
Ulianovskaya 5a, Petrodvorets 198504, St. Petersburg, Russia
e-mail: manshina@chem.spbu.ru

K. Yamanouchi (ed.), *Progress in Photon Science*, Springer Series
in Chemical Physics 115, DOI 10.1007/978-3-319-52431-3_24

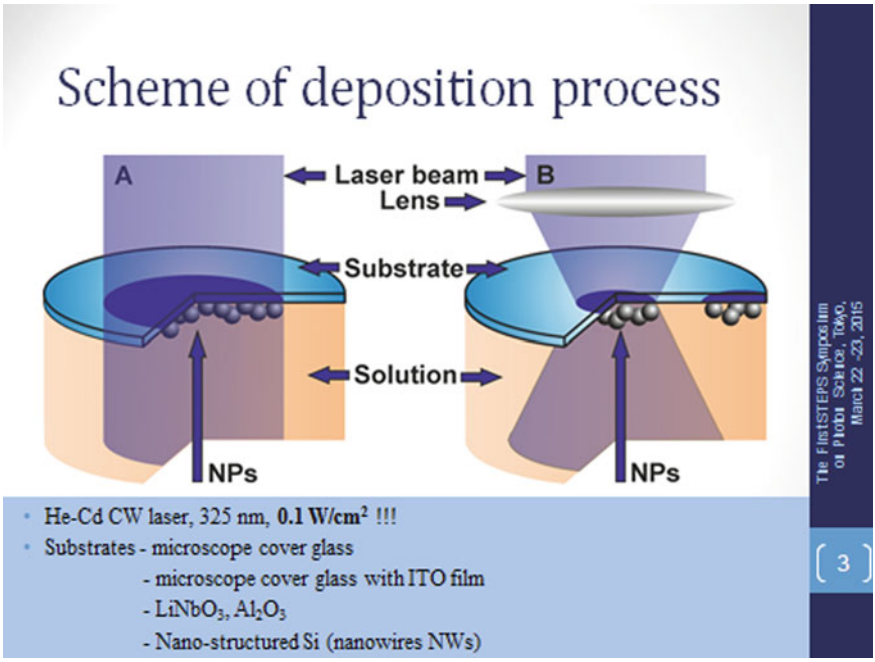

Fig. 24.1 Scheme of deposition process

directly control the morphology of the deposits by varying the solution parameters. Indeed, we succeeded in obtaining the deposition of agglomerated nanoparticles over a wide concentration range of different solvents (Fig. 24.3).

Through all the examples, we were able to obtain nanoparticles. It is very interesting to note that in some special cases, we observed formation of very exotic structures like flakes and even flowers. I would like to stress that nanoparticles can be obtained from almost any precursors of the family and on any surface. We succeeded in depositing nanoparticles onto such exotic substrates like silicon nanowires (Fig. 24.4a, c). We also succeeded in depositing nanoparticles onto the inner surfaces of capillaries, whose diameters are 95 and 140 μm (Fig. 24.4b, d).

As it is shown in which is high-resolution image of our nanoparticles, little bright spots can be seen in the dark matrix. From the characterization of the sample using a variety of techniques such as TEM, SEM, EDX analysis, absorption, and Raman and infrared spectroscopies, we found that the nano-structure is composed of carbon nanospheres, whose diameter is in the range 20–30 nm, incorporating metallic nanoparticles whose diameter is in the range 2–5 nm (it is an Au–Ag nano alloy). The carbon phase is amorphous hydrogenated carbon. In accordance with EDX analysis, the composition of the nano-structures was found to be C, Au, and Ag, with a component ratio about 90:5:5 at %, which is determined by the composition of the organometallic precursor.

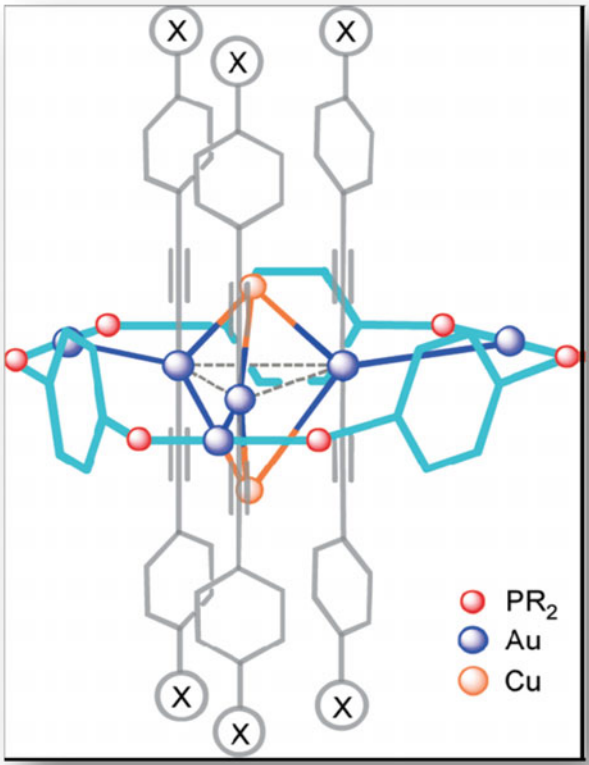

Fig. 24.2 Scheme of heterometallic supramolecular complexes—special features

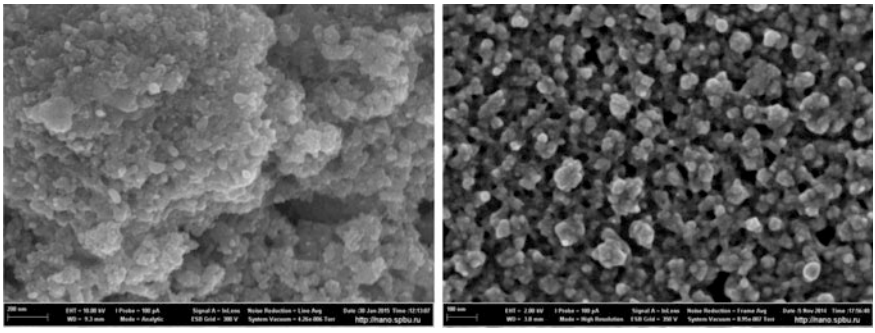

Fig. 24.3 SEM images of nanoparticles obtained as a result of laser-induced transformation of supramolecular complexes

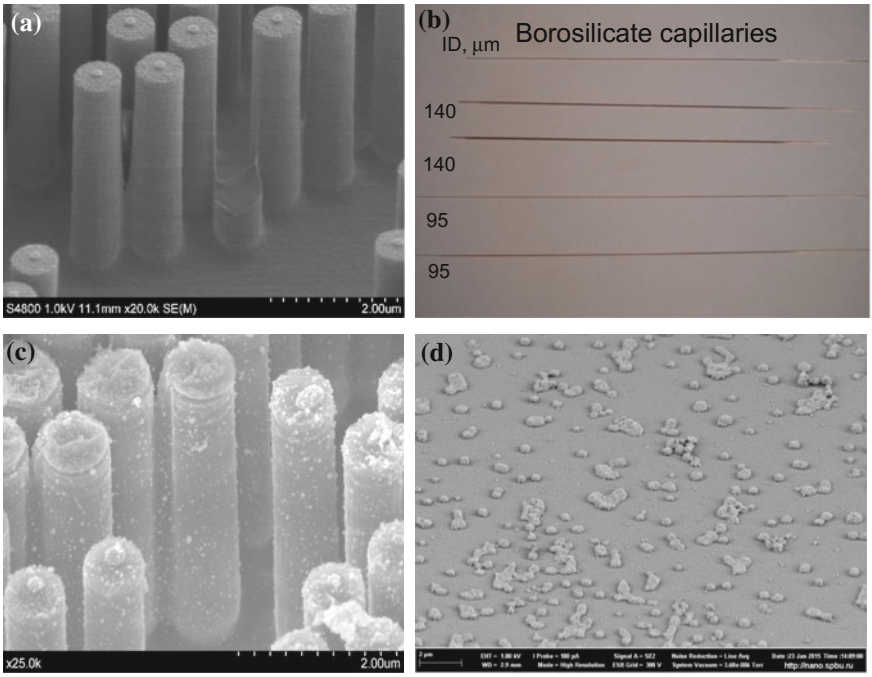

Fig. 24.4 **a** Si nanowires, **b** borosilicate capillaries, **c** NPs deposited onto Si nanowires, **d** NPs onto inner surface of capillaries

We then studied the functional properties of the nanoparticles that we had made. As was mentioned earlier, our nanoparticles contain metal nanophase, which means that they can induce surface-enhanced Raman scattering. For these experiments, we used anthracene as a test substance. Several different solutions with different concentrations of anthracene were prepared (10^{-4}–10^{-7} mol/l). The Raman spectra of the anthracene solutions on the surface of our nanoparticles were measured. We found that the detection limit can be as small as 10^{-7} mol/l, as shown in Fig. 24.5. The nanoparticles can be used for highly sensitive detection of lowly-concentrated impurities.

The other component of our nanoparticles is the carbon phase, which is characterized by pronounced absorption properties. As a test substance, in this case, we used a solution of human blood in small concentrations, 2 g/l. The experiment was carried out in the following way. First, we deposited a spot of nanoparticles onto the surface of the substrate. The diameter of the spot was about 3 mm. After that, we put one drop of blood solution onto the surface of our nanoparticles, and we tried to measure the Raman spectra. However, we did not find any peaks or any signals. Then we immersed the substrate with nanoparticles into the blood solution for 5 min and, then, recorded a Raman spectrum. This time, some peaks appeared clearly in the spectrum. Then we repeated the measurement of the samples with

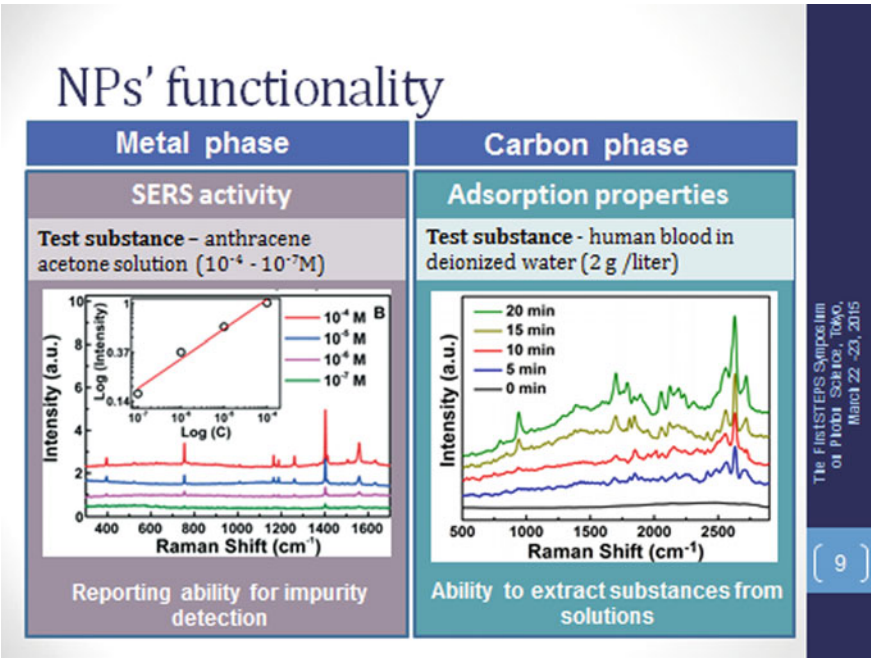

Fig. 24.5 Functional properties of nanoparticles

various immersion times. Figure 24.5 shows that the Raman signals increase as the immersion time increases. This result also show that the nanoparticles can be used to extract substances from solutions.

As was mentioned earlier, the nanoparticle-formation process takes place only in the laser-irradiated area. We used this process for creating a microchip having a matrix of 100 elements. The diameter of one element, which is an agglomerate of nanoparticles, is about 20 μm. We have found that this microchip is very promising for detecting ultralow volumes and concentration of analytes. We dropped a solution containing analytes of about a on the surface of each a microchip and measured the Raman spectra. By using a mixture of human blood and anthracene as an analyte, we succeeded in demonstrating a multiplex detection capability of the microchip. Indeed, in Fig. 24.6 (blue line), the peaks assignable to blood, as well at those assignable to anthracene, can be seen.

In this section, I would like to show that nano-flakes can be made on the crystalline surface through a laser-induced process. The size can vary, but generally speaking it varies from 2–7 μm with a thickness of 10–100 nm. The SEM (scanning electron microscope) image shows that the corners of the nano-flakes are right angled, and there are bright spots inside (which are metal nanoinclusions). From the TEM (transmission electron microscope) and EDX (energy dispersive

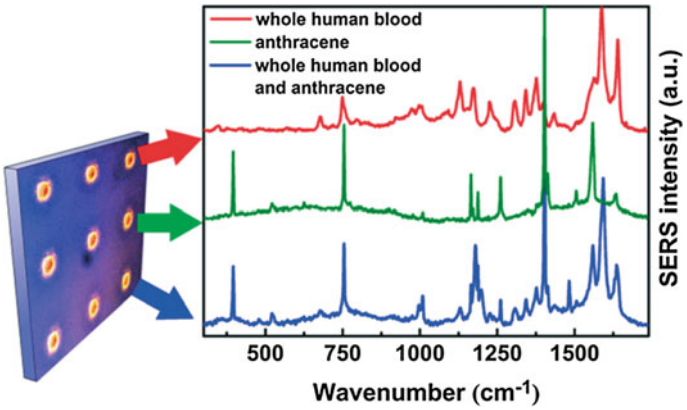

Fig. 24.6 Raman spectrum of human blood in deionized water (*red line*), Raman spectrum of anthracene in water (*green line*), and human blood/anthracene solution mixture (1:1 vol.%), (*blue line*)

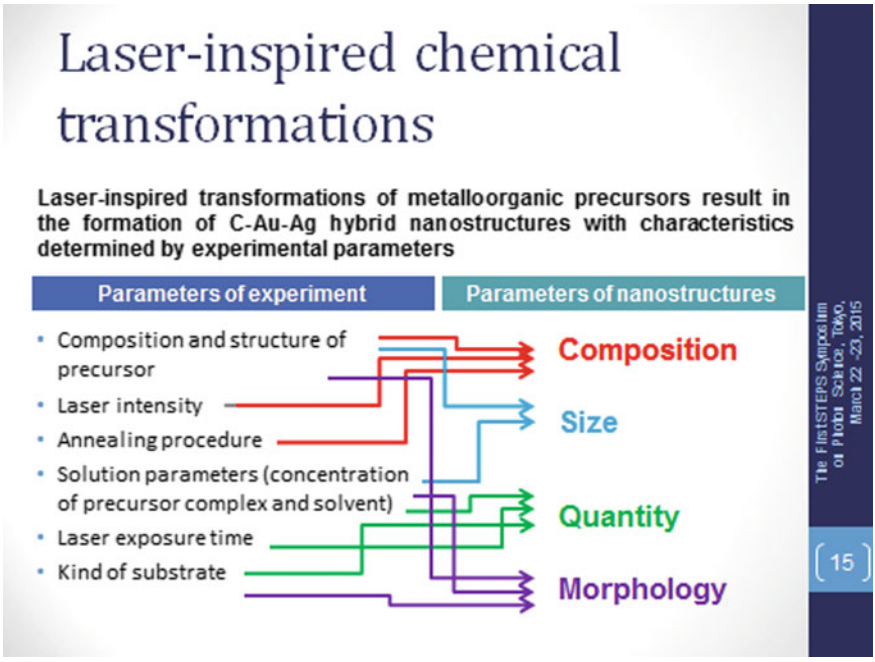

Fig. 24.7 Creation of hybrid nanostructures with controlled composition, size, quantity, and morphology

X-ray spectroscopy) analyses, we found that the nano-flakes are hybrid carbon-crystalline structures with incorporated Au–Ag nanoparticles. We also found that the nano-flakes can be fabricated into a variety of nicely shaped structures by a focused ion beam. By the fast ion-beam fabrication, we can vary the functionality of the nano-flakes, for example: we can create subwavelength plasmonic waveguides, optical nano antennas, and various plasmonic modulators and resonators.

Our experiments show that laser-induced transformations of metalorganic complexes result in the formation of hybrid nanostructures, which are sensitively influenced by experimental parameters (composition and structure of supramolecular precursor, and the solution parameters–concentration of supramolecular precursor and solvent, the substrate species, and the annealing procedure, as well by the laser parameters such as laser intensity and exposure time) (see Fig. 24.7).

It has been known that similar hybrid nanostructures can be prepared by rather complicated and multi-step chemical processes [1, 2]. On the other hand, through this series of our experiments, we have demonstrated that a variety of nanostructures can be synthesized by a one-step process.

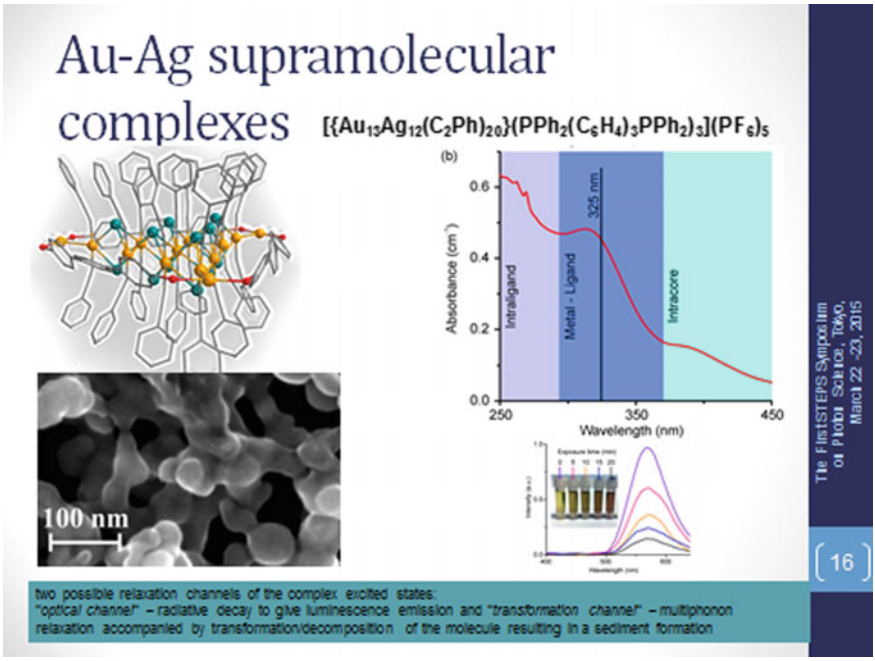

Fig. 24.8 Transformation process of supramolecular complexes

Now I would like to say a few words on the process of the transformation, and its mechanism. The structure of the precursor supramolecular complex used in most of our experiments is shown in Fig. 24.8. It consists of 13 Au atoms and 12 Ag atoms. As shown in the absorption spectrum on the right of this figure, there are three absorption bands that can be assigned to the intra-ligand, metal-ligand, and intracore transitions. When we irradiated the sample solution with He–Cd laser, we observed the luminescence and found that its intensity decreases with laser-irradiation time. Not only did we observe the decrease of the intensity of luminescence, but we also observed the darkening of the solution and the opacification of the solution that resulted from the formation of the solid phase.

There are two possible relaxation channels of the excited states of the complexes. The first possible channel could be an "optical channel", resulting in the radiative decay emitting the luminescence. The second one is a "transformation channel" due to multiphonon relaxation and decomposition or transformation of our complexes, resulting eventually in the formation of nanostructures shown on the bottom left of Fig. 24.8.

It means that the one-step synthesis of the nanostructure is a complex multi-step reaction process triggered by the irradiation of light, in which a ligand-to-metal charge-transfer process is involved. As a result, the precursor supramolecular complex loses chemical stability. We then have the stage of molecule reorganization; the reduction of the cluster core; and the self-organization of the building blocks the formation of the hybrid nanophase.

Through this experiment, we now know that, as a result of laser-induced process, we can obtain the nanostructures, but still little is known about the mechanism of this process. That is why, in the near future, we must study the stages of the charge-transfer process that is expected to play an important role. For this, probably, a pump-probe technique using short-pulsed laser light will be introduced. It will also be necessary to investigate energy-transformation processes, through which the reduction of a metal core would be achieved.

It is also important to examine the crystalline phase formation, to examine if it is a photo-induced process, and to study the effect of the substrate and defects in the substrate and surface defects on the process of hybrid-phase formation.

Acknowledgements I would like to thank and acknowledge my colleagues, all bright scientists, who contributed to the success of our research: the people from the group of from Professor Tunik's laboratory, the people from Research Centers of St. Petersburg State University: Nanocenter and Optical Center of Laser and Materials Research, and also the people from Max Plank Institute for the Science of Light and from Friedrich-Alexander University of Nuremberg. If it were not for the support from Ministry of Education and Science of Russia, Project 14.604.21.0078, the experiments would not have succeeded.

References

1. S.J. Henley, P.C.P. Watts, N. Mureau, S.R.P. Silva, Appl. Phys. A Mater. Sci. Process. **93**, 875–879 (2008)
2. S.C. Tang, S. Vongehr, X.K. Meng, J. Phys. Chem. C **114**, 977–982 (2010)

Chapter 25
Super-Ionic Nano-Composite Solid Electrolytes Prepared by Laser Ablation

Yury Tver'yanovich, S. Fokina and E. Borisov

The general aim of solid-state ionics is the development of solid electrolytes with maximum conductivity. It is well-known that an extensive interphase surface promotes ion conductivity. There are several explanations for this phenomenon: high concentration of crystal structure defects along the interphase boundary, influence of particular crystal structure of one phase on the structure of the other phase, atom diffusion across interphase boundary, existence of space-charge region along the interphase surface, and so on.

Nano-layered thin films are suitable for investigation of the interphase surface promoting the ion-conductivity phenomenon [1, 2] because the interphase boundary area and all geometry parameters of such an object are known and controllable. Of course, it is only true if the thickness of every layer is controlled during the deposition procedure. It is also possible to measure ion conductivity along and across the interphase boundary. As a result, you can measure the thickness and other properties of the interphase layer, and it is possible to understand its nature. The interphase layer is the thin layer along the interphase surface, properties of which differ from the properties of bulk phases.

Y. Tver'yanovich (✉) · S. Fokina
Institute of Chemistry, St. Petersburg State University,
Universitetskiy prospect 28, St. Petersburg 198504, Russia
e-mail: y.tveryanovich@spbu.ru

S. Fokina
e-mail: svetlanav.fokina@gmail.com

E. Borisov
Center for Optical and Laser Materials Research, St. Petersburg State University,
Ul'yanovskaya ulitsa 5, St. Petersburg 198504, Russia
e-mail: enbor@bk.ru

K. Yamanouchi (ed.), *Progress in Photon Science*, Springer Series
in Chemical Physics 115, DOI 10.1007/978-3-319-52431-3_25

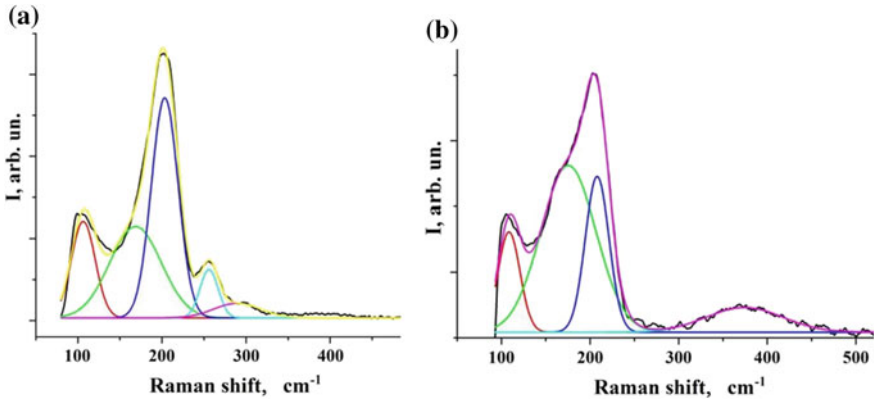

Fig. 25.1 Raman spectra of CG glass (**a**) and film (**b**) obtained by its laser ablation

Laser ablation in the vacuum makes the preparation of such multilayered thin films possible (Fig. 25.1). This method has some peculiarities and advantages. The chemical composition of thin films prepared with laser ablation is identical to the composition of the target. The thickness of every layer can be controlled by counting the number of laser pulses; the chemical composition of deposited material can be changed instantly by switching the laser beam from one target to another. Multilayered thin films can also be prepared by the atom-layer deposition (ALD) process. ALD technology works only in thermodynamic equilibrium conditions. This requirement is not necessary for the laser-ablation method. Combination options for chemical compounds of adjacent layers are unlimited for laser ablation. Furthermore, in contrast to ALD technology, pulse-layer deposition gives us the possibility to prepare multilayered film with large total thickness, up to several microns.

Alpha modification of silver iodide has the highest ion conductivity of all solid electrolytes. But this crystal modification exists only at temperatures above 150 °C. So it would be good to stabilize this crystal modification at room temperature. This problem was solved by Tatsumisago et al. [3]. Many similar studies were conducted after this paper appeared, but, in all these works, the composite material consisted of a bulk glass matrix and incorporated nanocrystals of silver iodide in alpha modification.

Morphology of such a solid electrolyte is not optimal for reach-through conductivity. Multilayered thin films composed of AgI and glass nanolayers are more suitable to obtain reach-through conductivity with alpha modification of silver iodide.

Here is one possible explanation of the α-AgI stabilization at room temperature. Suppose that glass-forming temperature is higher than the temperature of the AgI $\beta \rightarrow \alpha$ phase transition. Alpha modification of silver iodide strongly impacts the glass structure if the temperature of the multilayered film is higher than the glass-forming temperature and the glass layers are soft. When temperature

decreases below the glass-forming temperature, a glass structure adapted to the α-AgI structure freezes. During further a temperature decrease, when the temperature falls below the temperature of $\alpha \rightarrow \beta$ phase transition, the frozen glass structure preserves the alpha modification of AgI. All of this can be implemented only if the thickness of silver iodide layer is sufficiently small.

Using this model, we can conclude that the chosen glass should satisfy the following requirements: Its glass-forming temperature should be higher than the phase-transition temperature of AgI, the glass must have high crystallization resistance, and the concentration of silver iodide must be high enough to prevent silver diffusion across the interphase boundary.

The glass-forming region of a AgI-$GeSe_2$-Sb_2Se_3 system was selected for the development of the glass with said properties. Glasses with various chemical compositions were synthesized from this system. Based on the results of DTA of all synthesized glasses, it was concluded that the glass 0,4AgI-0,3$GeSe_2$-0,3Sb_2Se_3 (CG) has optimal properties. Its glass-forming temperature was 190 °C, and its crystallization temperature was 320 °C. Crystallization resistance of this glass was tested separately.

Heat treatment of glass (at 210 °C lasting one, five, ten, 15, and 20 h) does not change its crystallization temperature. The influence of glass-AgI contact on the glass crystallization resistance was also investigated. For this objective, a mechanical mixture of glass and AgI powders in 1:1 proportion was prepared. DTA shows that the glass crystallization temperature does not change. Moreover, the $\beta \rightarrow \alpha$ AgI phase transition was observed at 147 °C. The temperature of endothermic effect (melting at ≈420 °C) decreases due to the so-called phenomenon of "eutectic melting". It can be concluded from all these experiments that CG satisfies all the requirements mentioned above.

An experimental setup based on a Xe/HCl excimer laser was used for film sputtering. The laser's parameters are the following: impulse duration of 20 ns, wavelength λ = 308 nm, pulse frequency 13 Hz, and pulse energy of 15 mJ. Films were sputtered on oxide glass substrates at room temperature. The distance between substrate and target was 35 mm.

~1 μm thick films of CG were obtained using laser ablation (each film thickness was measured precisely using an interferometric method). XRD analysis of the films showed that they were amorphous. The results of EDS method showed that the elemental composition of the films is almost identical to that of a bulk CG (Table 25.1). The comparison of Raman spectra of bulk CG and of the thin film prepared by laser ablation of CG indicates that their short-range orders are similar. Their specific conductivity-temperature dependencies are also identical (Fig. 25.2). All the above indicates that the laser-ablation procedure does not alter the nature of sputtered CG in any significant way.

Table 25.1 Comparative analysis of elemental composition of $(GeSe_2)_{30}(Sb_2Se_3)_{30}(AgI)_{40}$ glass and film obtained by its laser ablation

	Composition, at.%				
	Ge	Se	Sb	Ag	I
Calculated from formula	9.4	47.0	18.8	12.4	12.4
Measured for bulk *glass*	9.1 ± 0.8	47.7 ± 0.8	17.7 ± 0.9	13.7 ± 0.6	11.8 ± 0.6
Measured for *films*	10.1 ± 0.4	46.6 ± 0.8	18.0 ± 0.3	14.1 ± 0.7	11.3 ± 0.6

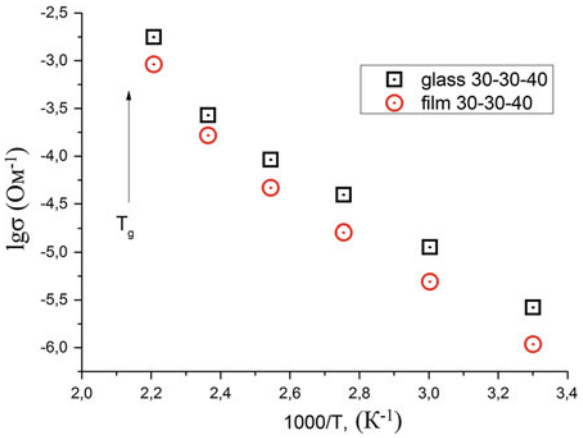

Fig. 25.2 Temperature dependencies of specific conductivity of CG glass and film obtained by its laser ablation

Similar research of polycrystalline AgI and micron-sized films obtained via its laser ablation showed that these films are formed by polycrystalline, stoichiometric β-AgI [4, 5]. The films have smooth surfaces and are formed by irregularly shaped crystals (Fig. 25.3). Temperature dependency of their conductivity clearly shows β → α phase transition at about 150 °C (Fig. 25.4).

Films composed of alternating AgI and CG nanolayers were prepared via laser ablation. Figure 25.5 depicts lateral shear of one of such film as an example. The film's layered structure is clearly seen. The thickness of two nearby layers is 30 nm. Total film thickness is 1 μm.

Temperature dependencies of multilayered-film specific conductivities (Fig. 25.6) were studied using impedance spectroscopy method. Heating was conducted up to 200 °C, a temperature that surpasses both the phase transition temperature and the CG glass-formation temperature. Specific conductivity values was were calculated for the total thickness of the multilayered film. When heated for the first time, a temperature dependency of conductivity that is characteristic for nanocrystalline β-AgI was observed. This dependency demonstrated β → α phase transition at about 150 °C. When cooled (as will be confirmed further via XRD method), α → β phase transition occurs at lower temperatures (about 70–80 °C).

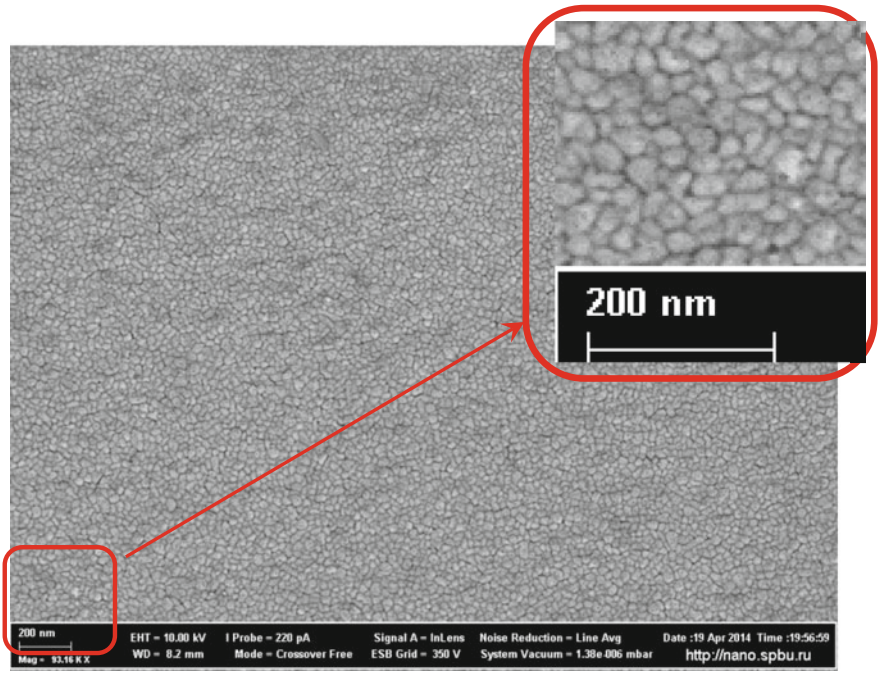

Fig. 25.3 Electron microscopic image of 1-μm thick AgI film obtained via laser ablation

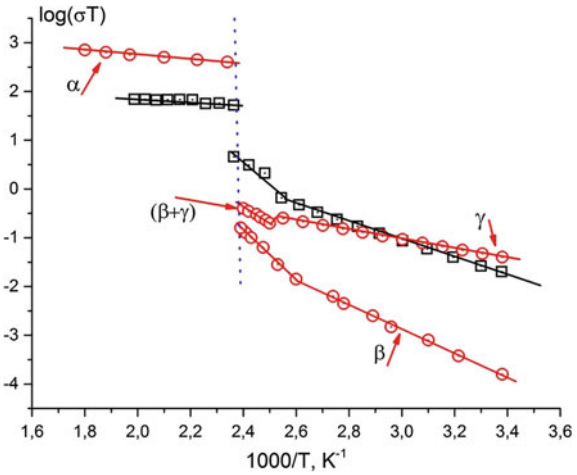

Fig. 25.4 Specific conductivity temperature dependencies for AgI thin film prepared by laser ablation (*open square*) [4, 5] and bulk AgI (*open circle*) [6]. *Greek letter* notations of the different branches correspond to different AgI crystal modifications according to [6]. Temperature corresponding to $\beta \rightarrow \alpha$ phase transition of AgI is marked by *dashed line*

Room temperature conductivity turns out to be two orders of magnitude greater than its initial value. The second cycle of thermal treatment increases room temperature conductivity even further. After the third cycle, it reaches 0,3 Ohm^{-1} cm^{-1}, and its activation energy decreases to 0.07 eV.

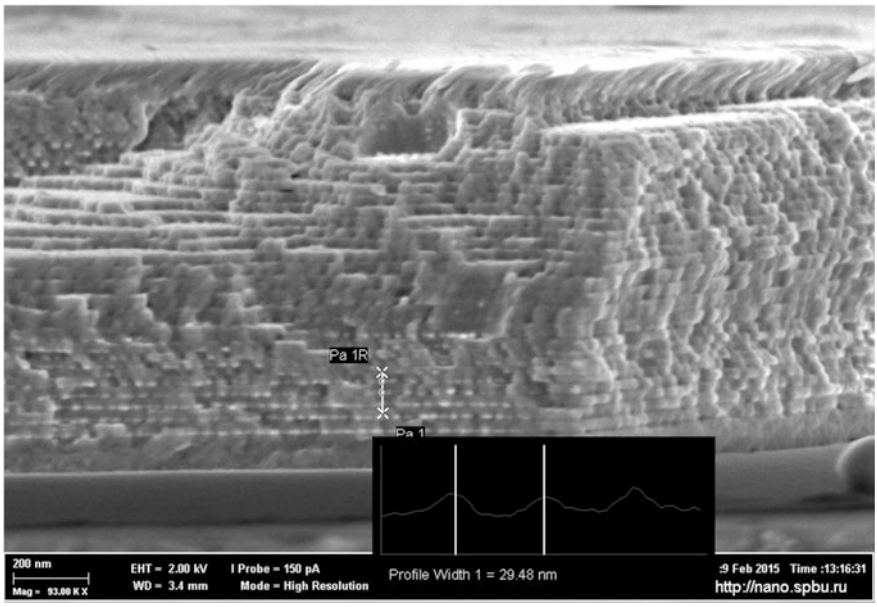

Fig. 25.5 Image of multilayered AgI/CG film lateral shear. *Insertion* shows alternation of image color fields along the vertical line

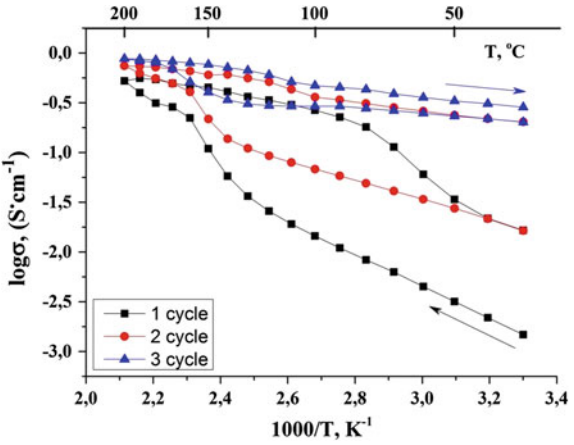

Fig. 25.6 The results of measurements of specific conductivity of AgI/CG multilayered film with 10 nm layer thickness during three thermal-treatment heating-cooling cycles

To specify phase transitions occurring in the thermally treated film, dependencies of XRD spectra on temperature were studied. A general view of spectra is shown in Fig. 25.7. The analysis of spectra shows the presence of β and α phases of AgI and a facet-centered cubic phase with a 0.581-nm lattice parameter. One of the AgI modifications (AgI-III) has such a lattice. This modification is stable in the 1.5–11.2-GPa pressure range. When changing pressure from 6.5 to 11 GPa, its

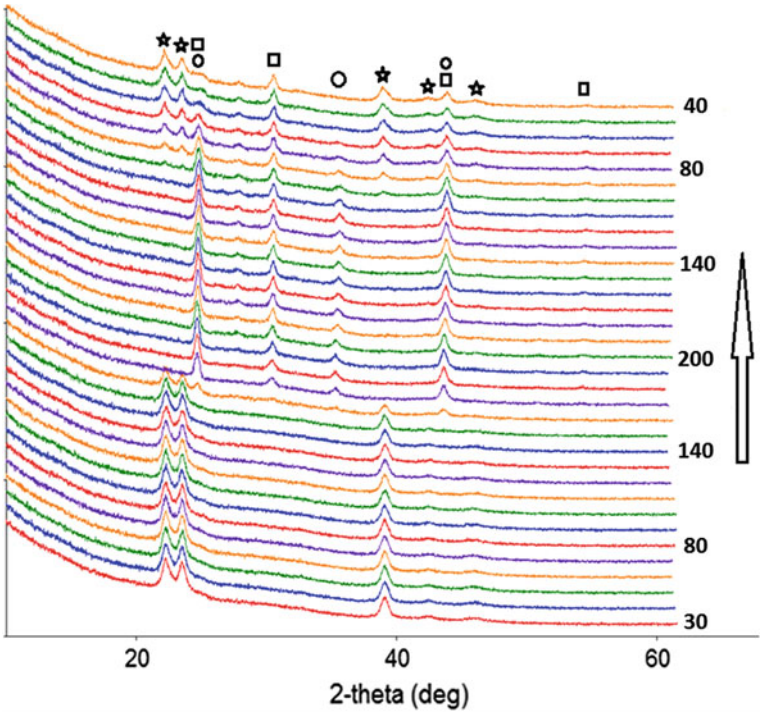

Fig. 25.7 X-ray pattern variation of AgI/CG multilayered film with 10-nm thick layers during first heating-cooling cycle of thermal treatment. Numbers denote temperature in °C, *arrow* shows direction of temperature change. Various AgI modifications are denoted by following signs: ★−β; ○−α; □−III-AgI

lattice parameter changes from 0.586 to 0.573 nm. At room temperature, before the multilayered film thermal treatment, its spectrum contains only β-phase reflections. When heated, in the β → α phase transition vicinity, the intensity of β-phase reflections subsides to the point of disappearance. α-phase and AgI-III reflections arise. The intensity of these reflections attains its maximum at 170 °C and remains constant up until 200 °C. When cooling, the intensity of AgI-III reflections remains constant at all temperatures, including room temperature. α-phase reflections disappear completely at about 50 °C. β-phase reflections arise and grow in the same temperature range. However, they do not attain their initial magnitude at room temperature.

The described variations illustrate the temperature dependencies of the relative intensities of the X-ray reflections that are calculated for some of the most intensive reflections for each of the three phases (Fig. 25.8).

Similar XRD experiments were conducted for multilayered films with layer thicknesses of 25, 50, and 100 nm (CG and AgI layer thickness were the same). The magnitude of temperature differences between the α → β phase transition

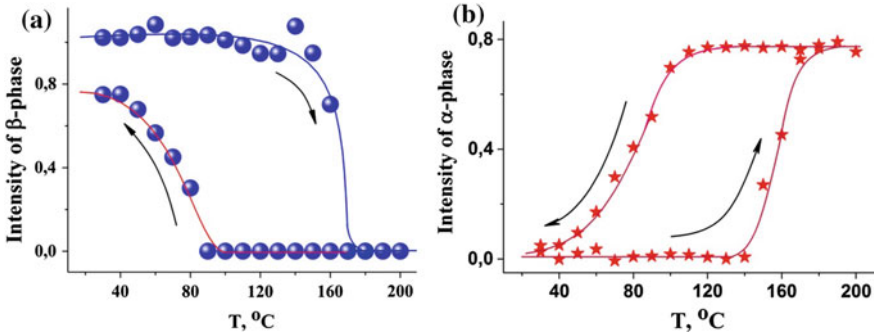

Fig. 25.8 Temperature dependencies of relative intensities of β-AgI (**a**) and α-AgI (**b**) X-ray reflections during the first heating-cooling cycle

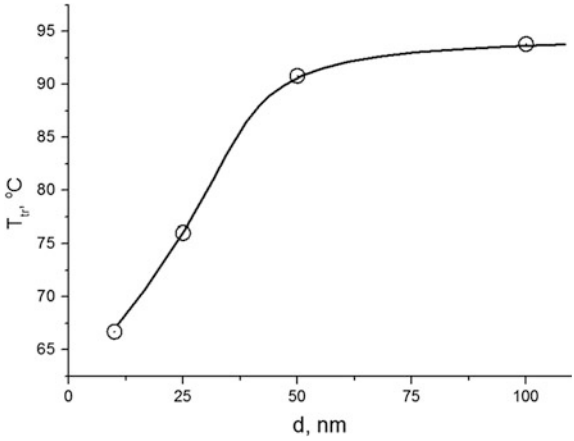

Fig. 25.9 Dependency of $\alpha \rightarrow \beta$ phase-transition temperature on multilayered film layer thickness when cooled

temperature, when cooled, and the $\beta \rightarrow \alpha$ phase transition temperature, when heated, predictably increases with a decrease in the thickness of the layer (Fig. 25.9). It is apparently due to the fact that the AgI-layer thickness of less than 50 nm limits the nanocrystal size of this compound. The dependency of said effect's magnitude on the AgI-nanocrystal size was pointed out already [7]. Attainment of saturation when layer thickness is close to 50 nm is due to the fact that, even in the 1-μm thick films, the nanocrystal size is approximately 30 nm (Fig. 25.3). Thus, a further increase in the thickness of layers does not result in an increase in the size of nanocrystals Extrapolation of this dependency in the region of thinner layer thickness leads to the conclusion that achieving alpha-AgI stability at room temperature solely due to a AgI-nanocrystal size decrease is impossible, and using additional factors is necessary. $\alpha \rightarrow \beta$ transition temperature is implied to be the temperature at which the X-ray reflection intensity of $\alpha \rightarrow \beta$ phase is half the intensity at temperatures higher than 160 °C.

Thus, solid-nanocomposite electrolytes with the highest ion conductivity magnitude were obtained. Nano-layered films obtained via laser ablation are promising objects suitable for solid electrolytes' research and development.

Acknowledgements The research is supported by RFBR (grant 17-03-00121). The measurements were performed at the following Research Centers of the SPSU: "X-ray Diffraction Studies", "Nanotechnology Interdisciplinary Center", "Diagnostics of Functional Materials for Medicine, Pharmacology and Nanoelectronics", and "Optical and Laser Materials Research".

References

1. N. Sata, K. Eberman, K. Eberl, J. Maier, Nature **408**, 946–949 (2000)
2. X.X. Guo, I. Matei, J.-S. Lee, J. Maier, Appl. Phys. Lett. **91**, 103–102 (2007)
3. M. Tatsumisago, Y. Shinkuma, T. Minami, Nature **354**, 217–218 (1991)
4. Yu.S. Tveryanovich, A.V. Bandura, S.V. Fokina, E.N. Borisov, R.A. Evarestov, Solid State Ionics **294**, 82–89 (2016)
5. S.V. Fokina, E.N. Borisov, V.V. Tomaev, I.I. Tumkin, Yu.S. Tveryanovich, Solid State Ionics **297**, 64–67 (2016)
6. M.B. Salamon, Phase transitions in ionic conductors, in *Physics of Superionic Conductors*, ed. by M.B. Salamon. Topics in Current Physics, vol 15 (1979)
7. R. Makiura, T. Yonemura, T. Yamada, M. Yamauchi, R. Ikeda, H. Kitagawa, K. Kato, M. Takata, Nat. Mater. **8**, 476–480 (2009)

Chapter 26
Magneto-Optical Functionalities in Cyano-Bridged Bimetal Assemblies and Metal-Oxide Nanomaterials

Shin-ichi Ohkoshi

26.1 Introduction

Today, I am going to talk about magneto-optical functionalities in cyano-bridged bimetal assemblies and metal-oxide nanoparticles. I have only short time to talk, so I would like to focus on our laboratory work, i.e., magneto-optical functionalities in cyano-bridged metal assemblies in these two compounds of $Fe_2[Nb(CN)_8] \cdot (4\text{-pyridinealdoxime})_8 \cdot 2H_2O$ and $Fe_2[Nb(CN)_8] \cdot (4\text{-bromopyridine})_8 \cdot 2H_2O$.

26.2 Light-Induced Spin-Crossover Magnet

Our laboratory has prepared of several families of magnetic materials based on cyano-bridged metal assemblies using metal complexes [1–9]. Until now, we have demonstrated several types of functionalities as shown in Fig. 26.1. For example, light-induced phase transition behavior of photomagnetism [2,3], electric field-induced phase transition in a magnetic material [4], and a coupling effect between spin and ionic conductivity [5]. Furthermore, we demonstrated humidity-sensitive magnetism [6] and transparent magnetic films. These features are based on metal complexes. Furthermore, we study metal-oxide nanoparticles [10-12]. For example, recently we demonstrated light-induced metal-semiconductor phase transition [10]and hard-magnetic ferrite with huge coercivity [11,12]. I would like to talk about these two topics.

S. Ohkoshi (✉)
Department of Chemistry, School of Science, The University of Tokyo, 7-3-1 Hongo, Bunkyo-ku, Tokyo 113-0033, Japan
e-mail: ohkoshi@chem.s.u-tokyo.ac.jp

K. Yamanouchi (ed.), *Progress in Photon Science*, Springer Series in Chemical Physics 115, DOI 10.1007/978-3-319-52431-3_26

To demonstrate photomagnetism in the material, we focused on the Light-induced excited spin state trapping (LIESST) effect (Fig. 26.2). The LIESST effect is light-induced excited spin-state trapping effect. This effect is very familiar in the field

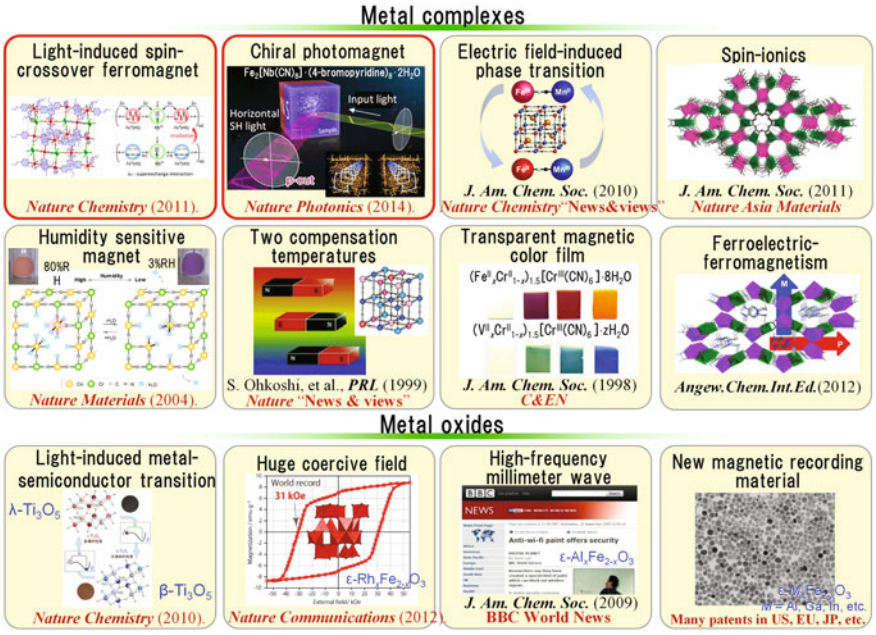

Fig. 26.1 Background researchs on metal complexes and metal oxides

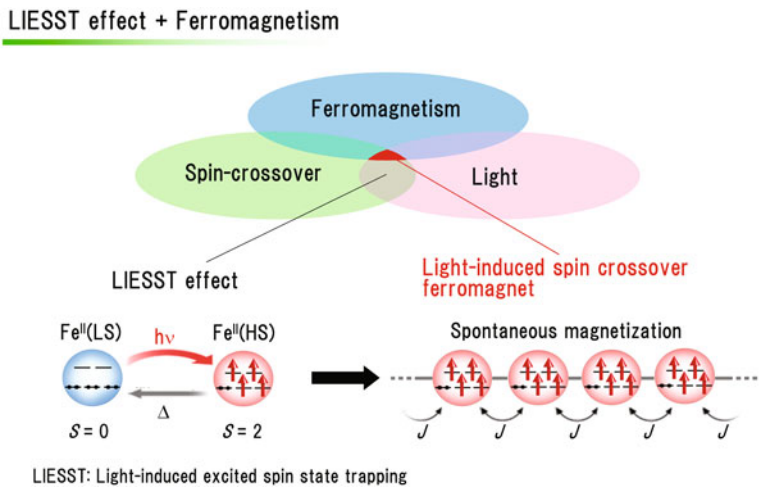

Fig. 26.2 Concept of combining LIESST effect and light-induced ferromagnet

of metal-complex and coordination chemistry. Spin-crossover is the change between iron low-spin and iron high-spin caused by stimuli, for example, light-irradiation. In this case, light irradiation changes the material's property due to the LIESST effect, or simply, photo-induced spin-crossover behavior.

If ferromagnetism is coupled with this property, we can image light-induced spin-crossover ferromagnetism, and spontaneous magnetization is expected to be caused by light-irradiation. This idea is very simple—I think that many scientists considered this simple idea—but before this work, nobody succeeded in observing this phenomenon. The reason is because, in this LIESST effect, the metal cation shows a very large volume change of 5 or 10%. Furthermore, the superexhange interaction between these two paramagnetic species depends on the distance between the metal cations. In the case of a spin crossover metal complex, the super-exchange interaction is very weak, and therefore, spontaneous magnetization cannot be observed.

According to this scenario, we considered demonstrating a light-induced spin-crossover magnetiztion using this material (Fig. 26.3). This material consists of iron and octacyanoniobate with 4-pyridinealdoxime. This material is prepared by mixing these reagents. Iron is coordinated to four nitrogen atoms of 4-pyridinealdoxime and two nitrogen atoms of cyano groups of octacyanoniobate. It has a three-dimensional complicated crystal structure.

We measured the magnetic property of this material (see Fig. 26.4). You can see that, at room temperature and higher temperatures, the magnetic property is derived from iron (II) high-spin and niobium paramagnetic spin. However, with decreasing temperature, magnetization drops abruptly at 130 K. In this low-temperature phase,

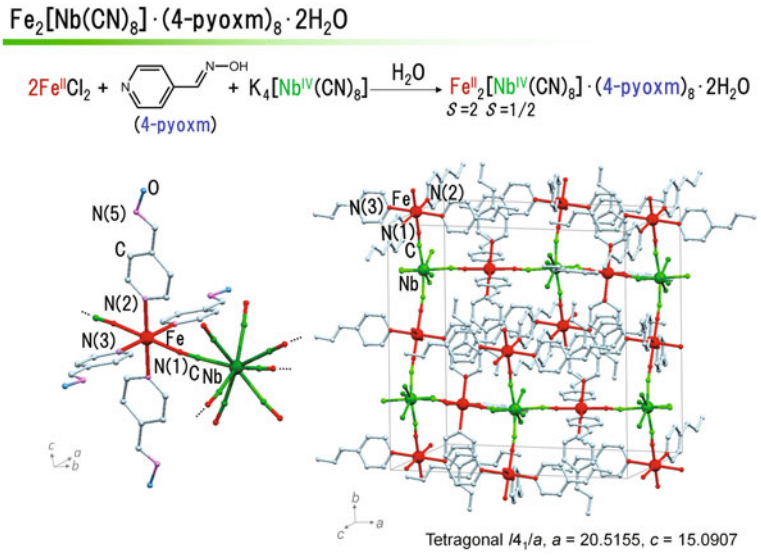

Fig. 26.3 Crystal structure of $Fe_2[Nb(CN)_8] \cdot (4\text{-pyoxm})_8 \cdot 2H_2O$

about 80% of the iron ion is converted from high-spin to low-spin. The iron in the low-temperature phase is basically in the low-spin state. This spin-crossover behavior was also confirmed by Mössbauer spectroscopy and low temperature UV-vis spectroscopy.

Next, we irradiated light onto the sample (Fig. 26.5). Before light irradiation, this material based on iron(II) low-spin and niobium does not show a long-range magnetic ordering, but, by light irradiation, high-spin state is induced, and then a spontaneous magnetization is observed. The Curie temperature is 20 K. At the same time, a

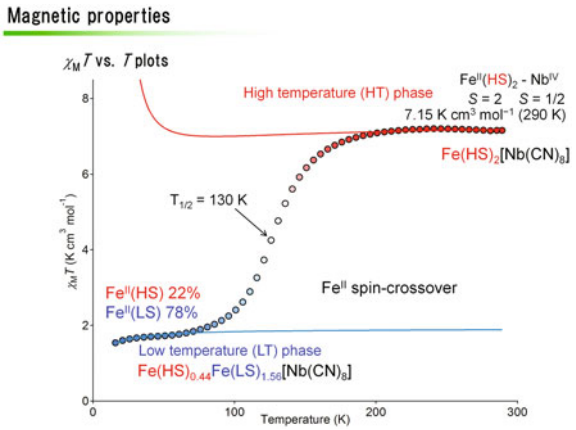

Fig. 26.4 Spin-crossover phenomenon in $Fe_2[Nb(CN)_8] \cdot (4\text{-pyoxm})_8 \cdot 2H_2O$ observed by magnetic measurements

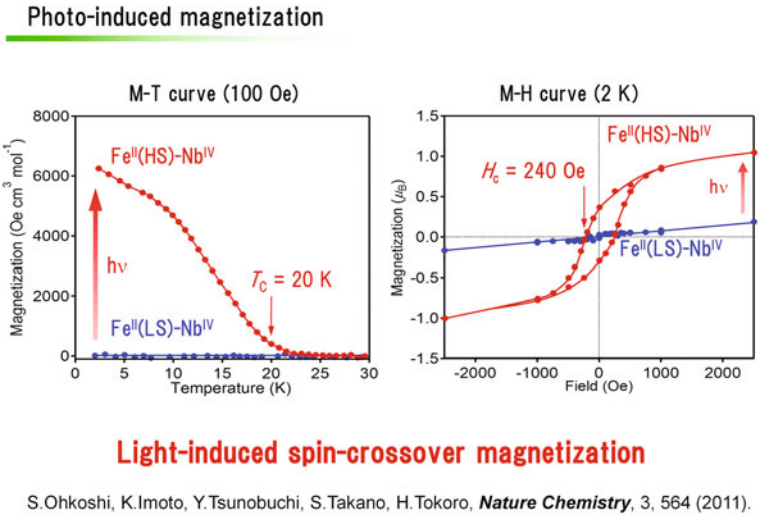

Fig. 26.5 Light-induced spin-crossover magnetization in $Fe_2[Nb(CN)_8] \cdot (4\text{-pyoxm})_8 \cdot 2H_2O$

magnetic hysteresis loop is also observed with a coercive field of 240 Oe. This is the first example of light-induced spin-crossover magnetism. In this case, the spontaneous magnetization is due to the ferrimagnetic ordering of niobium and iron(II) high-spin.

In the next material, we changed the ligand from 4-pyridinealdoxime to 4-bromopyridine (Fig. 26.6). The crystal structure is very similar. However, we checked this material using single-crystal analysis, and surprisingly, this material has two types of crystal structure. One of them is plus, the other is minus, and my student picked up many of these single crystals, about 200 crystals, and checked each of them. You can see that this material has a chiral structure.

In such a material, we can expect a new interesting phenomenon, i.e., coupling between chirality and photomagnetism (Fig. 26.7). This material is a chiral photomagnet. In such a chiral photomagnet, we expect several types of new phenomena. For example, optical control of magnetization-induced second-harmonic generation, the Magnetization-induced second harmonic generation (MSHG) effect, or optical control of the magneto-chiral dichroism behavior. Since this is the first example of a chiral photomagnet, we tried to measure these phenomena of MSHG and magneto-chiral dichroism (MChD).

Before moving on, it should be stated that we have previously reported magnetization-induced second-harmonic generation in various materials (Fig. 26.8) [13–19]. We have been studying this behavior for 15 years. Basically, in the case of magnetic materials, second-harmonic generation principally cannot be observed because the crystal structure of the usual magnetic materials are centrosymmetric. In such a case, second-harmonic generation is forbidden. But, chemists can prepare non-centrosymmetric crystal-structured materials using a molecule-based

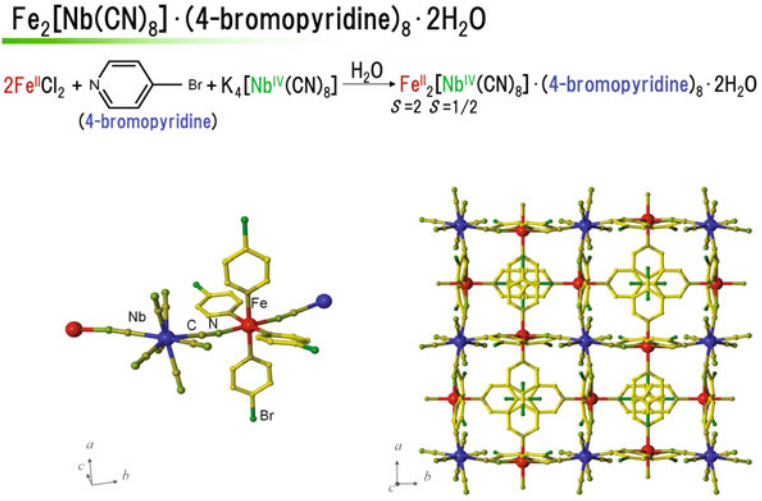

Fig. 26.6 Crystal structure of $Fe_2[Nb(CN)_8] \cdot (4\text{-bromopyridine})_8 \cdot 2H_2O$

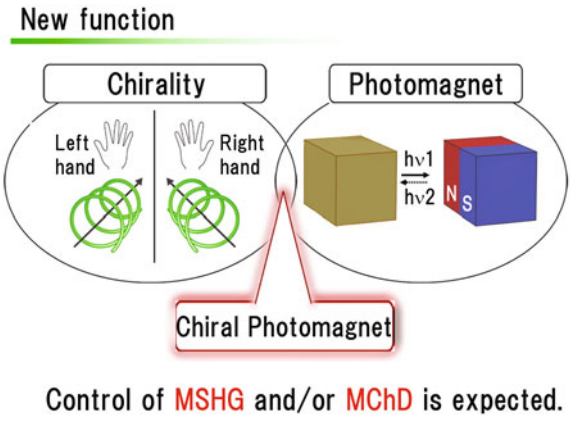

Fig. 26.7 Concept of combining chirality and photomagnetism to exhibit new functionalities such as control of MSHG and MChD by light

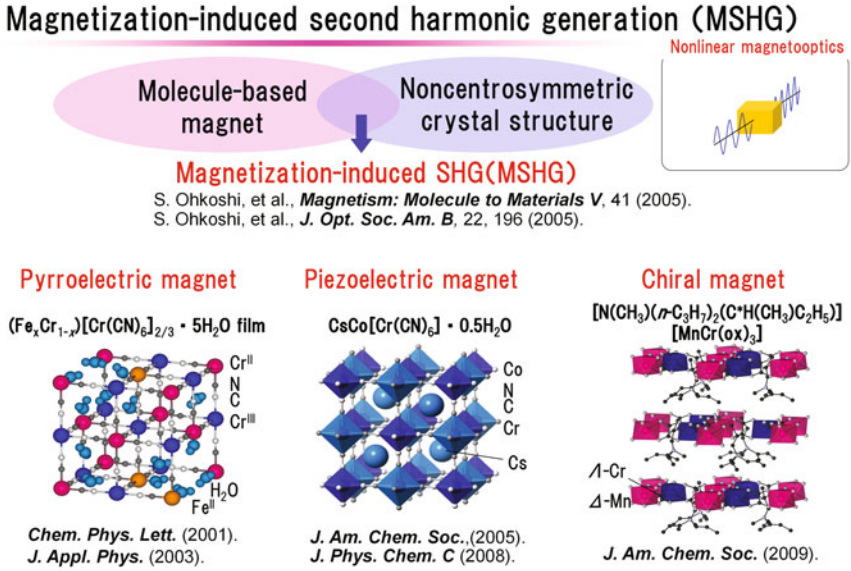

Fig. 26.8 Background researchs on magnetization-induced second-harmonic generation in molecule-based magnets with non-centrosymmetric crystal structures

magnet. Here are some examples that we have reported. In such materials, we observed magnetization-induced second-harmonic generation in a pyroelectric magnet, a piezoelectric magnet, and a chiral magnet.

26.3 Chiral Photomagnet

WWe studied the magnetic and optical properties of the chiral material, $Fe_2[Nb(CN)_8] \cdot (4\text{-bromopyridine})_8 \cdot 2H_2O$ (Fig. 26.9), e.g., the magnetic properties of this material. This material also exhibits spin-crossover behavior with a small hysteresis (Fig. 26.10). At the same time, we measured second-harmonic generation of this material because both the high-temperature phase and the low-temperature phase have non-centrosymmetric chiral-crystal structures.

First, we measured second-harmonic generation of this material at room temperature. Second-harmonic intensity is not so strong, and with decreasing temperature, the intensity increased with hysteresis, and with increasing temperature second

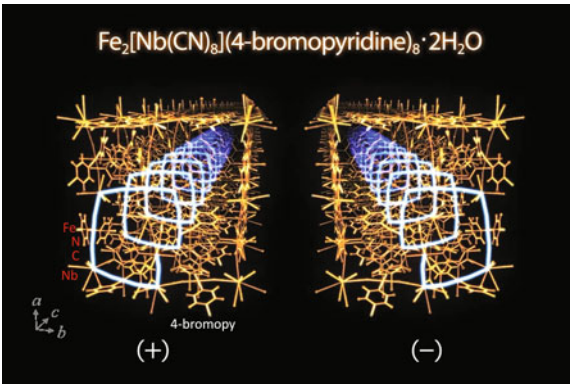

Fig. 26.9 Chiral crystal structure of $Fe_2[Nb(CN)_8] \cdot (4\text{-bromopyridine})_8 \cdot 2H_2O$

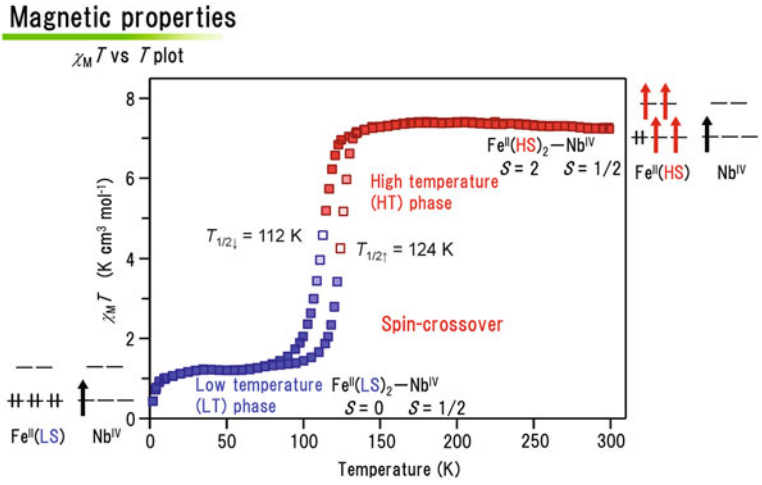

Fig. 26.10 Spin-crossover phenomenon in $Fe_2[Nb(CN)_8] \cdot (4\text{-bromopyridine})_8 \cdot 2H_2O$ observed by magnetic measurements

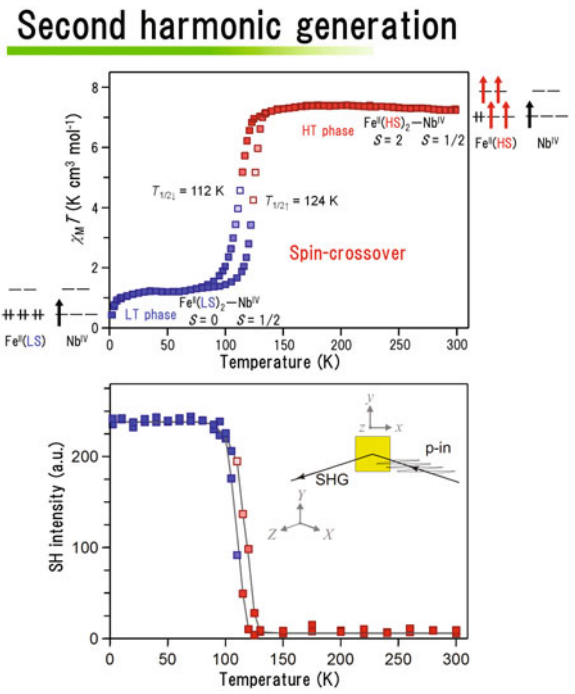

Fig. 26.11 Spin-crossover phenomenon observed in $Fe_2[Nb(CN)_8] \cdot (4\text{-bromopyridine})_8 \cdot 2H_2O$ by magnetic measurements (*upper*) and second-harmonic generation (SHG) (*lower*)

harmonic generation (SHG) intensity recovered to the original level (Fig. 26.11). In the present system, the high-temperature phase has a tetragonal structure with light color, but the low-temperature phase has an orthorhombic crystal structure and possesses deep color. Therefore, from the Kleinman's rule, the high-temperature phase shows weak second-harmonic generation, and the low-temperature phase exhibits strong second-harmonic generation.

Next, we checked the photomagnetic property of this material (Fig. 26.12). This material also exhibits photomagnetization with a Curie temperature of 15 K. This is caused by 473-nm light irradiation. Then, another light, a 785-nm light, was irradiated onto the sample. We observed a decrease of magnetization and Curie temperature. This phase is clearly a different phase because the Curie temperature is different. We named the first phase photo-induced phase I and the second phase photo-induced phase II. Before light-irradiation the material is in the low temperature phase. Photo-induced phase I and photo-induced phase II can be reversibly changed by irradiating with the two types of light sources (Fig. 26.13).

A magnetic hysteresis loop is also observed in the magnetization versus field, and the reversible change is observed by the irradiation of two different types of light (Figs. 26.14 and 26.15). The mechanism is shown in Fig. 26.16. Before light-irradiation, it is in the low-temperature phase, and by the light-irradiation, through the excited states, $^1A_1$ changes to $^5T_2$. This is the high-spin state. Conversely,

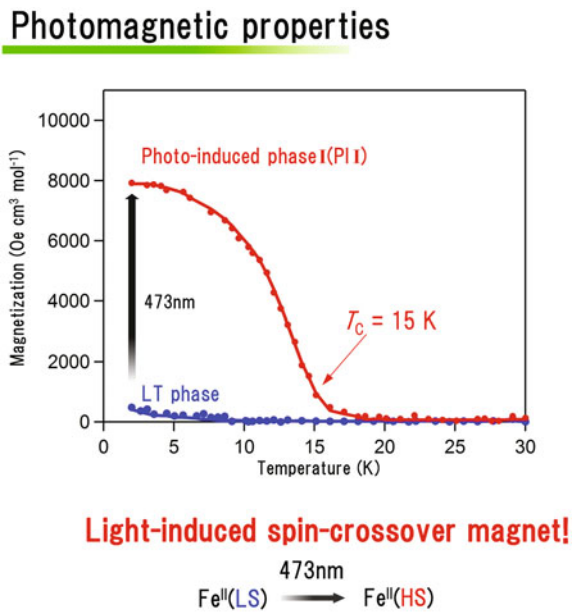

Fig. 26.12 Light-induced spin-crossover magnetization in $Fe_2[Nb(CN)_8] \cdot (4\text{-bromopyridine})_8 \cdot 2H_2O$

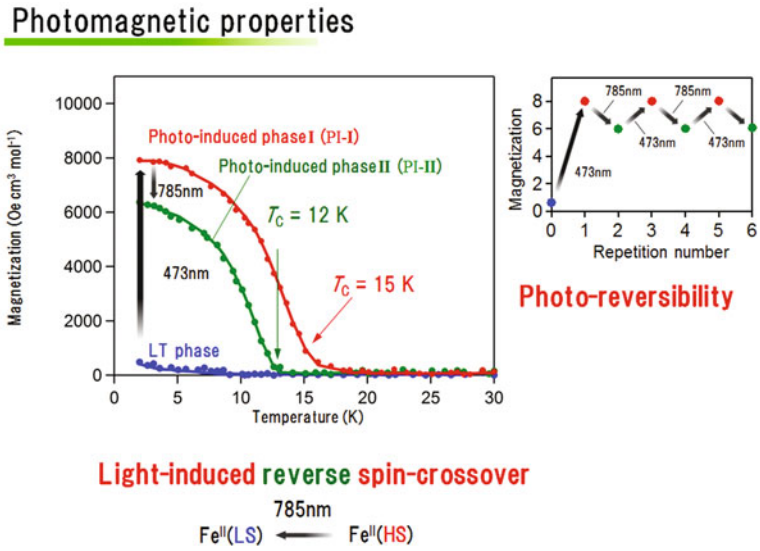

Fig. 26.13 Light-induced reverse spin-crossover magnetization in $Fe_2[Nb(CN)_8] \cdot (4\text{-bromopyridine})_8 \cdot 2H_2O$ with photo-reversibility

this high-spin state excited by the 785-nm light returns to the original low-spin state. This is reversible photo-induced spin-crossover.

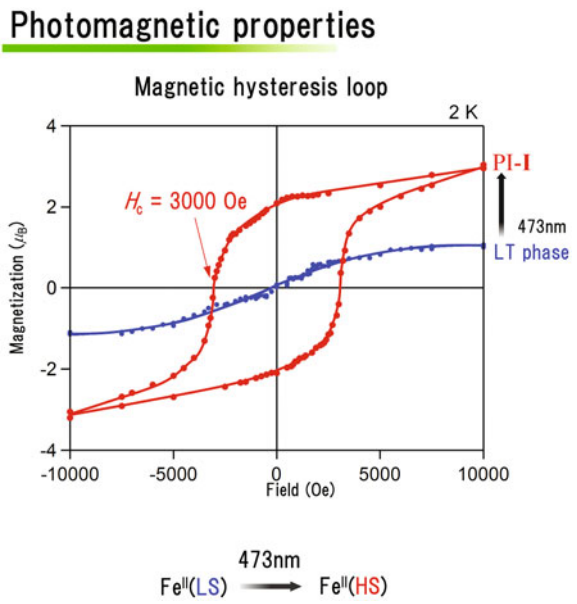

Fig. 26.14 Magnetic hysteresis of $Fe_2[Nb(CN)_8] \cdot (4\text{-bromopyridine})_8 \cdot 2H_2O$ by light-induced spin-crossover

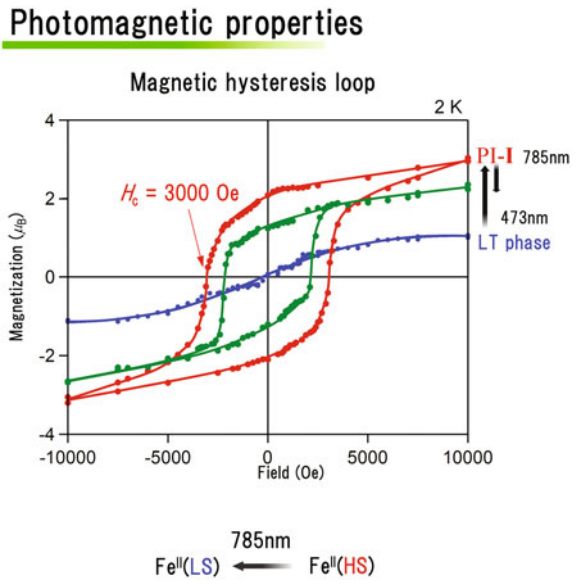

Fig. 26.15 Magnetic hysteresis of $Fe_2[Nb(CN)_8] \cdot (4\text{-bromopyridine})_8 \cdot 2H_2O$ by light-induced reverse spin-crossover

In this state, the iron site is bridged by the niobium ion, and niobium is $S = 1/2$. After light-irradiation, this effect occurs. High-spin iron and niobium leads to ferromagnetic ordering. The superexchange interaction is remarkably high, i.e., $-5.2\ cm^{-1}$. The reverse effect is also observed.

So, the low-temperature phase changes to photo-induced phase I, and then, to photo-induced phase II. We conducted measurements of various optical properties

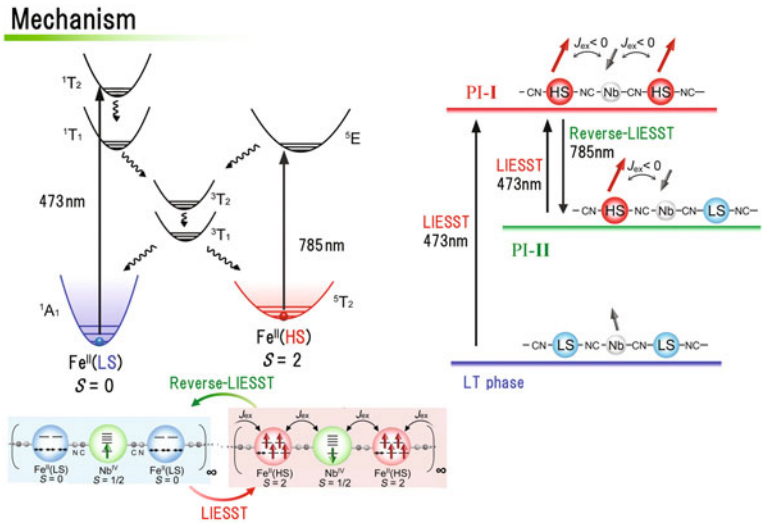

Fig. 26.16 Mechanism of light-induced spin state trapping (LIESST) and reverse LIESST effect in $Fe_2[Nb(CN)_8] \cdot (4\text{-bromopyridine})_8 \cdot 2H_2O$

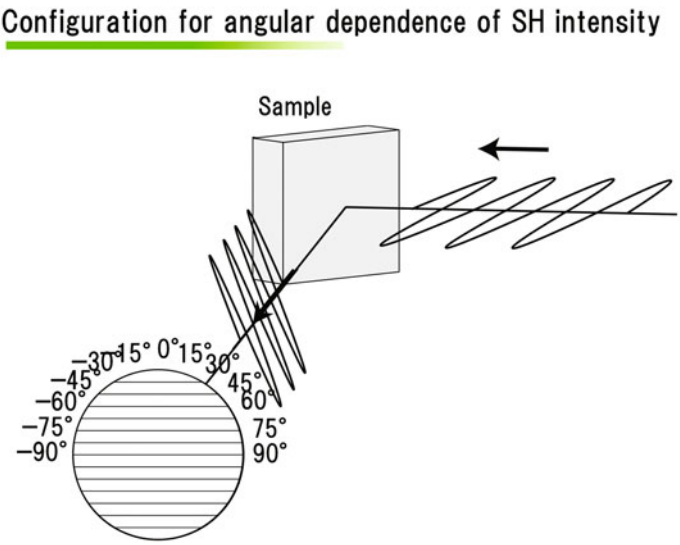

Fig. 26.17 Measurement method of angular dependence of SH intensity

and found that half of the high-spin iron is converted to low-spin iron from photo-induced phase I to photo-induced phase II. Unfortunately, this photo-induced phase I cannot be converted completely to the low-spin state and stops at an intermediate state, with a ratio of high-spin and low-spin of one-to-one. The photo-induced phase I and photo-induced phase II are reversible through light irradiation.

We measured second-harmonic generation of this photo-induced magnetization behavior using a simple optical-coordinate polarizer (Fig. 26.17). We measured the low-temperature phase, and also under light irradiation. As for low temperature phase, p-in light is irradiated onto the crystal, and then vertical second-harmonic-generation light is observed, as shown in the angle dependence of SH intensity (Fig. 26.18). By irradiation of 473-nm light, the direction of second-harmonic intensity is opposite. The minimum is at 0°. This means that horizontal second-harmonic-generation light is radiated from this sample. Furthermore, with 785-nm light, a maximum SH intensity is observed at 0° and returns to vertical SH light. Between these two phases, the reversible change of the polarization plane of SH light switches by almost 90°, without ellipticity.

vFigure 26.19 shows tensor analysis to understand the origin of the 90° switching by light irradiation. This is a very complicated analysis, but here shown is the simple explanation. After light-irradiation, photo-induced phase I and photo-induced phase II reversibly switch. Comparing the tensors of these two phases, the magnetic term shown with red circles is dominant in photo-induced phase I, and the crystal term shown with green circles is dominant in photo-induced phase II. This difference changes the polarization plane of the second-harmonic generation.

Second-harmonic intensity is expressed by the crystal term and the magnetic term (Fig. 26.20). When the crystal term is stronger than the magnetic term, the maximum of second-harmonic intensity is at 0°. When the magnetic term overcomes the crystal term, the minimum is at 0°. This is a simple explanation of this phenomenon.

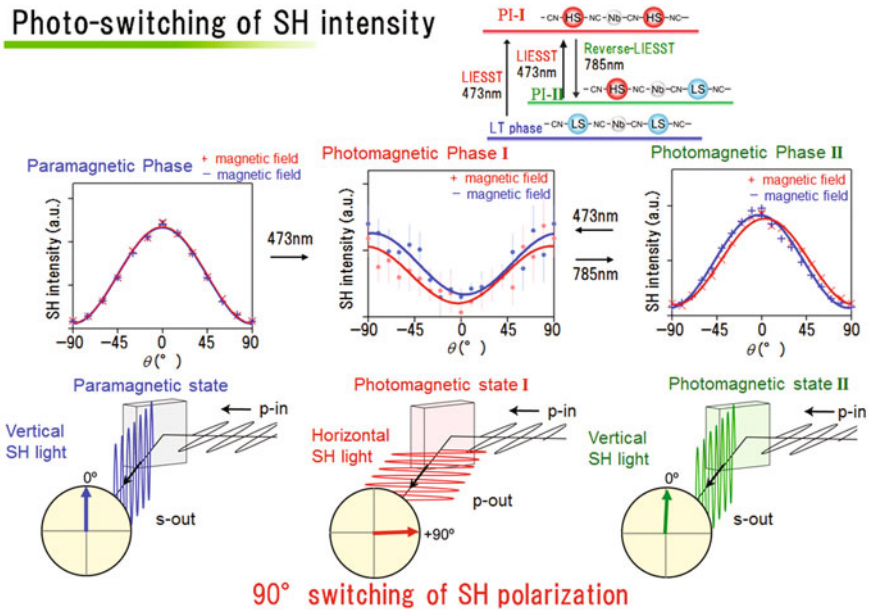

Fig. 26.18 Photo-switching phenomenon of SH polarization in $Fe_2[Nb(CN)_8] \cdot (4\text{-bromopyridine})_8 \cdot 2H_2O$

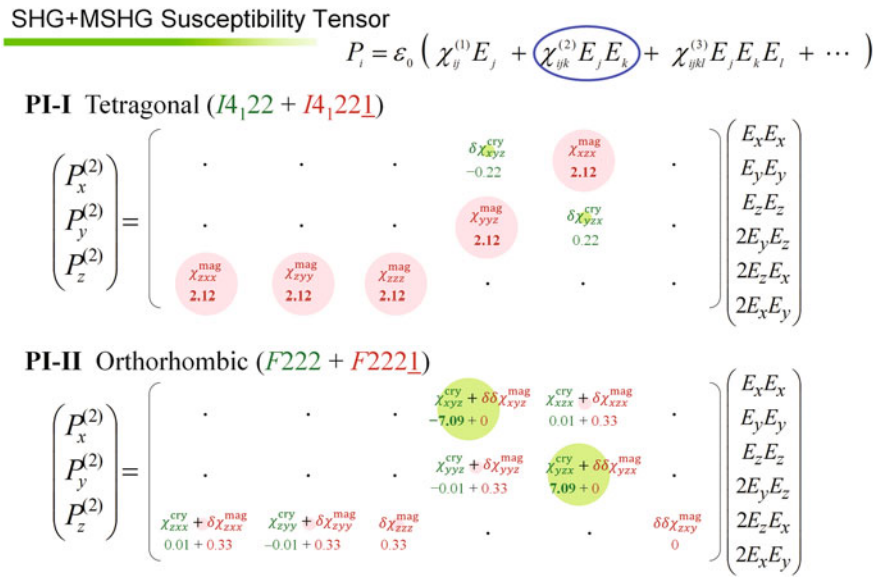

Fig. 26.19 SHG and MSHG susceptibility tensors of the photo-induced phase I and photo-induced phase II of $Fe_2[Nb(CN)_8] \cdot (4\text{-bromopyridine})_8 \cdot 2H_2O$

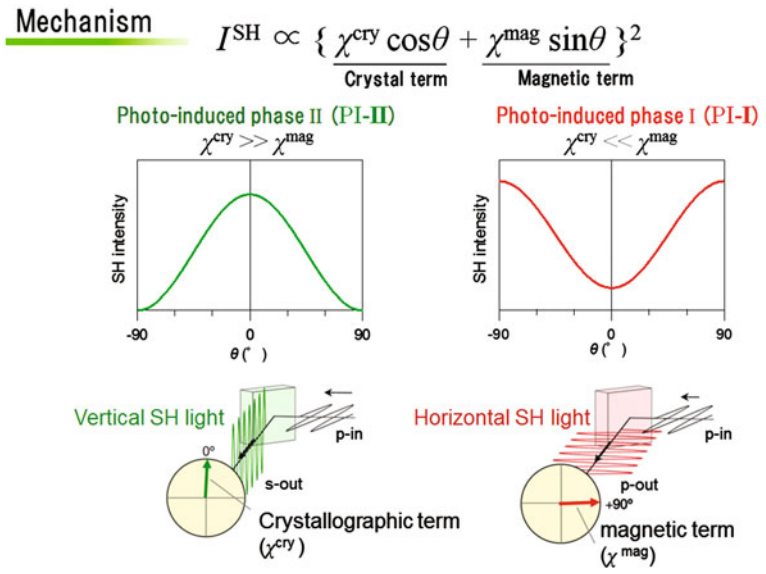

Fig. 26.20 Mechanism of 90° optical switching of the SH polarization in $Fe_2[Nb(CN)_8] \cdot (4\text{-bromopyridine})_8 \cdot 2H_2O$

Here is the future work that we are considering: Not only 90° switching, but also switching of intermediate angles is possible by controlling the light intensity or magnetization (Fig. 26.21). This means that this crystal is applicable not only in a binary system but also in denary or n-ary systems. For example, n-ary optical recording memory could be possible (Fig. 26.22).

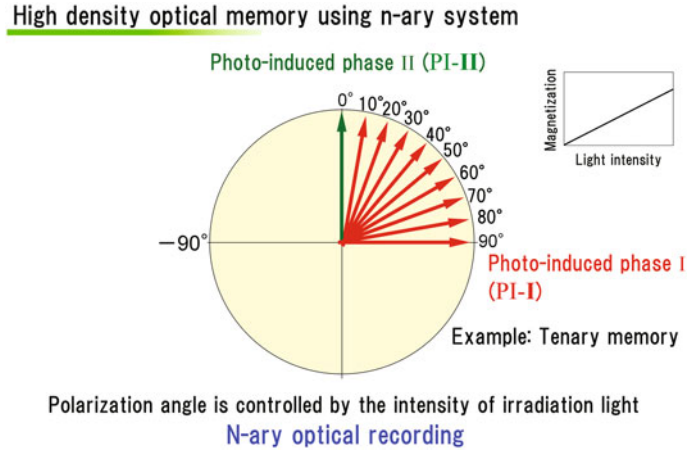

Fig. 26.21 Possible application of the observed optical-switching phenomenon as a high-density optical memory using n-ary system

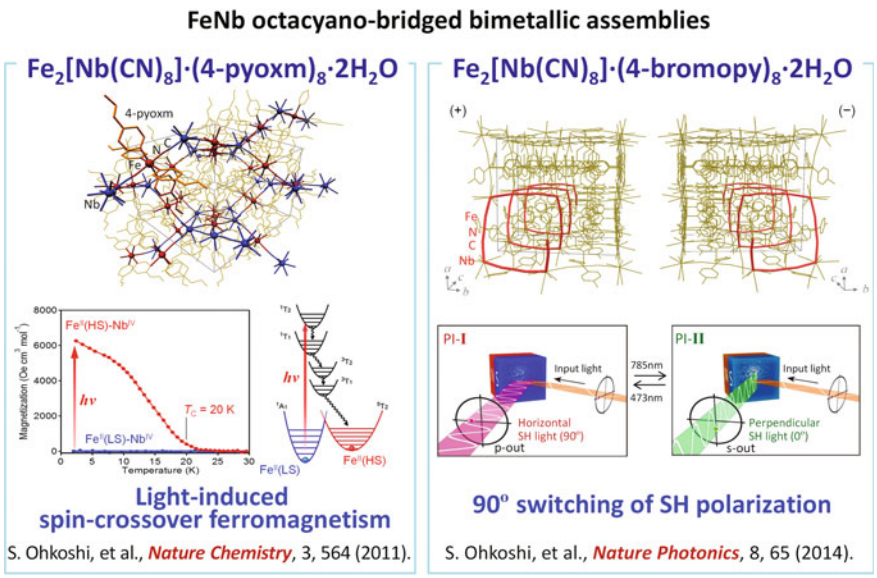

Fig. 26.22 Summary of "Magneto-optical functionalities in cyano-bridged bimetal assemblies and metal oxide nanomaterials"

References

1. S. Ohkoshi, H. Tokoro, Acc. Chem. Res. **45**, 1749–1758 (2012)
2. S. Ohkoshi, K. Imoto, Y. Tsunobuchi, S. Takano, H. Tokoro, Nat. Chem. **3**, 564–569 (2011)
3. S. Ohkoshi, S. Takano, K. Imoto, M. Yoshikiyo, A. Namai, H. Tokoro, Nat. Photonics **8**, 65–71 (2014)
4. T. Mahfoud, G. Molnar, S. Bonhommeau, S. Cobo, L. Salmon, P. Demont, H. Tokoro, S. Ohkoshi, K. Boukheddaden, A. Bousseksou, J. Am. Chem. Soc. **131**, 15049–15054 (2009)
5. E. Pardo, C. Train, G. Gontard, K. Boubekeur, O. Fabelo, H. Liu, B. Dkhil, F. Lloret, K. Nakagawa, H. Tokoro, S. Ohkoshi, M. Verdaguer, J. Am. Chem. Soc. **133**, 15328–15331 (2011)
6. S. Ohkoshi, K. Arai, Y. Sato, K. Hashimoto, Nat. Mater. **3**, 857–861 (2004)
7. S. Ohkoshi, Y. Abe, A. Fujishima, K. Hashimoto, Phys. Rev. Lett. **82**, 1285–1288 (1999)
8. S. Ohkoshi, A. Fujishima, K. Hashimoto, J. Am. Chem. Soc. **120**, 5349–5350 (1998)
9. E. Pardo, C. Train, H. Liu, L.M. Chamoreau, B. Dhkil, K. Boubekeur, F. Lloret, K. Nakatani, H. Tokoro, S. Ohkoshi, M. Verdaguer, Angew. Chem. Int. Ed. **51**, 8356–8360 (2012)
10. S. Ohkoshi, Y. Tsunobuchi, T. Matsuda, K. Hashimoto, A. Namai, F. Hakoe, H. Tokoro, Nat. Chem. **2**, 539–545 (2010)
11. A. Namai, M. Yoshikiyo, K. Yamada, S. Sakurai, T. Goto, T. Yoshida, T. Miyazaki, M. Nakajima, T. Suemoto, H. Tokoro, S. Ohkoshi, Nat. Commun. **3**, 1035 (2012)
12. A. Namai, S. Sakurai, M. Nakajima, T. Suemoto, K. Matsumoto, M. Goto, S. Sasaki, S. Ohkoshi, J. Am. Chem. Soc. **131**, 1170–1173 (2009)
13. K. Inoue, S. Ohkoshi, H. Imai, in *Magnetism: Molecules to Materials V*, ed. By J.S. Miller, M. Drillon (Wiley-VCH, Weinheim, 2005) (Chapter 2)
14. S. Ohkoshi, J. Shimura, K. Ikeda, K. Hashimoto, J. Opt. Soc. Am. B **22**, 196–203 (2005)
15. K. Ikeda, S. Ohkoshi, K. Hashimoto, Chem. Phys. Lett. **349**, 371–375 (2001)
16. K. Ikeda, S. Ohkoshi, K. Hashimoto, J. Appl. Phys. **93**, 1371–1375 (2003)
17. T. Nuida, T. Matsuda, H. Tokoro, S. Sakurai, K. Hashimoto, S. Ohkoshi, J. Am. Chem. Soc. **127**, 11604–11605 (2005)
18. S. Ohkoshi, S. Saito, T. Matsuda, T. Nuida, H. Tokoro, J. Phys. Chem. C **112**, 13095–13098 (2008)
19. C. Train, T. Nuida, R. Gheorghe, M. Gruselle, S. Ohkoshi, J. Am. Chem. Soc. **131**, 16838–16843 (2009)

Chapter 27
Helium-Ion Microscope as a Tool for Gentle Modification on the Nanoscale

Oleg Vyvenko

The "nanoobject" is defined as an object that has a size less than 100 nm in one direction. But the most pronounced differences in material properties between the massive and nano-sized object appear when one of its dimensions becomes typically less than 10 nm, due to quantum-confinement effects.

Today, there was a presentation on X-ray creation by a powerful laser with the goal of obtaining a new technique for photolithography to reduce the size of electronic components of a microprocessor. It was mentioned that an element size as small as 15 nm could be achieved with such a technique, but it is still above the crucial 10 nm.

Other size-dependent effects are known for pairs or arrays of nanoparticles. The excitation of them with the light or with electron beam generates localized surface plasmons, which are electron-density oscillations concentrated on the exterior of nanostructured materials. Research into plasmonic devices is an active field, with applications such as bio-sensing, chemical sensing, spintronics and nano-photonics. The interparticle coupling grows in strength inversely proportional to the cube of the spatial separation between them. Besides, the size and the inter-particle separation, their particular shapes affect the optical response drastically. For instance, when nanoparticles of the some size of sphere-like shapes show plasmonic resonance at about 400 nm, ones of the triangle-like shape will generate light with a wave length at around 800 nm. That is why it is very important to have a tool to modify nano-object dimensions and shapes on the scale of less than 10 nm.

One of the approaches to produce nano-scaled objects is self-organization that takes place in some forms of chemical reactions, molecular beam epitaxy growth of heterostructures, and so on. The conventional direct process to get the desirable predefined shape and size of the object is the already-mentioned photo-resist

O. Vyvenko (✉)
V.A. Fok Institute of Physics and Interdisciplicary Resource Center, St. Petersburg State University, Uliyanovskaja 1, Petrodvoretz, St. Petersburg 198504, Russia
e-mail: vyvenko@nano.spbu.ru

K. Yamanouchi (ed.), *Progress in Photon Science*, Springer Series in Chemical Physics 115, DOI 10.1007/978-3-319-52431-3_27

lithography that is used for industrial production of microelectronic devices. For this goal, one can use photons, electrons, and ions. However, there are some kinds of limitations of the technique due to particular properties of the photo-resist material. Direct pattern modification by the evaporation of material or defect creation can actually be done with the help of ions only.

Let us compare the minimum element size that can be achieved with various techniques. For state-of-the art photon lithography, it is about 30 nm; for electron-beam lithography, it is limited by 20 nm; and, for the direct pattering with an ion beam, it depends on the ion mass. The lighter the ion, the smaller the size of the modified region. It was demonstrated, for instance, that a heavy gallium ion could create holes in graphene of a diameter of 30 nm, whereas, with He ions, we were able to obtain them as tiny as 2 nm [1].

In our interdisciplinary resource center for nanotechnology, we have diverse ion-beam-assisted sample-preparation techniques: gallium Ga focused-ion beam (FIB), argon-beam etching, sputtering, and final ion-beam polishing. We also have diverse electron microscopes for imaging and for lithography processing. Today, I will talk about the He-ion microscope which is equipped also with a lithography system.

The helium-ion microscope (HeIM) is a direct descendant of the field-ion microscope invented by Mueller and Bahadur in 1950, which enabled obtainment of the first atomic images in the history of mankind (Fig. 27.1). However, the first scanning helium (He)-ion microscope became commercially available in 2007, and

Fig. 27.1 Helium-ion microscope at St. Petersburg State University

our microscope in St. Petersburg has a serial number 5. Presently, there are about 40 in the world, and recently three of them were installed in Japan. The problem that stopped earlier development of HeIM was the technology of the creation of the stable ion source that was solved only in 2001.

To understand how the He-ion source works, there are two types of electron sources. The first one is based on a simple thermal electron-emission process from metals into the vacuum. Usually, in this case, the source is a hot tungsten wire. Another type in use is the electron emission via electron tunneling through the triangle-potential barrier formed under application of a high electric field in the vicinity of the tungsten tip. The source of the ion microscope is just the second type, but it worked with the opposite direction of the electric field in the presence of a small amount of helium. When the ions approach the tungsten tip, they become ionized, and the electrons move from the helium atoms towards the metal. The temperature of the tip has to be sufficiently lowered to increase the probability of ionization.

The sharpest stable atomic configuration of the tungsten tip is the trimer (see Fig. 27.2). The most "intense" tungsten atom is selected by a diaphragm, and that

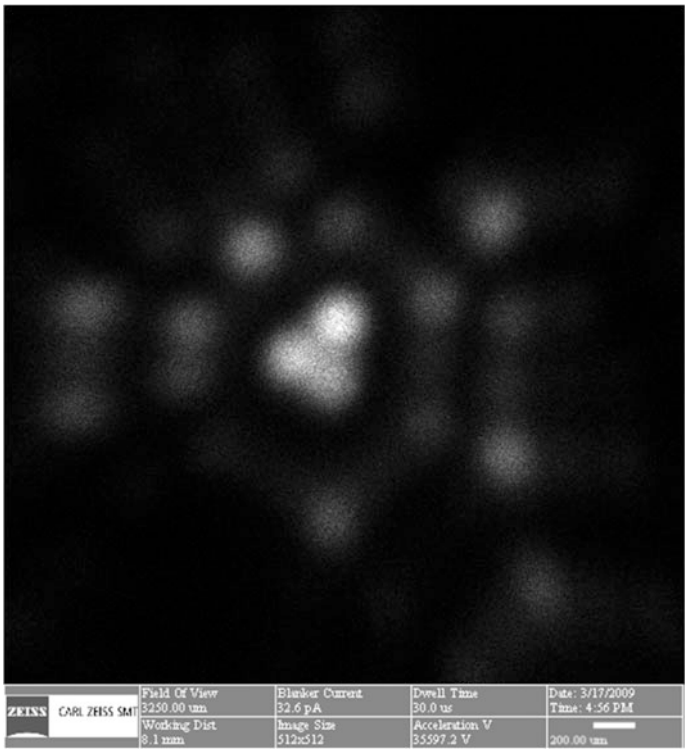

Fig. 27.2 The ion-microscopy image of tungsten atoms working as sources of the ions. The trimer of helium atoms is a stable atomic-tip configuration

single atom is used as an ion source in the He-ion microscope. Since the size of the tungsten atom is about 0.25 nm, the latter value defines the theoretical image resolution of HeIM.

In fact, the final practical resolution for nanofabrication and imaging is defined not only by the size of the source but rather by the ion-scattering process within the material under investigation. The lighter helium ions penetrate significantly deeper into the target without noticeable energy losses than, for instance, heavy gallium ions. Accordingly, a He-ion beam remains be well collimated beyond the depth of secondary-electron escape, making possible realization of the theoretical resolution defined by the ion-source size [2]. A resolution of 0.35 nm was demonstrated for some recent models of HeIM.

Beside the source size, there are also significant differences in the yield and angular and energetic distributions of secondary electrons (SE) that are produced due to the interaction of ions or electrons with the matter. Angular distribution of SE in SEM consists of a sharp peak in the direction of the incident beam and a broad maximum due to cold SE2, created by the back-scattered electrons within the target. For the He-ion microscope, there is really only one sharp peak, which is important both for imaging and for cutting. Another thing that we actually discovered [3] is that SE produced by helium ions have significantly lower energies ions than SE under electron excitation (see Fig. 27.3). This is very important just for the indirect lithography where secondary electrons play a major role in photo-resist damage and that reduce proximity effects.

At last, every He ion produces up to five secondary electrons, whereas the SE yield in SEM is less or slightly above unity. This implies that we can use a very low current (typically sub-picoamp), and a quite short acquisition time for imaging and for indirect lithography. For instance, the current that is needed to produce SE images in SEM is more than 10 pA, which is sufficient to melt gallium (Ga) arsenic

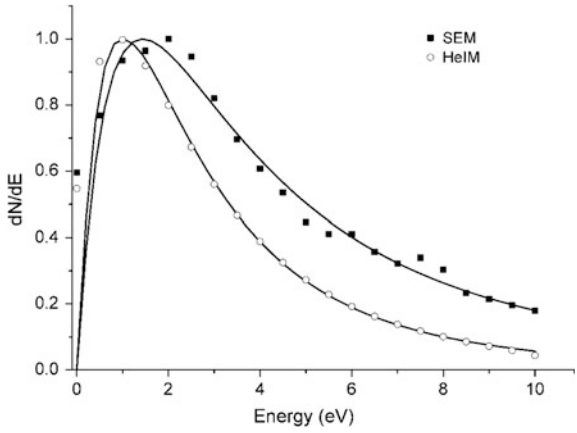

Fig. 27.3 Energy distribution of secondary electrons in scanning electron (SEM) and helium-ion microscopes (HeIM)

nanowires of a thickness below 50 nm. The corresponding current in a helium (He)-ion microscope can be reduced approximately by a factor 100 times, which does not destroy the investigated objects.

Finally, due to the high SE yield and the inherent positive charge of helium (He) ions, the surface of the investigated insulating samples becomes positively charged, but this charge can be easily compensated with the flux of negatively charged electrons. To reach this goal, a HeIM is equipped with a flat electron gun.

Fig. 27.4 demonstrate SEM and HeIM images of graphene on silicon dioxide [1]. One can see that the monolayer graphene can be perfectly imaged like a sheet of paper. The holes produced by Ga-FIB (Fig. 27.4A) is noticeably bigger that those produced by HeIM (Fig. 27.4B). Such kind of holes in 2D electronic system forms edge electronic states that exhibit some interesting physical properties.

The interaction of helium (He) ions with materials accompany the creation of the damaged region in the material under exposure. Conventionally, an organic photoresist is used for the patterning. A pattern size as small as 6 nm could be obtained as it was demonstrated in [4]. In applications for nanophotonics, a Fresnel lens or a network structure of the features of particular shapes (meta-materials) can be produced.

What we are developing now are some other improvements of this indirect technology without the usage of photoresist, but using the fact that, under the action of helium (He) ions, huge amounts of defects are created in crystalline materials. These defects produce changes in the local chemical potential. These results enhance chemical etching of the exposed region. An example of that is presented in Fig. 27.5 where the HeIM SE-image of a groove of a width of about 10 nm in silicon nitride is shown.

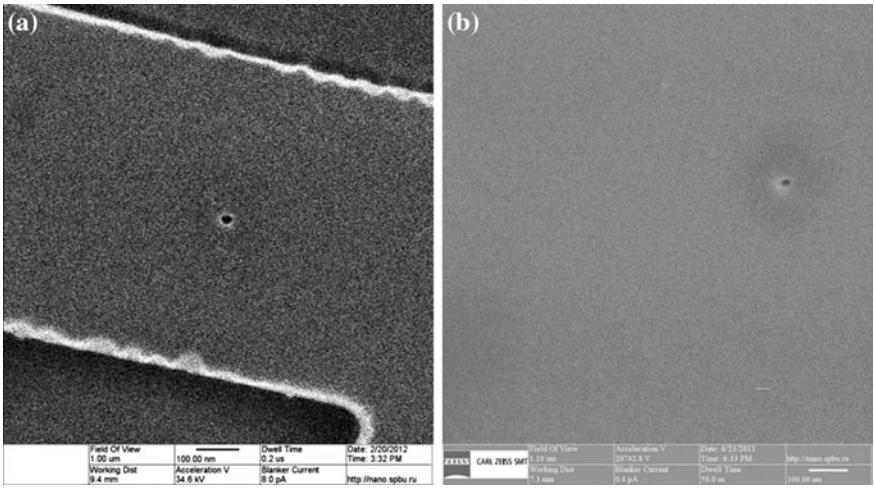

Fig. 27.4 SE HeIM images of graphene on silicon dioxide with the holes produced by Ga (*left*) and He (*right*) ion beam

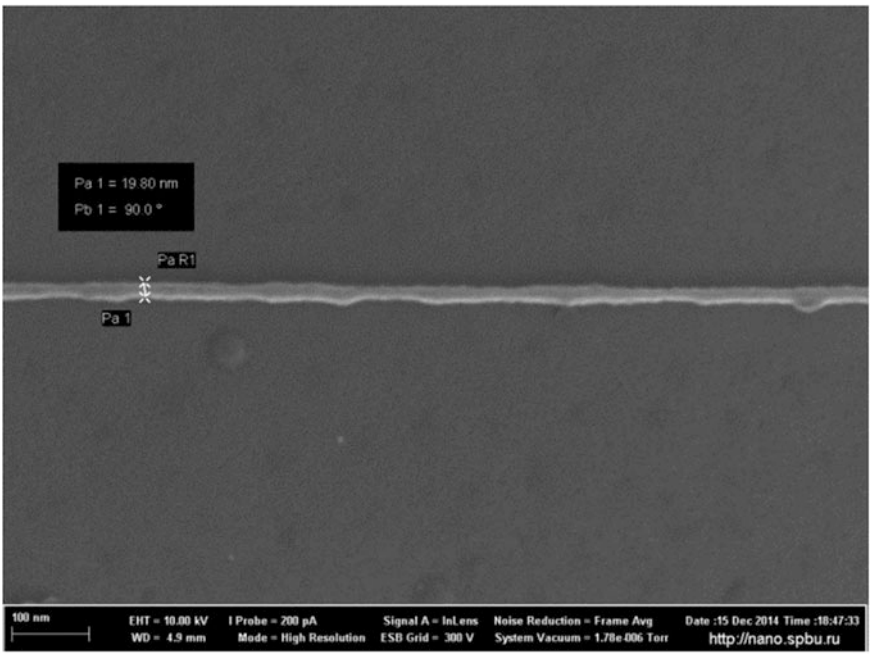

Fig. 27.5 The groove produced by chemical etching of a Si_3N_4 layer after the treatment with 40-kV He ions

Finally, I would like to mention a recent article from Daniel Pickard and other groups about a split-ball resonator [5]. It was shown that, when the slits are produced in nano-sized spheres, an effective plasmonic light source of various polarizations can be obtained.

Acknowledgements The experimental results presented in the figures were obtained by Dr. Yuri Petrov of the Interdisciplinary Resource Center for Nanotechnology of St. Petersburg State University, Russia.

References

1. Y.I. Latyshev et al., Sci. Rep. **4**, 7578 (2014)
2. K. Inai, K. Ohya, T. Ishitani, J. Electron. Microsc (Tokio), **56**, 163 (2007)
3. Y. Petrov, O. Vyvenko, in *Proceedings SPIE 8036, Scanning Microscopies 2011: Advanced Microscopy Technologies for Defense*, Homeland Security, Forensic, Life, Environmental, and Industrial Sciences, 80360O
4. V. Sidorkin et al., J. Vac. Sci. Technol. B **27**(4), L18–L20 (2009)
5. A.I. Kuznetsov et al., Nat. Commun. **5**, 3104 (2014)

Index

K. Yamanouchi (ed.), *Progress in Photon Science*, Springer Series in Chemical Physics 115, DOI 10.1007/978-3-319-52431-3